THE CONTROLLED CRYSTALLIZATION AND ANISOTROPY OF FIBROUS CALCIUM METASILICATE

RUTH MINNA WESTON, B.Sc., A.R.S.M.

A thesis submitted for the degree of
Doctor of Philosophy of the University of London

Metallurgy and Materials Science Department,
Imperial College of Science and Technology,
University of London.

1977

ABSTRACT

Surface nucleated, unidirectional fibrous crystallization of calcium metasilicate was investigated in approximately metasilicate composition glasses of the $CaO-Al_2O_3-SiO_2$ system, containing either zinc oxide or sodium oxide as a crystal growth accelerator, by an isothermal heat treatment technique. Two compositions were selected as giving densely nucleated, well aligned spherulitic type fibres of the low temperature calcium metasilicate polymorph, one with a mainly crystalline interfibre matrix and the other with a residual glass matrix. Specimens for mechanical and other tests were prepared by sectioning bulk samples of the selected materials. Transverse or perpendicular fibre specimens were prepared from isothermally crystallized tiles, manufactured from glasses with crystal growth rates up to 5 microns per second. Longitudinal fibre specimens were prepared from intra-crucible devitrified glasses for crystal growth rates up to 2 microns per second, and from unidirectionally crystallized rods pulled directly from the melt, using a $CaO-ZnO-SiO_2$ glass with a growth rate greater than 10 microns per second. This was a novel modification of a newly developed technique, and enabled T-T-T diagrams to be drawn for the crystallization in this system.

The crystal growth kinetics were studied and from this the Keith and Padden theory of spherulitic crystal growth was verified for the devitrification of calcium metasilicate.

The thermal expansion characteristics, found using an automatic recording dilatometer, and the mechanical properties, investigated using long and short beam three-point bend tests, revealed that in macroscopic specimens the unidirectionally crystallized materials could be regarded as ceramic matrix composite materials.

ACKNOWLEDGEMENTS

This project was supported by a Science Research Council Research Studentship, the receipt of which is gratefully acknowledged. I also wish to thank Professor Ball for the provision of laboratory facilities in the Department of Metallurgy and Materials Science, Imperial College, Mr. Monk and Mr. Staff of the Analytical Services Department, Imperial College, for the EPMA and wet chemical analyses respectively, and the British Museum (Natural History) for the provision of samples.

Last, but not least, I would like to thank all the personnel of the Chemical Metallurgy Group for their assistance, both practical and moral, during the past three years, especially my supervisor Dr. P.S. Rogers.

TABLE OF CONTENTS

	Page
Abstract	1
Acknowledgements	3
List of Tables	10
List of Figures	16
List of Symbols	25
Chapter 1. INTRODUCTION	
1.1. Anisotropic Ceramics	
1.1.1. In Situ Composites	28
1.1.2. Orientated Glass-Ceramics	30
1.2. Structure of Silicate Glasses and Melts	34
1.3. Nucleation	40
1.3.1. Surface Nucleation	44
1.3.2. Internal Nucleation in Metasilicate Glasses Using CaF_2	46
1.4. Crystallization from Glasses and Melts	
1.4.1. Crystal Growth	47
1.4.2. Crystal Morphology	53
1.4.3. Rod Pulling Technique	68
1.5. The Crystallography of Phases Produced in the Selected Materials	
1.5.1. Calcium Metasilicate	72
1.5.2. Secondary Devitrification Products	74

Page

1.6. Thermal Expansion Characteristics of Silicate Materials

1.6.1. Glasses 75

1.6.2. Crystalline Materials 76

1.7. Mechanical Properties of Ceramics

1.7.1. Brittle Materials 78

1.7.2. Ceramic Matrix Composites 81

1.7.3. Bend Tests 88

Figures, Chapter 1 95

Chapter 2. EXPERIMENTAL TECHNIQUES

2.1. Preparation of Glasses 104

2.2. Preparation of Specimens for the Preliminary Assessment of a Glass 106

2.3. Measurement of Crystal Growth Rates

2.3.1. Heat-Treatment of Specimens 107

2.3.2. Preparation and Measurement of Thin Sections 110

2.4. X-Ray Diffraction Analysis

2.4.1. Powder Diffraction Analysis 113

2.4.2. Pin-Hole Transmission Analysis 115

2.5. Preparation of Tiles

2.5.1. Preparation of Glass Surface 116

2.5.2. Casting and Heat-Treatment of Tiles 118

2.5.3. Heat-Treatment Schedules 120

Page

2.6. Preparation of Crucible Grown Material 122

2.6.1. Heat-Treatment Schedules 125

2.7. Preparation of Rods 126

2.7.1. Rod Pulling Apparatus 127

2.7.2. Production of Rods 134

2.8. Preparation of Mechanical Test Specimens

2.8.1. From Tiles 139

2.8.2. From Intra-Crucible Material 142

2.8.3. From Rods 143

2.9. Three-Point Bend Tests

2.9.1. 20mm Span Three-Point Bend Tests 144

2.9.2. 7mm Span Three-Point Bend Tests 146

2.9.3. Short Beam Tests 147

2.10. Scanning Electron Microscopy 147

2.10.1. Electron Probe Microanalysis 148

2.11. Dilatometry 149

2.12. Modal Analysis by Point Counting 151

Tables, Chapter 2 155

Figures, Chapter 2 157

Chapter 3. RESULTS AND DISCUSSION

3.1. Crystallization Characteristics of the Glass Compositions 170

3.1.1. Composition RW1 171

		Page
3.1.2.	Composition RW2	172
3.1.3.	Composition RW3	174
3.1.4.	Compositions RW4, RW5 and RW6	177
3.1.5.	Compositions RW7, RW8 and RW9	179
3.1.6.	Compositions RW10, RW11, RW12, RW13 and RW14	190
3.1.7.	Internally Nucleated RW14F Composition	196
3.1.8.	Compositions Used for Rod Pulling; RW14, RW15, RW16 and RW17	198
3.1.8.1.	Pinhole Transmission X-Ray Analysis of RW17 Rods	212
3.2.	Growth Kinetics of RW9, RW14 and RW17 Compositions	
3.2.1.	Activation Energies for Crystal Growth Found Using Arrhenius Plots	214
3.2.2.	Diffusion Energy for Spherulitic Crystallization	218
3.3.	Microstructure of Selected Materials	
3.3.1.	Densities	221
3.3.2.	Electron Probe Microanalysis of RW9 Materials	222
3.3.3.	Volume Fractions of Phases Present in Selected Materials	223
3.4.	Thermal Expansion Characteristics of Selected Materials	224
3.4.1.	Wollastonite Mineral	224

Page

3.4.2. RW9 Composition Materials 226

3.4.3. RW14 Composition Materials 230

3.4.4. RW14F Internally Nucleated Material 234

3.4.5. RW17 Composition Materials 235

3.5. Results of Mechanical Tests

3.5.1. Moduli of Rupture 240

3.5.2. Interlaminar Shear Strengths 249

3.5.3. Work of Fracture 252

3.5.4. Young's Moduli 254

Tables, Chapter 3 256

Figures, Chapter 3 297

Chapter 4. CONCLUSIONS

4.1. Glass Compositions 364

4.2. Crystal Growth 364

4.3. Fibre Morphology 365

4.4. Crystal Growth Kinetics 366

4.5. Thermal Expansion 367

4.6. Mechanical Properties 368

4.7. Suggestions for Future Work 370

Appendix I. Calculation of Dilatometer Results 374

Appendix II. Three-Point Bend Test Specifications 379

		Page
Appendix III.	Calculation of Modulus of Rupture and Young's Modulus from Long Beam Test Results	380
Appendix IV.	Calculation of Interlaminar Shear Strength from Short Beam Test Results	384
Appendix V.		385
References		387
Enclosed Paper.	Anisotropic thermal expansion characteristics of wollastonite	

LIST OF TABLES

Table Number		Page
2.1	Materials used in the preparation of glasses.	155
2.2	Glass compositions.	156
3.1	Experimentally determined X-ray diffraction intensities of wollastonite.	256
3.2	Experimentally determined X-ray diffraction intensities of pseudowollastonite.	256
3.3	Experimentally determined X-ray diffraction intensities of anorthite.	257
3.4	X-ray diffraction intensities of $Na_2Ca_2Si_3O_9$ (ref. 121).	257
3.5	X-ray diffraction intensities of devitrite (ref. 121).	258
3.6	X-ray diffraction intensities of hardystonite (ref. 121).	258
3.7	X-ray diffraction intensities of RW1 after 18 hours at 1080°C.	259
3.8	X-ray diffraction intensities of RW2 after 56 hours at 1075°C.	259
3.9	X-ray diffraction intensities of RW3 after 72 hours at 1075°C.	260
3.10	X-ray diffraction intensities of RW6 tile after 66 hours at 1025°C.	260
3.11	X-ray diffraction intensities of RW7, roughened surface, after 22 hours at 1020°C.	261
3.12	X-ray diffraction intensities of RW7, smooth surface, after 22 hours at 1020°C.	261

Table Number		Page
3.13	X-ray diffraction intensities of RW7 tile after 54 hours at 1020°C.	262
3.14	X-ray diffraction intensities of RW8 after 20 hours at 950°C.	262
3.15	X-ray diffraction intensities of RW8 after 20 hours at 975°C.	263
3.16	X-ray diffraction intensities of RW8 after 20 hours at 1025°C.	263
3.17	X-ray diffraction intensities of RW9 after 10 minutes at 1160°C.	264
3.18	X-ray diffraction intensities of RW9 after 20 minutes at 1160°C.	264
3.19	X-ray diffraction intensities of RW9 after 30 minutes at 1160°C.	265
3.20	X-ray diffraction intensities of RW9/3T tile after 1 hour at 1180°C.	265
3.21	X-ray diffraction intensities of RW9/4T tile after 1 hour at 1180°C.	266
3.22	X-ray diffraction intensities of RW9/6T tile after 1 hour at 1180°C.	266
3.23	X-ray diffraction intensities of RW9/7C intracrucible material after 9 hours at 1180°C.	267
3.24	Results of wet chemical analyses of selected compositions before and after heat-treatments.	268
3.25	X-ray diffraction intensities of RW10 after 30 minutes at 906°C.	267

Table Number		Page
3.26	X-ray diffraction intensities of RW10 after 30 minutes at 1059°C.	269
3.27	X-ray diffraction intensities of RW13 after 30 minutes at 990°C.	269
3.28	X-ray diffraction intensities of RW13 after 30 minutes at 1030°C.	270
3.29	X-ray diffraction intensities of RW14 after 30 minutes at 950°C.	270
3.30	X-ray diffraction intensities of RW14 after 30 minutes at 1000°C.	271
3.31	X-ray diffraction intensities of RW14 after 30 minutes at 1045°C.	271
3.32	X-ray diffraction intensities of RW14/2T tile after 30 minutes at 1104°C.	272
3.33	X-ray diffraction intensities of RW14/4T tile after 45 minutes at 1098°C.	272
3.34	X-ray diffraction intensities of RW14/5T tile after 45 minutes at 1091°C.	273
3.35	X-ray diffraction intensities of RW14F tile after 1 hour at 900°C.	273
3.36	X-ray diffraction intensities of RW14 rod, pulled from 1470°C at 52μm s^{-1}.	274
3.37	X-ray diffraction intensities of RW15 rod, pulled from 1450°C at 280μm s^{-1}.	274
3.38	X-ray diffraction intensities of RW16 rod, pulled from 1450°C at 114μm s^{-1}.	275

Table Number		Page
3.39	Results of investigation into the effects of pulling rate, nucleating agent and temperature gradient on the crystallization of RW17 rod.	276
3.40	X-ray diffraction intensities of RW17/a rod.	275
3.41	X-ray diffraction intensities of RW17/i rod.	277
3.42	X-ray diffraction intensities of RW17/s rod.	277
3.43a	X-ray diffraction intensities of RW17/n rod.	278
3.43b	X-ray diffraction intensities of RW17/m rod.	278
3.44	Indexed pinhole transmission X-ray diffraction patterns for wollastonite, RW17/30β and RW17/50β.	279
3.45	Crystal growth rate data for RW9 composition, see figure 3.22.	280
3.46	Crystal growth rate data for RW14 composition, see figure 3.47.	281
3.47	Crystal growth rate data for RW17 composition, see figure 3.67.	281
3.48	"Activation" and "diffusion" energies for crystal growth from RW9, RW14 and RW17 compositions.	282
3.49	Spherulitic crystallization data for RW9 composition.	283
3.50	Spherulitic crystallization data for RW14 composition.	283
3.51	Spherulitic crystallization data for RW17 composition.	283
3.52	Densities of RW9, RW14 and RW17 compositions glasses and devitrified materials.	284

Table Number		Page
3.53	EPMA analyses of RW9 crystallized materials.	285
3.54	RW9, RW14 and RW17 materials modal analyses results.	286
3.55	Thermal expansion characteristics of "spec-pure" silver.	287
3.56	Thermal expansion characteristics of wollastonite, transverse.	287
3.57	Thermal expansion characteristics of wollastonite, longitudinal.	287
3.58	Thermal expansion characteristics of RW9 glass.	288
3.59	Thermal expansion characteristics of RW9/3T, transverse.	288
3.60	Thermal expansion characteristics of RW9/7C, longitudinal.	288
3.61	Thermal expansion characteristics of RW14 glass.	289
3.62	Thermal expansion characteristics of RW14/2T, transverse.	289
3.63	Thermal expansion characteristics of RW14 residual glass.	289
3.64	Thermal expansion characteristics of RW14/5T, transverse.	290
3.65	Thermal expansion characteristics of RW14/5T, longitudinal.	290
3.66	Thermal expansion characteristics of RW14F, internally nucleated.	290

Table Number		Page
3.67	Thermal expansion characteristics of RW17 glass.	291
3.68	Thermal expansion characteristics of RW17/50β, transverse.	291
3.69	Thermal expansion characteristics of RW17/30β, transverse.	291
3.70	Thermal expansion characteristics of RW17/30α, transverse.	292
3.71	Thermal expansion characteristics of RW17/10, $Ca_2ZnSi_2O_7$, transverse and longitudinal.	292
3.72	Thermal expansion characteristics of RW17/50β, longitudinal.	292
3.73	Thermal expansion characteristics of RW17/30β, longitudinal.	293
3.74	Thermal expansion characteristics of RW17/30α, longitudinal.	293
3.75	Results of 20mm span three-point bend tests.	294
3.76	Results of 7mm span three-point bend tests.	294
3.77	Results of all mechanical tests.	295
3.78	Results of short beam tests, tile materials.	296
3.79	Results of short beam tests, rod materials.	296

LIST OF FIGURES

Figure Number		Page
1.1	$Si_3O_9^{6-}$ ring anion.	95
1.2	Rates of homogeneous nucleation and crystal growth in a viscous liquid (ref. 10, page 29).	96
1.3	Schematic binary phase diagram.	97
1.4	Composition versus distance plot corresponding to one-dimensional crystallization.	97
1.5	Situation at crystal/glass interface when isothermal conditions apply.	98
1.6	Transcrystallization.	99
1.7	Stages in the development of a spherulite.	100
1.8	Rod cooling rate and crystal growth rate profiles operating below the molten zone.	101
1.9	Thermal expansion curve for a glass (ref. 118, page 13).	102
1.10	Theoretical fracture stress versus fibre orientation.	103
2.1	Gradient heat treatment technique.	157
2.2	Heat-treatment schedule for RW9 tiles.	158
2.3	Heat-treatment schedule for RW14 tiles.	159
2.4	Heat-treatment schedule for RW9 intra-crucible material.	160
2.5	Heat-treatment schedule for RW14F tiles.	161
2.6	Transformer terminals and platinum collar.	162
2.7	Rod pulling apparatus.	163
2.8	Transformer circuit.	164

Figure Number		Page
2.9	Motorised drive circuit.	164
2.10	Type of bend test specimens.	165
2.11	Diagram of the 20mm span bend test apparatus.	166
2.12	Diagram of the 7 and 4mm span bend test apparatus.	168
2.13	Dilatometer circuit.	169
3.1	Experimentally determined X-ray diffraction intensities of wollastonite.	297
3.2	Experimentally determined X-ray diffraction intensities of pseudowollastonite.	297
3.3	Experimentally determined X-ray diffraction intensities of anorthite.	297
3.4	X-ray diffraction intensities of $Na_2Ca_2Si_3O_9$ (ref. 121).	298
3.5	X-ray diffraction intensities of devitrite (ref. 121).	298
3.6	X-ray diffraction intensities of hardystonite (ref. 121).	298
3.7	$CaO-Al_2O_3-SiO_2$ phase diagram (ref. 127).	299
3.8	Photomicrograph of RW1 after 18 hours at 1080°C.	300
3.9	X-ray diffraction intensities of RW1 after 18 hours at 1080°C.	301
3.10	X-ray diffraction intensities of RW2 after 56 hours at 1075°C.	301
3.11	X-ray diffraction intensities of RW3 after 72 hours at 1075°C.	301

Figure Number		Page
3.12	Photomicrograph of RW3 after 18 hours at 1040°C.	300
3.13	A portion of a heating or cooling tile (ref. 130).	302
3.14	X-ray diffraction intensities of RW6 tile after 66 hours at 1025°C.	303
3.15	X-ray diffraction intensities of RW7, roughened surface, after 22 hours at 1020°C.	303
3.16	X-ray diffraction intensities of RW7, smooth surface, after 22 hours at 1020°C.	303
3.17	X-ray diffraction intensities of RW7 tile after 54 hours at 1020°C.	304
3.18	Photomicrograph of RW7 after 54 hours at 1020°C.	305
3.19	X-ray diffraction intensities of RW8 after 20 hours at 950°C.	304
3.20	X-ray diffraction intensities of RW8 after 20 hours at 975°C.	304
3.21	X-ray diffraction intensities of RW8 after 20 hours at 1025°C.	306
3.22	Crystal growth rate versus temperature, RW9 composition.	307
3.23	X-ray diffraction intensities of RW9 after 10 minutes at 1160°C.	306
3.24	X-ray diffraction intensities of RW9 after 20 minutes at 1160°C.	306

Figure Number		Page
3.25	X-ray diffraction intensities of RW9 after 30 minutes at 1160°C.	308
3.26	Photomicrograph of α-$CaSiO_3$ dendrites grown at 1160°C in RW9.	305
3.27	Photomicrograph of surface nucleation in RW9 at 980°C.	309
3.28	X-ray diffraction intensities of RW9/3T tile after 1 hour at 1180°C.	308
3.29	Photomicrograph of β-$CaSiO_3$ spherulitic fibres and α-$CaSiO_3$ dendrites coexisting in RW9/3T tile.	309
3.30	X-ray diffraction intensities of RW9/4T tile after 1 hour at 1180°C.	308
3.31	X-ray diffraction intensities of RW9/6T tile after 1 hour at 1180°C.	310
3.32	Photomicrograph of surface nucleation of β-$CaSiO_3$ and $CaAl_2Si_2O_8$ secondary crystallization in RW9/4T tile.	311
3.33	X-ray diffraction intensities of RW9/7C intracrucible material after 9 hours at 1180°C.	310
3.34	Diagramatic section through crucible containing RW9/7C after 9 hours at 1180°C.	312
3.35	Na_2O-CaO-SiO_2 phase diagram (ref. 127).	313
3.36	X-ray diffraction intensities of RW10 after 30 minutes at 906°C.	310
3.37	X-ray diffraction intensities of RW10 after 30 minutes at 1059°C.	314

Figure Number		Page
3.38	X-ray diffraction intensities of RW13 after 30 minutes at 990°C.	314
3.39	X-ray diffraction intensities of RW13 after 30 minutes at 1030°C.	314
3.40	X-ray diffraction intensities of RW14 after 30 minutes at 950°C.	315
3.41	X-ray diffraction intensities of RW14 after 30 minutes at 1000°C.	315
3.42	X-ray diffraction intensities of RW14 after 30 minutes at 1045°C.	315
3.43	Photomicrograph of RW14 after 30 minutes at 1104°C.	311
3.44	X-ray diffraction intensities of RW14/2T tile after 30 minutes at 1104°C.	316
3.45	X-ray diffraction intensities of RW14/4T tile after 45 minutes at 1098°C.	316
3.46	X-ray diffraction intensities of RW14/5T tile after 45 minutes at 1091°C.	316
3.47	Crystal growth rate versus temperature, RW14 composition.	317
3.48	X-ray diffraction intensities of RW14F tile after 1 hour at 900°C.	318
3.49	Photomicrograph of RW14F after 1 hour at 900°C.	319
3.50	X-ray diffraction intensities of RW14 rod, pulled from 1470°C at 52μm s^{-1}.	318
3.51	Photomicrograph of RW14 rod, pulled from 1470°C at 20μm s^{-1}, quenched growth front.	319

Figure Number		Page
3.52	X-ray diffraction intensities of RW15 rod, pulled from 1450°C at 280μm s^{-1}.	318
3.53	X-ray diffraction intensities of RW16 rod, pulled from 1450°C at 114μm s^{-1}.	320
3.54	Hypothetical U versus T curves.	321
3.55	CaO-ZnO-SiO_2 phase diagram (ref. 127).	322
3.56	Cooling rates of RW17 rods, nucleated on β-$CaSiO_3$ and Pt/Pt 13% Rh T/C, no air blast.	323
3.57	X-ray diffraction intensities of RW17/a rod.	320
3.58	X-ray diffraction intensities of RW17/i rod.	320
3.59	T-T-T diagram for RW17 rods nucleated on Pt/Pt 13% Rh T/C wire.	324
3.60	X-ray diffraction intensities of RW17/s rod.	325
3.61	X-ray diffraction intensities of RW17/n rod.	325
3.62	X-ray diffraction intensities of RW17/m rod.	325
3.63	Photomicrograph of RW17/m rod, tabular directional crystallization of $Ca_2ZnSi_2O_7$.	326
3.64	T-T-T diagram for RW17 rods nucleated on β-$CaSiO_3$ seed crystal.	327
3.65	Photomicrograph of RW17/30β rod, pulled from 1410°C at 30μm s^{-1}.	326
3.66	Photomicrograph of RW17/30α rod, pulled from 1410°C at 30μm s^{-1}.	328
3.67	Crystal growth rate versus temperature for β-$CaSiO_3$ rods pulled from RW17 melts.	329
3.68	Pinhole transmission X-ray diffraction pattern of wollastonite.	330

Figure Number		Page
3.69	Pinhole transmission X-ray diffraction pattern of RW17/30β, pulled at 30μm s^{-1}.	330
3.70	Pinhole transmission X-ray diffraction pattern of RW17/50β, pulled at 50μm s^{-1}.	330
3.71	Log U versus 1/T plots for crystal growth in RW9, RW14 and RW17 glasses.	331
3.72	Log D versus 1/T plots for spherulitic crystal growth in RW9, RW14 and RW17 glasses.	332
3.73	Reflected light photomicrograph of RW9/7C EPMA specimen.	328
3.74	Photomicrograph of RW9 tile material.	333
3.75	Photomicrograph of RW9 intracrucible material.	333
3.76	Photomicrograph of RW14 tile material.	334
3.77	Photomicrograph of RW14F internally nucleated tile material.	334
3.78	Photomicrograph of RW17/30β rod material.	335
3.79	Photomicrograph of RW17/30α rod material.	335
3.80	Thermal expansion characteristics of "spec-pure" silver.	336
3.81	Thermal expansion characteristics of wollastonite, transverse.	337
3.82	Thermal expansion characteristics of wollastonite, longitudinal.	338
3.83	Thermal expansion characteristics of RW9 glass.	339
3.84	Thermal expansion characteristics of RW9/3T, transverse.	340
3.85	Thermal expansion characteristics of RW9/7C, longitudinal.	341

Figure Number		Page
3.86	Thermal expansion characteristics of RW14 glass.	342
3.87	Thermal expansion characteristics of RW14/2T, transverse.	343
3.88	Thermal expansion characteristics of RW14 residual glass.	344
3.89	Thermal expansion characteristics of RW14/5T, transverse.	345
3.90	Thermal expansion characteristics of RW14/5T, longitudinal.	346
3.91	Thermal expansion characteristics of RW14F, internally nucleated.	347
3.92	Thermal expansion characteristics of RW17 glass.	348
3.93	Thermal expansion characteristics of RW17/50β, transverse.	349
3.94	Thermal expansion characteristics of RW17/30β, transverse.	350
3.95	Thermal expansion characteristics of RW17/30α, transverse.	351
3.96	Thermal expansion characteristics of RW17/10, $Ca_2ZnSi_2O_7$, transverse and longitudinal.	352
3.97	Thermal expansion characteristics of RW17/50β, longitudinal.	353
3.98	Thermal expansion characteristics of RW17/30β, longitudinal.	354
3.99	Thermal expansion characteristics of RW17/30α, longitudinal.	355
3.100	SEM photomicrograph of fracture face of RW9/6T.8, transverse, 20mm span.	356

Figure Number		Page
3.101	SEM photomicrograph of fracture face of RW9/7C.1, longitudinal, 20mm span.	356
3.102	SEM photomicrograph of fracture face of RW14/2T.6, perpendicular, 20mm span.	357
3.103	SEM photomicrograph of fracture face of RW14F.1, random, 20mm span.	358
3.104	As fig. 3.103, close-up of interspherulite boundary.	358
3.105	SEM photomicrograph of fracture face of RW17/30β, longitudinal, 7mm span.	359
3.106	SEM photomicrograph of fracture face of RW17/30α, longitudinal, 7mm span.	359
3.107	SEM photomicrograph of fracture face of RW9/3T typical short beam test specimen.	360
3.108	SEM photomicrograph of fracture face of RW14/4T typical short beam test specimen.	360
3.109	SEM photomicrograph of fracture face of RW17/30β typical short beam test specimen.	361
3.110	SEM photomicrograph of fracture face of RW17/30α typical short beam test specimen.	361
3.111	Schematic load versus deflection curve for controlled crack growth.	362
3.112	Typical load versus deflection curves for the different types of bend test specimens.	363

LIST OF SYMBOLS

CAPITAL LETTERS

A Arrhenius equation prexponential term; area.

B Interlaminar shear strength; constant.

C Specific heat.

D Diffusion coefficient; specimen-to-film distance.

E Energy; Young's modulus.

G Gibbs free energy.

H Enthalpy.

I Intensity; rate of nucleation; second moment of area of the cross section about neutral axis.

K Stiffness; thermal conductivity; constant.

L Latent heat; span.

M Externally applied moment.

P Load; calculated percentage composition.

R Gas constant; radius of diffraction ring.

S Entropy; probability of fracture.

T Temperature.

U Energy; rate of crystal growth.

V Volume; volume fraction.

W Heat.

Y Geometrical factor.

Z Fraction.

SMALL LETTERS

a Atomic or molecular spacing; constant.

b Specimen breadth.

c Crack length.

d Specimen depth; spacing of crystallographic planes.

f Fraction.

g Acceleration due to gravity.

h Initial distance between neutral axis and point of maximum stress.

k Boltzman constant.

l Specimen length; fibre length.

m Weibull constant.

n Order of diffraction; number of observations.

p True percentage composition.

r Fibre radius; radius of spherulite.

s Distance.

t Time.

v Deflection at bottom of beam.

x Spacing.

z Density.

GREEK LETTERS

α Thermal expansion coefficient; Jackson's parameter.

γ Surface energy per unit area of surface.

Δ Differential.

δ Depth of boundary layer; width of spherulitic fibre.

ε Strain.

η Viscosity.

θ Bragg angle; angle.

λ Wavelength.

ν Molecular vibration frequency.

ρ Radius of curvature.

σ Tensile stress; surface tension; standard deviation.

τ Shear stress.

SUBSCRIPTS

a Activation; applied.

c Critical; composite.

D Diffusion.

E Elastic.

F Fusion.

f Fibre; fracture.

G Griffith.

g Glass transition.

H Heterogeneity.

L Liquid/melt.

m Matrix.

n Nucleus formation.

o Maximum.

p Constant pressure.

S Surface; softening; crystal.

t Transverse.

u Minimum.

V Volume.

CHAPTER 1

INTRODUCTION

1.1. ANISOTROPIC CERAMICS:

1.1.1. IN SITU COMPOSITES:

In situ composites are aligned two-phase materials in which the two phases are produced simultaneously by the decomposition of a single phase starting material. The unidirectional solidification of eutectic melts is the most widely investigated technique for the production of these materials, although in recent years the unidirectional decomposition of eutectoids or supersaturated solid solutions has also been used to produce successful composites. Livingston (1) has reviewed duplex (two-phase) crystal growth as applied to the production of aligned composites, both by directional solidification of eutectic, off-eutectic, monotectic or peritectic melts and by directional eutectoid or cellular solid-state transformations.

Most research has been done on metallic systems, which have been reviewed by Davies (2), but there has been work on the production of in situ ceramic composites. Several oxide system eutectics have been directionally solidified, e.g. the ZrO_2-MgO eutectic (3), and a rare-earth-oxide-metal eutectic composite has been prepared using a direct-rf-coupling internal molten zone technique (4).

Recently Carpay and Cense have developed a method for the production of in situ composites by unidirectional crystalline decomposition of non-crystalline solids (5, 6) using quenched salts and oxides, e.g. the Li_2O-B_2O_3 system (7). They have found that a large range of compositions will produce aligned composites by a unidirectional devitrification process, even systems without an eutectic or an eutectoid. The aligned structures were obtained by decomposition in a temperature gradient.

In situ composites may have a rodlike, ribbonlike or lamellar microstructure when produced by the growth of duplex crystals, and the type of morphology depends on the volume fraction of phases at the transformation temperature and the anisotropy of the solid-solid surface energies between the phases. If there are several low-energy interface planes and the volume fraction of the minority phase is less than about 30% then rodlike growth may be produced, although there are a great many factors affecting the morphology of the growing crystals and there are numerous exceptions to the above conditions (1). However it would generally seem that rodlike in situ composites, analogous to conventional unidirectional continuous fibre reinforced composites, can only be produced with relatively low fibre volume fractions.

Since the interphase spacing of aligned two phase materials formed by invariant reactions from the melt or a single solid phase (e.g. the eutectoid decomposition of austenite into pearlite) is controlled by the rate of

sideways diffusion (8, page 449) then this spacing decreases with decreasing temperature of transformation (many fabrication techniques use temperatures lower than the invariant transformation temperature in order to give a fine microstructure) (1). The rate of growth of these duplex crystals increases with decreasing temperature below the invariant temperature, reaches a maximum and then decreases again at lower temperatures (8, page 448), a similar type of behaviour to that found for crystallization from the vitreous state (see section 1.4.1.).

Davies et al (9) have described a different type of in situ composite produced by directional dendritic growth from the melt in a metallic system.

The physical properties of these composite materials are anisotropic and depend on the properties of the constituent phases and the volume fraction, the morphology and alignment of these phases (1).

1.1.2. ORIENTATED GLASS-CERAMICS:

Conventional glass-ceramics are polycrystalline solids prepared by the controlled internal nucleation and crystallization of a glass. They are therefore materials in which there is a random dispersion of one or more crystalline phases together with a small proportion of residual glass. The macroscopic physical properties of a material of this type are isotropic (10). Several attempts have been made to produce anisotropic glass-ceramics, usually in the form of a fibre suitable for

incorporation into a composite. Such a fibre could have several advantages over conventional E-glass fibres, such as a higher chemical stability, a higher elastic modulus, or a thermal expansion coefficient exactly matched to that of the matrix material (up to a certain limit) since glass-ceramic compositions can be modified to give materials with desired expansion coefficients (even zero) by adjusting the crystalline phases, and volume fraction of these phases, produced (10). Any of these properties may be required in a reinforcing fibre (11).

Veale (12) attempted to produce glass-ceramic reinforcing fibres from quenched glass fibres of compositions corresponding both to $CaMgSi_2O_6$ (synthetic analogue of diopside mineral) and to fluoride analogues of asbestos mineral compositions. However when the glass fibres were reheated all the crystallization nucleated at the fibre surface and grew into the fibre which resulted in very fragile fibres due to weak boundaries running across the fibre diameter. Nucleation at external surfaces occurs on dust particles, scratches, etcetera (see section 1.3.1.) which are almost impossible to eliminate completely. It would therefore seem to be very difficult to produce glass-ceramic fibres in which the crystallization is orientated along the fibre axis by an isothermal heat-treatment due to the large surface to volume ratio of the fine fibres (reinforcing fibres have to be very fine, about 10 microns, in order to give the required aspect ratio (11)).

Heinze et al (13) have patented a process for the

production of a reinforcing glass-ceramic fibre. In this a previously drawn, quenched glass fibre, about 20 microns in diameter, is crystallized by a two-stage heat-treatment (10) and at the same time stretching the glass fibre by at least 10% of its length over the entire heat treatment. These fibres have an elastic modulus considerably higher than the original glass fibre and also higher than similar glass-ceramic fibres produced without stretching, which indicates that the crystals are at least partioally orientated by the applied stress along the fibre axis during crystallization. These fibres are internally nucleated by a prolonged low temperature treatment prior to heating to the crystallization temperature, using titania or zirconia as the nucleating agent in lithia-magnesia-aluminosilicate glasses, or other glasses which can be uniformly crystallized.

Recently both Ashbee (14) and Atkinson and McMillan (15) have developed techniques to orientate glass-ceramic microstructures using hot-extrusion techniques. Ashbee, using a glass which devitrifies to a glass-ceramic containing synthetic fluorophlogopite (i.e. a mica having a platey microstructure) as the major crystalline phase, has achieved strict alignment of these crystals by subjecting the glass to pure extensional flow during preliminary crystallization. This alignment is maintained during the drawing down of a 2mm extruded rod into an approximately 100 micron diameter fibre and the subsequent completion of crystallization, during which some new, randomly orientated

crystals grow in addition to extra growth of the preorientated crystals. However these fibres contain a relatively low proportion of crystals and therefore cannot strictly be regarded as being a glass-ceramic material.

Atkinson and McMillan have produced aligned crystal microstructures in Li_2O-SiO_2 glass-ceramics. Although the extruded, crystallized material consists of two crystalline phases in a matrix of residual glass, only one of these phases is aligned to the extrusion axis. This material does not require any additional crystallization treatment after extrusion. The modulus of rupture and Young's modulus of this material tested in three-point loading were a maximum when the load was applied perpendicular to the extrusion axis and were both about twice the equivalent results for this material loaded parallel to the extrusion axis.

During the investigation of the effects of various transition metal oxides on the crystallization of CaO-MgO-Al_2O_3-SiO_2 glasses of approximately metasilicate composition Rogers et al found that for the glasses containing vanadium oxides (16) or zinc oxide (17) the crystalline phases had nucleated at the surface of the glass and had subsequently grown as thin needles towards the centre of the sample. The crystalline phases were β-$CaSiO_3$ (synthetic analogue of the mineral wollastonite) and $CaAl_2Si_2O_8$ (synthetic analogue of the mineral anorthite). Although the microstructure was very fine (due to the relatively low crystallization temperatures employed, see section

1.4.2.), generally the needles were less than 1 micron wide and so could not be resolved optically, it was concluded by comparison with previously published micrographs that the needle-like, i.e. fibrous, phase was β-$CaSiO_3$. Since the fibrous crystals grew inwards from relatively plane surfaces they formed a roughly aligned microstructure in which the cones of growing fibres impinged and mutual interference only allowed those fibres orientated within about 15 degrees of the normal to the surface to develop (see section 1.4.2.).

This type of microstructure is similar to that produced by Reaumur (18) who in 1729 showed that if glass bottles were packed with a mixture of sand and gypsum and held at red heat for several days, then these bottles converted into opaque, porcelain-like objects. It was found that fibrous crystals had grown unidirectionally from heterogeneous nuclei from the surface of the bottles into the glass walls.

1.2. STRUCTURE OF SILICATE GLASSES AND MELTS:

Jones (19) defined a glass as "a material, formed by cooling from the normal liquid state, which has shown no discontinuous change at any temperature, but has become more or less rigid through a progressive increase in its viscosity", and the ASTM "Standards for Glass" states that "a glass is an inorganic product of fusion which has been cooled to a rigid condition without crystallization". The difficulties with the above definitions are that some organic polymers can exist as a glass and that glasses can

be prepared without cooling from the liquid state (e.g. by vapour deposition). Doremus (20) has defined a glass in terms of its molecular structure, i.e. as a material in which there "is no regularity in the arrangements of its molecular constituents on a scale larger than a few times the size of these groups".

Silicon tends to form sp^3 hybrid orbitals (21), like carbon, and therefore there is a tetrahedral arrangement of bonds around a central silicon atom. Unlike carbon the Si-H and Si-Si bonds are weak and silicon only rarely forms multiple bonds, however the single Si-O bond is strong and this leads to a large number of silicate compounds. The relatively large electronegativity difference between silicon and oxygen results in a degree of ionic character in the bonds. At room temperature the covalent character is dominant but as the temperature increases the viscosity of silica glass, which can be regarded as a random arrangement of SiO_4^{4-} units linked by single Si-O bonds into an "infinite" network, decreases for two reasons. As the temperature rises the increased thermal energy allows twisting and flexing of network bonds, without actually breaking any covalent bonds, by rehybridization of the Si-O-Si bonds. At higher temperatures there is sufficient thermal energy available to break the covalent bonds leaving only the electrostatic attractive forces. Similarly the addition of a metal oxide, i.e. an ionic compound, to a silica melt causes a decrease in viscosity due to a break-down in the network. The cations tend to

remain around singly charged (negative) non-bridging oxygen atoms, i.e. the number of Si-O-Si linkages in the network is reduced. Alkali metal oxides are more effective at reducing the viscosity of a melt or glass than alkaline earth metal oxides since they have a higher cation to oxygen ratio.

The ability of oxides to form glasses has been classified according to several different criteria, which have been reviewed by Rawson (22). Sun (23) showed that the glass-forming ability of an oxide is directly related to the strength of the metal atom-oxygen bond, since the stronger this bond the more difficult the bond breaking and rearrangement necessary when a melt crystallizes and hence the more easy it is to quench the melt into a glass. Glass former oxides have bond strengths above about 335 kJ mol^{-1}, network modifier oxides (e.g. alkali metal oxides) have bond strengths in the region 120 to 170 kJ mol^{-1}, whilst intermediate oxides, which can act as a network former in the presence of a network modifier, have bond strengths of around 250 kJ mol^{-1}. Using this classification SiO_2 is a glass former, Al_2O_3 an intermediate oxide and CaO, ZnO and Na_2O network modifiers. Rawson (22) modified Sun's criterion to a comparison of bond strength and melting temperature, since this ratio takes account of the amount of thermal energy available to break bonds and to rearrange the melt into a crystal structure. Using the more recent criteria of Stanworth (24) SiO_2 is classed as a "strong" glass former.

Zachariasen's postulated structure of vitreous silica, i.e. a three-dimensional "random" network, lacking any long range order, formed by the union of silica tetrahedra at their corners (25) (the random-network model), has been subsequently supported by the X-ray diffraction studies of Warren et al (26). Urnes (27) has reviewed this method of structural analysis of glasses.

Zachariasen's postulated structure for more complex, two-component glasses, is also in agreement with the structure found by X-ray diffraction, i.e. a random-network structure with the modifying cations fitted into holes in the three-dimensional network. The presence of the modifying oxide increases the O:Si ratio to greater than 2 and therefore not all the oxygen atoms are bonded to two silicon atoms. The oxygen atoms linked to only one silicon atom are called "non-bridging oxygens" and those bonded to two silicon atoms "bridging oxygens". The cations are located in the vicinity of a non-bridging oxygen (negatively charged), and although the exact coordination number of alkali and alkaline earth ions in silicate glasses is uncertain, it is usual to assume that the cation is singly coordinated when considering ionic transport in glasses (20). Both Zachariasen and Warren considered that these modifying cations are randomly distributed throughout the network, however there is some evidence, from X-ray diffraction studies, that the average separation of the cations is less than for a uniform distribution, i.e. the cations are grouped into "clusters". Urnes (27) and

Doremus (20) both review this clustering of cations in glasses.

A more general approach to glass structure was made by Hagg (28) who stated that, rather than having a three-dimensional network structure, many silicate glasses could be made up of large, complex anionic groups. These groups, kept together in the melt by principally ionic forces (q.v.), would be too large and irregular to be easily assimilated into a crystal lattice as the melt cooled below the melting temperature. Such a melt could supercool below the temperature range of appreciable crystal growth and would therefore form a glass. Based on the observation that all glass forming materials are polymorphic in the crystalline state, Goodman (28a) has recently suggested that transient "flicker-clusters" of all the possible polymorphs should coexist in a glass above the transition temperature. All the clusters would fail to grow to the critical embryonic size (see next section) due to mutual impedence of growth. As the temperature decreased these clusters would become firmly bonded across parts of their surfaces, leaving liquid-like material in other, unbonded interstices, this stage corresponding to the glass transition temperature.

Mackenzie (29) has reviewed the theories describing the types of anionic structures formed in silicate glasses as the percentage of network modifying oxide (or oxides) is increased. Assuming a three-dimensional random-network structure for vitreous silica (q.v.) it can be seen that in a binary silicate glass, since the addition of a metal

oxide may give one Si-O-Si bond rupture for every oxygen atom added, then the degree of breakdown of the network is directly proportional to the amount of metal oxide present. However the SiO_4^{4-} tetrahedra remain as the basic unit in binary glasses, and therefore these tetrahedra can be linked into different structures depending on the Si:O ratio in the glass. The limit is the orthosilicate composition (two moles of metal oxide per mole of silica) when in liquid binary silicates the melt consists of metal cations and SiO_4^{4-} anions and cannot form a stable glass. In a glass of metasilicate composition (i.e. at 50mol % silica) Mackenzie considers that the following structures may be present:

1. $Si_3O_9^{6-}$ ring anions (see figure 1.1).
2. SiO_4^{4-} tetrahedra forming "infinite" chains.
3. A random network of continuous Si-O-Si linkages.

Huggins et al (30) compared binary silicate glasses to crystalline silicates of similar composition. They concluded that in glasses there may be "infinite" sheets, "infinite" chains and rings of linked SiO_4^{4-} tetrahedra, or small silicon-oxygen ions, depending on the Si:O ratio. A number of other theories have been proposed (see 29) but are in agreement that around the metasilicate composition the glass structure is made up primarily of chain and ring structures.

Hess (30a) has analysed the distribution of silicate species in silicate melts using the techniques of conventional organic polymer chemistry, i.e. the calculation

of degrees of random polymerization of SiO_4^{4-} structural units according to the statistical methods of Flory. Based on Bockris' measurements of the electrical conductivity of binary silicate melts, on Lentz's gas chromatography study of sodium silicate solutions, and on the structural models obtained by more indirect methods, Hess concluded that a silicate melt can be regarded as a complex mixture of ions rather than molecules, i.e. the melt consists of ion species of oxygen, metal cations and various ionic polymers of SiO_4^{4-} units. At low silica compositions the melt structure is dominated by the SiO_4^{4-} monomer, but with increasing silica content the silicate species polymerize to form larger branch and ring structures. If the silica units are considered as ionic polymers, then the formation of a dimer from two monomers is described by the reaction

$$SiO_4^{4-} + SiO_4^{4-} \longrightarrow Si_2O_7^{6-} + O^{2-}$$

in which an oxygen ion and a doubly bonded oxygen (i.e. Si-O-Si) are created, two singly bonded oxygens being eliminated. Hess found that when the results of the Flory analyses were combined with the Temkin model of ionic liquids, the activity-composition curves for several binary silicate melts could be reproduced so as to agree with experimental data.

1.3. NUCLEATION:

Tammann studied the crystallization of supercooled liquids, including inorganic glasses (31), and showed that below the equilibrium melting temperature there is

a metastable zone in which crystal nuclei do not form at a detectable rate (see figure 1.2). If the melt is "seeded", i.e. a crystal of some suitable material placed into the melt, crystals can grow. Tammann observed that the crystallization process in a liquid in which there are no foreign particles or surfaces, which could act as heterogenous nucleation sites, can be considered in two parts, i.e. the formation of homogeneous nuclei and their subsequent growth. The rate of crystallization in super-cooled liquids is zero at the equilibrium melting/freezing temperature, rises to a maximum at a lower temperature and then falls with decreasing temperature to zero at absolute zero, as shown in figure 1.2. Tammann (31) stated that a similar type of behaviour is shown for the rate of appearance of nuclei, except that in this case the maximum occurs at a lower temperature, and the metastable zone of super-cooling exists since the extremely small nuclei have a lower melting temperature than macroscopic crystals due to their large surface-to-volume ratios.

From a consideration of the contribution of the surface energy of embryonic nuclei to their total free energy it is concluded that at each temperature there must be a critical size below which embryos will redissolve and above which they will grow, i.e. there must be a sufficient volume of the crystal structure formed to give enough free energy (from the difference in free energy between the glass and crystal structure) to compensate for the surface energy generated by the formation of crystal/glass interfaces.

Turnbull's expression for the rate of nucleation (I) per unit volume is (32):

$$I = K \exp - (\Delta G_n/kT + \Delta G_a/kT)$$

where:

K = a quantity which is roughly constant from one substance to another (the "collision factor").

ΔG_n = free energy barrier for the formation of a nucleus of critical size.

ΔG_a = free energy of activation for transport of material across the phase boundary.

k = Boltzmann's constant.

T = absolute temperature.

Turnbull and Fisher (33) applied this expression to glasses by replacing ΔG_a by an expression involving D, a diffusion coefficient, i.e.

$$I = (ND/a^2) \cdot \exp(-\Delta G_n/kT)$$

where:

N = number of molecules per unit volume.

a = molecular spacing.

There is empirical evidence that D varies with viscosity (η) almost according to the Stokes-Einstein relationship (34), i.e.

$$D = kT/3\pi a\eta$$

Therefore at higher temperatures the rate of nucleation increases, as ΔG_n decreases, with decreasing T, until the viscosity term starts to dominate the nucleation rate and the rate decreases with temperature, as shown in figure 1.2.

In simple glasses, e.g. vitreous silica, homogeneous

nucleation does not occur as the viscosity is so great that the nucleation rate is very slow, and although η is lower in multicomponent glasses (see section 1.2.) special "nucleating agents" must be added to these glasses to ensure that a fine distribution of nuclei is formed for the production of glass-ceramics (10). The devitrification of silica glass usually gives crystals with the cristobalite type structure, however if a piece of quartz is added to the supercooled melt then crystals with the quartz structure will grow (this is also the case if quartz grains are melted and heated only a little above the freezing-point (19)), proving that nucleation in this glass must be heterogeneous.

The effect of surfaces in contact with a glass or melt (from small solid impurities, container walls, etcetera) is to reduce the free energy for nucleation (ΔG_n) by decreasing the amount of surface energy required for nucleation by a factor f (θ) (10). θ is the angle determined by the balance of surface tensions:

$$\sigma_{HL} = \sigma_{SH} + \sigma_{SL} \cos \theta$$

where:

σ_{HL} = interfacial free energy heterogeneity/melt.

σ_{SH} = interfacial free energy heterogeneity/crystal.

σ_{SL} = interfacial free energy crystal/melt.

Turnbull and Vonnegut (35) modified the expression for I (q.v.) to that for I_H for heterogeneous nucleation, and if the activation energy term is included (as suggested by Stookey (36)) then:

$$I_H = K \exp - (\Delta G_n f(\Theta)/kT + \Delta G_d/kT)$$

For any value of contact angle (θ) less than 180 degrees the free energy for nucleus formation is reduced and therefore heterogeneous nucleation will occur in preference to homogeneous nucleation.

1.3.1. SURFACE NUCLEATION:

Brockbank (37) investigated the surface devitrification of glass in 1913, but the exact cause of surface nucleation was not found until the work of Swift in 1947 (38). He briefly reviewed the different causes claimed to be responsible for surface devitrification, which included the presence of water vapour, inhomogeneity of the surface, loss of volatiles from the surface or molecular orientation. Swift, however, found from experiments on freshly broken glass surfaces which were exposed to the same conditions except for being subjected to filtered or unfiltered air atmospheres, that dust in the air (i.e. all kinds of foreign materials) is an important cause of surface nucleated devitrification. This result indicates that nucleation occurs heterogeneously (q.v.) on either these foreign particles or on the abraded surfaces produced by hard particles scratching the glass surface. Klause (39) found that a "high strength 'wollastonite' material for abrasive wheel binders" could be produced by pulverizing beads of a suitable glass with a "mineralizer" (a material known to promote devitrification in glasses) and a subsequent heat-treatment.

More recently Ainslie et al have investigated the devitrification kinetics of fused silica and concluded that the nucleation of cristobalite on the external surface of this glass is catalyzed by superficial condensed phase impurities but the gas atmosphere above the surface had no apparent effect on nucleation (34). Leko and Komarova (40) in their study of the crystallization kinetics of quartz glasses (fused silica) found that the presence of surface impurities markedly reduced the "induction period of crystallization by reducing the pre-exponential factor", i.e. they took as a measure of the stability of a glass the "duration of the induction period (prior to crystallization), the temperature dependence of which has an exponential appearance".

Petticrew (41) has found that if a zinc-calcium-alumino-silicate glass has its surface roughened until it has a frosted appearance and is heated to above the annealing temperature (i.e. a temperature at which nucleation will take place relatively quickly) and on up to a suitable crystallization temperature (without having to dwell at the nucleation temperature region), then a glass-ceramic surface layer is produced in the portions of the exposed surface of the glass that were roughened prior to heating. Since both the roughened and smooth surfaces were on the same glass block and therefore were subjected to the same heating conditions, atmosphere, etcetera, it is evident that the surface scratches heterogeneously nucleated the crystals. Burnett and Douglas found that

a scratched crucible surface gave a greatly increased nucleation rate for a soda-baria-silica glass (42).

During X-ray diffraction studies of glass fibres Banerjee (43) found that devitrification in B_2O_3 glass was surface nucleated, but he attributed this to the difference in the chemical and physical properties of the glass surface compared to the body of the glass.

1.3.2. INTERNAL NUCLEATION IN METASILICATE GLASSES CONTAINING FLUORINE:

Mukherjee and Rogers (44) studied the crystallization characteristics of a soda-lime-alumina-silica glass in which some oxygen was replaced by fluorine. They found that the internal nucleation rate (homogeneous nucleation) was a maximum at 662°C for all fluorine contents (up to 5 wt %), the Turnbull-Fisher apparent activation energy (see section 1.3.) for nucleus formation being about 80kJ mol^{-1} which is similar to that for the diffusion of sodium ions through this type of glass (45). From electron microscope studies it was found that glass in glass phase separation (20) occurred prior to nucleation, and from the crystalline phases produced it was deduced that nuclei formed in the droplets of the second glassy phase, i.e. the silica-poor phase. At low nucleation rates the primary crystalline phase (the first to appear) was a synthetic, fluor-substituted analogue of the double chain mineral xonotlite, $Ca_6Si_6O_{17}F_2$, whilst at higher nucleation rates phases with the pyroxenoid single chain structure,

synthetic analogues of fluor-pectolite and wollastonite, were given. They related this to the structure of the glass prior to nucleation, i.e. the more advanced the glassy phase separation the higher the concentration of fluorine in the droplets and this would favour the formation of single rather than double chain structures in the glass due to fluorine ions (single, negative charge) breaking the bonds between silica tetrahedra.

Roginskaya et al (46) have also investigated the influence of fluorine on the crystallization of glasses in the alkali-calcium-aluminosilicate system. They again found evidence of glass in glass separation, and established that crystallization of the fluorosilicate phases occurs from the droplets enriched in calcium and fluorine. They only found a synthetic fluor-substituted xonotlite phase crystallized from glasses with high fluorine content. They concluded that the sequence of crystalline phases produced in relation with the fluorine content is determined by the amount of fluorine-induced depolymerization of the silica-oxygen structures, i.e. breaking Si-O-Si linkages by forming Si-F bonds.

1.4. CRYSTALLIZATION FROM GLASSES AND MELTS:

1.4.1. CRYSTAL GROWTH:

From the work of Tammann (47) it is known that the rate of crystal growth in supercooled liquids is zero at the melting temperature, with decreasing temperature increases to a maximum and then falls to zero again at

absolute zero, see figure 1.2. Several theories were proposed to explain this phenomenon, briefly reviewed in (48), however the theory of Turnbull and Cohen (49) is now accepted as describing the rate of interface-controlled growth. Kirkpatrick (48) considers that interface-control is the rate determining step in crystal growth from silicate melts. Turnbull and Cohen stated that a molecule moving from the melt to join the crystal lattice must have sufficient activation energy, ΔG_a, to pass through the activated state at the interface. Since the crystalline state is the equilibrium stable state at all temperatures below the melting temperature, then the free energy of this state is lower than that of the melt, the difference being ΔG_c. Therefore, below the melting temperature, for a molecule transferring from the melt (or glass) state into the crystal state the energy barrier is ΔG_a, but for a molecule moving from the crystal into the melt the energy barrier is $(\Delta G_a + \Delta G_c)$. The overall rate of crystal growth (U) is equal to the rate at which molecules join the crystal lattice minus the rate at which they leave the crystalline state, i.e.

U = (Rate melt to crystal) - (Rate crystal to melt)

Therefore,

$$U = a\nu \exp(-\Delta G_a/RT)\left[1 - \exp(-\Delta G_c/RT)\right]$$

where:

a = molecular spacing.

ν = molecular vibration frequency.

T = absolute temperature.

R = gas constant.

For crystal growth from melts or glasses the ΔG_d term may be replaced by an expression involving the diffusion coefficient (D), i.e.

$$U = \frac{fD}{a}\left[1 - \exp\left(-\frac{\Delta G_c}{RT}\right)\right]$$

where f is the fraction of sites on the crystal surface available for attachment and D (a diffusion coefficient for the transport across the melt/crystal interface) is defined as

$$D = a^2 \nu \exp\left(-\Delta G_d/RT\right)$$

The Stokes-Einstein relationship relates diffusion coefficients to the viscosity (η) of the melt, i.e.

$$D = kT/3\pi a\eta$$

where k is Boltzmann's constant.

Therefore,

$$U = \frac{fkT}{3\pi a^2\eta}\left[1 - \exp\left(-\frac{\Delta G_c}{RT}\right)\right]$$

i.e. the crystal growth rate is inversely proportional to the melt viscosity. The melt viscosity increases with decreasing temperature, and also with decreasing concentration of modifying cations in the glass (e.g. U decreases with decreasing ZnO content in an approximately metasilicate glass (17)), see section 1.2. Also, this means that melts with high viscosities should have low rates of crystallization and it is found that these melts can be easily quenched into a "stable" glass, e.g. the viscosity of silica at its melting temperature is 10^6 Ns m^{-2} and this, of course, can be quenched into a glass whereas iron, with

a viscosity of 10^{-3} Ns m^{-2}, cannot be quenched into a glass by conventional means (29).

At low undercoolings U increases with decreasing temperature (see figure 1.2) due to the increasing difference in free energy between the melt and the crystalline state, i.e. the ΔG_c term dominates the growth rate equation. At high undercoolings U decreases with temperature since in this region the viscosity of the melt is very high and therefore dominates the growth rate kinetics.

The manner in which molecules, or molecular groups, are attached onto the growing crystal can fall into one of two mechanisms, i.e. lateral or continuous growth (50). Lateral growth occurs at specific sites on the growth interface, i.e. at one molecule high steps on the surface, and therefore the fraction of sites available (f) is less than one. There are two types of lateral mechanism, screw dislocation growth (51) and surface nucleation (52). For continuous growth, in which molecules can join the crystal at any surface site, f is generally assumed to be equal to unity (and independent of temperature). The mechanism operating is determined by the kinetics of growth (from plots of reduced growth rate versus undercooling), see review by Uhlmann (53).

Jackson (54, 55) has evolved a theory relating the nature of the melt/crystal interface and the kinetics of crystal growth. By plotting relative energy of interfaces against the occupied fraction of surface sites for different values of the factor α, where $\alpha = (\Delta S_f/R)Z$

(ΔS_F is the entropy of fusion and Z is the fraction of the total bonding energy represented by bonding parallel to the interface plane), he found that when the entropy of fusion is less than 2R the most closely packed interface planes should be rough on an atomic scale and new layers should form easily. The growth rate anisotropy between different crystallographic planes should be small. When the entropy of fusion is greater than 4R the close packed planes should be smooth on an atomic scale but the less closely packed planes should be rough and therefore form new layers easily due to the abundance of sites where an atom (or molecule) could join the crystal lattice. As a result the growth rate should be highly anisotropic and the crystals should be faceted.

In his review (53) Uhlmann has classified glass-forming materials with respect to their crystallization and melting behaviour by using the entropies of fusion, and Kirkpatrick (48) reports that the crystal morphology of all materials so far investigated corresponds to that predicted by Jackson's theory. Cahn et al (56) have made the suggestion that non-faceted crystals should grow by a continuous mechanism and faceted crystals should grow by one of the lateral mechanisms. Although there is no theoretical justification for this conclusion (57), it has been found to be applicable to the results of most of the experiments in which crystallization mechanism and morphology have both been investigated.

Cooper (58) noted the importance of the process of

molecular rearrangement at the crystal/melt interface, as evidenced by the interface-control of crystal growth, and has presented a new model for crystal growth kinetics. This is similar to the previous theories in that U is proportional to the amount of supercooling and to the reciprocal of viscosity, but in addition includes a parameter related to the amount of rearrangement required. Comparison with data for simple network melts shows that differing amounts of rearrangement are necessary.

The entropies of fusion for calcium metasilicate can be calculated from the specific heat data given in (59), since:

$$\Delta S_{T_2-T_1} = \int_{T_2}^{T_1} \frac{Cp}{T}\, dT$$

and:

$$\Delta S_F = \Delta S_S - \Delta S_L$$

where:

ΔS_S = entropy of crystal at crystallization temperature,

ΔS_L = entropy of melt at crystallization temperature, and

Cp = specific heat at constant pressure.

For the high-temperature polymorph, α-$CaSiO_3$, for crystallization at 1500K the entropy of fusion is equivalent to 3.4 x R, and for the low-temperature polymorph, β-$CaSiO_3$, for crystallization at 1400K the entropy of fusion is equivalent to 3.5 x R. Therefore both these crystal structures should display some evidence of anisotropic growth, and should grow by a lateral interface-control mechanism. Since the crystal structures of the two polymorphs are different (see section 1.5.1.) the amount

of structural rearrangement of molecular groups necessary at the interface for crystal growth may differ in the two cases.

Lisovskaya et al (60) have studied the crystallization kinetics of glass of calcium metasilicate composition using the Kolmogorov equation (which is equivalent to the Johnson-Mehl-Avrami equation), i.e.

$$\text{degree of crystallinity} = 1 - \exp(-\pi I U^3 t^n/3)$$

(where t is the elapsed time and n a constant). They calculated that the maximum growth rate should occur at about 1200°C, the maximum nucleation rate at about 1000°C, the activation energy for diffusion to be 138kJ mol^{-1}, and the potential barriers for crystal growth and nucleation to be 34.7kJ mol^{-1} and 34.3kJ mol^{-1} respectively.

1.4.2. CRYSTAL MORPHOLOGY:

Lofgren (61) during studies of the crystallization of plagioclase crystals from water-saturated plagioclase melts found a change in crystal morphology with increasing undercoolings. At small undercoolings tabular crystals were formed. At progressively larger undercoolings skeletal crystals, then dendrites appeared until finally spherulitic crystallization took place at high undercoolings. These results are in agreement with the theories of interface stability, i.e. the stable width of flat interface surface decreases with increasing undercooling, mainly as a result of the decreasing diffusion rates through the melt at decreasing temperatures. An unstable interface is formed when the crystal growth rate

increases with distance into the liquid or melt and therefore any small perturbation on the growth front can quickly grow away from the rest of the crystal. This may occur in two types of system, one in which the crystal and melt have the same composition (e.g. in the freezing of a small volume of a pure metal) and the other where the crystal and melt have different compositions (e.g. in metal alloys and inorganic glasses). These are known as thermal and constitutional supercooling respectively.

Thermal supercooling is due to the latent heat of fusion liberated when molecules leave the melt and join the crystalline phase. If crystallization is heterogeneously nucleated on the surface of a glass, or at the container surface, then any excess heat is removed through the already formed crystals. This system, in an isothermal furnace, is supercooled considerably below the equilibrium crystallization temperature. As a result of the liberated latent heat the temperature of the interface is greater than that of either the melt or the crystal phase. The resulting temperature contour in the melt, known as a temperature inversion (62), means that the supercooling is a minimum at the interface and increases as one advances into the melt. In liquid metals this type of interface is unstable, since their rates of crystal growths increase with increasing supercooling. However this is an unlikely mechanism in inorganic glasses for the following reasons. Firstly at typical supercoolings in these materials (particularly in glasses crystallized by reheating quenched

material) the crystal growth rate decreases with decreasing temperature (i.e. the crystallization temperature is below the maximum growth rate temperature, see section 1.4.1.) and therefore a protrusion from the growth front would grow more slowly than main interface. Secondly most glasses do not precipitate crystals with the same composition as the glass, and therefore material diffusion is necessary for crystal growth.

In multicomponent systems constitutional supercooling, as proposed by Rutter and Chalmers (63), is the main factor influencing the stability of the crystal growth interface (although thermal supercooling may still be present). Consider the simple case of one-dimensional crystallization, with linear heat abstraction through the crystalline region. Figure 1.3 represents a schematic binary phase diagram for this system. The first material to crystallize has composition A, and, if this is formed relatively quickly, it may be assumed that it grew from the liquid (or glass) layer adjacent to the interface and not from the entire volume of the melt. (This would be easily accomplished in a glass or melt having a low coefficient of bulk diffusion.) Since the solid is rich in one component (X) and depleted in the other (Y), assuming a binary system, then the liquid in contact with it is rich in Y and depleted in X. This liquid composition change just ahead of the interface increases as more solid is formed, but eventually stops when a steady-state situation is attained. Concurrent with this change in liquid

composition is a change in composition of the solid forming from it, i.e. the compositions travel down the liquidus and solidus lines on the binary phase diagram, see figure 1.3.

The concentration of excess Y atoms or molecules in the liquid adjacent to the interface reaches a maximum at composition E, when solid of composition B can crystallize and at this point the steady state has been attained. The solid crystallizing now has the same composition as the bulk of the melt, and the equilibrium crystallization temperature has reached T_3 on figure 1.3. The composition as a function of distance in the interface region is shown in figure 1.4. The composition of the crystallized material changes from its original value A to that of the bulk of the liquid B. At the interface there is a sudden rise in composition to the value E as one passes from the crystal into the melt. Further away from the interface in the melt there is an exponential decrease back to the composition of the bulk liquid, B. The shape of this curve in this exponential region is a function of the crystal growth rate and the diffusion rates in the melt, assuming that there are no liquid convection currents. The equilibrium crystallization temperature of the melt changes throughout this region of varying composition.

In a glass the amount of supercooling is very large, several hundred degrees, and crystal growth is generally slow. As long heat treatment times must be used, there may be no heat flow across the system, i.e. isothermal conditions, and in the absence of any type of temperature

gradient the situation shown in figure 1.5 would exist. Here the bulk of the glass is well below the theoretical equilibrium crystallization temperature, and because of the effect of the impurity layer at the crystal/glass (or melt) interface, this equilibrium crystallization temperature decreases as the interface is approached (i.e. decreases from T_1 to T_3 on figure 1.3). Figure 1.5 also shows a plot of the supercooling in the glass near the interface, and it is seen that this increases as one moves away from the interface, until the steady value beyond the impurity layer is attained. This means that the "driving force" for crystallization, the difference in free energy between the glass and crystalline states (see section 1.4.1.), increases as one moves away from the crystal growth face. Since the ambient temperature remains constant (isothermal conditions) it is unlikely that the viscosity of the melt would increase sufficiently as the melt goes from composition E to B to outweigh this increase in free energy (and the viscosity may even decrease across this region, depending whether the percentage of modifying cations decreases or increases, see section 1.2.), and therefore the crystal growth rate should increase with distance from the interface (from the Turnbull-Cohen equation, see section 1.4.1.). This means that protrusions could grow rapidly away from the interface and a plane crystal growth front is unstable.

For one-dimensional crystal growth (e.g. unidirectional crystallization from surface nuclei) the excess heat flow,

abstracted through the crystals (solid phase), i.e. the difference between the heat entering the melt or glass ("liquid" phase) and leaving solid phase, (ΔW) can be given by:

$$\Delta W = - zL \frac{dV_L}{dt} = zLA \frac{dx}{dt}$$

where:

L = latent heat of fusion per unit mass,

z = density of medium,

V_L = volume of liquid phase,

A = cross-sectional area of system, and

dx/dt = crystal growth rate.

Since any excess heat is removed via the solid phase, then:

$$zLA \frac{dx}{dt} = AK_S \left[\frac{dT}{dx}\right]_S$$

where:

K_S = thermal conductivity of solid, and

$(dT/dx)_S$ = temperature gradient in solid.

Therefore:

$$\left[\frac{dT}{dx}\right]_S = \frac{zL}{K_S} \frac{dx}{dt}$$

For calcium metasilicate crystallization from the melt, using the data given in (59) to find the latent heat of fusion,

$$L = \Delta H_S - \Delta H_L$$

where:

ΔH_L = enthalpy of melt (glass), and

ΔH_S = enthalpy of crystalline phase,

the temperature gradients produced during unidirectional crystallization can be calculated. For crystallization of

α-$CaSiO_3$ at 1500K (the high temperature polymorph, see section 1.5.1.):

$L = 134 J\ g^{-1}$, $z = 3 Mg\ m^{-3}$ (135), and

$K_S \triangleq 3 J\ s^{-1}\ m^{-1}\ K^{-1}$ (10), therefore

for $dx/dt = 10^{-6} m\ s^{-1}$, $dT/dx = 0.13 K mm^{-1}$,

for $dx/dt = 10^{-5} m\ s^{-1}$, $dT/dx = 1.3 K mm^{-1}$, and

for $dx/dt = 10^{-4} m\ s^{-1}$, $dT/dx = 13 K mm^{-1}$.

For crystallization of β-$CaSiO_3$ at 1400K:

$L = 107 J\ g^{-1}$, $z = 3 Mg\ m^{-3}$ (135), and

$K_S \triangleq 3 J\ s^{-1}\ m^{-1}\ K^{-1}$ (10), therefore

for $dx/dt = 10^{-6} m\ s^{-1}$, $dT/dx = 0.11 K mm^{-1}$,

for $dx/dt = 10^{-5} m\ s^{-1}$, $dT/dx = 1.1 K mm^{-1}$, and

for $dx/dt = 10^{-4} m\ s^{-1}$, $dT/dx = 11 K mm^{-1}$.

From these results it is seen that, except at extremely high growth rates (for crystallization from a viscous liquid) the thermal gradients set up due to the liberation of latent heat at the crystal/melt interface are neglibible compared to the degree of undercooling during crystallization (approximately 200 to 300°C).

Dendritic growth occurs in a system in which a plane crystal/melt interface is unstable. When the crystal growth rate of a protrusion is greater than the surrounding surface, a crystalline "spike" can shoot out from the interface into the melt. As each spike is formed the associated "impurity" layer is formed (as discussed above) and thus retards the formation of other projections in the immediate vicinity. The overall result is that a number of spikes are formed which are approximately equally spaced

and mutually parallel, all growing in the same crystallographic direction, known as the dendritic growth direction. The angle which these primary (or first-order), arms make with the original interface depends on the crystal structure of the material. Secondary, and in some cases, tertiary, arms may subsequently form on these spikes, by a process similar to the formation of the primary arms. The secondary branches form along a direction equivalent crystallographically to that of the primary spikes, and as the arms develop they grow in thickness and so become acute triangles in longitudinal cross-section. The resulting crystalline morphology, a branched crystal, has the appearance of a tree and so is called a dendrite, after the Greek "dendron", meaning "a tree".

Dendritic growth is observed in the crystallization, or devitrification, of glass. Taylor and Hill (64) describe the appearance of dendrites found as devitrification "stones", i.e. unwanted crystallization formed during commercial glass manufacture due to holding a glass for too long over the critical temperature range, or to insoluble inclusions such as pieces of refractory brick acting as heterogeneous nuclei in the glass. Two types of dendrites are formed by silica devitrification in soda-lime-silica glass. Dendrites with the tridymite crystal structure form with branches at 60 degrees to the main stem, or as dendritic hexagons, while the cristobalite crystal structure is usually found in the dendritic form with branches at 90 degrees to the main stem. α-$CaSiO_3$, the

high temperature modification of calcium metasilicate, may sometimes exist in devitrified glass in the form of dendrites or dendritic hexagons which show branching at 60 degrees. One very characteristic form which α-$CaSiO_3$ may assume is that of short hexagonal prisms with concave, or "dished" ends, these prisms being up to one centimetre across. However, when devitrification proceeds from heterogeneous nuclei on a plane surface, e.g. crystallization from a glass surface, geometrical restrictions are imposed upon crystal growth in any direction other than that normal to the surface, i.e. the crystal growth fronts impinge, stopping any more development in that direction. This is known as transcrystallization (43), see figure 1.6. By this process surface nucleated α-$CaSiO_3$ dendrites produce an almost fibrous microstructure, since only the primary branches of the dendrites are fully developed and are arranged so as to be mutually parallel and approximately equally spaced. (If a crystal forms such that growth along one crystallographic axis is much greater than growth in any other crystallographic direction then this may be described as fibrous crystallization.)

A spherulite consists of a radiating array of crystalline fibres, all having the same fibre axis, and possessing the unusual property of branching in such a way that the crystallographic orientation of a branch departs slightly from that of the parent fibre. Therefore spherulites are polycrystalline aggregates which are approximately radially symmetric. As a generalisation

it may be stated that spherulite-forming melts do not only have viscosities at least two orders of magnitude higher than those for simple liquids, but also that they exhibit small coefficients of self-diffusion and the spherulites crystallize slowly (65). If U is the velocity of the advancing growth front, and ΔT is the amount of supercooling, then for simple liquids:

$$U/\Delta T = 1 \text{ to } 10^{-2} \text{ m s}^{-1} \text{ K}^{-1}$$

but for spherulite-forming melts:

$$U/\Delta T = 10^{-6} \text{ to } 10^{-10} \text{ m s}^{-1} \text{ K}^{-1}$$

However this slow crystal growth still uses the lateral mechanism of two-dimensional surface nucleation, which is also used during crystallization in simple liquids (66), see section 1.4.1. The main difference is that a high melt viscosity impairs the diffusion processes for molecules to be orientated to join a growing crystal.

Under isothermal conditions spherulites grow at a constant radial rate, in accordance with a linear growth law:

$$U = dr/dt = f(T)$$

where:

r = radius of spherulite at time t, and

f(T) = function of temperature and system under study only.

The growth of a spherulite at a constant radial growth rate represents a steady-state, not an equilibrium, process. Since a spherulite has a large surface to volume ratio, and thus a high surface energy content, it is clear that a spherulite is not an equilibrium crystal structure.

The linear growth law applies equally to coarse fibred, open structure spherulites and to fine fibred, compact spherulites, which indicates that the diffusion of latent heat away from the growth fronts cannot be the rate determining step. Similarly, if diffusion of matter toward the growth fronts were rate determining this would again give a growth rate which would be proportional to $t^{1/2}$.

Bernauer (67) in 1929 suggested that impurities may be vital in order to produce spherulitic fibrous growth. Using Bernauer's work, Keith and Padden (65) proposed a universal mechanism for spherulitic growth. In this they considered that the growing crystal rejects impurities preferentially, and the concentration of impurities on the melt side of the interface increase to a value greater than that of the bulk melt. When a steady state is established, if the melt is not stirred, an impurity rich layer of "thickness" δ, where:

$$\delta = D/U$$

D = diffusion coefficient of impurity in the melt, and
U = crystal growth rate,
forms in the melt at the interface. This layer leads to the constitutional supercooling described above. (In this context "impurities" are any substance included in different concentrations in the melt and crystal and which therefore must be transported if the crystals are to grow.) Therefore a plane interface is unstable and projections into the melt or glass start to grow.

During spherulitic growth the crystal growth rate is

slow, so that the latent heat liberated can be carried away relatively quickly (as shown by the calculation for the crystallization of calcium metasilicate, q.v.) and the ambient temperature throughout the crystallizing system may be regarded as constant. As the fibres develop, therefore, the grooves of glass between them do not contain a steep temperature gradient at right angles to the fibre length and, due to the relatively slow growth rate, there is more time for the diffusion of impurities into these grooves than during dendritic growth, although the high viscosity of the glass or melt at high undercooling will tend to inhibit the diffusion of large molecules. Therefore, there will be a decrease in undercooling throughout the grooves (the presence of impurities decreases the equilibrium crystallization temperature, see figure 1.5) and no significant temperature gradient, so that lateral growth into the grooves will be inhibited. The overall result is that the morphology of the developing spherulites will be long, fibrous projections separated by uncrystallized melt or glass. As the ambient temperature is lowered, or over long times at the higher temperature, secondary crystallization in the grooves may take place, but in some systems these grooves always remain as a glass.

From consideration of the impurity diffusion coefficients Keith and Padden (65) calculated that the stable width of a fibre is approximately equal to the width of impurity layer. In any crystallizing system small heterogenities may cause imperfections to be incorporated

into the growing crystal, and these defects could cause fibres to branch. There is no special reason, however, why these branches should be non-crystallographic, as the fibre branching in spherulites appears to be. Instead, it is thought that this non-crystallographic branching occurs when the growth tip of a fibre thickens, due to a local fluctuation in conditions, and becomes wider than the steady state width of the fibres. Since this wide fibre has an unstable growth front it splits into two fibres of stable width, each growing along the same preferred crystal axis (the spherulite fibre axis) but slightly misaligned with respect to each other and the parent fibre. Dendrites generally grow in melts of relatively lower viscosity and higher diffusion coefficients than spherulites, and therefore have a relatively large stable growth front width. This means that a large defect would have to grow on the growth tip of a dendrite before low angle branching would occur.

This explanation of low angle branching stands up when the morphologies of spherulites grown at different temperatures are considered. At high temperatures δ is large (since the diffusion rates of impurities are relatively high) so that coarse fibres grow and these only branch to a limited extent resulting in an open structure. At low temperatures δ is small resulting in fine fibres and profuse branching, which gives fine, compact spherulites. This type of branching also explains the origins of a spherulite. If a single crystal is nucleated in a highly viscous melt

then, as soon as the dimension perpendicular to the preferred growth axis (the fibre axis) exceeds the value of $\bar{d}$ in the system small-angle branching will start, giving first a sheaf-like and then the approximately radial morphology as branching continues, see figure 1.7. Morse and Donnay have described the development of spherulitic structure (68).

When "spherulites" are heterogeneously nucleated on a plane surface transcrystallization results in a parallel array of fibres, which may still show small-angle branching, growing orthotropically (growth direction perpendicular to the plane of nucleation), as is shown in the crystallization of salol (69).

Spherulites occur naturally in silicate minerals found in igneous rocks. Hatch, Wells and Wells (70) describe the morphology of spherulites found in obsidian, a pure natural glass of rhylolitic composition. Lofgren (71) has reviewed spherulitic textures in glassy and crystalline rocks, and found that these often resemble "sheaves of wheat tied at the centre", i.e. the spherulitic crystallization has been halted, by impingement or a change of conditions so that the glass is no longer held in the crystallization zone, before the spherulites could fully develop, see figure 1.7. Taylor and Hill (64) describe the development of devitrification stones in commercial glass in the form of radiating feathers or spherulites. These spherulites may grow up to eight centimetres in diameter since the low nucleation density allows a

spherulite to develop without impinging on a neighbouring growing spherulite. The low-temperature polymorph of calcium metasilicate (β-$CaSiO_3$) can be a devitrification product from commercial glasses and can form true spherulites or bunches of fibrous growths. Degen and Toropov (72) used the electron microscope to study spherulite formation in silicate glasses. They found that spherulitic formation in glasses occurs by similar means to spherulite formation in polymers and minerals.

During an investigation of controlled nucleation and crystallization in the soda-baria-silica system, Burnett and Douglas (42) found that the first detectable crystal phase was the high temperature polymorph of barium disilicate which grows first as spherulites and later converts to the stable low temperature form. After more prolonged heating the spherulites break up and are transformed into lath-like crystals. The "driving-force" for this recrystallization is the reduction of the surface energy content of the material. The spherulitic structure gives a large area of internal surfaces in a material, giving a large amount of surface energy per unit volume (the spherulitic structure is not an equilibrium morphology), and this is reduced when the lath shaped crystals are produced.

Barry et al (73) found that the kinetics and dendritic or spherulitic morphology of crystal growth in a eutectic composition lithia-aluminosilicate glass, containing titanium dioxide as a nucleation catalyst, were modified

by Ti^{4+} ions becoming preferentially sited on certain crystallographic faces of the crystals (which had the β-eucryptite structure). This shows that crystal morphologies resulting from controlled heat-treatments of glasses which contain internal nucleation agents, i.e. glass-ceramic microstructures, may be more complex than those formed by devitrification of simple glasses and igneous rocks. Burnett and Douglas (42), however, found that the Keith and Padden theory (65) accounted extremely well for spherulitic crystallization from soda-baria-silica glasses which did not contain any added nucleation catalysts.

Freiman and Hench (74) analysed the crystallization kinetics of spherulites in lithia-silica glasses using the Johnson-Mehl-Avrami equation (75). They found that crystal growth should be rod-like and the nucleation rate constant (i.e. the Avrami exponent equals 2). This is in agreement with the work of Morse and Donnay (68) who found that spherulites occur by the nucleation and growth of individual rods and that the nucleation rate of rods is constant throughout the spherulitic growth process.

(See also appendix V.)

1.4.3. ROD PULLING TECHNIQUES:

Maries and Rogers (76) found that it was not possible to induce fibrous calcium metasilicate crystals to grow along the axis of 1mm diameter calcium oxide-zinc oxide-silica glass rods when these were subjected to a conventional zone heating technique. As the rods passed

through an annular heating element crystals nucleated on the rod surface (see section 1.3.1.) and grew into the rods, thereby forming weak interfaces across the rod diameter. Another problem was that as the glass rod was heated the glass became progressively less viscous and therefore the hot zone slumped. (When crystalline materials are zone melted the solid each side of the hot zone remains rigid and this supports the molten material which is held by surface tension forces.) However they found that if the rod was passed through an electrically heated platinum coil which is in contact with the rod surface and therefore supports the molten material, and the glass each side, then no surface nucleation occurred. Instead, if crystallization is nucleated just below the hot zone (by a platinum wire), then β-$CaSiO_3$ can crystallize in an aligned and fibrous habit. The rod does not pass through a low temperature before the crystals form and therefore neither spontaneous internal nor surface nucleation can occur, i.e. this is crystallization from the melt rather than from a quenched glass.

More recently Maries has adapted this technique (77) so that glass rods of varying diameters, up to about 1mm, may be pulled directly from a heated platinum hopper full of molten glass and immediately crystallized in the temperature gradient, as above.

The situation below the molten zone, or below the melt in the platinum hopper, is represented in figure 1.8. The rod cooling rate may be exponential (77a) and the

corresponding growth rate curve was found by Maries using hot stage microscopy on the glass composition ZnO 20 wt %, CaO 30 wt % and SiO_2 50 wt % (78), which was that used for rod pulling. Once the crystals have nucleated and the pulling rate is constant, the growth is self-stabilising. Since this is crystal growth from the melt, the crystal growth rate increases with decreasing temperature, increasing undercooling, and therefore if the growth rate exceeds the rate of travel of the rod (pulling rate) the crystal growth front approaches closer to the molten zone and thus moves into a region at a higher temperature, the growth rate decreases and the growth front drops back to the stable position. Conversely if the growth front drops down the rod, its temperature decreases, the growth rate therefore increases and the crystal growth front moves up again to the stable position where the growth rate equals the pulling rate.

Calcium metasilicate has a phase transition, from the high temperature α-$CaSiO_3$ phase to the low temperature β-$CaSiO_3$, which occurs in the critical devitrification region (see section 1.5.1.). This means, in the case of the glass used by Maries (76), that pulling rates below 20 microns per second will result in the crystallization of α-$CaSiO_3$ and at greater speeds β-$CaSiO_3$ is the crystallizing phase, but at pulling rates above 50 microns per second the rod quenches through the critical devitrification region and pulls out as a glass, see figure 1.8.

Livingston (79) has described a process somewhat

similar to this rod pulling. In order to produce very fine, aligned in-situ composites by solid-state transformations the samples are transformed by moving up a temperature gradient. The transformation rate versus temperature curve is bell-shaped (i.e. goes through a maximum below the equilibrium transformation temperature). The spacing of eutectoid, eutectic or cellular precipitation decreases with decreasing temperature of transformation (for similar reasons to those in crystal growth from the melt, see section 1.4.2.). If the material is transformed by cooling through the transformation region it will convert at a higher temperature than if it is first quenched and subsequently reheated so that the transformation occurs below the maximum rate temperature thereby resulting in a fine microstructure. Livingston has suggested that if a suitable quenched material is moved up through a temperature gradient then aligned composites with finer spacings could be produced. Carpay and Cense (6) have applied this technique to the in situ growth of composites from the vitreous state. They state that the position of the growth front is stable, "which means that variations in the pulling rate are followed automatically by the growth rate". This is not the case in the down-transformation of quenched materials, i.e. in the case of this research (crystal growth from a glass) since below the maximum transformation rate temperature the transformation rate (in this case crystal growth rate) decreases with

temperature. Therefore if the transformation front drops down the temperature gradient the transformation rate decreases, and since the rate of material travel remains constant, the transformation front drops further down the gradient, the transformation rate again decreases, etcetera. A similar "vicious circle" is set up if the transformation front moves too far up the temperature gradient.

1.5. THE CRYSTALLOGRAPHY OF PHASES PRODUCED IN THE SELECTED MATERIALS:

1.5.1. CALCIUM METASILICATE:

There are three structural modifications of crystalline calcium metasilicate, known by the mineralogical names wollastonite, parawollastonite and pseudowollastonite.

Wollastonite and parawollastonite are both referred to as the low temperature modification, designated β-$CaSiO_3$. Wollastonite (and parawollastonite) are pyroxenoids (80), and therefore have a structure which consists of chains of silicon-oxygen tetrahedra running parallel to the crystallographic b axis, the chain structure repeating after every three tetrahedra, i.e. Dreierketten. These single chains are linked by calcium atoms in irregular octahedral coordination with six oxygen atoms. Monoclinic parawollastonite is related to the triclinic wollastonite by a simple packing modification (81), and this explains why intergrowths of these two forms occur on a sub-microscopic scale (82). In natural wollastonite the calcium can be

replaced by iron, manganese and, to a lesser extent, magnesium, and synthetic wollastonites have been shown to form a solid solution series in the $CaSiO_3$-$FeSiO_3$ with compositions up to 76% $FeSiO_3$.

Pseudowollastonite is generally regarded as being triclinic, but there are planes of pseudosymmetry perpendicular to all three triclinic unit cell axes. The cell can therefore be regarded as pseudo-hexagonal, or a larger pseudo-orthorhombic cell (83). There is some evidence of polytypism in pseudowollastonite which can be explained in terms of a double sandwich layer of $Si_3O_9^{6-}$ rings (see figure 1.1) between hexagonally packed Ca^{2+} ions (84).

There is some disagreement about the temperature of inversion of wollastonite to pseudowollastonite. Although 1120°C $\pm$ 10°C is usually taken to be the true value (85), temperatures as high as 1190°C and 1200°C have been quoted. A small amount of diopside ($CaMgSi_2O_6$) in solid solution is known to raise the inversion temperature. Rostoker found that it is possible to sinter fibrous wollastonite at 1150°C without any transformation (86); he found the inversion to occur at 1160°C. The rate of the inversion has been reported as very slow below 1150°C, since this is a solid state phase transformation, although more recently Buckner and Roy found that this is not always necessarily the case (87).

In nature wollastonite occurs in coarse bladed aggregates, and is usually acicular or fibrous even in small particles, the crystallographic b axis (chain axis,

q.v.) coinciding with the fibre axis. The aspect ratios of these fibres (i.e. fibre length over fibre diameter) may be as much as 13 or 15, but are more usually 7 or 8.

Synthetic calcium metasilicate (β-$CaSiO_3$) has been produced commercially for some years. Many hydrothermal techniques have been used, e.g. (88), but the hydrated product does have the same properties as the anhydrous material. None of the anhydrous techniques produce a "pure" product, e.g. (89). A review of these synthetic materials, and also of the occurrence and properties of wollastonite mineral is given in the book by Andrews (85).

1.5.2. SECONDARY DEVITRIFICATION PRODUCTS:

$CaAl_2Si_2O_8$ has several known polymorphs. The mineral phase which is stable in contact with CaO-Al_2O_3-SiO_2 liquids is anorthite (90). This is a triclinic feldspar which melts congruently at 1553°C. It enters extensively into solid solutions, e.g. the plagioclase series between anorthite and albite ($Na_2Al_2Si_6O_{16}$).

$Ca_2ZnSi_2O_7$ occurs naturally as the mineral hardystonite. This has a melilite type structure, i.e. zinc tetrahedra are located at the corners and base-centre of the primitive tetragonal lattice. The structure of hardystonite can be described as consisting of $[ZnSi_2O_7]^{4-}$ sheets within which the nature of bonding is dominantly covalent, the adjacent sheets being held together by Ca^{2+} ions with the interlayer bonding predominantly ionic in character (91). The melilites are capable of extensive solid solution, e.g. the åkermanite-gehlenite continuous range of solid solution (92).

1.6. THERMAL EXPANSION CHARACTERISTICS OF SILICATE MATERIALS:

1.6.1. GLASSES:

Figure 1.9 shows a typical expansion curve for a glass. The temperatures Tl, Tu and Mg are at points of tangency; Tg and Ts are points of intersection. This curve is analysed as follows (93).

Tl is the lower annealing limit, the lowest temperature at which the residual stresses, produced when a glass is cooled after casting, can be relieved by small adjustments of the internal structure (see section 1.2.), a process requiring a prolonged isothermal treatment at Tl (19). There is insufficient thermal energy available for this process below Tl.

Tg is the "glass transition temperature", the lowest temperature at which the internal molecular structure of the glass can react to a change in conditions affecting its metastable internal equilibrium within the time scale of an experiment. Below Tg the equilibration time is so long that it is not normally measurable. The exact value of Tg depends on the rate of the experiment measuring the change in properties of the glass, i.e. experiments measuring only fast responses find a higher value of Tg than slow time scale measurements. The annealing state of a glass can also affect the value of Tg, i.e. a fast quenched glass with a high fictive temperature (a glass which would be in internal equilibrium at a relatively high temperature (19)) would have an open molecular structure

and therefore would begin to reach dimensional equilibrium at a relatively low temperature. This would result in low values for Tl and Tg.

Tu is the upper annealing limit and Mg is the point of incipient deformation, i.e. the temperature at which the viscosity of the glass is so reduced that the glass no longer behaves as a rigid solid. Ts is the dilatometric softening point, see section 3.4.

The linear expansion below Tl is associated with changing interatomic distances and angles, i.e. the changes in bond lengths and angles. It has been shown by Smyth (94) that those vibrations in a network whose frequency increases as the network expands make positive contributions to the thermal expansion, and vice versa. The vibrations of bridging oxygen atoms parallel to the line connecting the centres of the two adjoining silicon atoms make a negative contribution to the thermal expansion of the network, but the vibrations perpendicular to the line of centres leads to a positive expansion.

1.6.2. CRYSTALLINE MATERIALS:

The thermal expansion of a crystal structure can often be expressed empirically as a linear combination of the expansions of the units making up the structure. In the case of a silicate framework the macroscopic expansion is the algebraic sum of a bond-length expansion and a tilting effect (95), i.e. in a structure in which the coordination polyhedra are tilted with respect to each other the simple bond-length expansions are modified by

the manner in which the angle of tilt changes with temperature. (This is similar to the consideration of the Si-O-Si bond vibrations discussed above in section 1.6.1.) Megaw (95) has found that generally bond-length expansion coefficients are roughly equivalent to the inverse square of the Pauling valence but the effect of tilting on the thermal expansion is usually larger. She has found that thermal expansion always involves a straightening out of the angles between the structural polyhedra, resulting in an increase in the mean linear expansions over what would be expected from bond-length expansion alone. This change of tilt angle within a phase can lead to a phase transition.

From his study of thermal expansion anisotropy of oxide compounds Bayer (96) found that differences between thermal expansion coefficients in different crystallographic directions occur in single crystals and orientated polycrystalline ceramics of compounds with lower than cubic symmetry. The amount of anisotropy depends mainly on the atomic arrangement in the compound and on the microstructure of the ceramic. He found that the magnitude of the thermal expansion coefficient and degree of expansion anisotropy are determined primarily by the valency and size of the ions present on the structure, and only to a smaller extent by the type of structure, although the effect of structure type on the anisotropy may be more pronounced in crystals with highly distorted coordination polyhedra. However generally the lower the valency of the larger cations the

greater both the expansion coefficient and anisotropy.

1.7. MECHANICAL PROPERTIES OF CERAMICS:

1.7.1. BRITTLE MATERIALS:

Brittle materials are those materials whose crystal structures do not have any mechanism for the absorption of mechanical stresses by plastic deformation. A sinusoidal tensile force versus displacement curve is the closest approximation to the theoretical fracture of a material by the breaking of atomic bonds across unit area of fracture interface (11, 97). The area under this curve equals the energy expended in pulling atomic planes apart, i.e. twice the surface energy of each new surface.

$$\sigma_o \simeq (E\gamma/a)^{1/2}$$

where:

σ_o = theoretical strength of material,

E = Young's modulus,

a = atomic spacing, and

γ = surface energy per unit area of each new surface.

Using experimental values for E, γ and a, then empirically for most solids:

$$\sigma_o \simeq E/10$$

This value is only approached by crystal whiskers or carefully produced fibres. Typically for the fracture of brittle materials (or for yield of ductile materials):

$$\sigma_o \simeq E/1000$$

This discrepancy is due to the inevitable presence of small flaws in real materials.

For ideally elastic brittle materials, mechanical properties reviewed in (98) and (99), subjected to tensile stress, local stress concentrations build up at any structural imperfection. For a sharp crack in the surface of the material, of length c, a radius of curvature at the crack tip ρ and subjected to an applied stress σ_a, the stress at the crack tip is increased to:

$$\sigma_{TIP} = 2\sigma_a(c/\rho)^{1/2}$$

When this concentrated stress is equal to the theoretical strength of the material fracture occurs, i.e. when:

$$(E\gamma/a)^{1/2} = 2\sigma_a(c/\rho)^{1/2}$$

$$\therefore \quad \sigma_a = (\gamma E\rho/4ac)^{1/2} \qquad (1).$$

This equality gives the applied stress for fracture approaching zero as the radius of the crack tip approaches zero, which is physically unlikely. However, if it is assumed that the crack can only propagate catastrophically if the free energy of the system is lowered, then the work done by the applied stress in the form of stored elastic energy around the crack tip must supply the new surface energy for crack growth. The stored elastic energy per unit thickness perpendicular to the crack length (U_E) is, for plane stress:

$$U_E = (\pi c^2\sigma^2)/E$$

The surface energy required (U_S) is:

$$U_S = 2\gamma c$$

Therefore, for an unstable crack:

$$(\pi c^2\sigma^2)/E = 2\gamma c$$

$$\therefore \quad \sigma = (2\gamma E/\pi c)^{1/2} \qquad (2).$$

This is the "Griffith" stress.

Since the applied stress for fracture equals the Griffith stress for fracture in the presence of flaws, then from comparison of equations (1) and (2):

$$2/\pi = \rho/4a$$

and therefore the limiting value of crack tip radius is:

$$\rho = 8a/\pi \simeq 3a$$

A sharper crack would propagate, but although the Griffith criterion (equation (2)) is necessary and sufficient for atomically sharp cracks, i.e. perfectly brittle fracture, it is too small for real ceramic materials. In these crack blunting occurs (i.e. an increase in the radius of the crack tip) due to limited plastic flow at the crack tip induced by large shear stresses and/or by chemical corrosion at the crack tip (e.g. erosion of glass by water vapour). For real materials an empirical surface energy term must be used in equation (2), i.e. γ_i, which includes the results of the plastic flow, rough surface steps, crack blunting, etcetera. Therefore generally:

$$\sigma_F = 1/Y(2E\gamma_i/c)^{1/2}$$

where:

Y = geometrical factor depending on crack and specimen geometries, and

σ_F = fracture stress.

In ceramics at relatively low temperatures fracture occurs by the propagation of inherent flaws (100) (as described above). The initiating flaws may be surface scratches, internal pores or grain boundaries (101).

1.7.2. CERAMIC MATRIX COMPOSITES:

Unidirectionally crystallized fibrous materials could be regarded as composites, i.e. in situ composites, see section 1.1.1.

Donald and McMillan (102) and Davidge (103) have recently published reviews of ceramic matrix composites.

In unidirectional fibre reinforced ceramic matrix composites significant strengthening occurs if the Young's modulus of the fibres (E_f) is greater than that of the matrix material (E_m). For conditions of equal elastic strain in matrix and fibres the strength of the composite is expressed by a simple mixtures law (104):

$$\sigma_c = \sigma_f V_f + \sigma_m V_m$$

where:

σ_f = ultimate strength of fibres,

σ_m = ultimate strength of matrix,

σ_c = strength of composite,

V_f = volume fraction of fibres, and

V_m = volume fraction of matrix.

The strain is equal in fibre and matrix, i.e.:

$$\varepsilon = \sigma_f / E_f = \sigma_m / E_m$$

therefore,

$$\sigma_c = \sigma_m \left[1 + V_f . ((E_f / E_m) - 1) \right]$$

If the aligned fibres are discontinuous the stress in the fibres builds up to a maximum over a certain critical length, $l_c/2$ from the ends of the fibres, where:

$$l_c = r\sigma_f / B$$

r = radius of fibres, and

B = interlamellar shear strength.

The mean stress in fibres of length l is:

$$\overline{\sigma_f} = \sigma_f \left[1 - (1 - Z)\, l_c/l\right]$$

where:

$Z\sigma_f$ = the average stress in fibres within a distance of $l_c/2$ from their ends.

If the fibres are not in parallel alignment then $\sigma_f V_f$ is reduced by a geometrical factor.

Uniaxial aligned fibre composites under the action of a tensile stress applied at an angle θ to the fibre direction generally fracture by one of three mechanisms (97).

1. Failure in the plane perpendicular to the fibres due to tensile failure of the fibres, in this case:

$$\text{fracture stress} = \sigma_c/\cos^2\theta .$$

2. Failure by shear in the direction of the fibres on a plane parallel to the fibres,

$$\text{fracture stress} = 2B/\sin 2\theta ,$$

where B is the shear strength of the fibre/matrix interface, or failure stress in shear of the matrix.

3. Failure of the fibre/matrix interface in tension,

$$\text{fracture stress} = \sigma_u/\sin^2\theta ,$$

where σ_u is the tensile stress required to produce failure of the composite in a direction normal to that of the fibres.

The fracture mode that requires the lowest stress occurs, and therefore a curve showing the variation of composite fracture strength with varying angle θ can be plotted, see figure 1.10. Phillips et al found good agreement between this theoretical curve and that drawn from the results of

mechanical tests on a carbon fibre reinforced glass composite (13).

The fibre/matrix interface is vital in determining the properties of the composite. When both the fibres and matrix are brittle and are strongly bonded the composite behaves essentially as a homogeneous brittle solid. However if the fibre/matrix interface is weak then a matrix crack can pass the fibres without causing their immediate failure, i.e. to use the fibres efficiently the stress must be transferred from the matrix to the fibres. In ceramics the fibre/matrix bond is often mechanical, achieved by frictional forces between the fibre surface and matrix material, rather than a chemical reaction bond (105).

The work of fracture of the composite can be defined as the amount of energy required to produce unit area of fracture during controlled crack growth (106), and can be taken as a measure of the toughness of material. Brittle ceramics exhibit low works of fracture, since cracks are easily propagated (no crack blunting). The ratio of stored elastic energy at fracture to the work of fracture (104) is 0.2 for copper, and 25 for alumina, i.e. failure is expected to occur by cracking in alumina but not in copper. This provides a rough criterion of toughness for materials with widely differing capabilities for absorbing strain energy.

In a fibre reinforced ceramic the energy required to propagate the crack will be greater than that required for

initiation, since such a composite contains weak fibre/matrix interfaces which can blunt the crack tip. For this type of material the work of fracture technique yields a more realistic engineering parameter than conventional fracture mechanics analysis of fracture initiation energy (102).

The total work of fracture is increased by increasing the effective crack propagation area by providing weak directions within the material parallel to the tensile axis along which the crack can be deflected. In unidirectionally aligned fibrous composites a weak fibre/matrix interface may deflect a crack, therefore effectively blunting the crack tip, but although this mechanism gives a large work of fracture the composite material is relatively weak. If the fibre/matrix interface is strong the crack may propagate relatively unimpeded, and if the load is totally transferred to the fibres and the composite fracture stress occurs when the fracture load is reached in the fibres, then a planar fracture is given across the material and a low value for the work of fracture. There will always be some debonding of the fibres in the immediate vicinity of the crack. A composite containing continuous fibres usually fractures across a flat plane. A composite containing discontinuous fibres of less than critical length does not give any fracture through the fibres. Instead the fibres debond and pull-out of the matrix giving a large work of fracture. Strongly bonded, discontinuous fibres longer than critical length give a combination of

pull-out and fibre fracture. The composite strength of materials containing aligned fibres of critical length is half the law of mixtures strength.

In brittle fibre-brittle matrix composites multiple cracking of the matrix will only occur if the failure strain of the matrix is less than that of the fibres. In this case the matrix cracks when its failure strain is exceeded, the fibres adjacent to this crack debond and pull-out to span the crack giving an increase in the work of fracture. The strain builds up in the matrix as the distance from the crack increases and at half the critical length away from the crack the matrix failure strain is again exceeded and another matrix crack forms. This multiple cracking gives pseudo-ductility (apparent ductility in the load versus deflection curve). These cracks cannot propagate as they are limited by the degree of elastic strain in the fibres.

Therefore (102) for optimum strength and stiffness of a continuous fibre (or fibre length much greater than l_c) composite, the difference between the failure stress and strain of the matrix and those of the fibres should be as large as possible, the fibres should be aligned parallel to the tensile axis, and should have a strong fibre/matrix interface bond. However, for optimum toughness (fibre pull-out) parallel aligned discontinuous fibres of approximately critical length, and weak fibre/matrix interfaces to deflect cracks are required. The best compromise properties are obtained for materials with

aligned, discontinuous fibres of lengths somewhat greater than the critical length, or continuous fibres with varying fibre tensile fracture strengths, to give fractures at different distances from the primary fracture plane and therefore some fibre pull-out.

The thermal shock resistance of composites depends on the differential expansion between the matrix and fibre materials. This is an important parameter as it controls the residual stresses in the composite left after cooling from the fabrication temperature or after heat cycling.

On cooling from the fabrication temperature the effect of thermal shock depends on whether the matrix or fibres has the higher expansion coefficient. If the expansion of the matrix is greater than that of the fibres then the fibre/matrix interface is in compression radially, which strengthens a frictional bond, and perhaps also a chemical bond, and this is therefore desirable. However axially the fibres produce tension in the matrix parallel to the fibre axis, and if this tensile stress exceeds the matrix fracture stress then a network of cracks can develop in the matrix perpendicular to the fibre axis (i.e. thermally induced multiple cracking) which is undesirable. If the expansion of the matrix is less than that of the fibres then the fibre/matrix interface is in tension radially, and if this stress exceeds the tensile strength of the interface this will cause interfacial "decohesion". Axially a strong fibre/matrix interface will be in compression, which increases the stress necessary to

initiate fracture, but a weak interface will not transmit the stress (i.e. there will be no prestressing of the matrix) and voids may form at the fibre ends which debond.

Generally the thermal residual strain in the matrix (assuming there is either a chemical or a frictional bond, even if weak) is given by:

$$\varepsilon_m' = E_f V_f \Delta\alpha \Delta T / E_c \qquad (102).$$

$$E_c = E_f V_f + E_m V_m \quad \text{(law of mixtures)},$$

then:

$$\sigma_c = E_c (\varepsilon_m - \varepsilon_m')$$

where:

ε_m = matrix fracture strain in the absence of fibres, and

ε_m' = residual strain in the matrix.

Goan and Prosen (107) have tested both untreated (weak fibre/matrix interface) and whiskered (strong fibre/matrix interface) carbon fibre reinforced resin in shear using short beam tests (as in ASTM D2344-65T, but using flat specimens), scissors and University of Virginia method. They found that for both types of specimen the scissors method gave the lowest B (interlamella shear strength) value, the short beam test an intermediate result and the University of Virginia method the highest B results. In short beam tests weak interface specimens fractured under shear, giving a true B value, but strong interface materials failed in tension so, although the B strength calculated is very much higher than that for the weak interface material, this is a minimum B value for the strongly bonded material.

1.7.3. BEND TESTS:

Brittle materials are weaker in tension than compression, and therefore it is important to measure a tensile "modulus of rupture" for ceramics.

A bend test specimen, or any other mechanical test specimen, is a structural component subjected to a load of known magnitude and direction (108). Subsequent stress or strain analysis of this gives the strength value of the specimen material. This means the limits of stress analysis apply to strength testing, i.e. the assumptions of material characteristics, loading conditions and specimen geometry, and these are sources of error (109, 110).

Uniaxial tensile tests are difficult to achieve with ceramics, as these brittle materials cannot alleviate the effects of imperfect test apparatus and specimens as can ductile materials and therefore parasitic stresses can lead to erroneous strength results (111).

Bend tests, in which non-uniform stress distributions are developed, avoid the problems of setting-up uniform stress distributions in ceramic materials. A more complex analysis of the results is required, but this is compensated by the simplicity of the test apparatus and technique, although parasitic stresses which affect the final result can still be developed. Ideally the test should be perfectly "hard", i.e. the force developed is a function only of the compliance of the specimen to the imposed deflection. However this ideal can never actually be attained, because of the elastic deformation of the testing

machine, and of the specimen itself. A screw-driven test machine operated at a small fraction of its full capacity is reasonably hard. If the force required to produce unit deflection in the direction of the force, i.e. the stiffness, of the testing machine is K_n and of the load train is K_t, then when a load P is applied U, the stored energy is:

$$U = \frac{P^2}{2}\left[\frac{1}{K_n} + \frac{1}{K_t}\right] + \text{elastic energy stored in specimen.}$$

At the same surface stress the energy stored in the specimen in uniaxial tension is three times the energy stored in bending. The load necessary for fracture is less in bending and so the energy stored in the testing machine and load train is also less. Therefore a bend test is harder than a uniaxial tension test, the hardness depending on the specimen geometry, the material tested, the type of test machine and the loading conditions.

A beam loaded in bending has tensile stress on one face and compressive stress on the opposite face (109). The simplest type of bend test is three-point loading in which the maximum stress occurs below the central loading point. If the span to depth ratio, i.e. L:d, is sufficiently large then, assuming an elastically homogeneous specimen material, the stress at the outermost element of a three-point bend test specimen is:

$$\sigma_{MAX} = Mh/I \qquad (110, 109)$$

where:

M = externally applied moment,

I = second moment of area of the cross-section about the neutral axis, and

h = initial distance between the neutral axis and the extreme element where stress is a maximum.

For a beam of rectangular cross-section, depth d, breadth b, simply supported over a span L and carrying a concentrated load P mid-span (109):

$$M_{MAX} = PL/4$$

and:

$$I = bd^3/12$$

therefore, since h = d/2:

$$\sigma_{MAX} = \frac{3}{2}\frac{PL}{bd^2}$$

The Young's modulus (E) of the specimen material can be found using (109):

$$v = \left[\frac{M}{EI}\right] x\, dx$$

where:

v = deflection at the bottom of the beam, and

x = the distance along the beam.

Therefore:

$$v = \int_0^{L/2} \frac{3P}{Ebd^3} x^2\, dx$$

$$v = PL^3/4Ebd^3$$

and:

$$E = PL^3/4vbd^3$$

Bend tests are statistically indeterminate, i.e. the assumption made is that the strain is linearly distributed from a maximum tension at one surface to a maximum

compression at the opposite surface. This means that the resulting stress distribution depends on the stress versus strain characteristics of the material under test, i.e. if the stress/strain plot is linear then the stress distribution is linear, but if the stress/strain plot is non-linear the stress distribution is also non-linear. Since a combination of the assumed strain distribution and static equilibrium is not sufficient to completely determine the stress distribution, then bend tests are "indeterminate".

Phillips et al (13) used short beam three-point bend tests to measure the interlamella shear strength of carbon fibre reinforced glass composites. This technique is widely used to measure the shear strength of composites due to its experimental simplicity. Short beam tests have a span to depth ratio of less than five, and for three-point loading the distribution of vertical shear stress down the depth of the section is parabolic (109). The shear stress must be zero at the external surfaces since the complementary shear stress in the longitudinal direction must be zero at a free surface. The maximum shear stress (B_{MAX}) occurs on the specimen neutral plane:

$$B_{MAX} = \frac{P}{4I}\left[\left[\frac{d}{2}\right]^2 - h^2\right] \qquad (109)$$

therefore:

$$B_{MAX} = 3P/4bd$$

The maximum shear stress is 1.5 times the mean value.

The major sources of error in bend tests (108, 112) are:

1. Wedging effects below central loading point,

2. Frictional forces developed at the outer loading points, and

3. Twisting due to improper loading or specimen geometry, i.e. if the loading edge is not parallel to the specimen surface.

Wedging, crushing or local shear, can occur due to the high stresses produced under the knife-edges or small diameter rollers which transmit the load and contact the surface at right angles to specimen axis. However these failures can be easily distinguished from the desired fracture mode, and can be rejected. If this effect does not actually cause failure, then these stresses can make the maximum tensile stress in the specimen occur slightly to one side of the centre line below the top loading point.

The changes of length produced by the strains due to the test specimen surfaces curving gives longitudinal fictional forces at the outer loading points. The net effect is a reduction in the total stress at the specimen surface and, if not corrected, an increase in the apparent strength of test material. This can be reduced by using freely rotatable rollers, and, if the specimen has a high surface hardness, low rolling friction coefficients can be attained by using a hard material for the rollers.

The torsion due to non-uniform load distributions across the breadth of the specimen can be reduced by machining the top and bottom surfaces of the specimen exactly parallel, and by using an accurately constructed testing apparatus.

Using the Weibull weakest link model analysis the probability of fracture, S, can be expressed as (113):

$$S = 1 - \exp\left[- V \left(\sigma/\sigma_o\right)^m \right]$$

where:

σ_o = "classical" strength of a "flawless" specimen,

σ = stress at fracture,

V = volume of the body subjected to tensile stresses, and

m = constant related to the flaw density in the material.

There is a finite stress below which fracture will never occur, σ_u, and so empirically:

$$S = 1 - \exp\left[- V \left(\frac{\sigma - \sigma_u}{\sigma_o}\right)^m \right]$$

Therefore the probability of fracture depends on the volume of material under tension (tensile stresses usually cause fracture in brittle materials), as it can be shown (113) that for both tensile and bend tests the mean strength of the samples varies inversely with the (1/m)th power of the volume subjected to the maximum tensile stress. For three-point bend tests theoretically only the section of the specimen directly below the top loading point is subjected to the maximum stress, and therefore the "volume" of material tested depends on the breadth of the specimen beam. This means that the size effect is less important in three-point bend tests than in four-point bend tests.

Hasselman et al (114) discuss how the change in specimen volume is usually accompanied by a change in the specimen compliance, i.e. in the strain rate for a given cross-head speed. In three-point rectangular beam bend tests for an increase in span the strain rate and the

Weibull statistical effects are additive, whilst for an increase in beam depth these effects counterbalance one another.

When highly anisotropic materials are tested it has been found (115) that the end effects (effects of the local stress concentrations set-up at the loading points) may exert an influence over the stresses in the specimen for a far greater distance than that generally accepted for isotropic materials, which is St. Venant's principle (end effects zero within a distance equal to the maximum cross section of the specimen). Therefore the calculated experimental moduli found from beam tests performed on unidirectional composite materials will be below the "true" value for the material, especially from beams with small length to width ratios.

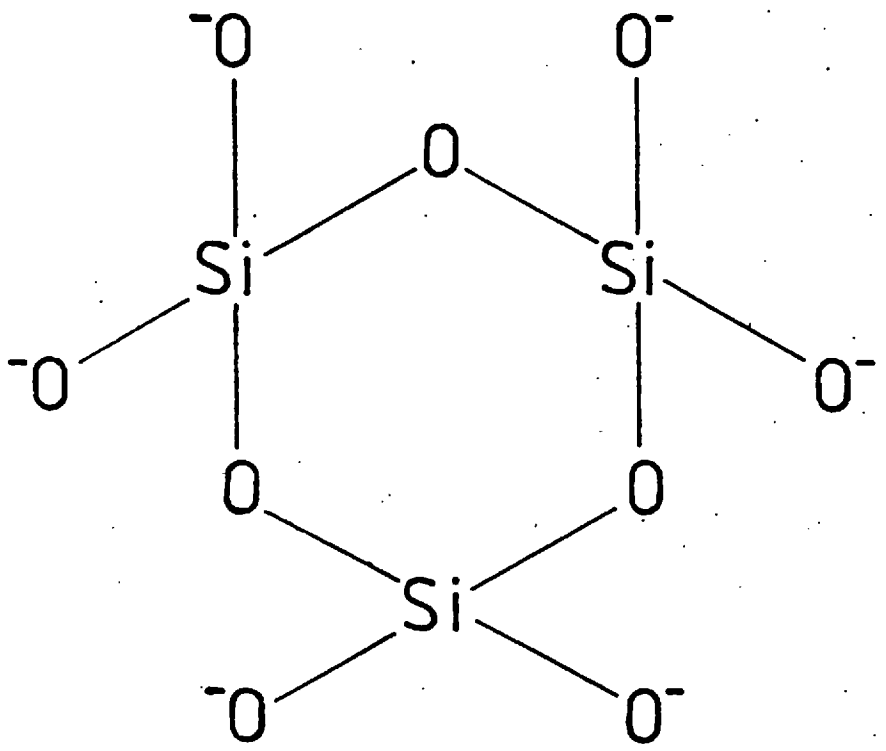


Fig. 1.1 $Si_3O_9^{6-}$ ring anion.

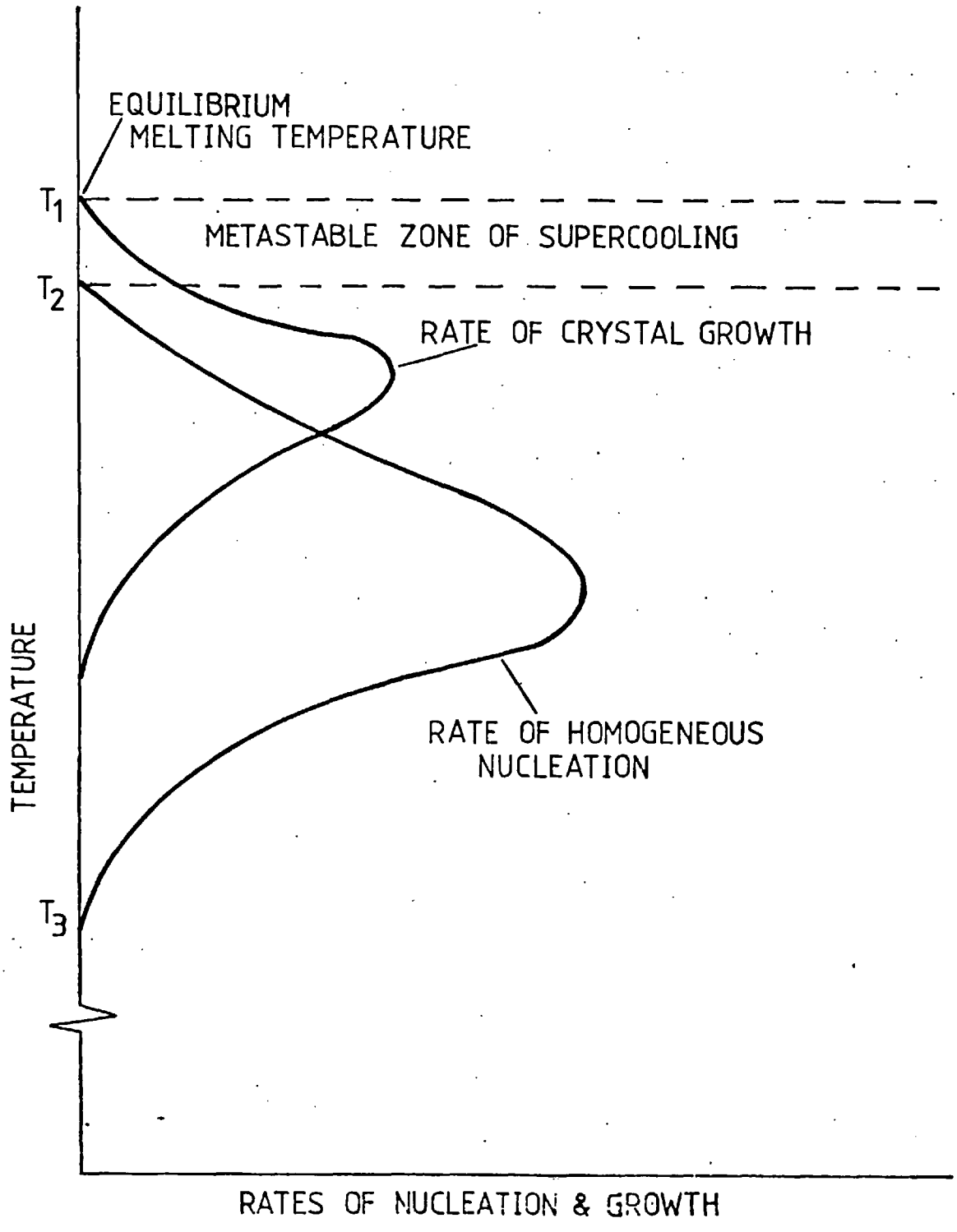


Fig. 1.2 Rates of homogeneous nucleation and crystal growth in a viscous liquid.
(ref. 10, page 29)

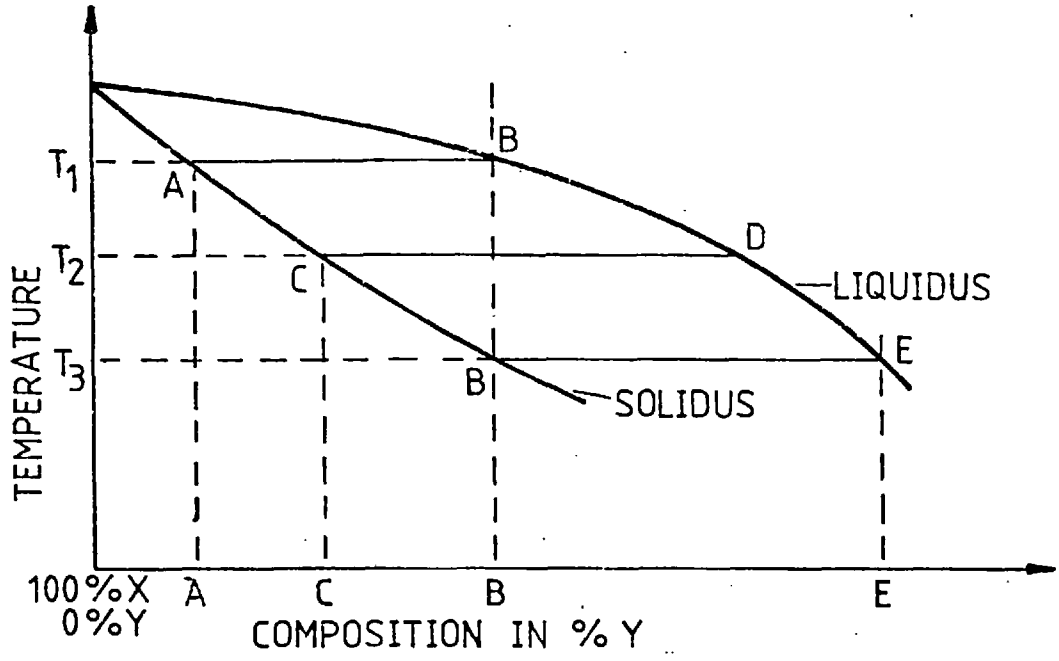


Fig. 1.3 Schematic binary phase diagram.

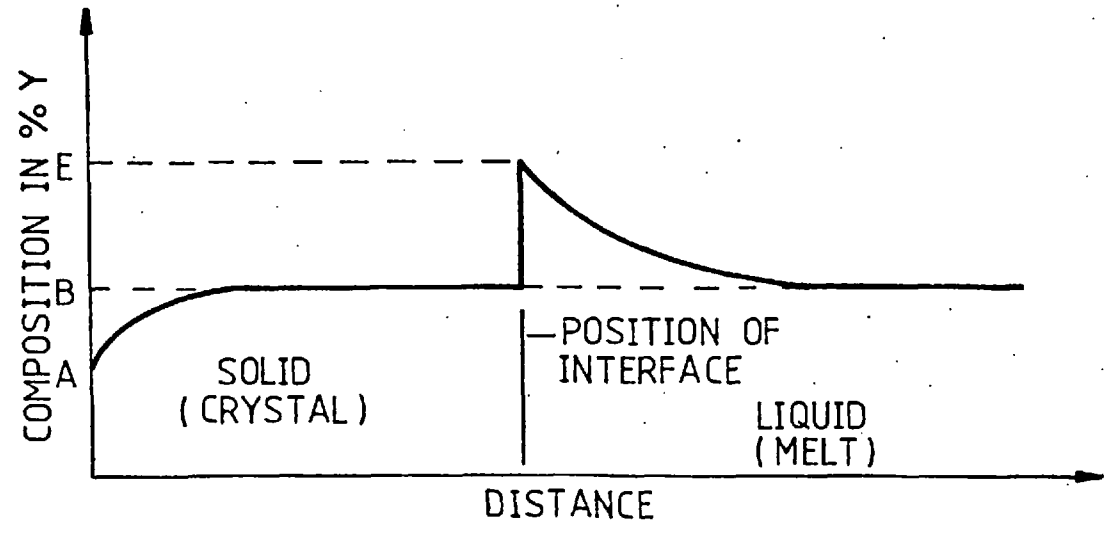


Fig. 1.4 Composition verus distance plot corresponding to one - dimensional crystallization.

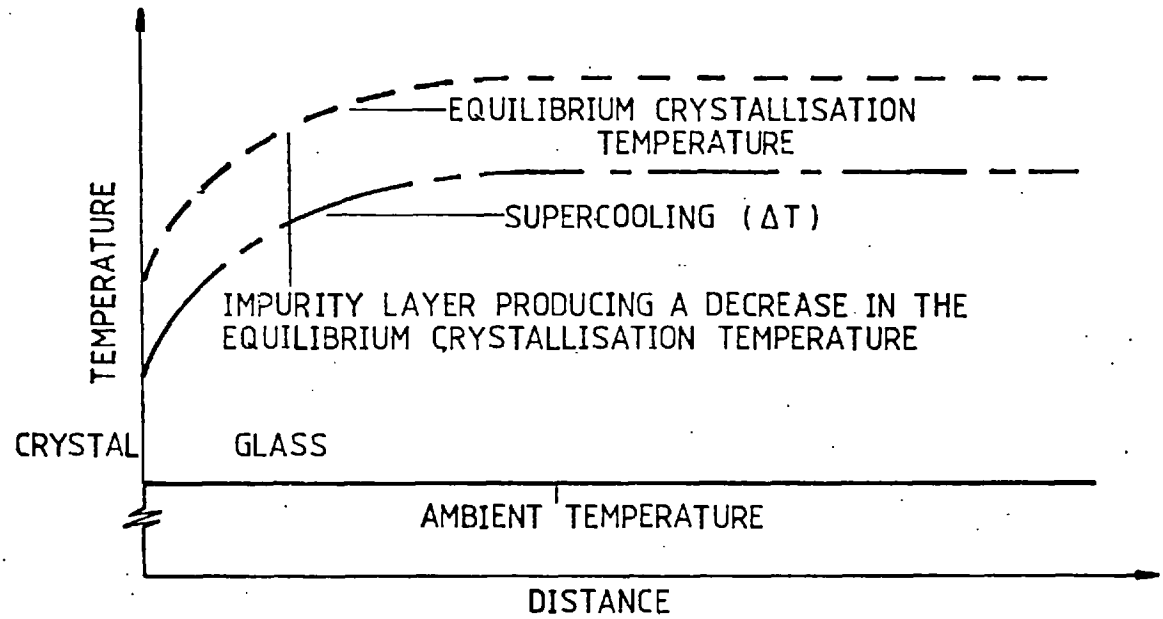
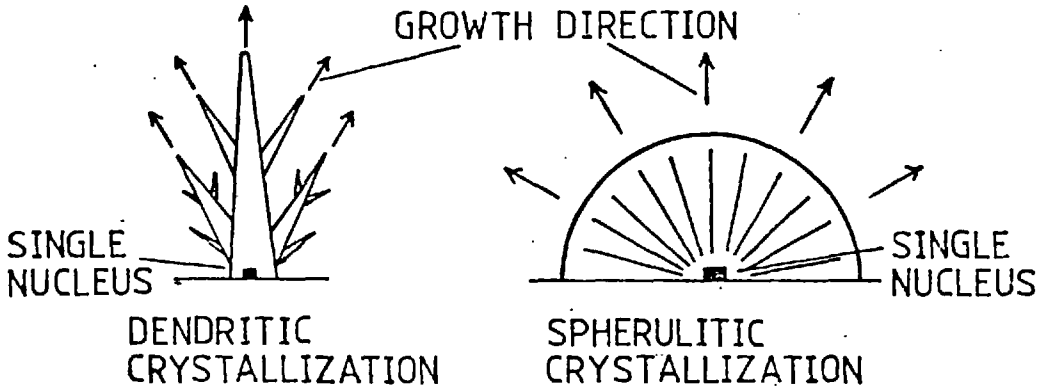


Fig. 1.5 Situation at crystal/glass interface when isothermal conditions apply.



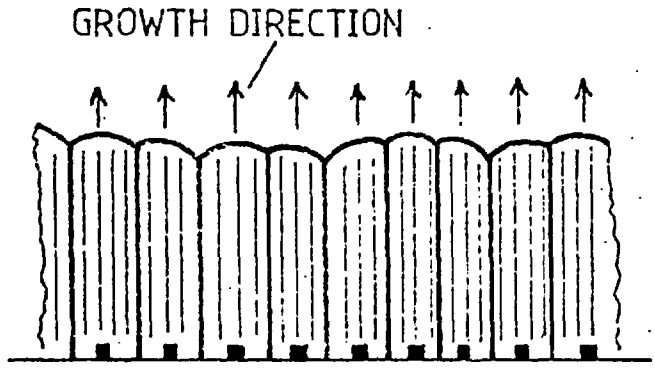


Fig. 1.6 Transcrystallization.

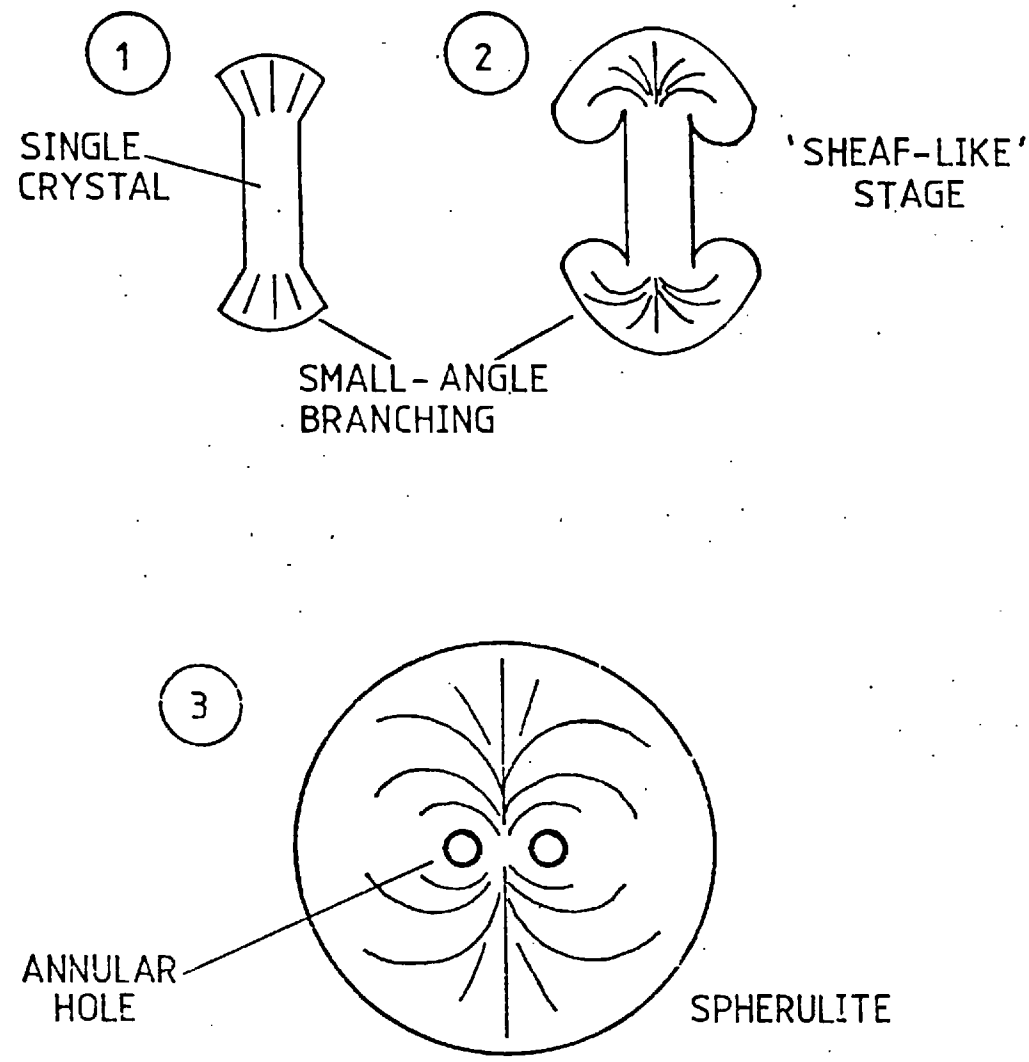


Fig. 1.7 Stages in the development of a spherulite.

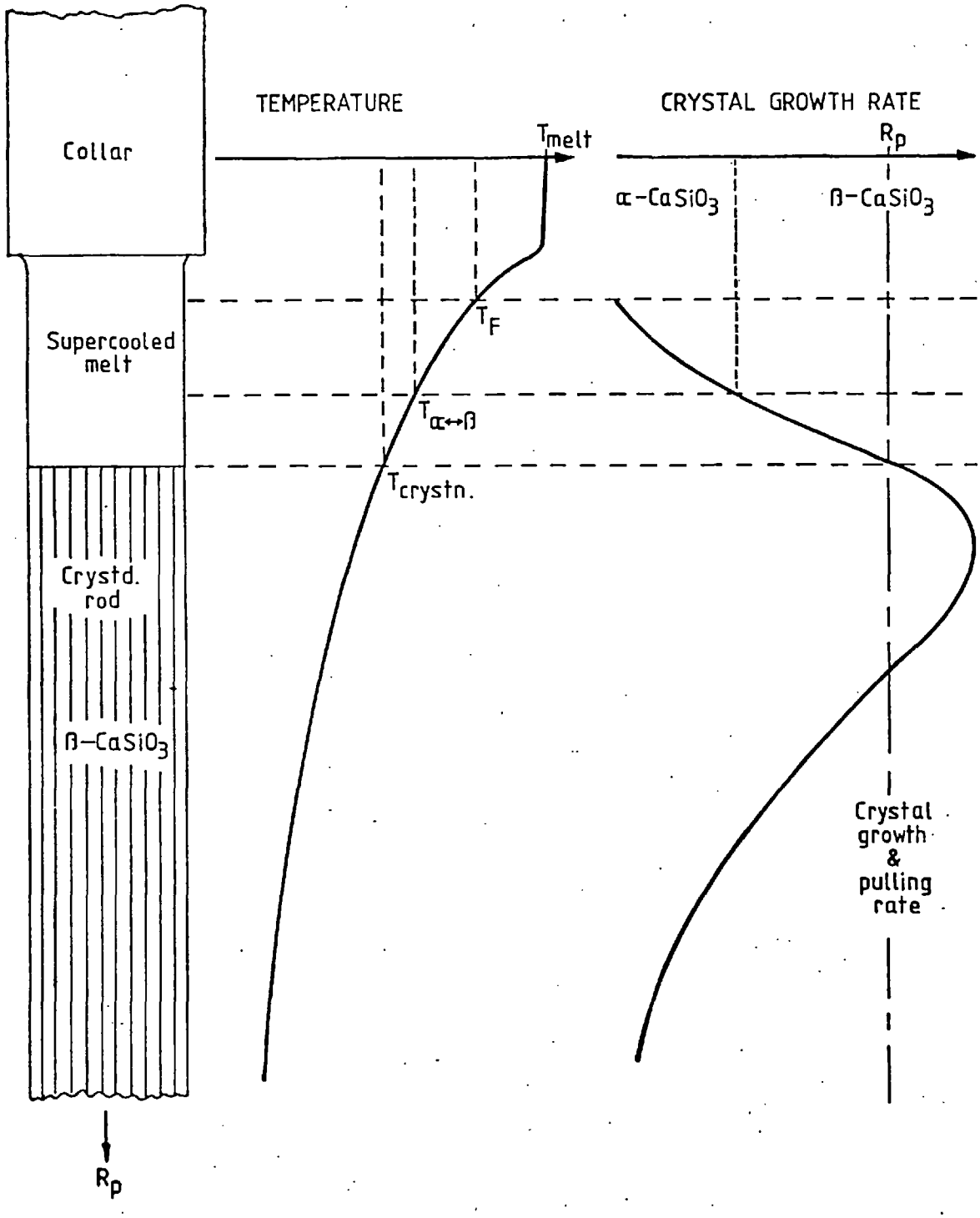


Fig. 1.8 Rod cooling rate and crystal growth rate profiles operating below the molten zone.

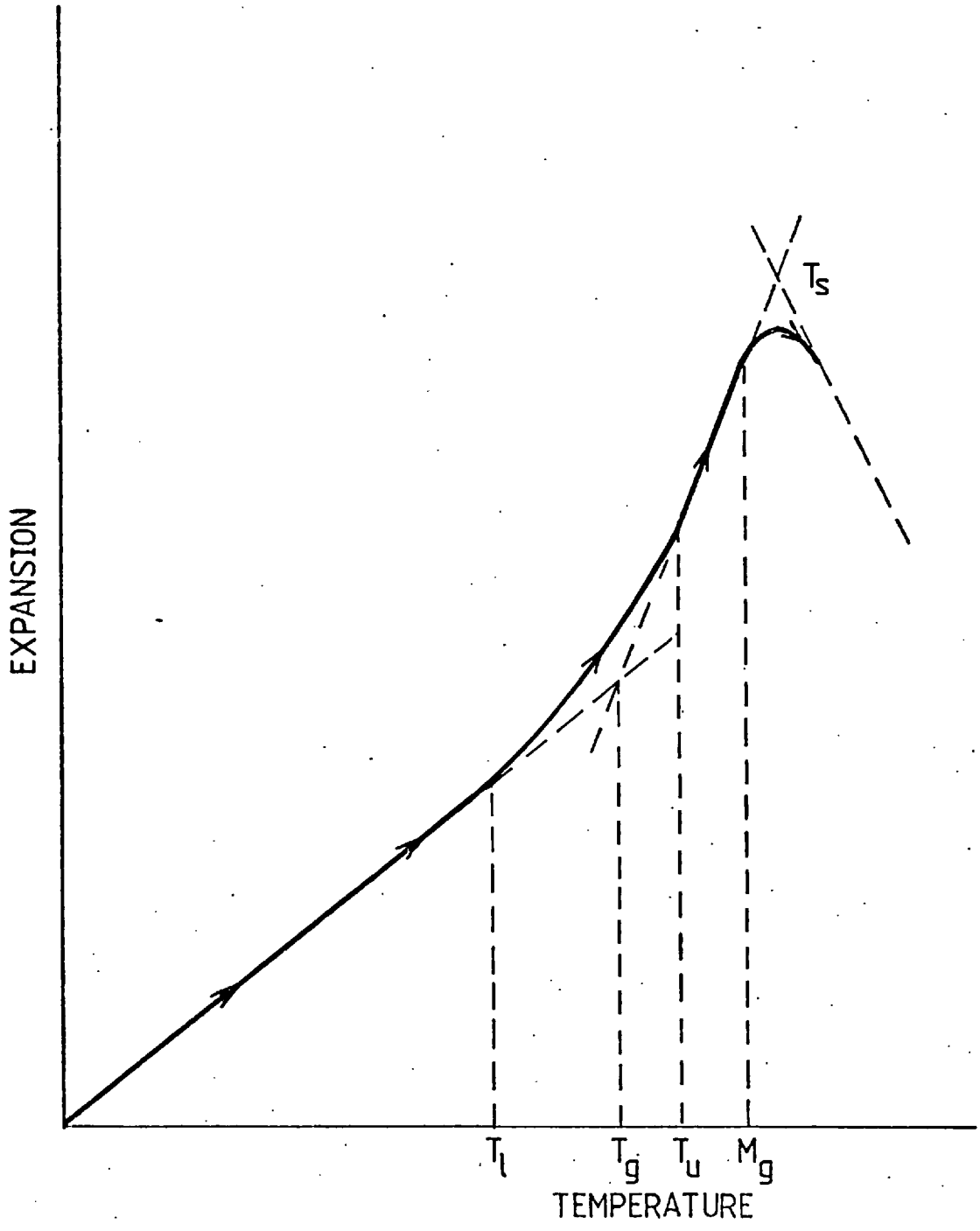


Fig. 1.9 Thermal expansion curve for a glass.
(ref. 118, page 13)

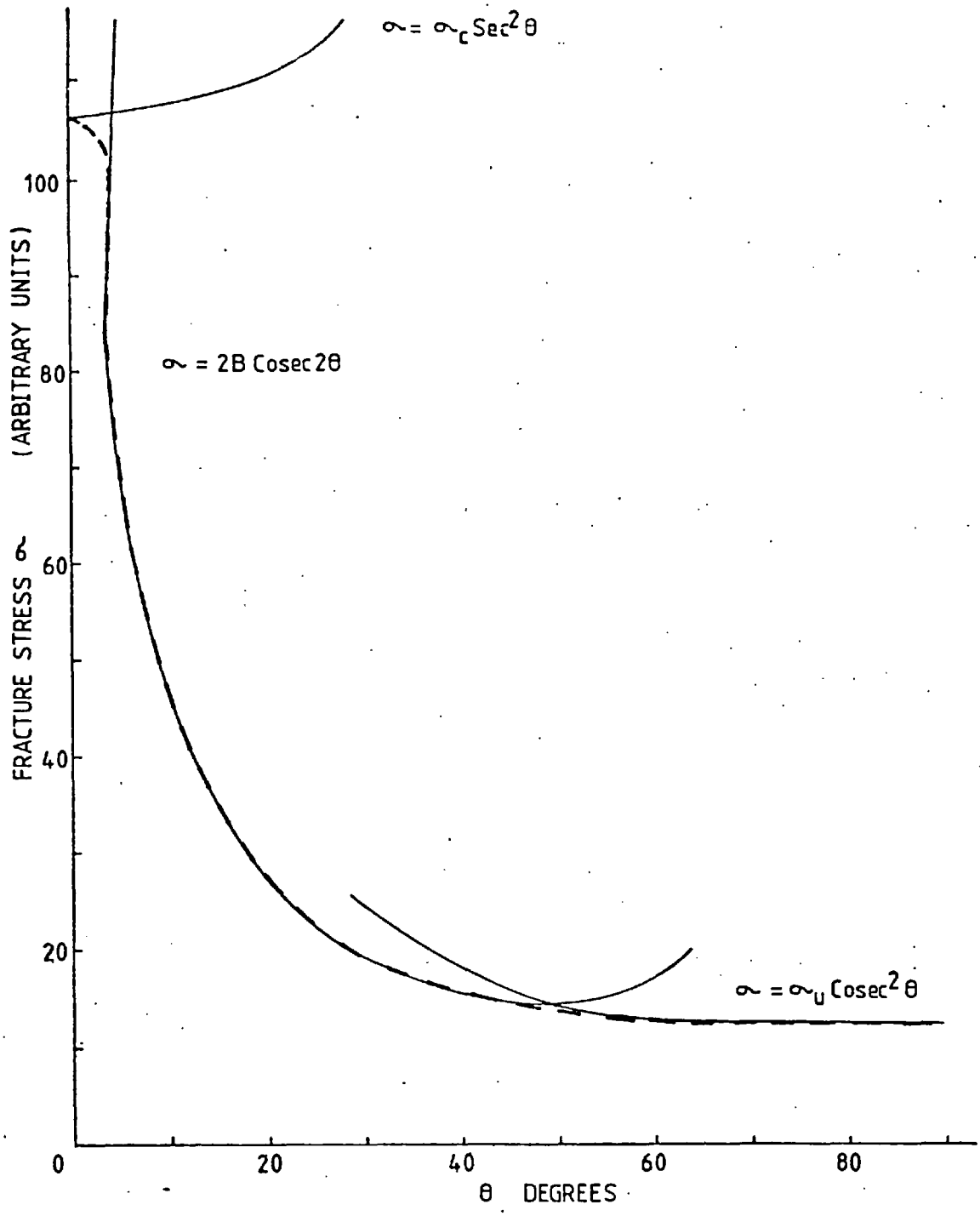


Fig. 1.10 Theoretical fracture stress verus fibre orientation.

CHAPTER 2

EXPERIMENTAL TECHNIQUES

2.1. PREPARATION OF GLASSES:

All the glass compositions used throughout this project were made up by fusing the dry constituents in a platinum crucible placed in an electric muffle furnace, powered by "crusilite" silicon carbide elements (manufactured by Morganite Electroheat Limited), in which the hearth temperature could reach 1450°C. After three hours at temperature the melts were water quenched, by standing the lower half of the crucible in a dish of water, and when cold knocked out of the crucible using a tack hammer. The glass was then crushed in a Torrington percussion mortar, replaced in the crucible and remelted. This process was repeated and the final melt was either quenched or cast depending on the use to be made of the particular glass batch. Previous workers have found that this method gives a homogeneous glass (116).

The starting materials for the glasses are shown in table 2.1. These powders were dried to keep the water solution, i.e. the formation of OH^- groups within the glass structure (117), to a minimum and to facilitate accurate weighings. The powders were then weighed out into a large glass bottle and were violently agitated before melting to ensure thorough mixing. Any excess

materials were stored in a desiccator over magnesium perchlorate. For every composition made at least one of the constituents was added in the form of a carbonate.

Swarts (118, page 280) has reviewed the main factors affecting the melting of glasses. The first stage in the conversion of a batch into a glass melt is the appearance of the lowest liquidus phase e.g. in compositions containing silica and sodium carbonate at about 800°C a liquid is produced corresponding to the sodium disilicate/silica eutectic. The carbon dioxide liberated by the reaction,

$$SiO_2 + Na_2CO_3 \rightleftharpoons Na_2SiO_3 + CO_2\uparrow$$

refines the batch since its evolution mixes the reactants so that concentration gradients are reduced and reactions accelerated. The decomposition of calcium carbonate above 825°C also liberates carbon dioxide. The active evolution of this gas continues as the reactants reach higher temperatures as continuous dissolution of silica into the melt decreases the carbon dioxide solubility. The limiting step in complete melting is the slow dissolution of the remaining silica residues into a viscous silica-rich melt (20, page 240), and at this final stage bubbles of carbon dioxide are nucleated at the glass/residue interface as the silica content is increased.

The particle sizes of the batch materials also control the rate of melting (118, page 284). Generally

the finer the particles and the more intimately they are mixed the faster the melting. At very fine particle sizes the voids between particles may be sealed by liquid at a very early stage of melting, these sealed holes fill with carbon dioxide, suppressing the reactions which produce this gas and therefore decreasing the melting rate.

Bubbles trapped within the molten glass are mainly formed by the accumulation of the gases evolved during the decomposition of the batch. They are removed by floatation in melts of sufficiently low viscosity and by dissolution in melts of suitable chemical composition.

The glass compositions investigated during the course of this project are shown in table 2.2.

2.2. PREPARATION OF SPECIMENS FOR THE PRELIMINARY ASSESSMENT OF A GLASS:

For each new glass composition a batch of powders was weighed out which would yield 100g of the fused glass. This batch was prepared as described above (section 2.1.), using a 70ml platinum crucible. After the final melt the crucible, now approximately half full of molten glass, was quickly removed from the furnace and the glass poured onto a clean brass slab. After about one minute the block of glass was sufficiently cool to be rigid enough to be slid onto a slice of firebrick and transferred to a wire-wound muffle annealing furnace. This furnace was set at 650°C, a temperature that was estimated to be higher

than the glass transition temperature of the glasses used for this project. At this temperature any internal stresses in the glass block, caused by rapid cooling, should have been removed as the glass structure approached an internal equilibrium (19, page 61). After thirty minutes the annealing furnace was turned off and allowed to cool slowly to room temperature, i.e. at less than $1°C\ min^{-1}$.

Once cold the glass block was sectioned using a slitting machine fitted with a diamond impregnated cutting wheel. Small pieces of the glass were cut to be approximately 10mm x 10mm x 10mm, each having four faces abraded by the action of the cutting wheel and the remaining two the smooth top and bottom surface of the cast block.

2.3. MEASUREMENT OF CRYSTAL GROWTH RATES:

2.3.1. HEAT-TREATMENT OF SPECIMENS:

The rate of surface nucleated crystal growth in the glasses of suitable composition was found from heating the prepared specimens of the glass for different times over a range of temperatures. The specimens were contained in firebrick trays, i.e. slices cut off a firebrick so as to be approximately 5cm deep and having a series of holes, approximately 15mm deep and 15mm in diameter, drilled into one surface. The bottom of these holes was filled with alumina powder so that if any of

the glass blocks softened and formed a bead, as occurred when the heat-treatment temperature exceeded 900°C, it could be easily removed from the tray with only a thin layer of the powder adhering to the glass.

In order to find the optimum range of crystallization temperatures for a particular glass composition a preliminary investigation was carried out using the temperature gradient in a horizontal tube furnace. A long firebrick tray was preheated in the furnace, removed, filled with glass blocks and quickly replaced in the furnace so as to span the temperature gradient. A chromel/alumel thermocouple placed in the centrol hot zone of the furnace indicated by the mV output measured using a potentiometer when the furnace temperature had returned to its equilibrium temperature, generally after about 2 minutes and the timing of the heat-treatment was then started. The thermocouple was slowly withdrawn from the furnace, over the heating tray, and its position could be seen by sighting through a filter over a slit in the end brick of the furnace. The thermocouple junction was rested over each glass specimen in turn and left until a steady temperature reading was obtained, i.e. the temperature of the specimen ±10°C. Heat-treatment times of between 66 hours and 30 minutes were used, depending on the estimated crystallization rate expected for a particular glass, and the temperature gradient in the furnace was from 700°C to 1100°C in 20cm. See figure 2.1..

Once the range of temperatures giving acceptably fast rates of crystallization had been determined, as described in section 2.3.2., and the crystalline phase or phases produced at those temperatures checked using X-ray powder diffraction, see section 2.4.1., then a series of heat-treatments in which specimens were held for a range of times at an accurately known temperature could commence.

A firebrick heating tray was preheated in a Kanthal wire wound muffle furnace. The furnace temperature could be set, and maintained within ±3°C of the set temperature, as it was fitted with a thyristor type (Eurotherm Ltd.) temperature controller. A chromel/alumel thermocouple was placed on the furnace hearth in contact with the side of the firebrick tray. (This type of thermocouple was used to measure the heat-treatment temperatures since it gives a larger mV output at a particular temperature than a platinum/platinum alloy thermocouple and therefore is more sensitive to small temperature variations.) Once the thermocouple registered the set temperature the furnace and its contents was left to "soak" at temperature for about thirty minutes. The furnace door was then opened, the glass specimens placed into the holes in the tray and the door shut as quickly as possible. Care was taken to locate the thermocouple sheath in the small slit cut in the bottom of the door as this allowed the door to be a close fit therefore eliminating any convection currents.

The thermocouple regained the set temperature after about two minutes, and therefore it was assumed that the glass blocks reached equilibrium in less than five. In order to standardize this technique the heat-treatments were timed from the moment that the thermocouple reached equilibrium. A specimen was removed from the furnace as quickly as possible after a certain measured time had elapsed, the timing for the specimens remaining in the furnace being restarted when the thermocouple again reached the set temperature. This process was repeated until all the specimens had been removed from the furnace.

Depending on the crystallization characteristics of a particular glass composition, the heat-treatment temperature was set at a value from 800°C up to 1180°C, and specimens were heated for time intervals varying from 10 minutes up to 72 hours.

2.3.2. PREPARATION AND MEASUREMENT OF THIN SECTIONS:

The heat-treated specimen blocks were sectioned normal to a flat surface (i.e. the bottom surface in the case of those specimens which had slumped into beads) using a diamond slitting wheel. One part was retained for powder X-ray analysis, whilst the other was made into a thin section, suitable for examination by transmitted light microscopy, by the standard technique described below.

The specimen was placed, sectioned face downwards, on a glass microscope slide and the whole heated on a

hot-plate to 140°C. The end of a bar of "Lakeside No. 70C" thermoplastic cement (Whithear Lapidary Co.) was touched onto the slide around the specimen. A small amount of the cement melted and flowed out in a uniform, colourless thin film both around and beneath the specimen. The slide was removed from the heat and allowed to cool to room temperature. The section, now firmly mounted on the slide, was ground parallel to the slide on silicon carbide abrasive papers (English Abrasives Ltd.) using a Metaserv rotary pregrinder (Metallurgical Services). The section was thinned down using a 220 grit coarse paper until it was about 1.5mm thick. It was then ground on a finer 600 grit size paper until a section approximately 1mm thick was obtained. The slide and specimen were now reheated and when the cement became fluid the specimen was inverted. When cold again the specimen was again ground on the 600 grit paper until a translucent, thin section about 30 to 50 microns thick was produced. If the top surface of this section was badly scratched after grinding a final polish was done by hand using gamma alumina powder (Gallenkamp Ltd.).

The thin sections were observed under transmitted light using a Reichert "Zetopan-Pol" binocular polarizing microscope. On this the analyser could be rotated through 90° with respect to the polarizer, enabling the sections to be observed under plane polarized or cross-polarized light. Since all the crystalline phases produced as a result of devitrifying the glass specimens displayed some

degree of birefringence (119), and unstressed glass is non-birefringent then the crystalline and glassy regions of the sections were easily distinguished by observation under cross-polarized light. All the glasses studied by this technique, i.e. RW1 to RW14 inclusive, nucleated and grew crystals only from the surface of the glass, except, of course, RW14F internally nucleated material. If the primary crystalline phase was β-$CaSiO_3$ this crystallization was in the form of transcrystallized, "spherulitic" fibres, but if α-$CaSiO_3$ was the primary phase then dendritic crystals grew from the surface of the glass towards the centre of the specimen (see section 1.3.1.). However, in both cases the crystal growth was virtually unidirectional and therefore the rate of crystal growth could be determined from the thickness of the layer of surface crystallization. The depth of surface crystallization was measured with a calibrated eye piece graticule in the optical microscope, the calibration being made by comparing the divisions in the graticule with the divisions on a stage micrometer.

In addition to measuring the depth of crystallization in the thin sections the microstructure of the crystalline region was examined. The morphology and alignment of the crystals was observed and the diameter of fibres, or dendrites, measured using the eye piece graticule. Photomicrographs were taken of typical regions of microstructure (see section 3.1.).

2.4. X-RAY DIFFRACTION ANALYSIS:

2.4.1. POWDER DIFFRACTION ANALYSIS:

A Guinier asymmetric focussing camera was used to record the front reflection region of the X-ray diffraction pattern produced from a powdered sample of a devitrified glass specimen. Azároff (120) gives a full description of the geometry of this camera, and the method of indexing the diffraction pattern produced.

A special feature of this camera is that up to four samples can be placed on the specimen grid, and therefore these diffraction spectra are recorded on the same film from the same exposure, thus enabling side-by-side comparisons to be made. This was especially useful when a series of heat-treatment specimens were being studied. In order to separate the individual spectra the specimen grid is divided into four rectangular "windows" by three horizontal metal bars. The powdered samples are held on the grid by sticking a piece of cellulose adhesive tape over one side of the grid and coating the adhesive areas exposed. The grid is then positioned in the camera so that the incident X-ray beam impinges upon the cellulose backing before reaching the samples and therefore the faint spectrum obtained from the tape will not distort the diffracted rays from the samples. An exposure in which one "window" is left uncoated with sample allows this faint spectrum to be identified so that it may be eliminated when spectra from samples are indexed.

The X-ray generator tube was operated at 30kV and 20mA, using a cobalt source and an iron filter to give a beam composed predominantly of the $K\alpha_{1,2}$ lines. At the diffraction angles in the front reflection region the α_1 and α_2 lines are unresolved, and therefore the intensity-weighted mean of the two wavelength components, that is $\frac{1}{3}(2K\alpha_1 + K\alpha_2)$, was used in the interpretation of the diffraction spectra. For cobalt this value is 1.7902Å.

The diffraction spectrum for a sample can be read directly as "d-spacings" using the calibrated rule supplied with Guinier camera. This rule is specific to the geometry of the particular camera and the wavelength of the X-ray beam used. It is constructed using the Bragg equation (120)

$$n\lambda = 2d \sin\theta$$

from which it is found that longer wavelength X-rays give a larger distance between the d-spacings recorded on the film. For this reason a cobalt source was preferred to a copper target tube, which produces shorter wavelength X-rays, in order to improve the resolution obtained in the recorded spectra. Since the calibrated rule is transparent it could be placed over the film on a light-box and the d-spacing, that is the spacing of the set of crystallographic planes acting as a diffraction grating, of each line measured. However, using this method the relative intensities of the lines comprising the spectrum can only be estimated.

In order to obtain accurate values for the relative

intensities of the lines in spectra a neutral wedge double photometer (or microdensitometer, Joyce Loebl Ltd.) was used. This gives a precise measurement of the optical density of a film in the form of a chart in which the ordinate gives the intensity and the abcissa the distance along the film. The intensity peak heights (I) were measured and the intensities relative to the maximum (I_o) calculated. The d-spacings were measured from the calibrated rule and diagrams of I/I_o versus dÅ drawn for representative spectra. (See section 3.1.).

The Powder Diffraction File (121) was used to identify the spectra obtained, but as an additional aid for the initial identification of devitrification products a series of "standard" films were taken using samples of those minerals likely to crystallize from the glasses studied. The mineral samples were obtained from the Department of Mineralogy, British Museum (N.H.).

2.4.2. PIN-HOLE TRANSMISSION ANALYSIS:

Pin-hole transmission X-ray analysis was used to find the crystallographic direction corresponding to the fibre axis. This technique is similar to the front-reflection Laue method (120), but a bundle of fibres is analysed in place of a single crystal. As it is necessary for the specimen to be a rod of well aligned fibres approximately 1mm diameter and 15mm long it was only possible to use this technique on the material produced using the rod-pulling technique (section 2.7.)

and on a sample of wollastonite obtained from the Department of Mineralogy, British Museum (N.H.).

A cobalt source X-ray tube was used, operating at 40kV and 20mA, and a 1mm diameter collimator. The rod of fibres was fixed co-axially onto the spindle of a 1 turn per minute synchronous motor by means of a small piece of "Plasticine". The motor assembly was then placed so that the specimen rotated about the vertical axis perpendicular to the X-ray beam and at a distance of 25mm from the collimator. This rotation of the fibres ensured that the resultant X-ray diffraction pattern was that of a bunch of fibres aligned along their axis but randomly orientated about the fibre axis. The film to record the diffraction pattern was positioned as nearly as possible at 50mm away from the specimen; however since envelope wrapped film was used (Kodak Ltd.) it was impossible to measure the exact specimen to film distance since several layers of paper covered the film.

Using the conditions listed above a satisfactory diffraction was obtained after a 1½ hour exposure. The developed films were analysed as described in section 3.1.8.1., the intensity-weighted mean of the cobalt K_{α_1} and K_{α_2} being used as the X-ray wavelength (see section 2.4.1.).

2.5. PREPARATION OF TILES:

2.5.1. PREPARATION OF GLASS SURFACE:

From observation of the specimens heat-treated

as described in section 2.3.1. it was found that crystals nucleated on both the glass/air and glass/alumina powder surfaces of the blocks. However, the nucleation sites are more numerous and evenly spaced on the surface in contact with alumina powder, a result of the powder particles abrading the glass surface and thus producing heterogeneous nucleation sites.

Petticrew (41) has found that a crystallized layer may be produced in the surface of a $CaO-ZnO-Al_2O_3-SiO_2$ glass by roughening the surface such that it has a frosted appearance and subjecting the glass to a heat-treatment at above its annealing and below its softening temperature. Therefore, some of the specimen blocks used to investigate the crystallization properties of the glasses were roughened by abrasion with 600 grit silicon carbide paper prior to heat-treatment. However, it was found that the optimum heat-treatment temperatures are greater than the softening temperatures of the glasses and therefore viscous flow tended to smooth out the surfaces before nucleation could occur. When sections of these specimens were examined it was found that the roughened surfaces appeared smooth after crystallization and that the effect of the abrasion was to promote the nucleation of α-$CaSiO_3$ at the expense of β-$CaSiO_3$.

Swift (38) investigated the effect of dust in the air on surface devitrification. When the furnace atmosphere was filtered he found that a freshly exposed surface showed only a few nucleation sites, whereas when

an exactly similar surface was exposed to a non-filtered furnace atmosphere dense, uniform surface devitrification occurred. From this he concluded that airbourn dust (referring to all kinds of foreign particles) is an important factor in surface devitrification.

From the observations on the small specimens and the above information it was decided that no special preparation was required to produce uniform, surface nucleated crystalline materials.

2.5.2. CASTING AND HEAT-TREATMENT OF TILES:

In order to produce material in a form from which rectangular prism test specimens having the fibre axis orientated either transverse or perpendicular (see section 2.8.1.) could be machined, rectangular tiles were prepared. A tile-press was made in which a mould of four steel bars was arranged on a flat steel plate, which was heated on its underside by a bunsen burner, and an upper steel plate could be swung round so as to be above the mould and then pressed down onto the top of the mould bars so as to be parallel to the heated plate. The mould bars were square section, of side 1cm, and approximately 10cm long. From these a square or rectangular mould could be constructed by abutting the end of one bar against the side of another, the end of which abuts against the side of the third bar, etc. The steel bars and the areas of the top and bottom plate comprising the interior of the mould were protected against

oxidation, caused when the mould is filled with hot, fluid glass, by a coating of "Aquadag", an aqueous suspension of colloidal graphite.

In addition to the casting mould a heat-treatment mould was prepared to support the glass tiles during crystallization above the glass softening temperature. A slice of firebrick was cut and a depression about 2cm deep and 0.5cm longer on each side than the casting mould made in one side. A layer of alumina powder was placed in the bottom and up the sides of the mould. A Kanthal wire-wound, electric muffle furnace was set at the required heat-treatment temperature and the firebrick mould was placed in this furnace to preheat.

A 100 gram glass batch, prepared as described in section 2.1., was given a final melt of 3 hours at 1450°C. When the glass was ready the firebrick mould was removed from the heat-treatment furnace and placed so as to be level with and adjacent to the heated steel plate. The glass was removed from the high temperature furnace and immediately poured from the platinum crucible into the heated casting mould until this was filled. This mould was sufficiently hot to reduce the cooling rate of the glass so that it remained fluid and flowed into the corners of the mould. The cold top plate was then pressed onto the mould and quenched the glass into a rigid block. The mould bars were knocked away from the sides of the glass and the tile was slid into place in the firebrick mould, which was quickly replaced in the

heat-treatment furnace.

A chromel-alumel thermocouple was placed along side the firebrick mould to enable the exact temperature to be measured, as described in section 2.3.1. The heat-treatment was timed from the moment when the thermocouple reached the set temperature. After the predetermined time had elapsed the furnace power was turned off and the furnace door opened to cool the tile at the rate of about 15°C per minute until the thermocouple registered a temperature 200°C below the crystallization temperature, thus effectively stopping any additional crystal growth in the tile. The furnace door was then shut and the tile allowed to cool to room temperature at about 2°C per minute, a slow cooling rate being used to minimise the damage produced by thermal shock and thermal expansion anisotropy in the unidirectionally orientated material, and to allow any residual glass to anneal.

After removal of the cold tile from the firebrick mould it was sectioned and examined in the same way as the small specimens (see sections 2.3.2. and 2.4.1.).

2.5.3. HEAT-TREATMENT SCHEDULES:

The investigative heat-treatments of small specimens of the different glass compositions revealed two compositions which gave well-aligned, fine, fibrous crystals of β-$CaSiO_3$ at sufficiently rapid crystal growth rates (see sections 3.1.5. and 3.1.6.).

On devitrification RW9 composition, see table 2.2, gives transcrystallized, "spherulitic" type fibres of

β-$CaSiO_3$ in a crystalline matrix of $CaAl_2Si_2O_8$ (i.e. a synthetic analogue of the mineral anorthite) together with a small amount of residual glass. Some α-$CaSiO_3$ crystals were also produced in this material even at temperatures 100°C below the nominal $\alpha \rightleftharpoons \beta$ transition temperature of approximately 1120°C. The optimum crystallization temperature to achieve a relatively rapid growth rate, the primary phase as β-$CaSiO_3$ and an undistorted final microstructure was found to be 1180°C, although this is higher than the nominal $\alpha \rightleftharpoons \beta$ transition temperature. This anomaly is discussed further in section 3.1.5. Therefore to produce a tile of crystallized RW9 the heat-treatment furnace temperature was set at 1180°C on the "Eurotherm" controller and, since the crystal growth rate at this temperature is about 1 micron per second, the time at temperature was 90 minutes for a 1cm deep tile. The furnace was cooled rapidly until the thermocouple registered 900°C and then left to cool slowly to room temperature, as discussed in the last section. A diagrammatic representation of this heat-treatment schedule is shown in figure 2.2.

On devitrification RW14 composition, see table 2.2, gives transcrystallized, "spherulitic" type fibres of β-$CaSiO_3$ in a matrix of residual glass, or with less than the detectable limit of X-ray analysis of a secondary crystalline phase (i.e. less than 5%). The optimum crystallization temperature was found to be 1100°C and, as the growth rate at this temperature is 5 microns per

second, the heat-treatment duration was 30 minutes for a 1cm deep tile. For the 2cm deep tiles of this material, used to produce short beam test specimens, the time at temperature was increased to 45 minutes. The furnace was cooled rapidly to about 850°C and then left to cool slowly, as above. A diagram of this heat-treatment schedule is shown in figure 2.3.

RW14F, see table 2.2, a modification of the RW14 material designed to produce internally nucleated, spherulitic β-$CaSiO_3$ on devitrification was also made in tile form. However this composition required a nucleation period at a temperature somewhat below the crystallization temperature in order to produce the nuclei (see section 1.3.2.). Therefore after this tile had been cast it was placed into the heat-treatment furnace which was at 660°C and left for 60 minutes. The furnace was then heated to 900°C at the rate of 5°C per minute and left for 90 minutes at this crystallization temperature. This time was rather longer than was required from a knowledge of the crystal growth rate and approximate nucleation density, but it was necessary to ensure that the interior of the 1cm deep tile had attained 900°C. After heat-treatment the furnace was cooled rapidly to about 700°C and then slowly to room temperature. Figure 2.4 is a diagram of this heat-treatment schedule.

2.6. PREPARATION OF CRUCIBLE GROWN MATERIAL:

In order to produce material in a form from which rectangular prism test specimens having the fibre axis

longitudinally orientated (see section 2.8.2.) could be machined, it was necessary to grow the crystals radially inwards from the surface of a cylinder of glass. However, in order to produce test specimens about 3cm long the glass cylinder would need to be about 8cm in diameter and it was found to be impossible to cast a cylinder of this size without it cracking due to thermal shock. Therefore it was decided to melt a batch of glass in a ceramic crucible and then to subject the crucible and glass to a controlled heat-treatment. In this way the crucible containing the melt would become an approximately cylindrical mould in which to crystallize the glass.

Since molten glass is generally corrosive to refractory ceramics the glass batch was given all three melts in a platinum crucible and the resultant glass was crushed into about 1mm size particles using the Torrington percussion mortar. The crushed glass was then placed into a Morgans Refractories "A"-shape size one fused alumina crucible, which had been slowly heated to about 1000°C in the wire-wound muffle furnace, and this crucible was immediately put into the silicon carbide element furnace at 1450°C. The wire-wound furnace was set to equilibriate at the required heat-treatment temperature. After an hour at 1450°C the alumina crucible was removed from the high temperature furnace, stood in still air until the exterior of the crucible cooled to yellow heat and then put into the heat-treatment furnace, along side a chromel-alumel thermocouple. The

heat-treatment was timed from the moment when this thermocouple reached the required temperature, and the furnace power was turned off at the end of the treatment. However, in this case the furnace door was not opened to give a rapid cooling rate since the crystallized material had grown directly onto, and was therefore joined to, the walls of the crucible and the thermal shock due to differential thermal contraction between the crucible and material may have caused cracks to develop in the material. The crucible was therefore cooled from the heat-treatment temperature at about 2°C per minute.

When completely cold the crucible was sectioned through a diameter. This section revealed that very little corrosion of the crucible by the glass had occurred, and therefore the glass was not badly contaminated by impurities. It also showed that any major cracks, due to thermal shock, occurred either across the thickness of the crucible wall or in the glassy areas remaining in some parts of the crucible. It was found that although nucleation was not uniformly distributed around the crucible/glass interface, enough nucleation developed to produce crystalline material from which test specimens could be machined. Some disordered crystalline regions were formed both at the bottom of the crucible and at the glass/air interface at the top, due to the nucleation and subsequent growth of fibrous crystals at right angles to the radial growth. Samples of the crucible grown material were examined as described above (sections 2.3.2.

and 2.4.1.).

This intra-crucible growth method was found to be suitable for glasses in which the rate of crystal growth is of the order of 1 micron per second, e.g. RW9. However when this technique was applied to glasses in which the rate of crystal growth is of the order of 5 microns per second or greater, e.g. RW14, it was found that a disordered mass of crystalline material resulted. This was apparently due to crystal nuclei forming in the interior of the melt and subsequent spherulitic crystal growth from these nucleation sites. The nuclei could have occurred heterogeneously on small particles of fused alumina which had become detatched from the crucible wall by the corrosive action of the molten glass and been carried into the interior of the melt by a convection current. It was also found that some of the crystallization had been distorted from a fibrous, spherulitic morphology to a lath type structure due to the relatively long heat-treatment times necessary to grow fibres of sufficient length, see section 1.4.2. Therefore a modified zone-heating technique was developed to produce longitudinally orientated bend test specimens from the glasses in which the crystal growth rate is greater than 10 microns per second.

2.6.1. HEAT-TREATMENT SCHEDULES:

The same heat-treatment temperature was used for the RW9 composition, see table 2.2, glass intra-crucible

crystallization as for the tile method (see section 2.5.3.). Therefore, after removal from the 1450°C furnace and cooling to yellow heat (i.e. about 1000°C), the alumina crucible containing the RW9 glass was placed into a furnace at 1180°C and left for 9 hours after the equilibrium temperature had been regained. This allowed fibres to grow up to 3cm in length, at the rate of 1 micron per second. The furnace was then cooled slowly to room temperature, as explained in the previous section. Figure 2.5 is a diagram of this heat-treatment schedule.

2.7. PREPARATION OF RODS:

Maries and Rogers (76) describe a novel technique for directional devitrification from a zone of molten glass in which a rod of glass of a suitable composition is passed through an electrically heated platinum coil. The coil is wound in contact with the glass rod in such a way that in addition to producing a zone of molten glass within the coil, i.e. the viscosity of the glass is reduced to about 10 N s m^{-2}, the hot coil also supports the molten zone. This is necessary as glasses display a continuous increase or decrease in viscosity as they are cooled or heated respectively and therefore an unsupported hot zone in a conventional type of zone-heating apparatus would flow and distort and produce a misorientated final product.

Maries' apparatus can form 1mm diameter rods containing a parallel array of β-$CaSiO_3$ crystalline fibres from 1mm

diameter vitreous rods. However, an attempt to scale up this type of apparatus to produce 1cm diameter directionally crystallized rods from RW14 glass rods failed for several reasons. It was found to be necessary to use ceramic tube heat shields in order that the coil could heat the larger mass of glass sufficiently for it to become fully molten, but this caused the glass above the coil to overheat and slump onto and over the coil as the rod passed downwards through it and the cooling gradient below the coil to change, therefore changing the crystallization characteristics. Since RW14 has a relatively high "melting" temperature, i.e. above 1400°C, the platinum furnace-wire coil had to be operated near its melting temperature, i.e. at about 1700°C (melting point of platinum is 1772°C), and any local overheating caused the coil to burn out. Also, at this temperature platinum becomes extremely flexible and the surface tension forces in the molten glass between adjacent turns of wire drew these wires together until electrical contact was made and the coil shorted out.

It was therefore decided to design and build an apparatus in which a rod of glass could be drawn out from the bottom of a heated platinum collar containing molten glass and the pulling rate adjusted so as to allow the rod to crystallize in the temperature gradient below the collar.

2.7.1. ROD PULLING APPARATUS:

The basis of this apparatus is a ten times

voltage step down transformer, i.e. a 10 volt, 30 amp input gives a 1 volt, 300 amp output, similar to the type of transformers used for welding applications. The terminals of this transformer were modified by bolting on 0.4cm thick, 3.5cm wide copper strips. These were fixed onto the front of the transformer and fabricated such that the terminals are now 3.5cm apart and are about 10cm in front of the transformer windings, see figure 2.6.

A platinum cylinder 1.5cm long and 0.5cm diameter was constructed from 0.3mm sheet, using a simple overlap seam and spot-welding by having a 0.5cm diameter copper rod as the lower anvil. The diameter of the collar thus produced was limited by the electrical power available from the transformer, i.e. a maximum of 400 amps, and this was the reason why the diameter of the rods produced by this apparatus was smaller than that which was ideally required. In fact in order to give a 1.5cm long hot zone the collar was slit by five equally spaced cuts on each side of the seam, leaving enough material at the seam and down the strip opposite it to maintain the integrity of the collar. The 1mm wide slits were made using a small silicon carbide wheel. This arrangement gives a collar with about one and a half times the electrical resistance of the simple cylinder and therefore will reach a higher temperature at the same input amperage. The mass of glass within the collar was large enough to eliminate any thermal gradients caused by the slits in the collar by convection, and at the operating temperatures used the glass was too viscous

and had too high a surface tension to flow out of the slits. This collar was connected to the centre of the long sides of two platinum strips 4cm long by 1.5cm wide, cut from the 0.3mm sheet, by four small platinum rectangles, one at each end of the continuous areas on the collar. These were spot-welded to both the collar and the large strips, and the centre line of each of the strips was also spot-welded to the side of the collar. The large strips were bent back on themselves and were clamped onto the transformer terminals, thus forming a circuit between the collar and the transformer, see figure 2.6.

It is important that all the glass in the collar is at the same temperature when heated, since if the glass at the top of the collar is at a lower temperature than that being withdrawn from the bottom the more viscous glass prevents the free flow of glass down the collar. The current should therefore be fed into the collar along the entire side of the collar, as in the design described above. The double thickness and large areas of the platinum strip connectors enabled them to carry large currents to the collar whilst not themselves overheating and thus dissipating power. Even so, it was found that the copper terminals were oxidizing at the clamps holding the platinum strips due to excess heating and this produced an oxide scale on the copper which increased the resistance at the copper/platinum contact and reduced the amount of power received by the collar. To combat this the ends of the terminals were water cooled.

To protect the transformer and other equipment from the radiative heat from the collar, and to ensure that the maximum amount of energy is used to heat the glass, an alumina tube (Morgan's Refractories Ltd.) heat shield is put around the collar. The 2.5cm O.D. tube used had two opposed slots machined up its walls such that the shield could be slid onto the platinum strips and extend about 1mm below the bottom of the collar. The top extended about 5mm above the collar, and a removable alumina lid fitted exactly into the top of the tube, as shown in figure 2.7. This size of heat shield allowed enough room around the collar to give free access whilst loading with glass, yet efficiently conserving heat.

The amount of power through the collar was controlled by a variac, a variable voltage transformer, on the input circuit of the large transformer. Since to maintain the collar full of glass at 1450°C required a transformer input of about 39 amps at 18 volts, i.e. a collar current of nearly 400 amps with a 2 volt voltage drop, it was necessary to "double-gang", i.e. connect in parallel, two 20 amp variacs. The input current was measured on a 0 to 50 amp moving iron ammeter. This circuit is shown in figure 2.8. It was found that the variac control was sufficiently sensitive to set the collar temperature to within 10°C.

The temperature of the glass melt was measured using a Leeds and Northrup optical pyrometer which sighted onto the bottom of the collar via a 45° mirror placed below

the collar. With the heat shield and lid in position this approximates to black-body conditions and therefore a precision of about ± 10°C may be obtained when sighting into the mass of the melt.

A motorised drive unit was constructed so that glass could be pulled out of the bottom of the collar at a constant, known rate. This was built by modifying a pair of screw driven vernier calipers (Mitutoyo Mfg. Co.), as shown in figure 2.7, (77). The short length of studding and knurled drive nut were removed from the calipers and replaced by a 20cm length of 6BA studding, and the thread guide was now clamped at the far end of the vernier scale. The shims in the mobile jaw were adjusted so as to allow very free movement along the scale. The calipers were bolted with the fixed jaw at the bottom onto a frame built onto the transformer body, ensuring that they were exactly vertical and positioned slightly to one side of the vertical centre-line of the platinum collar. A ceramic type electrical connection block was joined onto the side of the mobile jaw so that one of the clamping holes of the block was directly in line with the platinum collar. Therefore the seed crystal or wire used to pull out the glass from the collar could be fixed so to be exactly vertical and to give a straight pull.

A 60-toothed, 2.5cm diameter "Meccano" gear wheel had a 6BA nut fitted coaxially inside the boss, using "Araldite" adhesive, and this was threaded down the upper end of the studding until it rested on top of the thread

guide. A "Meccano" 3 to 12 volt D.C. motor and six-ratio gearbox was bolted onto the apparatus frame and adjusted until a 2mm pitch worm gear engaged with the gear wheel. This motor is reversible and its speed can be controlled by varying the input voltage. A circuit was designed, shown in figure 2.9, which allowed remote control of both the motor speed and spindle rotation direction. The capacitor included in this circuit enabled the motor to be started, when extra power is needed to overcome the initial inertia, even when the variable resistance is adjusted to give only 3 volts across the motor terminals (77). The double pole switch reversed the polarity of the motor terminals and therefore reversed the drive direction.

By using the gearbox, which is variable between 6:1 and 60:1, and adjusting the speed of the motor by use of the variable resistance, the movable jaw of the calipers could be driven downwards at a continuous range of rates between 5 and 450 microns per second. Of course, a corresponding range of speeds could be obtained for the upwards motion of the jaw. (When driving downwards the motor and gear assembly are acting as a check against the fall of the jaw, i.e. the wire clamp, due to gravity, but when driving upwards the motor is pulling up the jaw as the threaded boss of the gear wheel rotates around the fixed studding. Therefore, there is considerably more load on the motor as it is driving upwards compared to the downwards drive and so the rates of upwards movement are

all relatively slower.)

This drive mechanism was calibrated for the downwards mode by measuring the distance travelled by the jaw, using the calipers own vernier scale, over a fixed time interval, measured using a stop clock, for the full range of gear ratios and motor speeds. This allowed the pulling rate to be preset to the desired value, but since an additional load was introduced by the resistance of the glass to leave the collar, in each case the exact pulling rate had to be checked by timing the duration of the pulling run on the stopclock and recording the initial and final readings on the vernier scale to find the distance moved.

The vibration due to the motorised drive was minimised since the apparatus frame was attached to the large mass of the transformer. Also, since the pulling-wire clamp and the platinum collar were connected via the frame and transformer, then any transmitted vibration should have affected them equally.

A small, horizontal slit air blast outlet was fitted slightly below the level of the bottom of the platinum collar, i.e. level with the bottom of the ceramic tube heat shield, and between the collar and the transformer coils so as to avoid blowing hot air onto the transformer which anyway tended to become warm (about 50°C) during operation at full power. The air line was equipped with a diaphragm reducing valve and a 9 to 2000cm per minute rotameter to control and monitor the flow rate. The air blast increases the thermal gradient below the collar and

allows rods to be pulled at fast rates without the glass necking off, i.e. the rapid decrease in temperature quenches the rod into a rigid glass that does not flow under the pulling stress. However, this change in the thermal gradient also affects the devitrification of the rods. The full theory of the crystallization of the rods produced by this pulling technique is discussed in section 1.4.3.

2.7.2. PRODUCTION OF RODS:

After ensuring that the water cooling system was operating the transformer circuit was turned on with the variac setting at zero volts. The voltage was then increased in stages so as to maintain the input current, measured on the ammeter, at about 35 amps, since as the platinum collar heats its resistance increases and therefore, at constant voltage, the current would decrease and the collar cease to increase in temperature. Once the collar reached about 1400°C the lid of the heat shield was removed and chips of glass, prepared as described in section 2.1., about 2 to 3mm in diameter were poured slowly into the top of the collar from a nickel hopper. The glass chips immediately softened and flowed so as to fill the collar with a bath of molten glass, but since the removal of the heat shield lid and the addition of cold glass caused the collar temperature to drop to about 1350°C some of the glass at the bottom of the collar crystallized. However, once the lid was replaced and the power increased to approximately 17 volts, 38 amps transformer input (about

1.7 volts, 380 amps through collar) the melt temperature inside the collar reached 1450°C and any crystals melted to give clear, bubble free molten glass. Surface tension forces held the glass inside the collar.

A length of Pt/13% Rh thermocouple wire, which is less susceptible to embrittlement at high temperatures than pure platinum, was clamped into the connector block so as to be directly below the collar and either a small spiral, less than 4mm diameter, made in its upper end or twisted around a 2mm square section rectangular block "seed crystal" so as to hold it vertically. These seed crystals were prepared by sectioning a piece of a RW14 crystallized tile using a "Capco" diamond slitting wheel (see section 2.8.2.) so that square section, rectangular prisms were produced in which the β-$CaSiO_3$ fibre axis ran along the long axis. Therefore, when a block was positioned beneath the collar the fibre axis was vertical and in line with the long axis of the collar.

In order to measure the temperature gradient experienced during rod pulling at different rates the pulling wire was replaced by a Pt verses Pt/13% Rh thermocouple, arranged with the junction at the top and the two wires either vertical, or wrapped around a seed crystal (taking care not to short out the wires). The thermocouple was connected to a pen chart recorder via compensating cables.

Any of the above arrangements acts both as a heterogeneous nucleus for the initiation of crystallization

and as a means of securing the bottom of the rod so that it may be pulled vertically out of the collar. The motorised drive was turned on at about 200 microns per second upwards and stopped when the top of the wire or "seed crystal" was about 5mm below the bottom of the heat shield. The drive controls were set to give the required downwards pulling rate and then again turned on upwards. The bottom of the melt was observed through the optical pyrometer and as soon as the wire or block broke through the surface tension on the melt the drive was switched from the upwards to the downwards mode. The temperature was checked and any necessary adjustment made to the "variac". The position of the scale vernier as it passed a convenient division was recorded and the timing started.

Throughout the pulling run the melt temperature was checked, and the power through the collar was slightly reduced as the collar emptied of glass and therefore its thermal capacity decreased. The crystallization front in the rod was observed, via a suitable filter, to ensure that the rod was being pulled out as a glass, supercooling and then crystallizing about 3 to 5mm below the collar. This is the correct mode of crystallization to ensure alignment down the long axis of the rod. When the collar had been emptied the downwards drive remained on until the top of the rod had crystallized and was about 10mm below the bottom of the collar, thereby allowing the rod to cool relatively slowly as it passed down the temperature gradient. The drive was turned off, the timing stopped

and the exact pulling rate found after reading the final position of the vernier, and the collar allowed to cool (the water cooling remaining on until the collar reached room temperature). When the rod had cooled down the pulling wire was removed from the connector block and the wire cut off next to the bottom of the rod, or the "seed crystal" removed from the wire twist, in order to free the rod.

If the air cooling blast was required to increase the cooling rate of a particular rod this was turned on only once pulling had started, as it caused the bottom of the melt to cool and crystallize inside the collar, even when the bulk melt temperature was over 50°C above the liquidus.

Using the above technique it was attempted to grow rods of aligned, β-$CaSiO_3$ fibres using RW14 composition glass, see table 2.2. However after using various melt temperatures, the full range of pulling rates possible with, and without, air blast cooling, and both wire and seed crystal nucleation this was not achieved. The collar was removed from the apparatus, cleaned by immersion in 40% hydrofluoric acid for 24 hours, washed and dried using acetone and replaced. This investigative process was repeated using both RW15 and RW16, other soda-type glass compositions, see table 2.2, but with no greater success. This problem is discussed in section 3.1.8.

Therefore it was decided to try the lime-zinc

oxide-silica glass used by Maries and Rogers (76), i.e. composition RW17 in table 2.2. This was found to be far more suitable for rod pulling both in its crystallization and in the manner in which its viscosity changes with temperature. Using this glass it is possible to produce very well aligned, small diameter β-$CaSiO_3$ fibres in a matrix of $Ca_2ZnSi_2O_7$ (a synthetic analogue of the mineral hardystonite) and some residual glass, by pulling rods at rates above 25 microns per second up to about 60 microns per second, above which rate the rod is cooled too quickly for a stable crystal growth front to form and therefore a glass rod is formed. Up to 60 microns per second the crystallization rate equals the pulling rate, as is explained in section 1.4.3. To grow these β-$CaSiO_3$ rods it was found to be unnecessary to use the air blast, but the β-$CaSiO_3$ block "seed crystals" were required. The optimum melt conditions were found to be to start pulling with the melt at 1430°C, but to allow this to drop to 1410°C as the glass is removed from the collar. It is very important to ensure that the seed crystal only just breaks the surface of the melt before it is pulled out or else the bottom of the melt becomes chilled and premature crystallization takes place.

Cooling rate determinations during rod pulling RW17 at different rates were done using both a thermocouple as the nucleation/pulling wire and a "seed crystal" plus thermocouple arrangement.

Representative examples of the rods produced were

examined by X-ray powder diffraction analysis, see section 2.4.1., and optically by transmitted light thin sections, see section 2.3.2. The results are given in section 3.1.8.

2.8. PREPARATION OF MECHANICAL TEST SPECIMENS:

2.8.1. FROM TILES:

Strips about 3cm wide were cut from the middle section of the selected tiles using a diamond impregnated, tube-slitting wheel. The ends of each strip were cut off at the point at which the surface crystallization became distorted due to growth from the sides of the tile. (The orientation of the β-$CaSiO_3$ fibre axis can be easily seen with the naked eye on sections through both RW9 and RW14 composition tiles.)

A mild steel block, approximately 6cm by 10cm by 5cm deep, having its two large faces ground parallel, was heated to 150°C on a hot plate and a sheet of plate glass, 6cm by 10cm, was fixed to one of the ground faces using "Lakeside" thermoplastic cement (see section 2.3.2.). The slices of tile were stuck by one of the sectioned faces on top of the plate glass, using the cement, so as to expose the join at the middle of the tile where the two crystal growth fronts from the top and bottom surfaces met. The steel block, etcetera, was allowed to cool and then lined up on the magnetic chuck of a "Universal Rock Cutting and Grinding Machine" (model GF3, Impregnated Diamond Products, Ltd.) (122) so that the traverse axis

of the machine (the cutting orientation) was parallel to the growth front join of the tile sections, i.e. perpendicular to the fibre axis. Slices were cut along the growth front join using a diamond slitting disc type DIAIR (Triefus Ltd.) having 180 grit (about 80 micron) diamond chip embedded in a bronze bond. This wheel gives a cut approximately 1mm wide.

The strips of tile were now about 3cms wide and 0.5cm deep, down the fibre axis direction. For the 2cm span three-point bend tests (see section 2.9.1.) the specimen size used was the length greater than 30mm, the breadth 5.0mm and the depth 2.5mm (73). The tolerance on the breadth and depth was plus, or minus, 0.25mm. Therefore the sections of the tile could be machined, being remounted on the cutting block in the required orientations, to produce two types of specimen, i.e. a transverse type in which the β-$CaSiO_3$ fibre axis runs across the width of the specimen, or a perpendicular type in which the fibre axis runs down the depth of the specimen, see figure 2.10. The sides of the specimens were left as cut by the slitting wheel, but the tension and compression faces, i.e. the bottom and top faces respectively, were ground to size using first a coarse 200 grit (about 65 microns diameter chips) and then a fine 600 grit (15 to 30 microns chips) diamond impregnated bronze peripheral grinding wheels type DIAI. This gave a standard abrasion treatment to the specimens which, in theory, should have limited the flaw size to 30 microns assuming that the specimens were

otherwise undamaged.

The finished specimens were removed from the plate glass cutting block and any excess cement removed by immersing them for a few hours in methylated spirits. When clean they were carefully dried, wrapped in cotton wool and placed in a desiccator over magnesium perchlorate until they were required for testing. Storage in a dry atmosphere ensured that the corrosive effect of water vapour, particularly on any residual glass areas on the surface of the specimens, was minimised. Extreme care was taken when handling the prepared specimens not to damage the ground surfaces, and, indeed, not to fracture these specimens which were comparatively weak.

To enable the bend test apparatus to be calibrated using a material the mechanical properties of which are known and are reproducible, specimens were prepared in an identical manner from the wall of a large diameter "Purox" recrystallized alumina tube (Morganite Refractories Ltd.).

All the short-beam test (4mm span) specimens were of the longitudinal type, i.e. where the fibre axis runs along the length of the specimen beam, see figure 2.10, and had the dimensions of length 5.0mm or greater, breadth 2.5mm, $\pm$0.2 mm, and depth 1.0mm, $\pm$ 0.2 mm, (13). Due to the small size of these specimens they could be cut using the "Capco" annular slitting wheel, a very thin blade containing a fine diamond grit which gives an accurate cut only 0.3mm wide. The specimens were mounted on the glass cutting block using "Durofix" adhesive (Rawlplug Ltd.)

which is easily dissolved using acetone.

As the "Capco" wheel gives a good, almost polished surface, and due to the fragility of these small specimens, only the tension, i.e. the bottom, surface of the beams was given the standard abrasion treatment described above. When completed the specimens were cleaned, dried, wrapped and stored in the same way as the 2cm span specimens.

2.8.2. FROM INTRA-CRUCIBLE MATERIAL:

Specimens for the 2cm span three-point bend test were prepared so that the β-$CaSiO_3$ fibre axis runs along the length of the specimen, i.e. longitudinal specimens, see figure 2.10. The finished dimensions were again length greater than 30mm, breadth 5.0mm, $\pm$ 0.25mm, and depth 2.5mm, $\pm$ 0.25mm.

On the section which had already been cut across the crucible and its contents to examine the crystallization obtained after heat-treatment, the orientation of the fibres could be seen. The crucible and any redundant interior material was cut away using the tube cutting wheel. The selected fibrous material was mounted on the cutting block in the necessary orientation and cut and ground to shape, as described in section 2.8.1. The top and bottom faces of the specimens were given the standard abrasion treatment, and when finished these specimens were cleaned, dried and stored in the same way as those fabricated from the tiles. These specimens were carefully handled, of course, but it was noted that these longitudinal specimens were far less fragile than either the transverse

or perpendicular ones.

2.8.3. FROM RODS:

As the diameter of the rods grown was only 5mm and the length 15mm or less, the three-point bend test specimen dimensions were scaled down from a 20mm to a 7mm span in the ratio of 20:7. Therefore the specimen dimensions were 10mm or greater in length, breadth 1.7mm, ± 0.2 mm, and depth 0.9mm, ± 0.2 mm. It was also only possible to prepare the longitudinal type of specimen, see figure 2.10. Short beam test specimens, as described in section 2.8.1. were also prepared from the rods.

Both of these types of specimen were small enough to be prepared using the "Capco" slitting wheel and therefore only grinding down the tension surface to the standard abrasion, for the reasons explained in section 2.8.1. The finished specimens were cleaned, wrapped and stored in a desiccator as described above, and it was again observed that longitudinal orientation specimens are less fragile than the other types.

In addition to the specimens in which the β-$CaSiO_3$ fibre axis ran along the length, specimens for both types of test in which α-$CaSiO_3$ dendrites had the primary arms parallel to the long axis were prepared.

In order to calibrate the 7mm span bend tests "Purox" recrystallized alumina specimens were prepared in an identical manner to the rod specimens.

2.9. MECHANICAL TESTING:

2.9.1. 20mm SPAN THREE-POINT BEND TESTS:

These tests were performed using a steel rig mounted on an "Instron" testing machine. The rig was fixed by a coupling system containing pin-joints, which should have eliminated any non-linearity in the apparatus, and was connected to the Instron cross-head and load cell in the reversing mode. This means that a tension type of load cell is used and the apparatus constructed so that the block containing the single, upper roller moves downwards under the Instron cross-head and applies a load to the specimen which is recorded by the load cell as it weighs the block containing the two lower rollers. A diagram of this apparatus is shown in figure 2.11.

The rollers used to test the ceramic materials were made of tungsten carbide, a material that has a high Young's modulus and does not yield under the loads used for these bend tests. These rollers were completely free to roll along the specimen surface and since the ceramic specimens had a high surface hardness and hard rollers were used then low rolling friction coefficients should have been obtained, (112). Friction during testing produces longitudinal surface strains in the specimen surface and the net effect is to reduce the total surface stress and therefore increase the apparent strength of the test material. The rollers were fitted into circular section slots in steel blocks and were 5mm in diameter.

They were carefully aligned so as to be exactly parallel and the upper roller positioned exactly over the mid-point between the lower rollers. The ram containing the upper roller was self-adjusting to ensure a uniform contact of this roller across the specimen width.

The Instron was set up, zeroed and balanced to allow for the weight of the lower roller block suspended from the load cell, and calibrated using standard weights. A 100kg load cell was used, giving a smallest full scale deflection of 2kg on the load versus distance travelled by cross-head pen chart out-put. The cross-head speed used was 0.1mm per minute, a slow speed to ensure that the correct mode of fracture took place (see section 1.7.3.), and the chart speed was selected at 50mm per minute to enable the slope and shape of the load versus deflection curve to be measured accurately.

Before testing each specimen was marked with a coloured stripe on both extreme ends of the compression face. After fracture this enabled the fracture faces to be identified and correctly interpreted and the colour indicated the type of material tested. The specimens were also numbered so that they could be matched with the correct load versus deflection curve. Care was taken to line up each specimen exactly at right angles to the rollers.

After testing the breadth and depth of the specimens were measured with a micrometer screw gauge accurate to 0.01mm each side of the fracture surface, and each specimen

was wrapped in cotton wool and stored in a desiccator in order to keep the fracture surfaces as fresh as possible until they could be examined under the scanning electron microscope.

2.9.2. 7mm SPAN THREE-POINT BEND TESTS:

These tests were performed in a similar manner to the 20mm span tests, but a smaller, table-top type of Instron was used and the small three-point test rig was not fitted with rollers. Instead the arrangement shown in figure 2.12 was used. In this hardened steel knife edges transmit the load to the specimen, the top knife edge being located above the mid-point between the two lower edges by means of two locating pins. This rig was connected to the Instron by a reversing apparatus, as described in section 2.9.1., the load being transferred from the upper ram to the top knife edge via a steel ball bearing which ensured that no twisting or wedging moments were transmitted to this knife edge. In order to minimise the frictional forces on the specimen both the top and bottom knife edges were covered with "Teflon", polytetrafluoroethylene, tape, a material with an extremely low frictional coefficient. This tape also served to retain the pieces of the specimens after fracture, as small, brittle specimens tend to "fly off" the lower knife edges at the moment of fracture and are easily lost.

The 7mm span specimens were marked, measured and stored after testing in the same way as those tested in

the 20mm span apparatus, as described in the previous section.

2.9.3. SHORT BEAM TESTS:

The three-point bend test apparatus used for the 7mm span tests was set up exactly as described in the previous section except that the lower knife edges were replaced by a set with a span of only 4mm, see figure 2.12. The short beam tests were conducted in exactly the same way as the bend tests, but in addition to the dimensions of the fractured specimen the type and position of the fracture was also recorded, in accordance with the recommendations in ASTM D2344-72. "Teflon" tape was again used to cover the knife edges and the tested specimens were wrapped and stored, as described in section 2.9.1., prior to examination in the scanning electron microscope. The tests were carried out at an Instron cross-head speed of 0.1mm per minute (13).

2.10. SCANNING ELECTRON MICROSCOPY:

The fracture surfaces of selected specimens, i.e. an example of the strongest and weakest specimen of each material for each type of mechanical test, were mounted on aluminium stubs using "Durofix" adhesive and stored in a vacuum desiccator for one day. The stubs were then coated with a 100Å layer of vacuum deposited gold. This produced a conducting layer over the non-conducting ceramic specimens which provided electrical contact with the aluminium stub without obscuring the details of the fracture

surface.

The prepared stubs were examined using a Cambridge Stereoscan 600 scanning electron microscope using the reflected electron mode. Photographs of representative regions and any special features were taken at suitable magnifications up to a maximum of two thousand times.

2.10.1. ELECTRON PROBE MICROANALYSIS:

This technique could only be applied to the RW9 composition specimens as the other compositions gave too fine a microstructure on devitrification, i.e. the diameter of the fibres and inter-fibre distance are smaller than the limit of resolution of the instrument (about 10 microns). Another problem with the crystallized glasses containing Na_2O in the residual glass is the high mobility of the Na^+ ion which results in the X-ray intensity for this species changing as a function of time when an electron beam remains stationary on a glass specimen, with an accompanying change in the intensities observed for other atomic species in the glass (123).

The RW9 composition specimens included both tile and crucible grown material. Small chips of material were embedded in cold setting plastic so that the fibre axis ran in the plane of the exposed surface. The specimens were ground on coarse (180 grade) and fine (600 grade) silicon carbide wheels and then polished on an automatic polisher using successively 6, 3 and 1 micron diamond pastes. Optical micrographs were taken of these specimens,

see figure 3.73, prior to them being coated with an electrically conducting carbon film. The specimens were analysed on the microprobe and the results were obtained as a pen chart record of a line scan taken as the beam traversed at right angles to the fibre axis of the specimen.

2.11. DILATOMETRY:

An automatic recording dilatometer was used to measure the thermal expansion characteristics of the materials studied. Specimens were prepared in the form of rectangular prisms approximately 5mm by 5mm in section and up to 15mm in length, by cutting using the accurate "Capco" diamond slitting wheel (see section 2.8.1.). Examples from all the synthetic calcium metasilicate materials which had been mechanically tested were prepared, together with specimens of the original, uncrystallized glasses and, in the case of the RW14 material, a glass of approximately the same composition as the inter-fibre residual glass (see table 2.2). Specimens were also made up from a piece of unidirectionally aligned, fibrous wollastonite, sample number BM 1913, 253 obtained from the British Museum (Natural History). In all cases of specimens fabricated from the materials containing parallel fibres, or parallel primary dendritic arms, examples in which the fibre axis is aligned both along and exactly at right angles to the specimen long axis were prepared.

One end of each specimen was carefully ground into an approximate hemisphere on a fine silicon carbide wheel,

and the length of the finished specimen was measured using a micrometer screw gauge. The specimen was placed in the dilatometer so that one end of a horizontal silica-glass thrust-rod bore on to the square end whilst the curved end rested against the end of an outer silica-glass tube. This system provides a self-aligning, point contact between the specimen and the measuring mechanism, thus avoiding the necessity of accurate alignment. A Pt./Pt.Rh. thermo-couple junction was positioned over the specimen and the specimen, support tube, thrust-rod and thermocouple assembly was placed inside a draught-free Kanthal wound furnace.

The dilatometer furnace was fitted with a cam-type temperature controller which allowed the expansion to be measured over complete heating and cooling cycles at the linear rate of 2°C per minute, when the maximum temperature was set at 650°C. The thrust-rod emerged from the furnace and was connected to a linear variable differential transducer. This transducer was supplied with a constant voltage of exactly 10 volt so that a 22mV output from the transducer was equivalent to 2.54×10^{-5} m movement of the thrust rod. This output from the transducer was recorded on a two pen chart recorder, together with the output from the specimen thermocouple. An automatically adjusting back-off unit was connected to the transducer output to allow a sensitive scale to be used on the recorder, yet not be distorted due to any drift in the "constant" voltage. This circuit is shown in figure 2.13.

Control, "blank-run" experiments were made periodically,

in which the end of the thrust-rod bore directly onto the end of the outer support tube, and these enable the dilatometer results to be corrected for the changes in dimension of the silica-glass system with temperature. It is also necessary to add the small additional expansion due to the expansion of the silica-glass outer tube, which extends the length of the specimen beyond the thrust-rod, to the result obtained for that particular specimen. When all these corrections are applied it is possible to find the expansion of a 10mm long specimen to within 1.2×10^{-6} m.

2.12. MODAL ANALYSIS BY POINT COUNTING:

Modal analysis by point counting is widely used in quantitative petrographic studies, but it is usually applied to rock structures which do not display any marked preferred orientation. However, Chayes (124) has proved that this technique can be applied to banded rocks, i.e. rock composed of alternating bands of different modal composition, and provided that certain conditions are fulfilled, then the areal proportions found on measurement of a section will lead to consistent estimates of the volumetric proportions.

Chayes states that the measurement area should be at a high angle, and preferably normal, to the plane of the banding, in order to include as many bands as possible in the area. He then demonstrated how the inclination of the bands to the modal analysis grid affected the relative proportions of the bands included inside the grid, and

found that if one corner of the measurement grid area coincides with a band boundary and the bands are inclined at any angle between 30° and 50° to the shorter side of grid then the banding introduces no bias into the sample. The banding does however make a small contribution to the random variation (or analytical error) of the method, but even this may be greatly reduced by the size of the measurement area being large compared to the band width.

Therefore, when it was desired to find the volume per cent of fibres, and any other phases, present in the materials on which mechanical tests had been performed, thin sections were prepared (see section 2.3.2.) in which the fibre axis orientation was approximately 45° to the side of the glass slide. (In these analyses it was assumed that the fibre and inter-fibre regions of the materials constituted a banded structure.) The sections were examined on the polarizing microscope to which an automatic stage, Swift point counter had been attached. The fibre orientation was measured using the rotating stage. The point counter stage moved the slide in 0.05mm steps along a traverse axis parallel to the long side of the glass slide every time a counter button was depressed. A set of counters allowed a different one to be used for each phase whilst one kept the overall total of counts as a check. An eyepiece containing cross-hairs was used and the grid points were taken as the intersection of these. As the slide was moved under the cross-hairs the button corresponding to a particular phase was pressed if that

phase came to rest under the intersection, thus moving on the slide to the next grid position. At the end of a traverse the stage was returned to the other edge of the section and the slide moved 0.33mm parallel to the short side of the glass slide before beginning another traverse. In this way a grid of points was built up and the average measurement area was about 1cm by 2cm. Since the average fibre diameter in the calcium metasilicate materials is about 10 microns, and the inter-fibre distance even less, (see section 3.1.) then Chayes' conditions are fulfilled.

The counts for the individual phases were calculated and placed over the total number of counts to find the volume percentages for each phase.

The reliabilities of the percentages calculated were found using the chart devised by Van de Plas and Tobi (125). This chart is based on the standard deviation, and the operator error, due to mis-identification of phases, etc., usually much smaller than the counting error, introduced during estimation of areal fractions, is not considered. The standard deviation is given by:

$$\sigma = \sqrt{\frac{p(100 - P)}{n}}$$

where:

σ = the standard deviation

p = the true percentage composition

P = the calculated percentage composition

n = the total number of points counted.

The 95% confidence limits are:

$$p \pm 2\sigma$$

and this and the corresponding relative 2σ values are plotted on a chart of n versus P. Thus knowning n and P for any phase in any section the reliability of the modal analysis can be found.

Table 2.1 : Materials used in the preparation of glasses

Material	Manufacturer	Grade	Drying Temperature °C	Mean Particle Size x 10^6m
Al_2O_3	Hopkin and Williams Ltd.	Analar	1000	4
$CaCO_3$	British Drug Houses	Analar	150	5
CaF_2	British Drug Houses	Extra Pure 99.9% Pure	150	5
Na_2CO_3	Hopkin and Williams Ltd.	Analar	150	120
SiO_2	Thermal Syndicate Ltd.	Crushed Brazilian Quartz Analysis: Na 4 ppm. Mg 0.026 ppm. Fe 0.074 ppm. Ca 0.07 ppm. Cu 0.4 ppm. B 0.05 ppm. Sn 0.023 ppm. Al 5 ppm.	1000	225
ZnO	Hopkin and Williams Ltd.	Analar	600	300

Table 2.2 : Glass compositions

Glass	Weight % Composition						Mol. % Composition					
	SiO_2	CaO	Al_2O_3	ZnO	Na_2O	CaF_2	SiO_2	CaO	Al_2O_3	ZnO	Na_2O	CaF_2
RW 1	60.0	30.0	10.0				61.2	32.8	6.0			
RW 2	53.0	32.0	15.0				55.1	35.7	9.2			
RW 3	48.0	36.0	16.0				50.0	40.2	9.8			
RW 4	55.0	35.0	10.0				55.9	38.1	6.0			
RW 5	60.0	32.0	8.0				60.6	34.6	4.8			
RW 6	60.0	31.0	9.0				60.9	33.7	5.4			
RW 7	55.0	32.0	13.0				56.7	35.4	7.9			
RW 8	52.9	30.8	12.5	3.8			55.0	34.3	7.7	3.0		
RW 9	50.9	29.6	12.0	7.4			53.5	33.3	7.4	5.7		
RW10	50.0	42.5			7.5		48.6	44.3			7.1	
RW11	50.0	45.0			5.0		48.5	46.8			4.7	
RW12	55.0	40.0			5.0		53.6	41.7			4.7	
RW13	49.2	41.0	5.0		4.8		48.8	43.6	2.8		4.8	
RW14	55.0	35.0	5.0		5.0		54.9	37.4	2.9		4.8	
RW14 Residual	64.0		17.0		19.0		69.2		10.8		19.9	
RW14F	54.7	29.9	4.3		4.3	6.8	55.4	32.5	2.6		4.2	5.3
RW15	50.0	40.0			10.0		48.4	42.1			9.5	
RW16	52.5	40.0			7.5		51.0	42.2			6.8	
RW17	50.0	30.0		20.0			51.2	33.4		15.4		

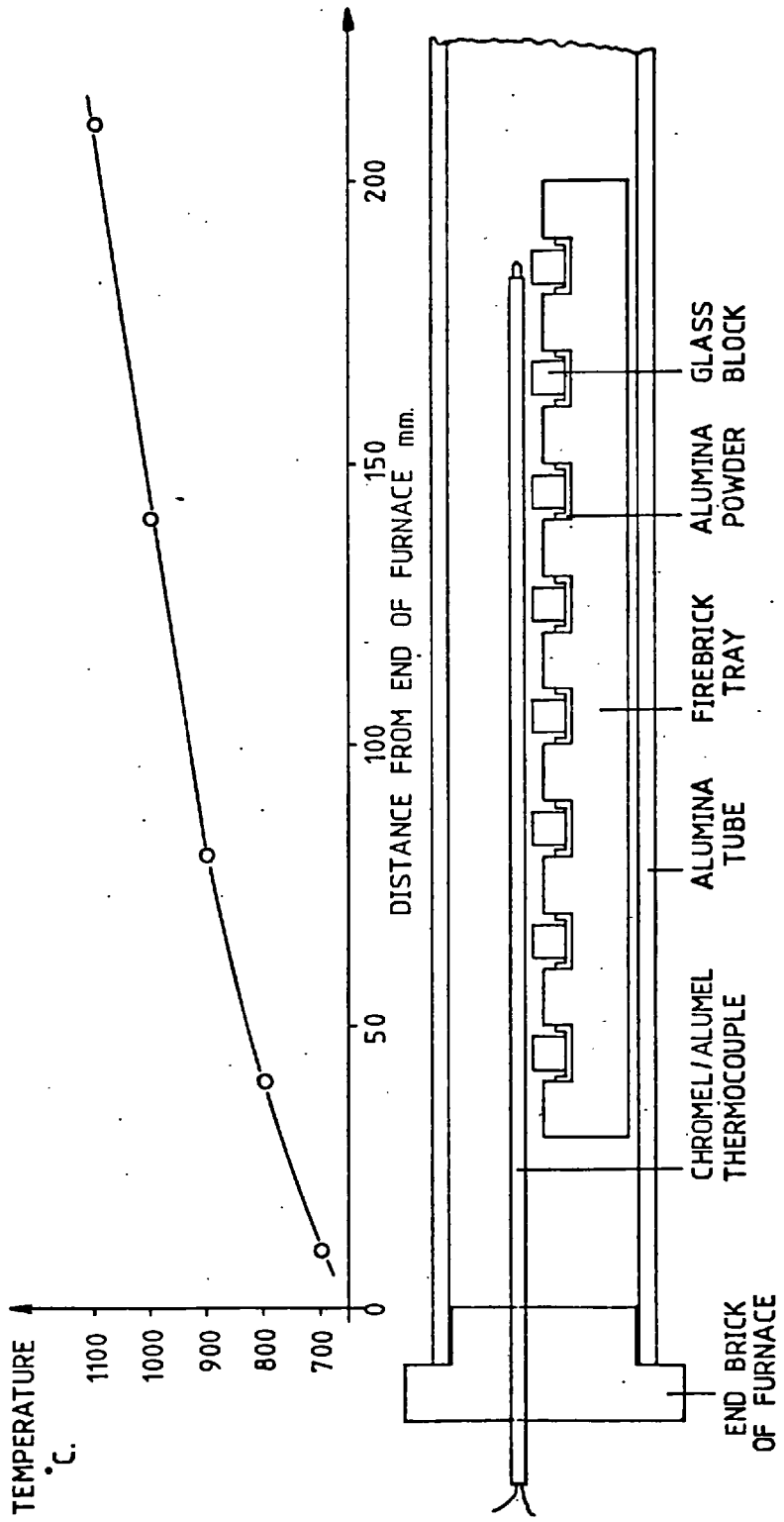


Fig. 2.1 Gradient heat-treatment technique.

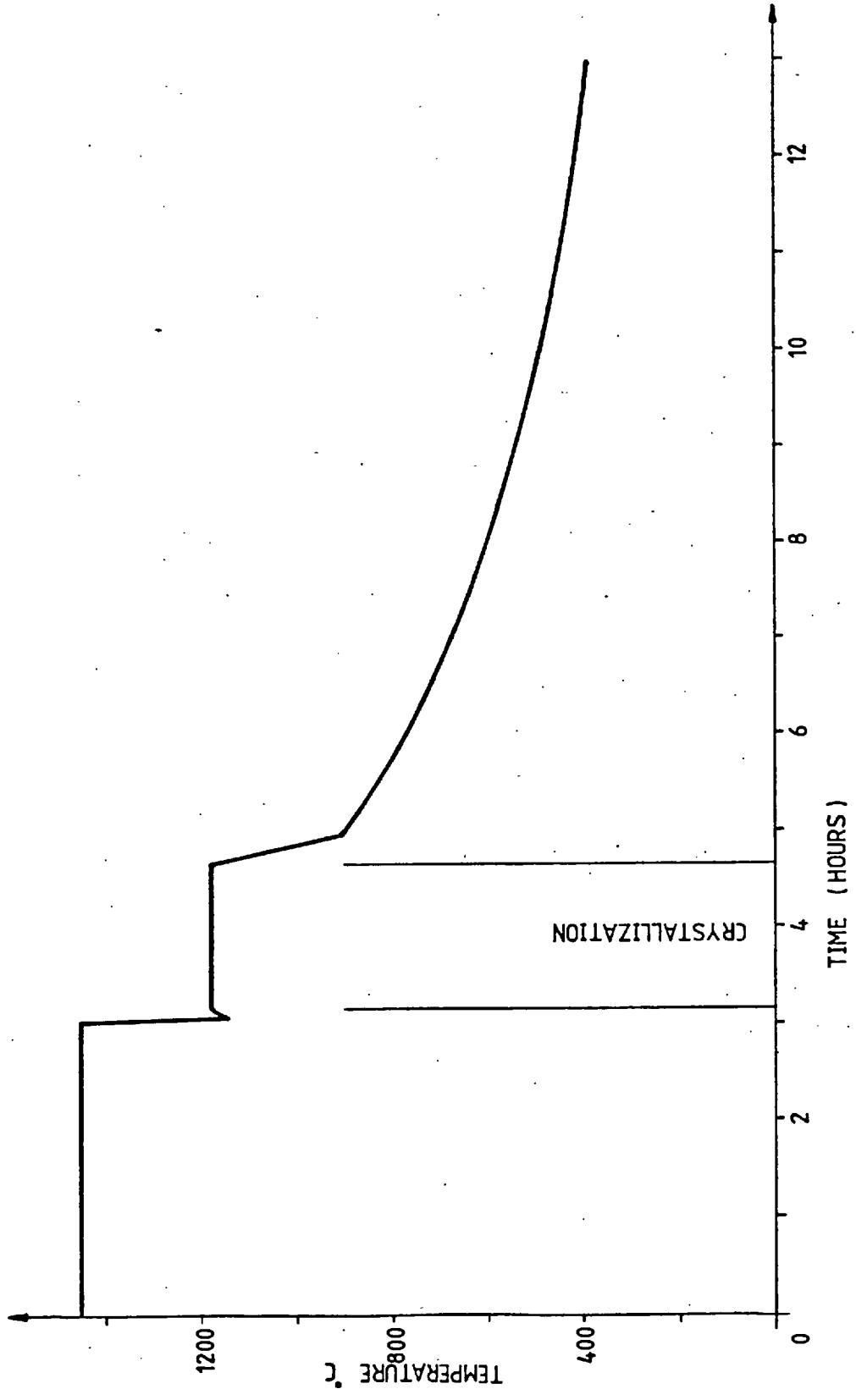


Fig. 2.2 Heat-treatment schedule for RW9 tiles.

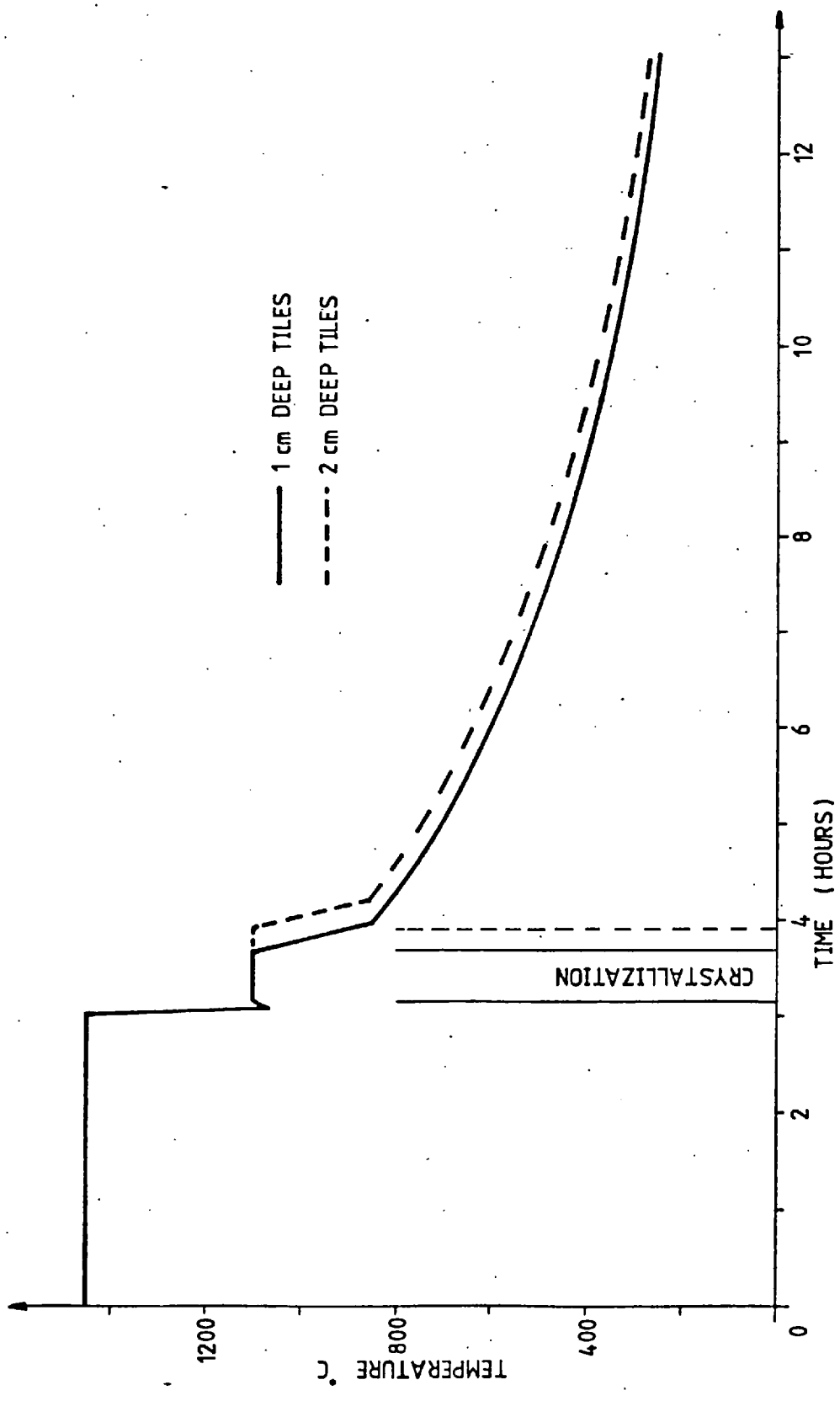


Fig. 2.3 Heat-treatment schedule for RW14 tiles.

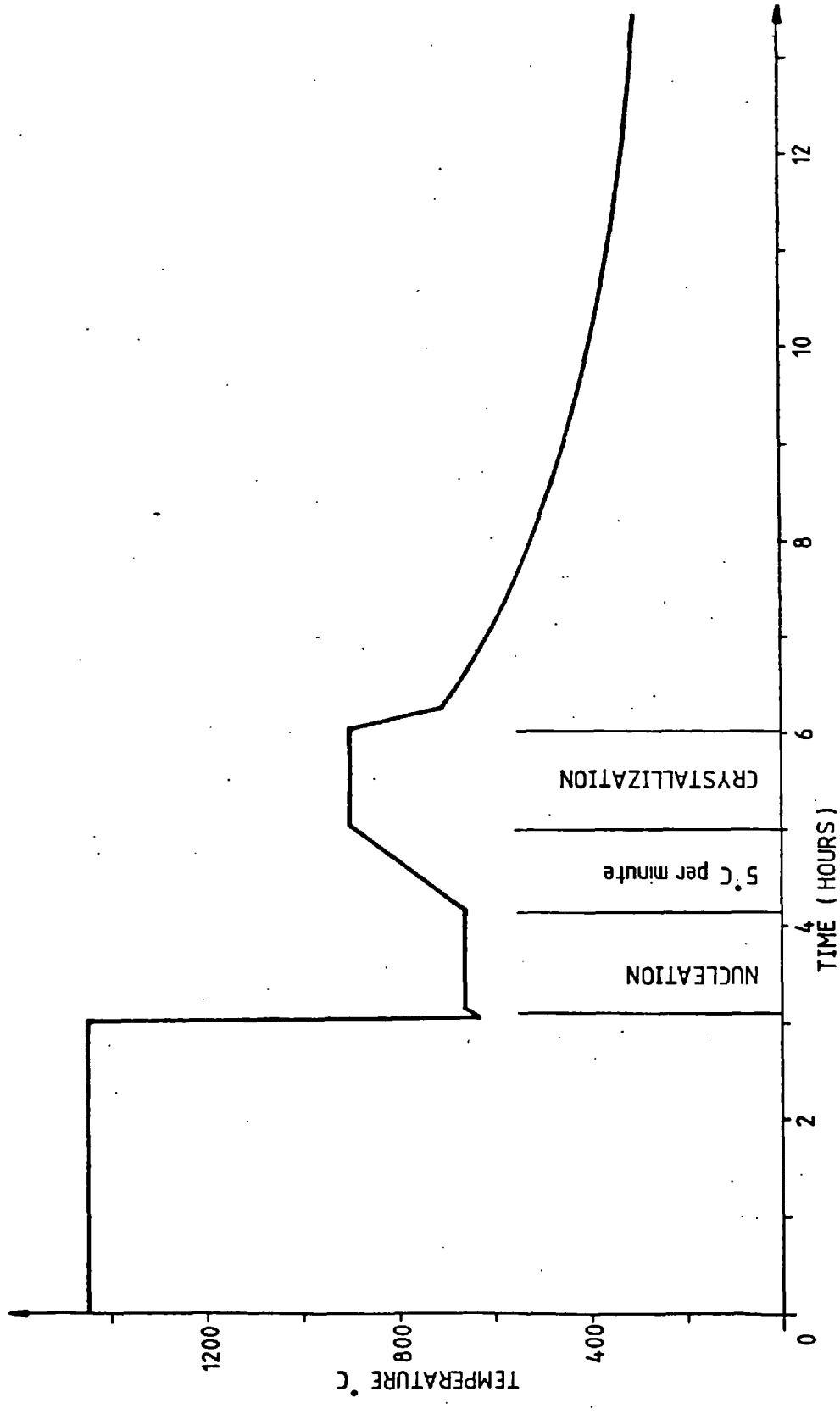


Fig. 2.4 Heat-treatment schedule for RW9 intra-crusible material.

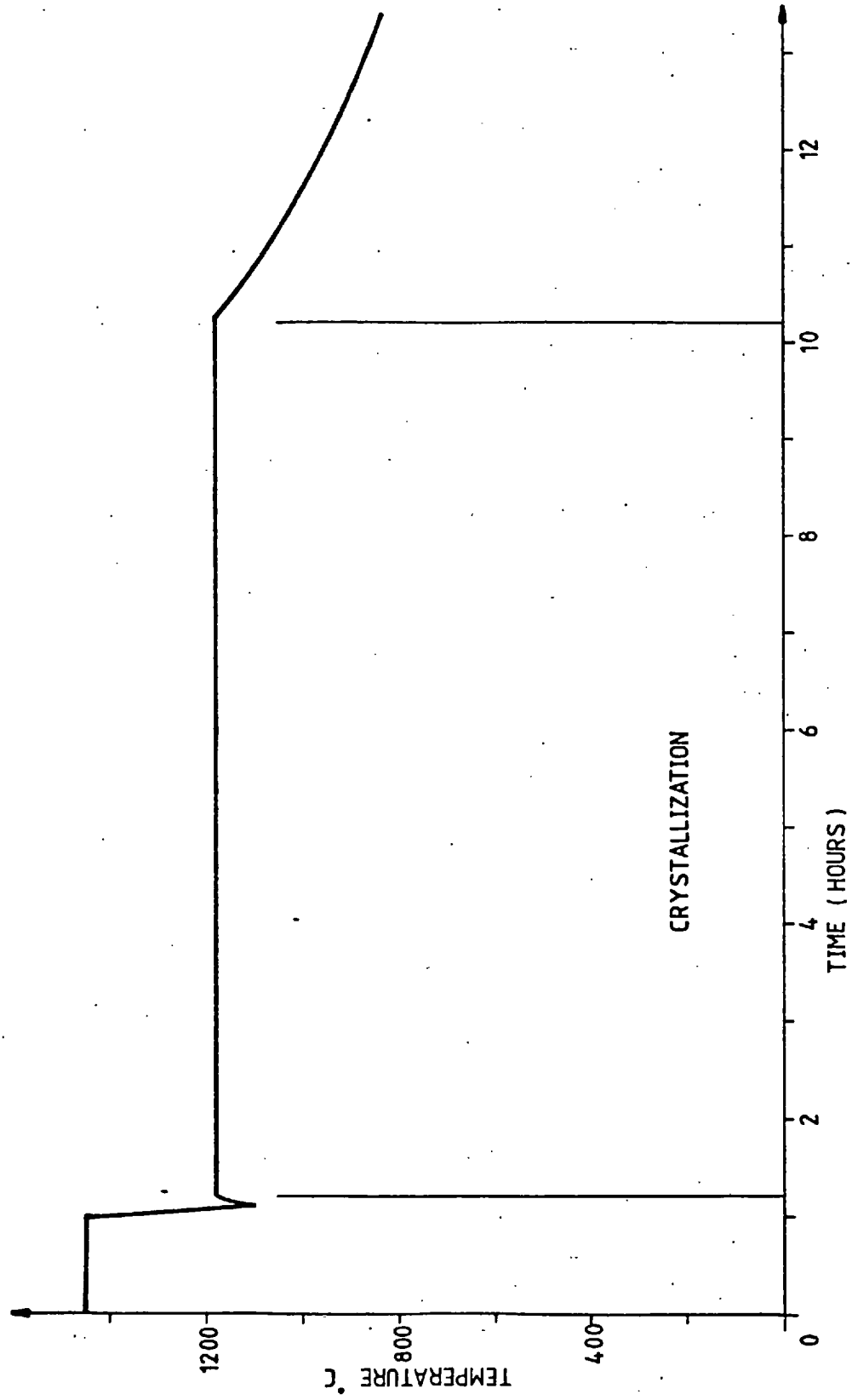


Fig. 2.5 Heat-treatment schedule for RW14F tiles.

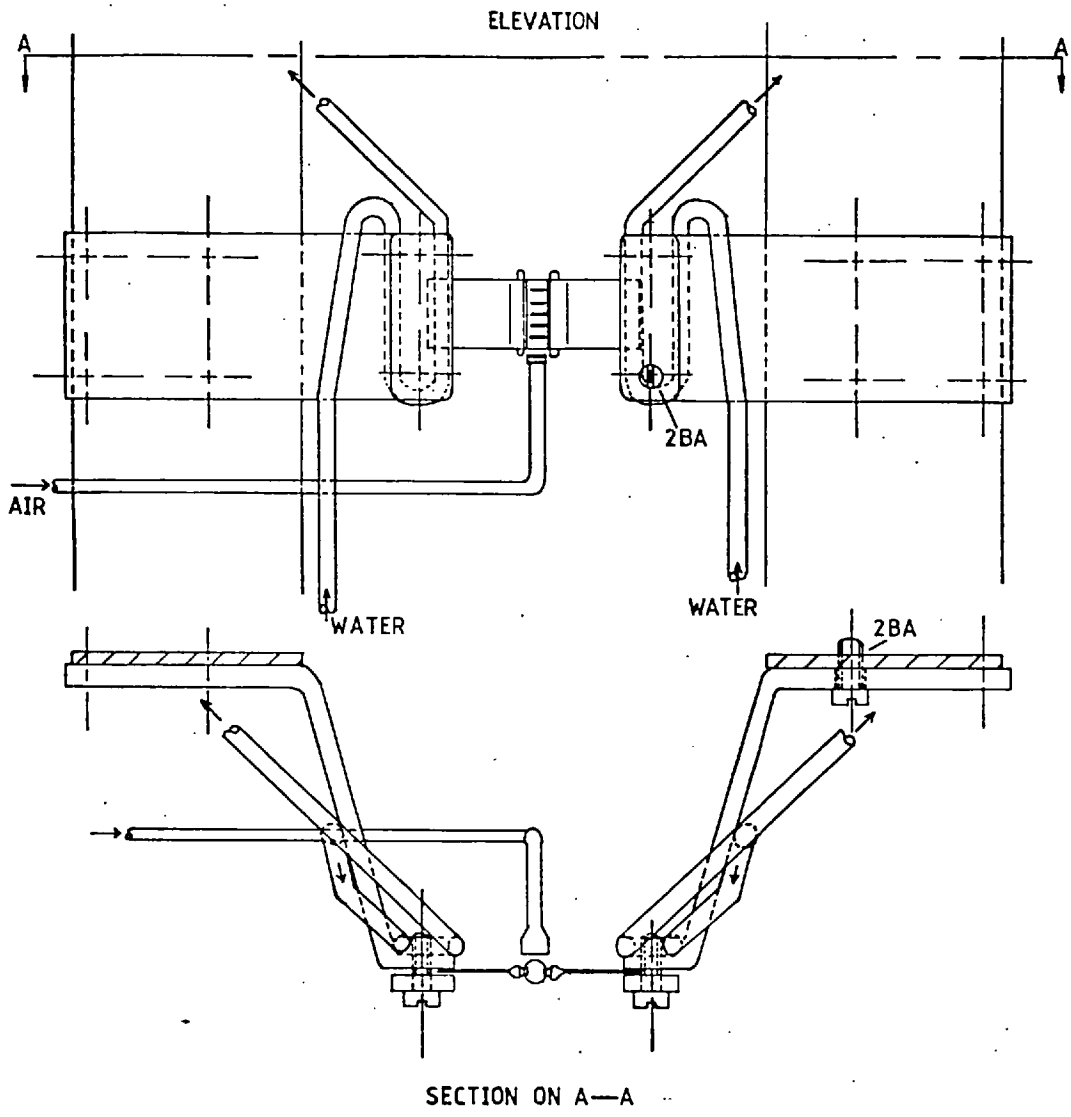


Fig. 2.6 Transformer terminals and platinum collar.

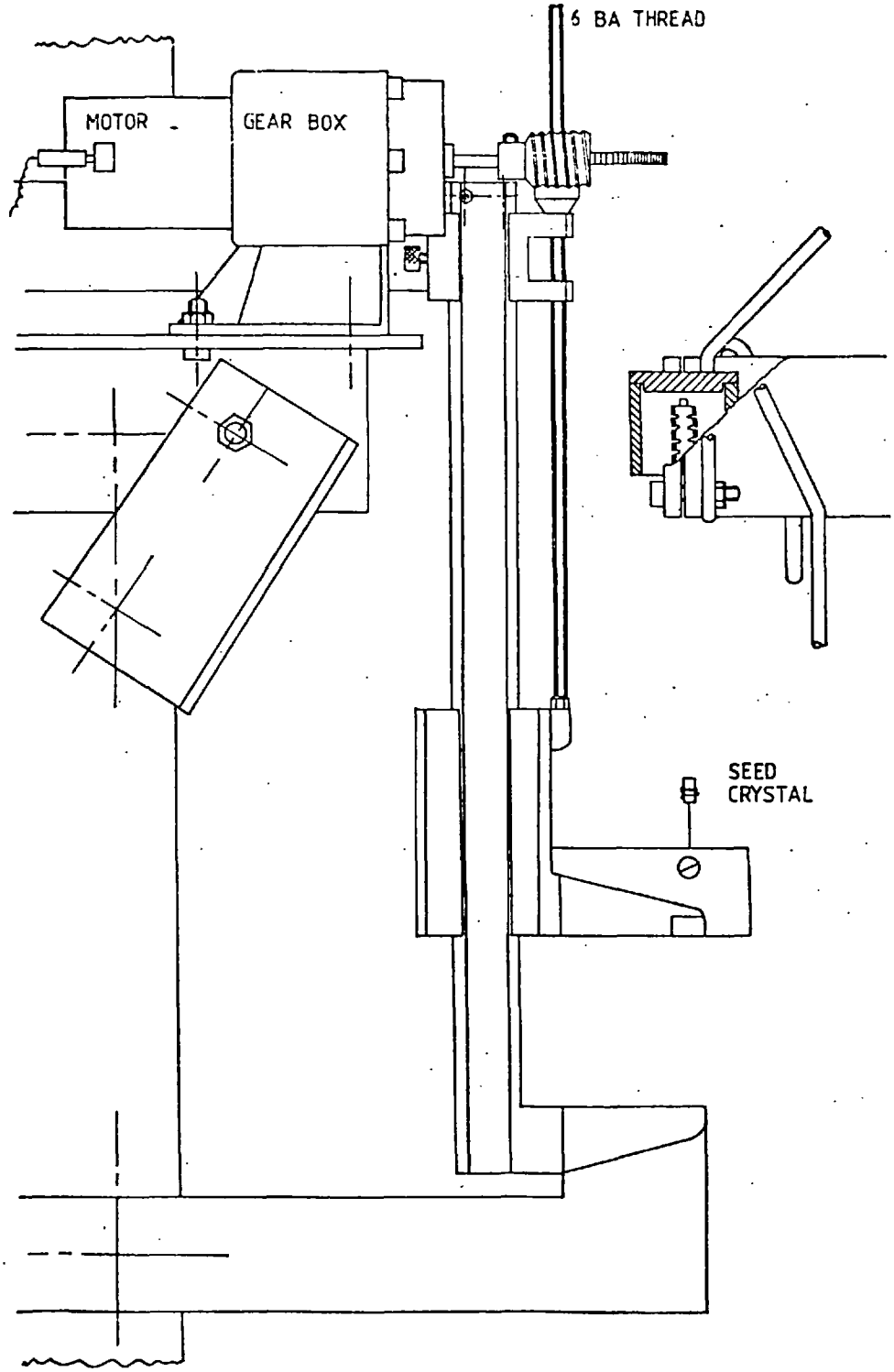


Fig. 2.7 Rod pulling apparatus.

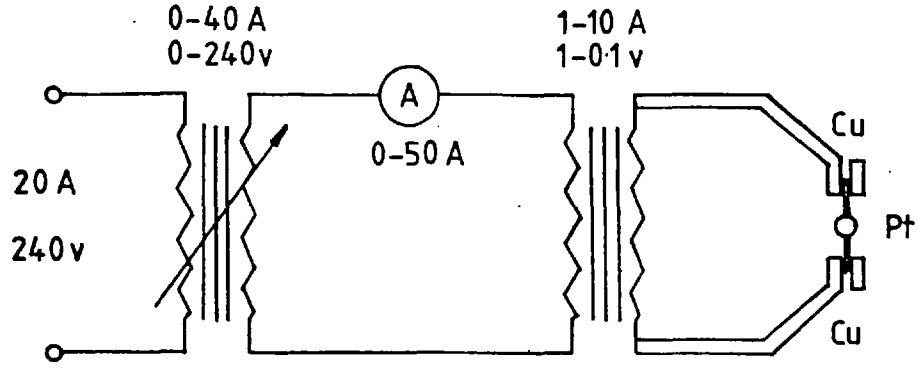


Fig. 2.8 Transformer circuit.

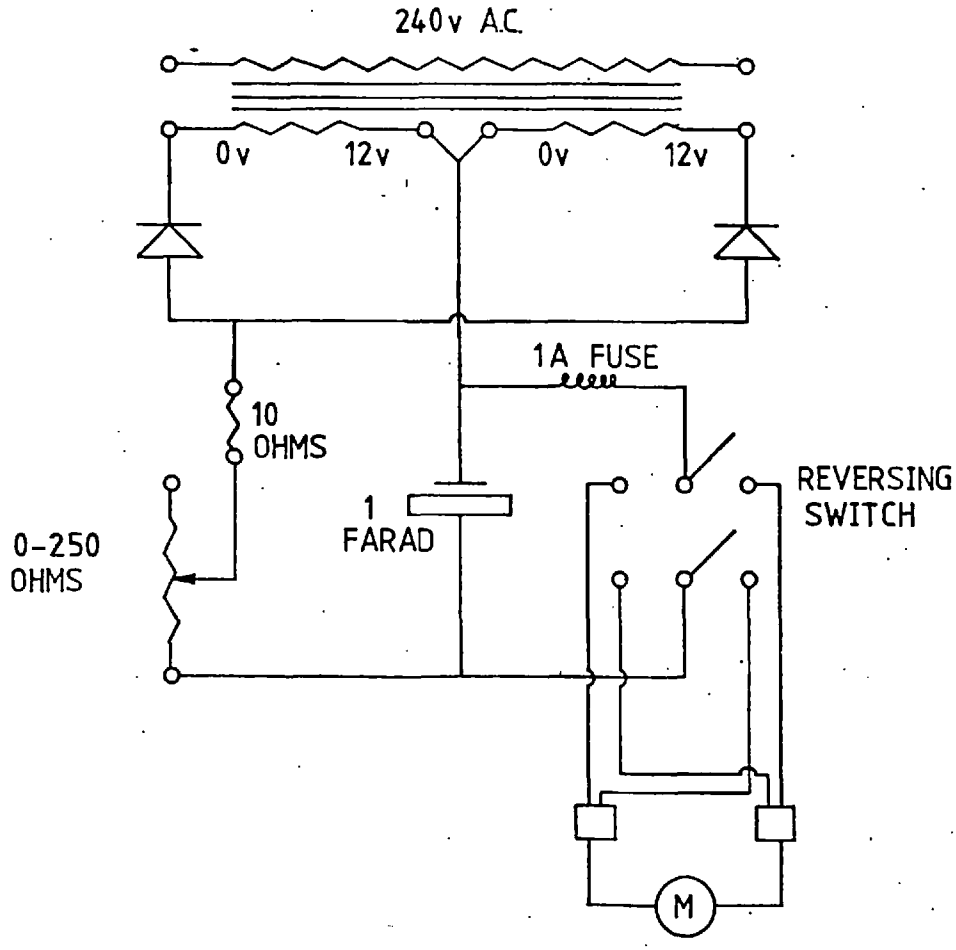


Fig. 2.9 Motorised drive circuit.

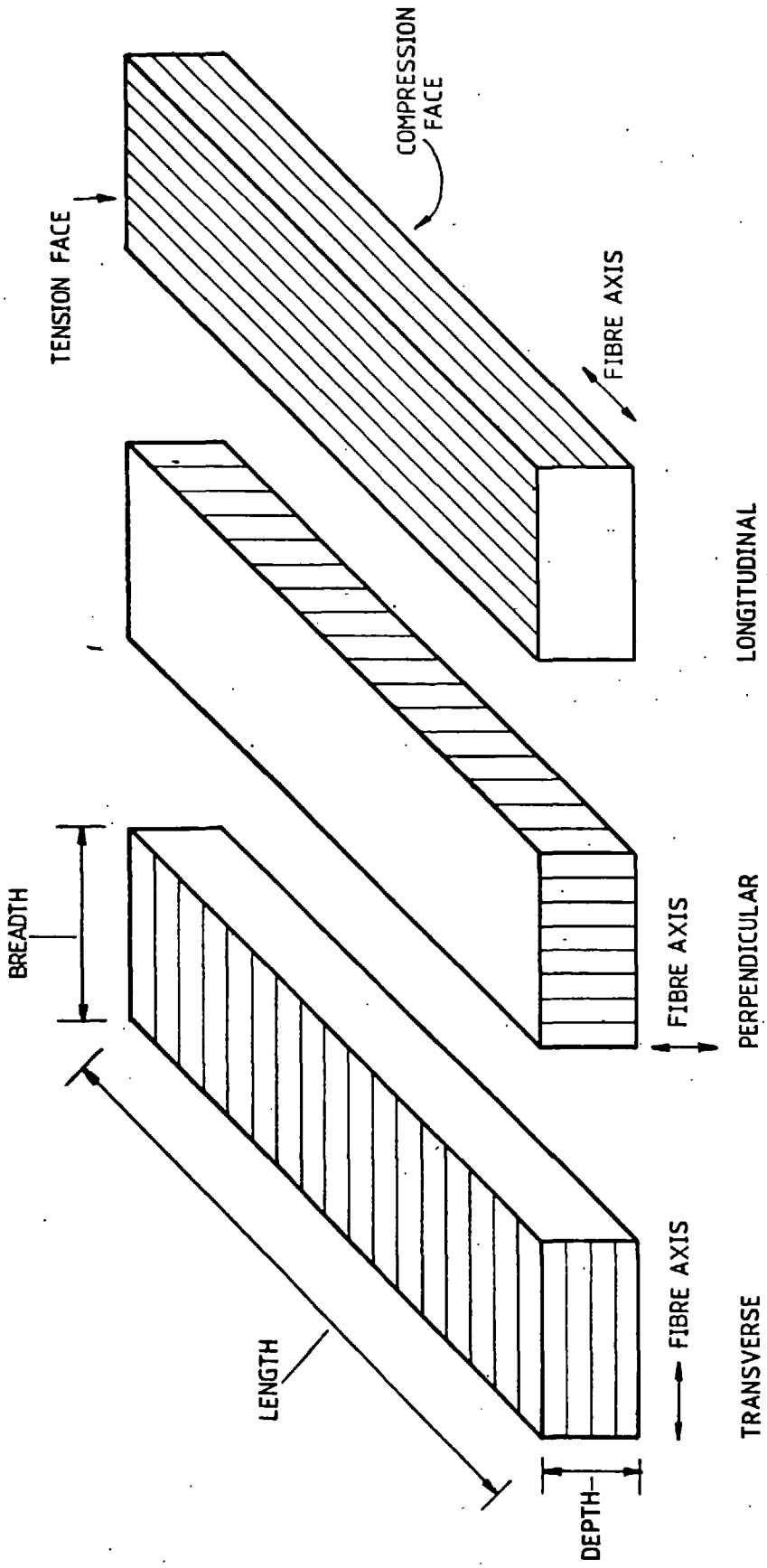


Fig. 2.10 Type of bend test specimens.

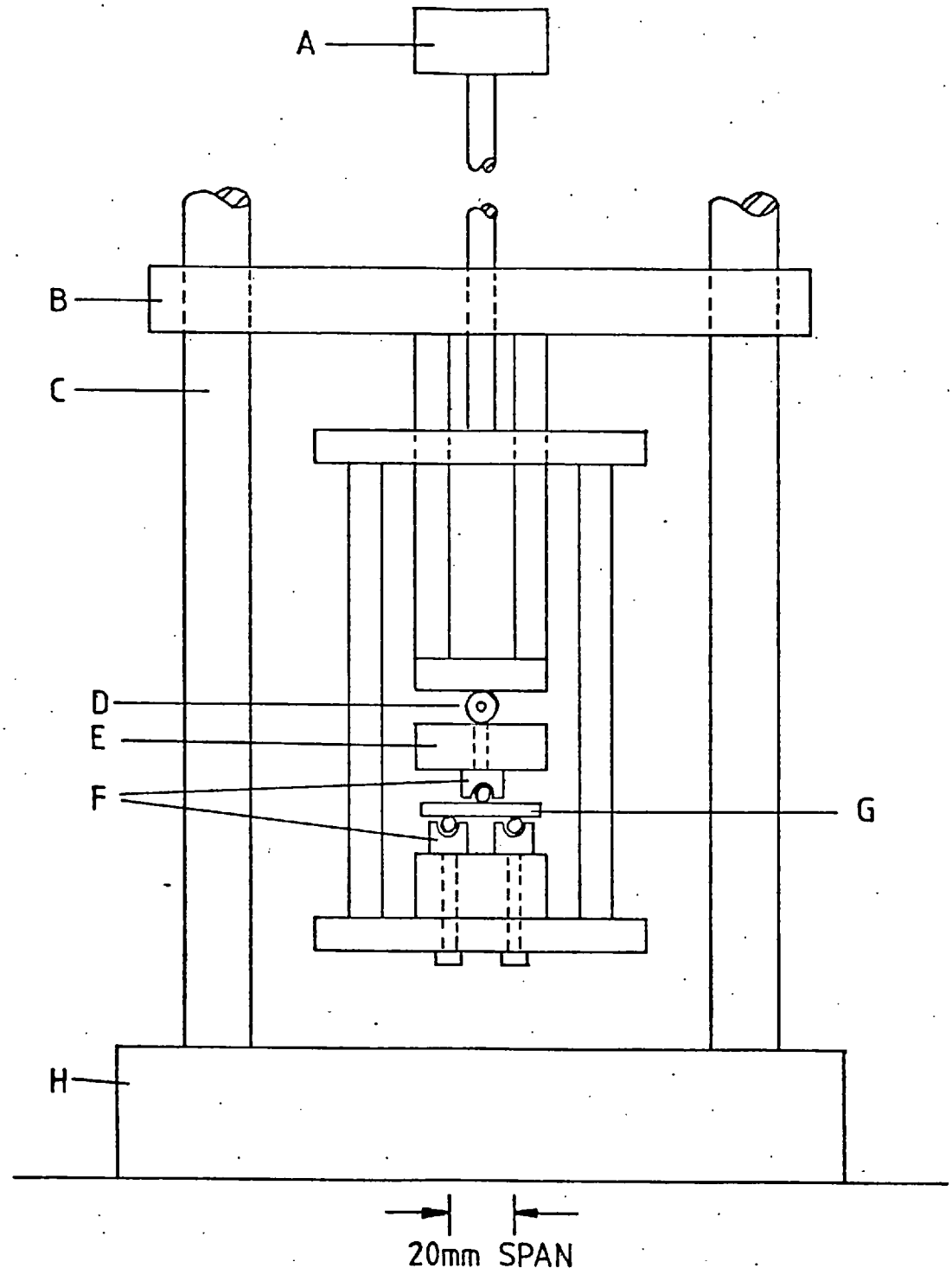


Fig. 2.11 Schematic diagram of the 20mm span bend test apparatus, key overleaf.

KEY TO FIG. 2.11

A Tension load cell

B Instron cross-head

C Instron lead screws

D Self centering joint

E Upper part of test apparatus

F Tungsten carbide rollers in steel slots

G Specimen

H Base of Instron

KEY TO FIG. 2.12

A Tension load cell

B Instron cross-head

C Instron lead screws

D Ball bearing

E Upper part of test apparatus

F Steel knife edges

G Specimen

H PTFE tape

I Base of Instron

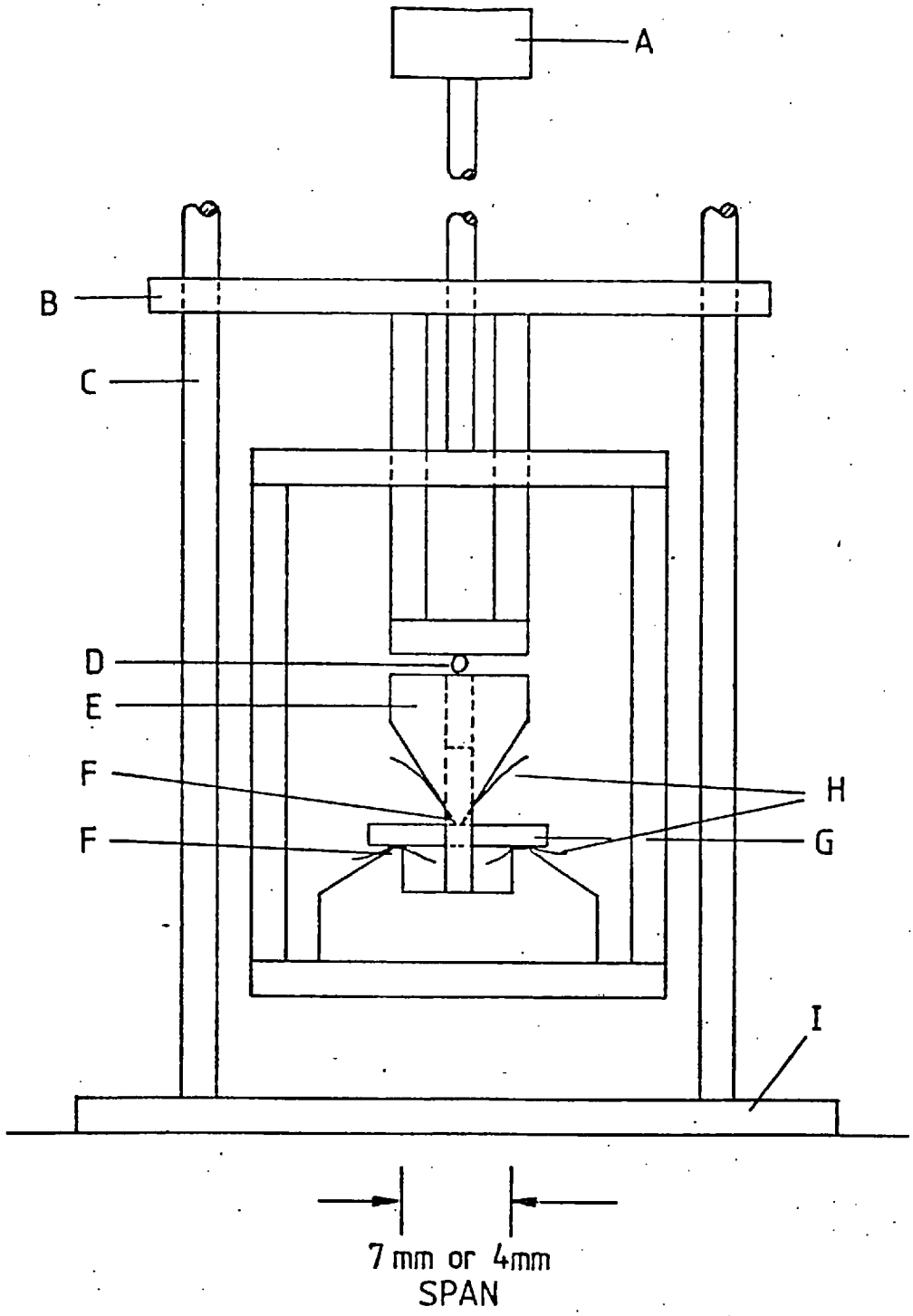


Fig. 2.12 Schematic diagram of the 7 and 4 mm span test apparatus, key on preceeding page.

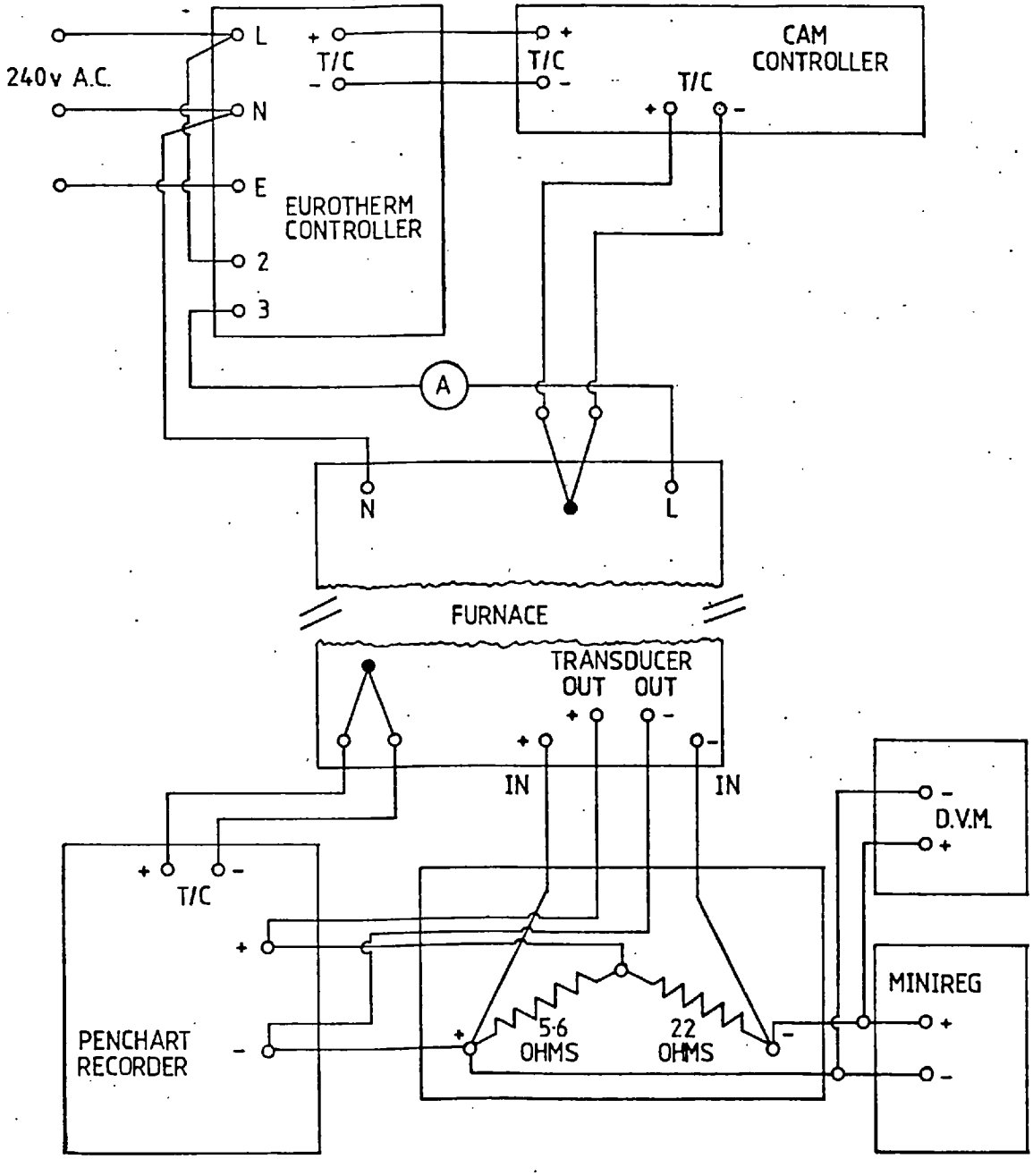


Fig. 2.13 Dilatometer circuit.

CHAPTER 3

RESULTS AND DISCUSSION

3.1. CRYSTALLIZATION CHARACTERISTICS OF THE GLASS COMPOSITIONS:

The compositions of the glasses discussed in this section, expressed both as weight per cent and moles per cent, are listed in table 2.2.

In order to facilitate the interpretation of the powder X-ray diffraction patterns obtained from devitrified samples of these glasses, the patterns given by the mineral species which may appear were found. Those of wollastonite, pseudowollastonite, and anorthite were prepared by taking an X-ray powder photograph of a sample of the mineral, as described in section 2.4.1., and this ensured that any aberration in the camera influenced a sample X-ray photograph and that of the "standard" mineral equally. However pure samples of devitrite, $Na_2Ca_2Si_3O_9$, and hardystonite were not available and therefore the patterns for these minerals where found in the Powder Diffraction File (121). For each mineral the normalised peak intensity expressed as a percentage, either found from measurement of microdensitometer traces or directly from the index cards, was tabulated with the corresponding d-spacing of the planes of the crystal structure, see tables 3.1 to 3.6, and also expressed diagramatically in

figures 3.1 to 3.6.

The crystallization of glass compositions RW1 to RW14F inclusive was investigated by the heat-treatment techniques described in section 2.3.

3.1.1. COMPOSITION RW1:

From the investigation of crystal growth rates in the $CaO-Al_2O_3-SiO_2$ ternary system made by Kumm and Scholze (126) composition RW1 was chosen as having a relatively low liquidus temperature, about 1340°C, and giving $CaSiO_3$ as the primary devitrification product. From the $CaO-Al_2O_3-SiO_2$ phase diagram (127), see figure 3.7, this composition is found to be on the silica rich side of the $CaSiO_3$ phase field. Glasses with high silica contents tend to have high viscosities (19, 118) and therefore slow rates of crystallization (see section 1.4.1.), and this is in agreement with Kumm and Scholze's data.

RW1 was found to require 18 hours at 1080°C to produce a 3.5mm depth of crystallization, i.e. approximately 0.025 microns per second. This surface nucleated crystallization was composed of coarse, spherulitic-type fibres up to about 30 microns in diameter, as is shown in the photomicrograph of a thin section of this sample, figure 3.8. Although this sample shows a straight crystal/glass interface the fibres are not well aligned due to the large distance between the developed surface nuclei , i.e. about 100 microns apart, which allows the fibres to fan out into a "cone", i.e. a three-dimensional segment of a

spherulite, before mutual impingement allows only those fibres orientated within 5° each side of the perpendicular to the sample surface to continue to grow, i.e. the transcrystallization mechanism (see section 1.4.2.).

The X-ray data obtained from the same sample, 18 hours at 1080°C, are given in table 3.7 and figure 3.9. From this it is seen that β-$CaSiO_3$ is the primary devitrification product but that approximately one third of the total crystallization is made up of $CaAl_2Si_2O_8$, a synthetic analogue of the mineral anorthite. The relative proportions of the crystallization products were estimated from the relative sizes of the maximum I/I_o values of each phase, an inaccurate method which neglects the effects due to the background scatter from any residual amorphous phase and the effect of any solid-solution in either, or both, phases altering the structure-factors of the crystal lattice and hence the intensities of the diffracted X-rays, (120). (An accurate, quantitative determination of the relative amounts of the crystalline and glass phases in a glass-ceramic can only be made by X-ray methods when an X-ray diffractometer is used and a number of assumptions, which must be verified for each material, tested (128, 129).)

This glass showed no evidence of the formation of internal nuclei at any of the heat-treatment temperatures used during the investigation.

3.1.2. COMPOSITION RW2:

Samples of RW2 composition glass were heat-treated in the temperature range 1000°C to 1075°C for

various times between 1 and 71 hours.

All the thin sections made from these samples show surface nucleated, fibrous crystallization, but the fibres are not in parallel alignment. Instead the fibres are branched and distorted so that they have a "feathery" appearance. On analysis of the X-ray data obtained from a typical sample it was found that $CaAl_2Si_2O_8$ was the dominant phase whilst β-$CaSiO_3$ only constituted about 40% of the total crystallization. RW2 is in the primary α-$CaSiO_3$ region in the liquidus projection of the CaO-Al_2O_3-SiO_2 phase diagram (127), but it is close to the boundary with the $CaAl_2Si_2O_8$ region (see figure 3.7), and, of course, the limits of these regions may be altered for transformations at sub-liquidus temperatures. (Since the devitrification of a glass is a transformation from a non-equilibrium state to the equilibrium state at the particular temperature concerned, then an equilibrium phase-diagram, which is constructed such that each composition is in its equilibrium state at all temperatures, can never give an exact forecast of the products of devitrification.)

From the above information it appears that although β-$CaSiO_3$ is the primary phase, i.e. on crystallization it was the first phase to nucleate and grow into the glass, since the "spherulitic" type of crystallization only occurs in growth from the melt (see section 1.4.2.), the $CaAl_2Si_2O_8$ phase rapidly nucleates on the developing fibres and the growth of this secondary phase distorts these fibres.

At 1020°C the growth rate in this composition was found to be about 0.02 microns per second.

3.1.3. COMPOSITION RW3:

This was an attempt to produce a totally crystalline material, i.e. a material containing no residual glass after crystallization. This composition lies on the compatability join (pseudo-binary) between α-$CaSiO_3$ and $CaAl_2Si_2O_8$, on the pro-α-$CaSiO_3$ side of the 1307°C eutectic, as shown on the liquidus projection phase diagram, figure 3.7.

Small samples were heat-treated at temperatures between 1045°C and 1075°C for times up to 72 hours, and in these well aligned fibres grew, i.e. transcrystallization occurred almost immediately as the surface nuclei are spaced at only about 20 microns (see section 3.1.1.), and unbranched fibres approximately 15 microns in diameter were formed. In those samples heated for too long a time the fibres nearest the surface, i.e. those which grew first, became distorted into lath-type shapes (see section 1.4.2.). The X-ray analysis of a typical sample, table 3.9 and figure 3.11 shows that the crystallization produced approximately equal amounts of β-$CaSiO_3$ and $CaAl_2Si_2O_8$.

However, when tiles of RW3 composition were fabricated, as described in section 2.5.2., and heat-treated for 18 hours at 1040°C, the crystal growth rate being 0.1 microns per second at this temperature, the material produced was found, on observing thin sections prepared from pieces

cut from all parts of the tiles, to have a network of fine cracks running through it. The cracks run at 45° and 135° to the tile surface and therefore form a mutually perpendicular lattice pattern. The cracks are 50 microns wide and run through both the fibres and inter-fibre, secondary crystallization, as shown in the photomicrograph figure 3.12.

This cracking is thought to be due to the complete absence, or at most the presence of only a small amount, of residual glass in this material. When other compositions were made up into tiles this type of cracking was not found, whether the inter-fibre matrix was crystalline or glass, and all these compositions must have contained a proportion of residual glass from a consideration of their compositions and those of the crystals formed. A tile cooled from a high temperature may contain permanent stresses between adjacent "layers", even if cooled moderately slowly, due to the thermal gradient built up across the relatively large cross section as the exterior cools more rapidly than the interior. The magnitude of these stresses for a given rate of cooling will depend mainly upon the expansivity, thermal conductivity and elasticity of the materials constituting the tile. However if the tile contains a significant amount of residual glass then at all temperatures above the glass transition temperature Tg this glass is capable of stress relaxation and permanent stresses cannot build up in the material, i.e. above Tg the glass behaves as a viscoelastic solid (see reference 19).

From the spalling tests performed on refractory bricks (130) it has been found that both shear stresses and tensile stresses build up in a large body during cooling. If the body is suddenly cooled its surface tends to contract but this contraction is prevented by the interior of the body which is still at a higher temperature. Therefore tensile stresses are set up in the cooler, surface material, and, if the tensile strength of a brittle material is less than the shear strength, the body will fail in tension by cracks running at 90° to the sides. However, if the cooling is not sufficiently rapid to produce tensile failure the shear stresses built up in the body may still cause sudden failure.

Figure 3.13 represents an isothermal plane ab in a portion of a heating or cooling tile at a given instant of time. The temperature of the plane ab is T and that of another isothermal plane dx distant is T + dT, i.e. the temperature gradient is dT/dx. The normal plane cd cuts the isothermal surfaces at a neutral point of shear. The distance between planes cd and ef along ab is s, but under the existing conditions ef cuts isothermal T + dT at a distance s + sαdT from cd, where α is the coefficient of linear expansion. The shear strain may be measured as the deflection of one plane relative to another divided by the distance between them, i.e. shear strain = (sαdT)/dx = sαdT/dx and therefore,

$$\text{shear stress} = Es\alpha dT/dx$$

where E is the elastic modulus of the material. The

shear fracture should occur at 45° to the isothermal. This shows that the magnitude of the shear stress built up on cooling a tile relatively slowly is proportional to the dimensions of the tile, the coefficient of expansion and the temperature gradient which is itself dependent on the cooling rate and the thermal conductivity of the material.

Some of the RW3 composition small samples did not show the 45° cracking as their dimensions were not large enough for the shear stress built up to exceed the shear strength of the material, but others were found to be cracked and in these the rapid cooling rate could have caused large shear stresses to occur. RW3 devitrified material should have a relatively low thermal conductivity of the order of 3J s^{-1} m^{-1} K^{-1}(10), a typical value for a glass-ceramic. The above reasons, and the fact that the cracks are orientated at 45° to the tile surface (the isothermal planes will be parallel with the exterior surfaces of the tile), suggests that the cracking of the RW3 tiles is due to the shear stresses produced during cooling which cannot be relieved in this nearly perfectly elastic material.

3.1.4. COMPOSITIONS RW4, RW5 and RW6:

In order to eliminate the cracking formed during the cooling of RW3 tiles, compositions containing a higher percentage of silica were made up. It was expected that these would contain about 20%, a relatively large amount, of residual glass after crystallization and

would therefore be sufficiently viscoelastic at high temperatures to avoid the build up of thermal stresses.

Composition RW4, shown on the phase diagram (figure 3.7), is reported in Kumm and Scholze's data (126) to have a liquidus temperature of 1371°C and to give $CaSiO_3$ as the primary phase on devitrification. However it was found to be impossible to completely fuse this composition to give a clear, homogeneous glass. Similarly, composition RW5 (shown on figure 3.7) could not be melted and cast into a homogeneous, bubble-free block although the silicon carbide furnace elements were heated to 1490°C giving a furnace hearth temperature of at least 1450°C. The reported liquidus temperature of this composition is about 1360°C, but the problem with these high silica content glasses is their high viscosity (see section 1.2.) which means that they must be at a high temperature to flow easily when poured.

Composition RW6, see figure 3.7, is further away from the $CaSiO_3$ composition, which should give a smaller proportion of β-$CaSiO_3$ on crystallization, than either RW4 or RW5 but it has a lower liquidus temperature and could be cast into a homogeneous, bubble-free glass from a hearth temperature of about 1435°C. Heat-treatment of RW6 samples between 950°C and 1077°C for times up to 66 hours gave surface nucleated crystallization composed of misaligned fibres. A tile was prepared as described in section 2.5.2. and heat-treated at 1025°C for 66 hours, as the growth rate at this temperature is about 0.02 microns

per second. This gave a tile which showed evidence of coarsening and recrystallization of the fibres which had been the first to form from the melt, a result of the long heating time required to complete the crystallization at the centre of the tile.

The RW6 tile contains about 20% of residual glass, assuming the maximum amount of the crystalline phases of exactly stoichiometric composition, and no cracking was visible in this tile. However due to the relatively high viscosity of RW6 glass the crystal growth rate was very slow (see section 1.2.), and although the individual fibres are fine (about 10 microns diameter) the surface nuclei are very widely spaced (about 100 to 300 microns apart) and this allows divergent cones of fibres to develop. The fibres are therefore orientated up to 20° away from the normal to the tile surface and the material cannot be regarded as unidirectionally crystallized. The X-ray data, figure 3.14 and table 3.10, show that the devitrification is composed of approximately 60% β-$CaSiO_3$ and 40% $CaAl_2Si_2O_8$.

3.1.5. COMPOSITIONS RW7, RW8 and RW9:

Composition RW7, see table 2.2, was chosen as a compromise between RW3 which gives unidirectionally crystallized fibres but contains trans-fibrillar cracks (see section 3.1.3.) and RW6 which is not cracked after crystallization but in which the fibres grow in cones and are therefore misaligned (see section 3.1.4.). From the phase diagram, figure 3.7, it can be seen that RW7 has a

liquidus temperature of 1310°C, and so this composition could be fused and cast into a clear, bubble-free glass.

On devitrification at 1020°C two types of crystallization were observed. On surfaces which had been abraded, as described in section 2.5.1., α-$CaSiO_3$ nucleated and grew in the form of primary dendrites (i.e. needle-like morphology) at the rate of 0.02 microns per second. The results of the X-ray analysis of this material are shown in figure 3.15 and table 3.11, and these indicate that approximately 10% of the total crystallization is $CaAl_2Si_2O_8$, precipitating as the secondary phase. On smooth surfaces transcrystallized β-$CaSiO_3$ spherulitic fibres, nucleated at sites spaced about 50 microns apart on the surface, grew at the rate of 0.006 microns per second. The X-ray analysis from this material, see figure 3.16 and table 3.12, reveals that it consists of nearly equal proportions of β-$CaSiO_3$, α-$CaSiO_3$ and $CaAl_2Si_2O_8$. The high proportion of α-$CaSiO_3$ was due to the inclusion of some of the crystallization which had nucleated and grown from surfaces abraded by the action of the diamond saw used during the preparation of the small sample (see section 2.2.).

The alpha/beta transition in calcium metasilicate is usually quoted at around 1120°C, although solid-solution could alter this temperature (see section 1.5.1.). However, assuming that β-$CaSiO_3$ is the equilibrium phase at 1020°C, then the driving force for nucleation (i.e. the difference in free energy between the glassy state and the

crystalline phase) of β-$CaSiO_3$ will be greater than that for the nucleation of α-$CaSiO_3$. This may result in β-$CaSiO_3$ nucleating on a smoother surface than α-$CaSiO_3$, but since β-$CaSiO_3$ has a much slower growth rate than α-$CaSiO_3$ then on a rough surface on which both can nucleate the faster growing phase dominates the crystallization. The relatively rapid growth of α-$CaSiO_3$ may be due to having $Si_3O_9^{6-}$ groups in the crystal structure, ions which could be already present in the RW7 glass (see sections 1.2. and 1.5.1.). The crystal structure may also explain why α-$CaSiO_3$ precipitates dendritically whereas β-$CaSiO_3$ forms spherulitic fibres. In section 1.4.2. the effect of viscosity on the morphology of crystals was discussed. At 1020°C the glass viscosity should be uniform, and both the calcium metasilicate polymorphs are therefore growing from identical melts. However, the amount of structural rearrangement in the glass necessary to orientate the molecular species such that they may join into the crystal lattice is different for the two structures. As already stated $Si_3O_9^{6-}$ ions may join the α-$CaSiO_3$ structure directly from the glass without breaking an Si-O or other strong bonds, i.e. only reorientation of existing structures is required for crystal growth. The β-$CaSiO_3$ structure (see section 1.5.1.) requires that the "backbone" silica tetrahedra are arranged at the correct angles and that each tetrahedron is linked to only two others, since this is a chain type of silicate, and therefore the silica tetrahedra network in the RW7 glass structure must be

broken down for crystallization to proceed. This means that bonds must be broken and tetrahedra rotated in addition to simple reorientation, and therefore the effective viscosity of the glass is greater for the growth of β-$CaSiO_3$ as more energy is required to adapt the existing glass structure to the crystal structure.

Figure 3.17 and table 3.13 show the X-ray data obtained from a piece of an RW7 composition tile produced by a heat-treatment of 54 hours at 1020°C. This consists of about 40% β-$CaSiO_3$, 50% $CaAl_2Si_2O_8$ and 10% α-$CaSiO_3$, the small amount of the alpha phase is due to the tile surface being smooth and there being no surfaces cut by a diamond saw. However the prolonged heat-treatment required to crystallize the full depth of this tile resulted in the fibres near the surface recrystallizing. This is shown in figure 3.18 in which the parallel 10 microns diameter fibres are seen alongside a dark region of lath-type, recrystallized material, see section 1.4.2. It was decided that as the β-$CaSiO_3$ crystallization obtained in RW7 was the best aligned and least cracked or deformed obtained in the CaO-Al_2O_3-SiO_2 system then this composition should form the basis for the production of mechanical, and other test, specimens. However the crystal growth rate in RW7 glass is too slow to grow fibres of sufficient length, i.e. about 5mm.

Rogers and Williamson (17) studied the effect of the addition of a small amount of zinc oxide on the crystal growth rate in an aluminosilicate glass of very similar

composition to RW7. They found that the presence of a few weight per cent of zinc oxide in the base glass gave a large increase in the crystal growth rate, a linear relationship being discovered between the square of the zinc oxide content and the growth rate for each crystallization temperature. The activation energies for crystallization (see section 3.2.1.) ranged from 560 kJ mol^{-1} for the base glass to 280 kJ mol^{-1} for the base glass plus 8 wt % ZnO (i.e. 8g ZnO added per 100g of base glass). At low zinc oxide concentrations this activation energy corresponds to that for viscous flow in the base glass at the crystallization temperature and confirms that a substantial rearrangement of the structure of this type of glass is required for the growth of β-$CaSiO_3$. As zinc oxide is added the divalent Zn^{2+} ions take up modifying positions, and hence break up the network of silica tetrahedra in the glass structure. It therefore requires progressively less rearrangement for the growth of the β-$CaSiO_3$ chain-type silicate from the glass and the activation energy is correspondingly reduced.

RW8 composition was made up by the addition of zinc oxide to RW7 base glass, in the ratio 4g per 100g glass, and giving this mixture two melts to homogenise the new composition. RW8 calculated composition is given in table 2.2. This glass was easily cast after the final melt since the addition of zinc oxide acts to reduce the viscosity as it breaks up the network structure in the glass, q.v. Small samples were heat-treated between

950°C and 1050°C. Figure 3.19 and table 3.14 give the X-ray analysis results from an abraded surface of a sample heated for 20 hours at 950°C and at this temperature about 55% of the total crystallization is β-$CaSiO_3$ and the remainder consists of $CaAl_2Si_2O_8$ only. Figure 3.20 and table 3.15 give the results from an equivalent sample heated for 20 hours at 975°C and show that $CaAl_2Si_2O_8$ now comprises 55% of the total crystallization, β-$CaSiO_3$ 40% and α-$CaSiO_3$ 15%. After 20 hours at 1025°C another rough surfaced sample formed α-$CaSiO_3$ as 50% of the total crystallization, $CaAl_2Si_2O_8$ 35% and β-$CaSiO_3$ only 15%, see figure 3.21 and table 3.16. These results confirm those found from the RW7 rough surfaced samples, i.e. that a roughened surface will allow α-$CaSiO_3$ to nucleate and grow at the expense of the stable beta phase, but they also show that below 975°C, for this particular glass, it is impossible for the alpha phase to nucleate as the difference in the driving force of nucleation of the two phases is increased as the alpha phase becomes increasingly unstable when the temperature is lowered away from the transition temperature.

The β-$CaSiO_3$ growth rate increased by ten times in RW8 as compared with RW7 at the same temperature, whilst the α-$CaSiO_3$ growth rate is only five times greater. This confirms Rogers and Williamson's findings and the fact that as the silica tetrahedra network is broken down in the glass structure chains of tetrahedra may be formed which can be relatively easily accommodated into a chaim silicate crystal structure. This process would not aid

the growth of the ring structure of the alpha phase, although the decrease in viscosity of the glass will increase the crystal growth rate (see section 1.4.1.).

RW9 composition was made up in the same way as RW8, but in this case 8g of zinc oxide were added per 100g of RW7 base glass. The calculated composition of RW9 is shown in table 2.2. Heat-treatments of samples over the range 900°C to 1200°C allowed the crystal growth rate versus temperature curves to be plotted, see figure 3.22. There are two curves on this graph, the upper one corresponding to nucleation on a rough surface giving α-$CaSiO_3$ as the primary phase, and the lower to smooth surface nucleation giving β-$CaSiO_3$ as the primary phase. The growth rates for both primary phases are approximately five times greater than at the corresponding temperature in RW8 glass. Both curves are in the region below the maximum growth rate, although both flatten off as 1200°C is approached suggesting that this may be close to temperature giving the maximum rate, and therefore are in the region where the kinetic term of the crystal growth equation predominates (see section 1.4.1.). The primary β-$CaSiO_3$ curve is in fact two curves, since it appears that when only the low temperature polymorph nucleates it can grow at a faster rate than that possible when a small proportion of α-$CaSiO_3$ nucleates concurrently.

Figures 3.23, 3.24 and 3.25, with tables 3.17, 3.18 and 3.19, show the X-ray analysis of samples heated at 1160°C for 10, 20 and 30 minutes respectively. The

10 minute sample is composed of approximately 55% α-$CaSiO_3$ as the primary phase, with β-$CaSiO_3$ making up the remainder of the crystallization in a sample which is translucent, i.e. it has a low percentage crystallinity. In the 20 minute sample β-$CaSiO_3$ constitutes 60% of the total crystallization, with 20% each of α-$CaSiO_3$ and $CaAl_2Si_2O_8$, and in the 30 minute sample $CaAl_2Si_2O_8$ predominates at 40% of the total whilst α and β-$CaSiO_3$ each contribute 30%, both these samples being densely crystalline, i.e. opaque. These results were confirmed by observation of the thin sections prepared from these samples, in which the initial crystallization was seen to be highly birefringent α-$CaSiO_3$ dendrites which are sufficiently widely spaced for the secondary arms to develop at right angles to the primary spines, see figure 3.26. This is followed by a dense infilling of spherulitic β-$CaSiO_3$ fibres of about 10 microns diameter and finally the material becomes almost totally crystallized due to the growth of the inter-fibre matrix of $CaAl_2Si_2O_8$.

It was found during examination of the thin sections used to determine the growth rate in RW9 composition (as described in section 2.3.) that the crystallization morphology of α-$CaSiO_3$ phase altered over the range of temperatures studied. Above 1150°C it crystallized in the form of dendrites which develop secondary arms, between 1150°C and 1050°C only the primary dendritic spine could grow (distinguished from a spherulitic type of fibre by the triangular cross-section) and from 1050°C to 1000°C,

the lowest temperature at which α-$CaSiO_3$ formed, it grew as branched spherulitic fibres making up wide angled cones, segments of spherulites, with the open, "feathery" type of microstructure typical of growth at "low" temperatures. These crystal/temperature characteristics are explained in section 1.4.2.

A photomicrograph of the smooth surface of a sample heated at 980°C for 10 hours, see figure 3.27, shows the dense surface nucleation obtained in this composition, the nucleation sites being spaced at about 25 to 30 micron intervals. At this temperature the crystallization consists of $CaAl_2Si_2O_8$ and β-$CaSiO_3$ fibres but these are too fine to be resolved at this magnification. In figure 3.27 the birefringence effects are produced by zones made up of fibres having the same (010) orientation, in addition to the nearly parallel alignment of the [010] fibre axis, each zone having originated from the same protruberence on the nucleus. The crack running parallel with the surface probably formed during cooling and is at the disordered region where the cones of fibres impinged and only those orientated within 5° of the normal to the surface continued to grow.

There was no evidence of any internal nucleation in RW9 glass.

It was decided that RW9 composition is suitable for the preparation of test specimens as the growth rate of β-$CaSiO_3$ in this glass is over one micron per second at 1180°C, and although this temperature is above the nominal

transition temperature it was found to be possible to nucleate and grow material composed of substantial amounts of fibrous crystals of the low-temperature polymorph from a smooth glass/air interface. Several tiles were prepared as described in section 2.5.3., and from these test specimens were fabricated. Samples were also taken for X-ray analysis and optical microscopy.

Figure 3.28 and table 3.20 give the X-ray data for a sample from the RW9/3T tile which show that this consists of β-$CaSiO_3$ together with a large proportion of $CaAl_2Si_2O_8$ and a small amount of α-$CaSiO_3$. A thin section revealed that the beta phase is present in the form of transcrystallized spherulitic fibres, 60 microns in diameter, whereas the alpha phase crystallized as widely spaced dendrites, and figure 3.29 is a photomicrograph which shows the coexistance of these two phases at the crystal growth front.

The X-ray data for two other tiles are shown in figure 3.30 and table 3.21 for RW9/4T and figure 3.31 and table 3.22 for RW9/6T. In both these tiles β-$CaSiO_3$ is the major crystal phase, with between 33% and 45% of the total crystallization as $CaAl_2Si_2O_8$ inter-fibre matrix and if any α-$CaSiO_3$ is present in these tiles it must constitute less than 5% of the total crystallization (i.e. the limit of resolution of the powder X-ray technique). Figure 3.32 is a photomicrograph of a cone of fibres grown from a surface nucleus and in which the inter-fibre matrix, nucleated on the fibres, can be seen.

The RW9 composition was also used to produce intra-crucible growth material. Figure 3.33 and table 3.23 give the X-ray data for RW9/7C, and this shows that this material consists of approximately equal amounts of β-$CaSiO_3$ and $CaAl_2Si_2O_8$ with less than 5% of the total crystallization made up of α-$CaSiO_3$. The photomicrograph of RW9/7C, figure 3.74, reveals that the β-$CaSiO_3$ fibres are orientated within 10° of parallel alignment and the material was therefore acceptable for the production of mechanical, and other, test specimens. Figure 3.34 is a diagram which shows the part of the crucible from which well aligned, undistorted material was obtained.

Table 3.24 gives the results of the wet-chemical analyses of a sample of RW9 glass and a sample taken from an RW9 composition tile after heat-treatment. Both analyses are in quite good agreement with the nominal, weighed-out composition, but that for the crystalline material is the worse. On examination of the analyses of the other devitrified glass it is apparent that these are always further from their nominal composition than the corresponding glass. This may be due to the reduced solubility of the crystalline phases compared to the glasses, or the increased difficulty in grinding the crystalline materials, which were generally harder than the glasses, resulting in the sieved samples being non-representative of the bulk.

3.1.6. COMPOSITIONS RW10, RW11, RW12, RW13 and RW14:

Strnad and Douglas found evidence of rapid, surface nucleated crystal growth in the Na_2O-CaO-SiO_2 system (131). In the compositions they used the devitrification products $Na_2Ca_2Si_3O_9$ and $Na_4CaSi_3O_8$ formed, however it was aimed to adapt the composition in this system such that rapid crystallization of β-$CaSiO_3$ could result, producing a material consisting of parallel fibres in a glass matrix which may have contrasting properties to the RW9 crystalline matrix material.

Composition RW10, see table 2.2, was chosen with reference to the Na_2O-CaO-SiO_2 phase diagram (127), see figure 3.35, from which it was found that this composition should have a liquidus temperature of about 1400°C, be in the primary α or β-$CaSiO_3$ phase field, and give $Na_2Ca_2Si_3O_9$ as secondary crystallization. (Of course, crystallization from the supercooled melt may not produce the phases predicted from the equilibrium phase diagram, since it is quite common for intermediate, metastable phases to be precipitated during the crystallization of a glass-ceramic (10).) A clear, bubble-free glass was obtained after melting the batch at about 1450°C and, although this glass has a relatively high liquidus temperature, it could be easily poured as the addition of sodium oxide to a silica glass greatly reduces the viscosity at a particular temperature (see section 1.2.). On quenching about 75g of this glass on a cold brass plate the glass devitrified. Large, surface nucleated crystals grew up to 1cm in

diameter in the red-hot glass and subsequent X-ray analysis revealed that these consisted of both α-$CaSiO_3$ and a small amount of $Na_2Ca_3Si_6O_{16}$. Therefore this glass is not sufficiently stable to form a homogeneous glass block. On reheating and devitrifying small glass samples $Na_2Ca_2Si_3O_9$ and some $Na_2Ca_3Si_6O_{16}$, a synthetic phase with the mineralogical name devitrite, grew from the external surfaces at high growth rates, approximately 3 microns per second at 800°C and greater than 17 microns per second at 900°C. Figure 3.36 and table 3.25 show the X-ray analysis of a sample heat-treated at 906°C for 30 minutes. Another sample, which was heated at 1059°C for 30 minutes, produced a complex mixture of phases on devitrification, i.e. α-$CaSiO_3$, $Na_2Ca_2Si_3O_9$ and a small amount of $Na_2Ca_3Si_6O_{16}$ as shown in figure 3.37 and table 3.26, since $Na_2Ca_3Si_6O_{16}$ decomposes above 1047°C to calcium metasilicate and a liquid phase (127).

Composition RW11 is nearer the calcium metasilicate composition, see figure 3.35. The lower sodium oxide content, see table 2.2, resulted in a glass with a high liquidus temperature, nearly 1450°C, but it could be fully melted and poured from about 1450°C as sodium oxide is an extremely efficient fluxing agent (19). When a melt of RW11 composition was cast onto a cold brass sheet the resultant glass was unstable and surface nucleated crystals developed during cooling, particularly near the centre of the top surface of the glass block where the glass surface cooled most slowly. The coarse, 1cm diameter crystals

were shown by X-ray analysis to consist of $Na_2Ca_2Si_3O_9$. This glass composition is not sufficiently stable to form a homogeneous block from which controlled crystallization during heat-treatment would produce a required micro-structure.

The RW12 composition, see table 2.2 and figure 3.35, was chosen as a glass which may have been more stable than RW10 and RW11 due to the higher silica content increasing the viscosity and decreasing the crystal growth rate (see sections 1.2. and 1.4.1.). But when cast from 1450°C a 50g block of RW12 glass devitrified during cooling to give about 2cm diameter, hemi-spherulitic, surface nucleated crystals which were identified as α-$CaSiO_3$.

In order to improve the stability of these types of glasses it was decided to make up a quaternary glass containing aluminium oxide. This intermediate type oxide can be incorporated into the glass network structure and therefore increases the viscosity and decreases the crystal growth rate, see sections 1.2. and 1.4.1. To reduce the amount of residual glass or secondary crystalline phase present after controlled crystallization to a minimum RW13 composition was designed to have the same ratio of SiO_2 to ($CaO + Na_2O$) as SiO_2 to CaO in calcium metasilicate i.e. 51.8 SiO_2 to 48.2 CaO wt %. The sodium oxide is combined with the calcium oxide as both these oxides act as glass modifiers (19), and it was considered necessary to have at least 50 wt % silica in the glass to give calcium metasilicate and not one of the ternary sodium containing

phases as the primary devitrification product. This composition was successful in that a stable glass block could be quenched from a 50g melt, but after 30 minutes at 990°C the devitrification product was found to be $Na_2Ca_2Si_3O_9$, see table 3.26 and figure 3.88, whilst after 30 minutes at 1030°C β-$CaSiO_3$ was also produced, see table 3.28 and figure 3.39.

RW14 composition, containing 55 wt % silica (see table 2.2) forms a stable, clear and bubble-free glass when cast from about 1430°C onto a cold brass plate and annealed for 1 hour at about 550°C. On heat-treatment of small specimens at a range of temperatures up to 1200°C β-$CaSiO_3$ was the major phase detected from X-ray analysis. Figure 3.40 and table 3.29 give the results of the X-ray analysis of a sample treated at 950°C for 30 minutes and show that the crystallization consists of about 60% β-$CaSiO_3$ and 40% $Na_2Ca_2Si_3O_9$, whereas for another sample heated to 1000°C for 30 minutes only 30% of $Na_2Ca_2Si_3O_9$ together with the β-$CaSiO_3$ primary phase was found, see figure 3.41 and table 3.30. After 30 minutes at 1045°C X-ray analysis of the resultant crystalline material revealed β-$CaSiO_3$ only, i.e. at most 5% of a secondary crystalline phase could be present, see figure 3.42 and table 3.31. A sample maintained at 1250°C for 50 hours gave an X-ray pattern corresponding to that of α-$CaSiO_3$, see figure 3.43 and table 3.32.

The fibres in samples heat-treated below about 1040°C are too fine to be resolved in the optical microscope

(i.e. less than 1 micron in diameter), but it was observed that spherulitic cones are surface nucleated very densely, only about 20 microns apart, and that the number of nucleation sites and the nature of the nucleated phase is the same on the glass/air interfaces as on the glass/alumina powder interfaces whether or not the glass surface had been abraded by the diamond saw used to prepare these samples. At 1050°C the fibres were seen to be 2 microns in diameter and, as expected in fine spherulitic type fibres grown at relatively low temperatures (see section 1.4.2.), they exhibit frequent non-crystallographic branching giving a "feathery" appearance, whereas at about 1100°C the fibres are 5 microns diameter, showing little branching and are within 10 degrees of parallel alignment. Figure 3.43 is an optical micrograph of RW14 material crystallized at 1104°C.

RW14 was selected as a suitable composition for the production of test specimens containing aligned β-$CaSiO_3$ fibres in a predominantly, possibly completely, glass matrix, the tiles from which the specimens were to be sectioned being heat-treated at about 1100°C. This temperature was chosen as that which gave aligned, unbranched fibres whilst still being low enough for the glass tile not to sag too much during heat-treatment as this would have distorted the fibrous material. On sectioning these tiles it was found that the surface nuclei are spaced 50 to 100 microns apart and the cones of fibres impinge about 1mm below the surface allowing only the zones of fibres which

were growing approximately normal to the surface to develop. At the centre of the tiles the two growth fronts, nucleated from the top and bottom surfaces, meet forming an almost flat plane across the tile.

The X-ray data for RW14/2T, RW14/4T and RW14/5T are given in figure 3.44 and table 3.32, figure 3.45 and table 3.33, and figure 3.46 and table 3.34 respectively. These results show that at least 95% of the total crystallization in these tiles consists of β-$CaSiO_3$.

Table 3.24 gives the results of the wet-chemical analyses made on samples of RW14 glass and RW14 crystallized tile. These show that only a small amount, if any, of sodium oxide was lost by volatilization during melt of the batch into glass, but a larger amount of sodium oxide is missing after heat-treatment. This would not be expected as the temperature and duration of the crystallization procedure were both less than those used during glass formation, but the explanation may lie in the fact that the sodium ions are not incorporated into the growing crystals of calcium metasilicate and are therefore concentrated in the residual glass phase. The resultant increased activity of the sodium, and the large ratio of exposed surface to internal volume in the flat tiles, may allow a significant amount of volatilization even at relatively low temperatures. The high alumina content of the tile material is probably due to a layer of the refractory alumina powder used to line the heat-treatment mould adhering to the surface of the tile.

The growth rate of β-$CaSiO_3$ in RW14 over a range of isothermal temperatures was determined by the method described in section 2.3. and a plot of crystal growth rate versus heat-treatment temperature is shown in figure 3.47. From this it can be seen that at the tile heat-treatment temperature, 1100°C, the growth rate is nearly 5 microns per second, i.e. an order of magnitude faster than β-$CaSiO_3$ growth in RW9 composition at this temperature. This reflects the relative ease with which the necessary structural rearrangements prior to incorporation of units into the crystal lattice may occur in the RW14 glass, the network structure of which is broken up by the action of monovalent sodium ions (see section 1.2.).

3.1.7. INTERNALLY NUCLEATED RW14F COMPOSITION:

It was desired to produce an internally nucleated material of similar composition to one of the selected unidirectional materials in order to compare approximately homogeneous physical properties with the highly anisotropic properties of an aligned fibrous structure. Mukherjee and Rogers (44) investigated the nucleation and crystal growth in silicate glasses containing fluorides. In the soda-lime-alumina-silica system, using glass compositions similar to RW14, they found that the nucleation rate showed a sharp maximum at 662°C (see section 1.3.2.) and spherulites consisting of β-$CaSiO_3$ developed on these nuclei when the heat-treatment furnace temperature was increased to 900°C.

RW14F composition was made up by the addition of

calcium fluoride to crushed RW14 glass, together with a sufficient amount of silica to maintain a constant Si to Ca ratio. The nominal, weighed-out RW14F composition contains 3.3 wt % of fluoride ions. This composition was only given one melt at 1400°C for 3 hours in order to minimise the loss of fluorine to the atmosphere, and since the RW14 glass was freshly prepared it therefore had a minimal water content. A tile of RW14F composition was prepared as described in section 2.5.3.

Figure 3.48 and table 3.35 give the results of the X-ray analysis of the RW14F tile, which confirms that the internally nucleated spherulites consist of β-$CaSiO_3$. Figure 3.49 is an optical micrograph of a thin section prepared from the RW14F tile. A section through a spherulite is shown in which a "sheaf-type" of region has developed from the nucleus and which displays the "Maltese-cross" effect under the cross-polarised light, both typical features of spherulitic crystallization. The boundary between two spherulites can be seen to be about 5 microns wide. This region is probably still in the vitreous state since ahead of the growth fronts of each of the developing spherulites was a layer of glass into which the excess constituents not included in the growing crystals had been rejected. Therefore when these growth fronts impinge there is actually a layer of glass between them and since this residual glass composition, resulting from the crystallization of calcium metasilicate in RW14F glass, will be relatively high in silica and alumina it will not

devitrify at the heat-treatment temperature and duration used to produce the RW14F tile. The maximum diameter of the spherulites was found to be approximately 1mm, and the individual fibre diameter 2 microns. Some transcrystallized, surface-nucleated crystallization occurred at the external surfaces of the tile and extended some 1.5mm into the tile. This was also made up of spherulite-type fibres of β-$CaSiO_3$, again about 2 microns diameter, proving that the mechanism of the unidirectional fibrous growth produced from surface nucleation is identical to unrestricted spherulitic growth (see section 1.4.2.).

3.1.8. COMPOSITIONS USED FOR ROD PULLING; RW14, RW15, RW16 AND RW17:

The rod pulling apparatus and the technique for the production of unidirectionally crystallized rods direct from a melt are described in section 2.7.2.

Composition RW14, from which tiles composed of unidirectional β-$CaSiO_3$ fibres were produced (see section 3.1.6.), was found to be unsuitable for the production of rods of aligned β-$CaSiO_3$ fibres from which longitudinal type mechanical test specimens could be machined (see section 2.8.3.). Although this glass could be easily melted at 1450°C in a platinum crucible heated in a muffle furnace, it was found to be necessary to maintain the melt in the platinum collar on the rod pulling apparatus at over 1470°C in order to keep the bottom surface of the melt from crystallizing. When rods were pulled from this melt either using platinum wire or β-$CaSiO_3$ seed

nucleation, and with or without the air blast increasing the temperature gradient down the rod, only rods consisting of α-$CaSiO_3$ crystallization were produced over the range of pulling speeds up to 100 microns per second when, even using a strong air blast to quench the glass as it emerged from the collar, the glass necked off at the bottom of the melt. From the theory of the rod pulling technique (see section 1.4.3.) it should be possible to quench the glass rod pulled out from the melt by a sufficiently fast pulling rate so as to pass through the temperature range in which α-$CaSiO_3$ may nucleate and only allow nucleation to occur at temperatures where β-$CaSiO_3$ is the stable phase. Figure 3.50 and table 3.36 give the X-ray data for a rod pulled from RW14 melt at 52 microns per second and show that any crystallization produced consists entirely of α-$CaSiO_3$. Figure 3.51 is an optical micrograph taken of a thin section from an RW14 rod cut along its long axis. The area shown is the growth front of crystals in the rod which was quenched to room temperature. The α-$CaSiO_3$ has crystallized as spherulitic fibres, indicating that crystal growth, if not nucleation, took place at a relatively low temperature (see section 1.4.2.). (It was found throughout this investigation of the crystallization of calcium metasilicate that once one of the polymorphs had nucleated that particular crystal structure continued to grow, even if it was not the "stable" phase under the prevailing conditions, rather than the structure transform into the "stable" polymorph.) The fibres are about 5 microns in

diameter, are widely spaced and are divergent over 20°. At the end of these fibres growth has continued for a short time whilst the melt cooled and very fine spherulitic fibres have grown, since the spherulite fibre diameter is directly proportional to the growth temperature (65), as explained in section 1.4.2. The fibres had all originated from a hemispherulite which had nucleated at the bottom of the rod. There was no evidence of surface nucleated crystallization on the sides of the rod. Apart from being the wrong phase, i.e. this fibrous material would be not directly comparable to the RW14 β-$CaSiO_3$ fibre material, these RW14 rods have other disadvantages. They are translucent and all show a conchoidal type of fracture surface, typical of a glass (118), indicating a low percentage crystallinity. Only short lengths of rod could be produced, i.e. about 5mm, due to the need to maintain the melt at above 1470°C, a temperature that could only be attained in the platinum heating coil when this was only partially filled with glass, and the α-$CaSiO_3$ fibres did not grow parallel to the long, pulling axis of the rods.

RW15 composition has a lower proportion of silica than RW14 and is a ternary glass containing no alumina, see table 2.2 and figure 3.35. It was hoped that since this composition has a relatively low liquidus, about 1340°C, rods could be pulled out as glass since the melt could be maintained far above the liquidus to avoid any premature crystallization occuring inside the platinum collar.

However, on pulling rods of RW15 composition over a range of speeds it was found that at slow speeds the major phases produced are $Na_2Ca_2Si_3O_9$ and $Na_2Ca_3Si_6O_{16}$ with a small proportion of α-$CaSiO_3$, although the amount of α-$CaSiO_3$ produced increases with the pulling rate. Figure 3.52 and table 3.37 show the results of the X-ray analysis of an RW15 rod pulled at 280 microns per second in which α-$CaSiO_3$ is the primary phase. This suggests that α-$CaSiO_3$ is the first phase to nucleate and grow and is followed by the "soda-phases" which grow more slowly and infill the gaps left between the widely spaced spherulitic fibres.

RW16 composition, see table 2.2 and figure 3.35, is a compromise between 50% silica compositions which have low liquidus temperatures but give "soda-phases" on devitrification, and 55% silica compositions which, in the ternary Na_2O-CaO-SiO_2 system, have too high a melting point to be used in the rod pulling apparatus. This glass behaves very similarly to composition RW14 in the rod pulling apparatus, i.e. α-$CaSiO_3$ was produced as the major crystalline phase at all possible pulling speeds, but in the case of RW16 very small amounts of $Na_2Ca_2Si_3O_9$ and $Na_2Ca_3Si_6O_{16}$ were also produced, see figure 3.53 and table 3.38.

The failure of RW14, RW15 and RW16 compositions to crystallize as β-$CaSiO_3$ even when pulled at very high speeds may lie in the shape of their crystal growth rate (U) versus crystallization temperature (T) curves and in

the temperatures of their maximum rates of crystal growth. Figure 3.54 illustrates two types of U versus T curves. Curve A may represent the crystal growth rate characteristics in soda-lime-silica glasses, as a curve of this shape was found by Swift (132) for the crystallization of β-$CaSiO_3$ from a soda-lime-silica glass in which some of the silica had been replaced by alumina. In this curve the temperature of the maximum growth rate is above the α/β transition temperature, and the slope of the crystal growth rate curve is steep as it approaches the liquidus, Tm. Due to the fast α-$CaSiO_3$ growth rate at temperatures only just below Tm, then as the cold pulling wire, or seed crystal, entered the melt prior to pulling out a rod sufficient heat was extracted from the melt to cool the lower part of the melt (the coolest area of the collar anyway) below Tm and therefore for α-$CaSiO_3$ to crystallize inside the collar. On examination of these rods pulled using a β-$CaSiO_3$ block seed crystal it is found that the end of the block is covered by a thin layer of glass, quenched as the cold block was placed into the melt, and this negated the nucleation properties of the seed. As the wire or seed comes into contact with the surface of the melt in the bottom of the collar the surface tension in the melt surface pulls down some of the molten glass below the bottom of the collar, and this would also act to cool the melt below Tm. Once α-$CaSiO_3$ has nucleated, as a hemi-spherulite across the bottom of the emerging rod this phase will continue to grow however fast the pulling

rate since the transition temperature is below the maximum growth rate, as the experimentally determined U versus T curve for RW14 composition shows, see figure 3.47. When the pulling rate exceeds the maximum growth rate the button-shaped crystalline region, i.e. the α-$CaSiO_3$ crystallized inside the collar, stops growing and the rod pulls out as a glass. The above hypothesis is supported by the observation that there is no glassy region visible between the bottom of the collar and the crystal growth front in the rod, i.e. the rod was not quenched to a glass and subsequently crystallized as would be expected from the theory behind the rod pulling technique (see section 1.4.3.).

The problem of the extra high liquidus temperature of the RW14 composition when this was melted in the platinum collar was solved when some RW14 rods were ground, mixed and analysed by wet-chemistry, see table 3.24. From this it was found that only half the nominal, weighed-out amount of sodium oxide was present after the RW14 composition had passed through the rod-pulling apparatus. This was probably due to loss by volatization while the melt was in the collar when the high temperature and the large surface area to volume ratio would aid this process.

Curve B in figure 3.54 shows the type of behaviour required to pull rods containing β-$CaSiO_3$ fibres. On this curve the α/β transition temperature is higher than the temperature corresponding to the maximum growth rate so that rods pulled faster than a certain critical rate will crystallize in the β-$CaSiO_3$ region. Curve B has a

relatively gentle slope near the liquidus, i.e. the α-$CaSiO_3$ growth is not significant until the melt is substantially undercooled, and therefore if the nucleating wire or seed crystal is only kept in the bottom of the melt inside the collar for the minimum time necessary to break the surface tension skin on the melt, so that a surface tension link to the wire or seed is formed via which the rod may be pulled, then the melt will not be sufficiently chilled for α-$CaSiO_3$ to nucleate and grow. This would be helped by using a glass with a relatively low liquidus temperature so that the melt could be substantially superheated.

Maries and Rogers used a composition in the CaO-ZnO-SiO_2 system for the production of 1mm diameter rods containing a parallel array of fibrous β-$CaSiO_3$ aligned along the rod axis and in which there is no evidence of side surface nucleation (76). They found that a glass composition corresponding to RW17 in table 2.2 possesses the required growth rate/temperature characteristics, i.e. curve B in figure 3.53, by a hot stage microscopy investigation of the crystallization kinetics of various compositions in the calcium metasilicate phase region of this ternary system. The location of RW17 on a liquidus projection of the CaO-ZnO-SiO_2 system is shown in figure 3.55, from which it can be seen that the liquidus of this composition is about 1340°C.

When RW17 glass was used in the rod-pulling apparatus it was found that three types of crystallization could be

obtained depending on the pulling rate used, whether a platinum wire or β-$CaSiO_3$ seed crystal was used as the nucleating agent and on the temperature gradient below the collar (i.e. whether the air blast was used or not, and if used on what air flow rate was employed). A series of experiments were performed using either a seed crystal held in place by a Pt/Pt13% Rh thermocouple, the junction being positioned just below the top of the β-$CaSiO_3$ block, or the thermocouple on its own as the nucleating medium. The thermocouple was connected to a penchart recorder which allowed the cooling rate in the rod to be measured, and since RW17 quenched to a glass below the collar prior to crystallization, the moment of the appearance of the initial crystal growth could be marked on the chart so that an approximate value of the crystallization temperature for a particular set of conditions could be obtained. The accuracy of this technique depends on the rate of pulling, since at high pulling speeds the temperature recorded via the thermocouple falls very quickly while as the speed decreases the crystal growth front approaches the bottom of the collar, the glare from which makes it more difficult to identify the onset of crystallization. From the chart recorder output thermocouple temperature versus time plots were drawn. Figure 3.56 shows a series of typical results obtained from pulling at various speeds using the seed crystal but without an air blast. It was generally found that two slopes could be drawn for the cooling rate, the initial slope, which increased rapidly

as pulling rates increased, and a gentler slope, less dependent on pulling speed, corresponding to the crystallized rod slowly cooling to room temperature. Table 3.39 gives the results of this investigation.

For nucleation on the thermocouple wires only two major phases were produced. In samples pulled at 40 microns per second, or less, without an air blast, α-$CaSiO_3$ was the primary phase together with $Ca_2ZnSi_2O_7$ (a synthetic analogue of the mineral hardystonite), the proportion of the secondary phase increasing as the pulling rate decreases. Figure 3.57 and table 3.40 show the X-ray analysis of the RW17/a rod, see table 3.39, pulled on a thermocouple at 19 microns per second, in which 60% of the total crystallization is α-$CaSiO_3$ and the remaining 40% $Ca_2ZnSi_2O_7$. Between 40 and 50 microns per second β-$CaSiO_3$ is the major phase but there is still a large amount of α-$CaSiO_3$ and a small amount of $Ca_2ZnSi_2O_7$ present, as shown in figure 3.58 and table 3.41 for rod RW17/i, see table 3.39, in which 60% of the total crystallization consists of β-$CaSiO_3$, 30% α-$CaSiO_3$ and 10% $Ca_2ZnSi_2O_7$. Above 50 microns per second (at 50 with an air blast of 2000cc per minute, rod RW17/1) the cooling rate was sufficiently fast to quench the rod to a stable glass. From the results listed for rods RW17/a to RW17/1 inclusive in table 3.39 a T-T-T (time-temperature-transformation) diagram was constructed for RW17 rod crystallization nucleated on thermocouple wires, see figure 3.59. Pulling rates less than about 20 microns per second were not

investigated.

Nucleation on a β-$CaSiO_3$ seed in addition to a Pt/Pt 13% Rh thermocouple was more successful in producing rods which are mainly composed of β-$CaSiO_3$. At pulling rates greater than about 70 microns per second the rods quench to a stable glass, but at speeds between 70 and 25 microns per second crystalline rods were produced in which the primary phase is β-$CaSiO_3$ together with a lesser amount of $Ca_2ZnSi_2O_7$ which must exist as very small crystals since the lines in the X-ray analyses of these rods corresponding to this minor phase are very diffuse, i.e. the line broadening effect produced by very small crystals (120). Figure 3.60 and table 3.42 give the X-ray analysis for RW17/s rod pulled at 50 microns per second, see table 3.39, from which it is found that 90% of the total crystallization consists of β-$CaSiO_3$ together with 10% of $Ca_2ZnSi_2O_7$. The proportion of $Ca_2ZnSi_2O_7$ in the crystallized rods is inversely proportional to the pulling rate. Between 25 and about 15 microns per second the primary phase produced is α-$CaSiO_3$, but now a substantial amount of $Ca_2ZnSi_2O_7$ is also present. Figure 3.61 and table 3.43a give the X-ray data for rod RW17/n, see table 3.39, in which only half the total crystallization is α-$CaSiO_3$. To investigate the crystallization of the $Ca_2ZnSi_2O_7$ phase, rods were pulled at rates as low as 10 microns per second. The results of the X-ray analysis of RW17/m, see table 3.39, are given in figure 3.62 and table 3.43b and correspond to the pattern for hardystonite, figure 3.6 and table 3.6,

except that all the dÅ spacings are shifted to larger values. This approximately 10% increase in dÅ spacing was not found in the $Ca_2ZnSi_2O_7$ crystallized in association with calcium metasilicate, therefore the larger unit cell found when only the "zinc phase" crystallized may have been due to the solid solution of excess calcium ions, by Vegard's rule (120a, p. 174), since the RW17 composition is calcium rich compared to $Ca_2ZnSi_2O_7$. Hardystonite has the melilite type of structure, see section 1.5.2., the crystal structure of the åkermanite-gehlenite solid solution series and therefore known to be capable of substantial replacement in the lattice. Figure 3.63 is an optical micrograph of rod RW17/m which shows that the $Ca_2ZnSi_2O_7$ crystallized in the form of layers of elongated laths, the long axis aligned parallel to the pulling axis. There appears to be a high percentage crystallinity.

From the results listed for rods RW17/m to RW17/u inclusive in table 3.39 a T-T-T diagram was constructed for RW17 rod crystallization nucleated on a β-$CaSiO_3$ seed, see figure 3.64. Comparison of this diagram with figure 3.59, the T-T-T diagram for nucleation on platinum wire, reveals that nucleation and growth of β-$CaSiO_3$ can occur over a wider range of pulling speeds when a seed is used. This may be another example of the unstable phase developing if already nucleated, i.e. the β-$CaSiO_3$ phase will grow at low pulling rates and at correspondingly higher temperatures (above the transition temperature) in the presence of a block of this phase. Since this block

was orientated with the fibre axis parallel to the rod pulling axis the new fibres could grow directly from those in the seed. The fact that the seed blocks were cut from RW14 composition tiles was an advantage in that RW14 has a higher liquidus temperature than RW17 and therefore the blocks did not melt in the brief time that they were in contact with the molten glass.

One problem that occurred with both types of nucleating agent was the formation of cracks across the rods just above the nucleation region. These were probably the result of thermal shock as the rods were subjected to a sharp temperature gradient below the collar and at high pulling speeds the cooling rates of the interior of the rods were very rapid (see figure 3.56). Around the nucleus a misaligned region of crystallized material was formed until transcrystallization (see section 1.4.2.) and the enforced temperature gradient down the rod allowed only those fibres or dendrites aligned parallel to the pulling axis to grow. In this disordered region anisotropic thermal expansion coefficients set up internal stresses during cooling and when these stresses exceeded the fracture stress cracks were formed.

In RW17 rods the β-$CaSiO_3$ phase always forms spherulitic type fibres whilst α-$CaSiO_3$ always grows as dendrites with well developed secondary arms. This is in contrast to the RW14 rods in which α-$CaSiO_3$ forms spherulitic fibres and is evidence that this phase grows at relatively low temperatures in that glass but in RW17

it crystallizes in its usual temperature range i.e. between the transition temperature and the liquidus, (see section 1.4.2.).

In order to minimise the thermal shock to which the rods are subjected after crystallization it was decided to use the slowest pulling speed at which β-$CaSiO_3$ can be reliably obtained for the production of rods from which longitudinal mechanical test specimens could be cut (see section 2.8.3.). No air blast was used as this introduces additional thermal gradients in the cooling rods, and increases the severity of the temperature gradient below the collar, and seed nucleation was employed so as to obtain the low temperature polymorph at a slow pulling speed. It was found that 30 microns per second is the best speed for the production of uncracked rods containing a parallel array of β-$CaSiO_3$ fibres. Figure 3.65 is an optical micrograph of a section from a typical rod showing the fibres to be evenly spaced and about 15 microns in diameter. Since RW17 has a relatively low liquidus temperature, see figure 3.55, the collar could easily melt a full load of glass and therefore rods nearly 15mm long could be grown, but as some cracking and disordered growth occurred in the bottom 4mm of the rods the maximum length of aligned growth was about 11mm.

Using the same conditions as in the growth of RW17/30β rods but substituting a wire nucleus for the seed rods containing aligned dendrites of α-$CaSiO_3$ were obtained and so RW17/30α rods were grown and longitudinal test specimens

cut out from them. In this way the physical properties of two materials of the same chemical composition and prepared under the same conditions, except that the α-$CaSiO_3$ phase crystallizes at a higher temperature i.e. the growth front is nearer the bottom of the collar, one consisting of aligned fibres and the other aligned dendrites, may be compared. Figure 3.66 is a micrograph showing the dendritic structure in a typical RW17/30α rod. The primary dendritic spines are about 15 microns diameter, spaced at about 75 microns and are aligned parallel to the pulling axis. The secondary arms emerge at right angles to the primary spine, are approximately 5 microns in diameter and are regularly spaced at 10 microns intervals.

All the rods contain some $Ca_2ZnSi_2O_7$ as a secondary phase, but this is in too fine a dispersion to be visible in the micrographs since its X-ray diffraction pattern shows the effects of line broadening due to a very small crystal size (120). This secondary phase probably nucleates on the calcium metasilicate fibres or dendrites in a manner similar to that of the secondary phase produced in RW9 composition devitrified material, see figure 3.32. As less $Ca_2ZnSi_2O_7$ is formed the faster the pulling rate it may be assumed that the maximum growth rate for this phase occurs close to the liquidus temperature (q.v. RW17/m in table 3.39) and therefore its growth rate decreases with decreasing crystallization temperatures, or that a certain induction time is required for the nucleation of this phase (133) and as the cooling rate (pulling rate) increases

the time spent in the critical temperature region decreases and less nuclei form. Since the interior of the rod cools more slowly than the exterior the effect of increasing the pulling rate is a slow decline in the amount of $Ca_2ZnSi_2O_7$ formed, not a sharp cut-off at one particular rate.

A chemical analysis was performed on a mixture of RW17/30α and RW17/30β rod material and the result is given in table 3.24. This shows that there is a small zinc oxide content loss during rod pulling, caused by volatilization of zinc vapour from the melt whilst it was held above its liquidus in the heated platinum collar.

Figure 3.67 is a crystal growth rate against temperature plot for the growth of seed nucleated β-$CaSiO_3$ in rods pulled from RW17 melts.

3.1.8.1. Pinhole Transmission X-Ray Analysis of RW17 Rods:

The fibres produced in β-$CaSiO_3$ RW17 rods were sufficiently long to be investigated using the pinhole transmission X-ray diffraction technique (see section 2.4.2.). It was found that a 1mm diameter bundle of fibres could be obtained from a lightly crushed rod. Diffraction patterns were also obtained of fibre bundles from a sample of wollastonite from Meldon, Devon (BM 1913, 253) obtained from the British Museum (Natural History).

The mean radius of the strongest reflection was measured for each set of patterns corresponding to each material, i.e. the distance from the centre of the pattern

to darkest diffraction spot (actually, since there is 4-fold symetry in these patterns, half the mean of the two diameters was used), see figures 3.68, 3.69 and 3.70 (tracings made from the negative films).

The diffraction angle of each diffraction spot may be determined by (120, page 535):

$$2\Theta = \tan^{-1} \frac{R}{D}$$

where:

Θ = diffraction angle (Bragg angle)

R = radius of the diffraction ring

D = specimen-to-film distance.

Since the exact specimen-to-film distance is unknown it was found using the radius of the most intense diffraction spot of wollastonite (310) and the corresponding diffraction angle obtained from the ASTM index (121). Having established the mean value of D for the patterns from each material this may be substituted in the above expression to index the corresponding set of patterns, see table 3.44.

From figures 3.68, 3.69 and 3.70 it can be seen that a series of strong reflections are arranged in a horizontal line across the diameter of the pattern i.e. the equatorial reflections. When these reflections were indexed, see table 3.44, it was found for each material that they corresponded to the {h 0 l} axis, i.e. the crystallographic b-axis. From the theory of fibre texture X-ray patterns (120) it is known that the equatorial reflections correspond to the vertical (rotation) axis of the specimen, therefore

the b-axis of both the wollastonite and synthetic RW17 rod specimens corresponds to the fibre axis. This is in agreement with the known crystallography of the wollastonite structure, see section 1.5.1.

Comparison of the patterns shown in figures 3.68, 3.69 and 3.70 reveals that the parallel alignment of the fibres, i.e. the sharpness of the equatorial diffraction spots, is better in the synthetic, directionally crystallized RW17 rods than in the sample of the natural mineral examined.

3.2. GROWTH KINETICS OF RW9, RW14 AND RW17 COMPOSITIONS:

3.2.1. ACTIVATION ENERGIES FOR CRYSTAL GROWTH FOUND USING ARRHENIUS PLOTS:

The apparent activation energy for crystallization of each of the glasses was calculated using the Arrhenius equation (17)

$$U = A \exp(-E_a/RT)$$

where:

U = the crystal growth rate at temperature T

A = a constant for a particular glass

R = the gas constant

E_a = the apparent activation energy, related to the activation energy required for the transportation of structural units from the melt into the crystal lattice (i.e. related to $\Delta G'$ in the Turnbull-Cohen equation, see section 1.4.1.).

Therefore the value of E_a could be found from the slope of a ln U versus 1/T plot.

Figure 3.71 shows log U versus 1/T plots for crystallization in RW9, RW14 and RW17 glasses. These were constructed from the crystal growth rate data given in tables 3.45, 3.46 and 3.47 respectively, and the U versus T curves for these glasses are shown in figures 3.22, 3.47 and 3.67 respectively. The accuracy of the measured growth rates depends on the heat-treatment method used. For the RW17 glass the growth rate of seed nucleated β-$CaSiO_3$ produced by the rod pulling technique equalled the pulling speed used (see section 1.4.3.) and, even at high speeds (about 60 microns per second), this could be found to within $\pm$ 1 second and $\pm$ 10 microns, i.e. within $\pm$ 0.5%. For RW9 and RW14 glass the growth rates were found by the method described in section 2.3., and since the exact time required to heat the blocks was not known and the sections may not have been taken exactly at right angles to the nucleating surfaces the 95% estimated error is $\pm$ 3% for the samples with the fastest growth rates. For the samples with relatively slow crystal growth rates, i.e. less than 0.1 micron per second, the duration of the heat treatments was sufficiently long to make the error in timing almost negligible and therefore the overall error was reduced to approximately $\pm$ 1%. The temperature measurement for the RW9 and RW14 static furnace samples was accurate to within $\pm$ 0.25%, but for the rod pulling technique used with the RW17 composition glass the temperature of the crystal growth front could only be estimated and therefore the error is approximately $\pm$ 2%.

The growth rates quoted in tables 3.45, 3.46 and 3.47 are the mean values of at least three measurements.

Table 3.48 gives the values of the slopes found from the log U versus 1/T plots and, for RW9 and RW14 compositions, the corresponding values of E_a found using

$$E_a = 2.303 \times \text{slope} \times R$$

The log U versus 1/T, see figure 3.71, plot for RW17 rods has a positive slope and would give a "negative activation energy" (a meaningless concept) when substituted into the Arrhenius equation. This is due to the fact that in the rod pulling technique crystallization occurs at temperatures above that corresponding to the maximum crystal growth rate (see section 1.4.3.), i.e. in the region of the U versus T curve where the magnitude of the free energy difference between the glassy and crystalline states controls the growth rate (see section 1.4.1.). Therefore the crystallization temperature in the RW17 rods decreases as the crystal growth rate increases, see figure 3.67. The energy value found for RW17, -147 kJ mol^{-1}, is related to the thermodynamic free energy term in the Turnbull-Cohen equation (see section 1.4.1.) but it contains a contribution from the kinetic term (activation energy) as the growth rates at very low undercoolings, where the kinetic term is negligible, could not be measured since α-$CaSiO_3$ is the phase produced at crystallization temperatures close to the liquidus.

The log U versus 1/T plots for RW9 and RW14 compositions, see figure 3.71, have negative slopes from which the

positive E_a values were calculated. From these results it can be seen that the "activation energy" required for the growth of α-$CaSiO_3$ from RW9 composition glass is only half that necessary for β-$CaSiO_3$ growth, which substantiates the reason proposed in section 3.1.5. to explain the more rapid growth rate of the high temperature modification. The comparative ease with which $Si_3O_9^{6-}$ groups, pre-existing in glasses of this type of composition (29, see section 1.2.), can join the α-$CaSiO_3$ crystal structure is due to the fact that no strong bonds need to be broken; only reorientation of these groups prior to incorporation into the crystal lattice is necessary. The pseudowollastonite crystal structure is made up of layers of $Si_3O_9^{6-}$ and Ca^{2+} ions in approximately hexagonal arrangements (134, see section 1.5.1.). Since calcium metasilicate has a higher percentage of calcium ions than RW9 composition glass (see table 2.2), these ions must diffuse through the glass to the crystal growth front. The activation energy for the diffusion of calcium ions through calcium aluminosilicate glasses varies between about 117 and 294 kJ mol^{-1} (45) and the E_a value for the growth of α-$CaSiO_3$ from RW9 glass is 160 kJ mol^{-1} which suggests that the diffusion of calcium is the major barrier to the advancement of the crystal growth front.

For β-$CaSiO_3$ growth from both RW9 and RW14 compositions the apparent activation energies, 319 kJ mol^{-1} and 383 kJ mol^{-1} respectively, are high and are in the same range of values as those obtained from studies of viscous flow in glasses

near their crystallization temperatures (116). Therefore for the growth of a wollastonite type of crystal lattice in a glass of approximately metasilicate composition strong Si-O bonds have to be broken and reorientated in order to build up the "Dreierketten" chain structure (84, see section 1.5.1.). The value found for RW9 is in good agreement with the value of 280 kJ mol^{-1} found by Williamson (17) for the crystallization of a glass of similar composition.

3.2.2. DIFFUSION ENERGY FOR SPHERULITIC CRYSTALLIZATION:

The Keith and Padden theory (65) relates the rate of growth of a spherulite fibre (U) to the stable diameter of the fibre (δ) and the "diffusion coefficient for impurity in the melt" (D), i.e.

$$\delta = D/U$$

By "impurity" is meant any constituent which appears in the crystal and melt at different concentrations and therefore must be transported towards, or away from, the crystal growth front through the melt. In the case of calcium metasilicate crystallization from RW9, RW14 or RW17 composition glasses all the constituents appear in different concentrations in the two states and therefore the rate determining step (the slowest process) of the transportation process is the diffusion of silicon through the melt. (The diffusion coefficients of calcium, aluminium and silicon through a calcium aluminosilicate slag have been found to be in the ratio 1:4:10 respectively (20)). Since the diffusion of silicon through a silicate

glass involves reorganization of the silica tetrahedra, including breaking the strong Si-O bonds, this could be regarded as analogous to viscous flow.

Diffusion is an activated process and can be represented by an Arrhenius type of equation

$$D = B \exp(-E_D/RT)$$

where:

B = a constant for a particular material

E_D = apparent activation energy for diffusion.

Therefore the value of E_D can be calculated from the slope of a log D versus 1/T plot, and D can be calculated knowing the rate of spherulitic growth and the width of the fibres produced at that growth rate. Tables 3.49, 3.50 and 3.51 give the spherulitic growth data for the crystallization of β-$CaSiO_3$ from RW9, RW14 and RW17 glasses respectively, and figure 3.72 shows the log D versus 1/T plots drawn from this data. The slopes of these plots and the calculated "diffusion" energies are given in table 3.48.

An apparent activation energy could be found for RW17 using this method, i.e. the log D versus 1/T plot for RW17 has a negative slope. This is a result of the spherulite fibre width decreasing rapidly with the temperature of crystallization (65) and dominating the growth rate term (T decreases as U increases for rod pulling) so that the calculated diffusion coefficients decrease with decreasing crystallization temperatures which, of course, corresponds to the known diffusion behaviour in glasses (20).

The calculated "diffusion" energy values for all three compositions, see table 3.48, fall in the activation energy range corresponding to viscous flow (116), or the diffusion of silicon through a silica network (q.v.). The results for RW9 and RW14 are somewhat higher than the corresponding apparent activation energies for crystal growth but, since these calculated energies are very dependent on the slopes chosen for the Arrhenius plots, they are close enough to enable the two energies to be approximately equated. Both the crystal growth and diffusion energies are therefore due to the necessity for the silica tetrahedra structure in the glass to be broken up prior to the incorporation of the tetrahedra into the growing crystal. This equality could be taken as a verification of the validity of the Keith and Padden theory (65) for spherulitic growth from silicate glasses.

The "diffusion" energy for the RW17 composition is less than the other glasses which were crystallized isothermally as blocks or tiles. In the rod pulling technique used with RW17 the melt ahead of the growth front is at a higher temperature than the crystallization temperature since it is nearer the bottom of the hot platinum collar. This means that the melt ahead of the growth front in a rod is less viscous and can allow correspondingly more rapid structural rearrangements at lower activation energies than the glass ahead of the crystals in isothermal growth which, of course, is maintained at the crystallization temperature.

3.3. MICROSTRUCTURES OF SELECTED MATERIALS:

3.3.1. DENSITIES:

Table 3.52 gives the mean densities found from samples of each of the three compositions from which test specimens were prepared. The densities were measured by the standard displacement of water technique, using a balance accurate to 0.001g.

All the crystallized materials show a small decrease in density compared to the parent glasses. The density of a glass-ceramic is an additive function of the densities of the various crystal and glass phases present (10), and therefore if the volume increases during crystallization this does not necessarily indicate that voids are developing since this volume increase could be due to the production of crystals of lower density than the original glass. Porosity does not usually develop during the formation of internally nucleated glass-ceramics since the overall volume changes are very small and the final grain size is only about 1 micron. However there is evidence, from the manner in which these materials fracture (see section 3.5.), that there are cracks running along the fibre/matrix (residual glass or secondary crystallization) interface in the unidirectionally crystallized materials, probably formed during cooling from the fabrication region. In these fibrous structures this interface area is large and therefore even extremely narrow cracks may make significant contributions to the total volume of material. The internally nucleated RW14F

tile material has the same density as the unidirectional RW14 tiles, which would indicate that these cracks also form inside the spherulites which make up this material.

The crack theory is supported by the fact that the RW17/30α rods have approximately the same density as RW17 glass and their mode of fracture does not indicate the presence of dendrite/matrix interfacial cracking. Since the measured density of wollastonite is 2.88Mg m^{-3} (calculated density 2.96Mg m^{-3}) and the measured density of pseudowollastonite is 2.912Mg m^{-3} (calculated density 2.90Mg m^{-3}) (135), then as one of the calcium metasilicate modifications is the predominant phase in all the materials in table 3.52, the density of the crystallized materials should have been of the order of 2.9Mg m^{-3}.

3.3.2. ELECTRON PROBE MICROANALYSIS OF RW9 MATERIALS:

Only the RW9 crystalline materials had a sufficiently coarse microstructure for the EPMA technique to give meaningful results. Specimens were prepared as described in section 2.10.1. Figure 3.73 is a reflected light photomicrograph of a prepared intracrucible material (RW9/7C) specimen, in which the β-$CaSiO_3$ fibres appear as the light grey phase.

Table 3.53 gives the results of the analyses, together with the calculated percentage composition of the parent glass, and wollastonite and anorthite (127), the mineral analogues of the synthetic phases identified by X-ray analysis as being present in RW9 devitrified

materials. The EPMA analyses of the fibres are in good agreement with the composition of wollastonite and show that there may be some small amount of solid solution with zinc ions. The interfibre analyses, however, do not correspond to the composition of anorthite, but this can be explained by two reasons. Firstly the volume available for analysis was much smaller for the interfibre material than for the fibres which are about 60 microns in diameter but are spaced so as to leave an interfibre region only about 20 microns across, i.e. near the limit of resolution of this analytical technique. Secondly the interfibre region not only contains $CaAl_2Si_2O_8$ crystals but also residual glass which, from a consideration of the compositions and proportions (see section 3.3.3.) of the crystalline phases formed from RW9 glass, should consist mainly of silica and zinc oxide.

3.3.3. VOLUME FRACTIONS OF PHASES PRESENT IN SELECTED MATERIALS:

Table 3.54 gives the results obtained from the modal analyses made on sections taken from bend test specimens, see section 2.12.

Figures 3.74, 3.75, 3.76, 3.77, 3.78 and 3.79 are high magnification optical micrographs of RW9 tile, RW9 intracrucible, RW14 tile, RW14 internally nucleated, RW17/30β rod and RW17/30α rod material respectively. These materials are described in detail in sections 3.1.5., 3.1.6., 3.1.7. and 3.1.8.

3.4. THERMAL EXPANSION CHARACTERISTICS OF SELECTED MATERIALS:

The thermal expansion coefficients were found using an automatic recording dilatometer as described in section 2.11. The results were measured off the pen chart recorder output and the percentage expansions and expansion coefficients, with the associated errors, were calculated as described in appendix I. Graphs of percentage expansion versus temperature and expansion coefficient versus temperature were plotted for each type of specimen tested. Unidirectionally crystallized materials were tested both parallel to the fibre (or dendrite) axis (longitudinal specimens) and perpendicular to the fibre axis (transverse specimens) if the dimensions of the bulk material allowed suitable specimens to be machined.

To calibrate the dilatometer the thermal expansion of "spec-pure" silver was measured, see table 3.55 and figure 3.80. The coefficient of expansion was found to be $20.35 \times 10^{-6} K^{-1}$ (20 to 650°C) which is within 1.5% of the tabulated value of $20.6 \times 10^{-6} K^{-1}$ (0 to 500°C) (136).

3.4.1. WOLLASTONITE MINERAL:

Wollastonite has a triclinic crystal structure and forms orientated aggregates and therefore is likely to exhibit anisotropic thermal expansion (96), but values quoted in the literature for the linear thermal expansion coefficient of wollastonite do not specify the orientation measured or the form of the temperature dependence. It was therefore necessary to measure thermal expansion

characteristics of wollastonite, see enclosed paper "Anisotropic thermal expansion characteristics of wollastonite", by Weston, R.M. and Rogers, P.S. (137).

Table 3.56 and figure 3.81 show the results calculated for a wollastonite transverse specimen and table 3.57 and figure 3.82 the results for a longitudinal specimen. The sample of mineral from Meldon, Devon (BM 1913, 253) in the form of an aggregate of parallel fibres was obtained from the British Museum (Natural History). It can be seen that the longitudinal specimen, i.e. along the fibre axis, shows a linear increase in dimension with temperature, but for the transverse specimen the rate of expansion increases with increasing temperature. Therefore the longitudinal specimen has an approximately constant expansion coefficient over the range 20 to 650°C but the transverse specimen has a coefficient which increases linearly with temperature over this temperature range. It can be seen from the tabulated results that the transverse coefficient rises from a value below the longitudinal coefficient at room temperature to one above it at 650°C, the expansion anisotropy of wollastonite reversing at 300°C. The larger errors associated with the results for the transverse specimen are a result of the shorter length of this specimen (determined by the dimensions of the mineral sample), the less rigid crystallographic orientation in this specimen, and the effect of inter-fibre grain boundaries. For both specimens the "up" and "down" measurements were so close that they were amalgamated.

The factors influencing the thermal expansion behaviour of silicate structures are discussed in section 1.6. From this it would appear that the expansion along the wollastonite fibre axis is controlled by the rate at which the angles of tilt between the silica tetrahedra making up the chain structure changes (95), whereas perpendicular to the fibre axis the influence of the calcium ions present between the silica tetrahedra chains may determine the magnitude of the expansion coefficient and therefore the expansion anisotropy (96).

3.4.2. RW9 COMPOSITION MATERIALS:

Table 3.58 and figure 3.83 show the thermal expansion characteristics of RW9 glass after annealing at about 650°C. From the point of intersection of the slopes of the two linear regions on the percentage expansion versus temperature graph it was found that the glass transition temperature (Tg) of this glass is about 475°C and the dilatometric softening temperature (Ts), i.e. the temperature at which the glass becomes sufficiently soft to yield under the pressure of the thrust-rod, is 760°C. The thermal expansion behaviour of glasses is discussed in section 1.6.1.

Only the "up" (see appendix I) mV values could be measured for the glass specimens which softened since the expansion trace went off the chart above the softening temperature and therefore no trace could be recorded whilst the temperature decreased.

The thermal expansion coefficient of a glass is an

approximately additive property and, over the range of temperatures in which the expansion increases linearly with temperature, the coefficient of linear expansion for a multicomponent glass may be calculated by the means of the equation (138)

$$\alpha = (a_1p_1 + a_2p_2 + ... + a_np_n)/3$$

where:

p_1, p_2, ... p_n are the percentages by weight of the various components,

a_1, a_2, ... a_n are the constants for the various oxides. Several authors have proposed values for these constants but for this study the factors proposed by Hall (139) were used, since these allow the value for silica to vary with the proportion of silica in the glass and have been found to be in good agreement with the experimental results on sodium-calcium aluminosilicate glasses (140). Using this method to calculate the expansion coefficient of RW9 glass (composition given in table 2.2) the value $7.8 \times 10^{-6} K^{-1}$ was obtained which is somewhat higher than the experimental result for the coefficient between 20 and 400°C (below Tg) of $6.9 \times 10^{-6} K^{-1}$.

RW9/3T tile crystallized material (see sections 2.5 and 3.1.5.) was used to produce transverse type dilatometry specimens. The results obtained from these specimens are given in table 3.59 and figure 3.84. It can be seen that like the results from a transverse wollastonite specimen the expansion coefficient increases with increasing temperature, however for this multiphase material the rate of increase increases at higher temperatures.

The thermal expansion coefficient of anorthite has been reported as $4.5 \times 10^{-6} K^{-1}$ (100 to 200°C) (141), and a synthetic analogue exists as a secondary phase in RW9 tiles (see section 3.1.5.). The magnitude of the expansion coefficient perpendicular to a unidirectional fibre axis should be an additive property. Therefore for RW9/3T material, using the volume percentage of phases found by modal analysis (see table 3.54) and only considering the two major phases present, i.e. β-$CaSiO_3$ fibres and $CaAl_2Si_2O_8$ matrix, at 650°C the calculated composite expansion is

$$\alpha_{20 \rightarrow 650°C} = \frac{(7.8 \times 62) + (4.5 \times 26)}{(62 + 26)} \times 10^{-6}$$

$$= 6.8 \times 10^{-6} K^{-1}$$

This is somewhat higher than the experimental result for RW9/3T transverse

$$\alpha_{20 \rightarrow 650°C} = 6.2 \times 10^{-6} K^{-1}$$

(The coefficient at 650°C was chosen as this is the most accurately determined result, i.e. has the lowest percentage error). At 100°C the experimentally determined coefficient, $4.7 \times 10^{-6} K^{-1}$ is very close to that for the matrix phase only. These results may be explained by considering the state of the fibre/matrix interfaces in RW9 tile material which has been cooled from the fabrication temperature. Since at high temperatures the expansion coefficient of wollastonite is approaching twice that of anorthite this is a case when on cooling the fibre/matrix interface is put into tension (see section 1.7.2. on the properties of ceramic matrix unidirectional composites) and may fracture and open out on further cooling to form a crack. Therefore

on reheating this material initially the transverse expansion of the fibres only fills these cracks and the bulk transverse expansion measured corresponds to the matrix material only. As some of the cracks are closed the bulk expansion coefficient increases with temperature as the contribution from the relatively high expansion coefficient fibres increases. However since the fabrication temperature of RW9/3T tile was 1180°C and the dilatometry measurements only went to 650°C it is possible that not all the cracks were closed at this temperature and this would explain the discrepancy between the measured and calculated coefficients at 650°C.

RW9 devitrified material must contain a small amount of residual glass (see section 3.1.3.), but since there is no indication of the material softening at 650°C there is either only a very minor proportion present or it has a high softening temperature and therefore it would be unable to compensate for the large difference in the expansion coefficients of the fibres and matrix.

The results for RW9/7C longitudinal type specimens, given in table 3.60 and figure 3.85, are very similar to those found for the RW9/3T transverse specimens. This intracrucible material is a coarser, less exactly aligned fibrous material than tile type crystallized products and has a low volume percentage of fibres (only 46%, see table 3.54). Therefore the effect of cracks at fibre/matrix interface may also control the expansion behaviour of this material since the expansion could not be measured along a

unique fibre axis.

3.4.3. RW14 COMPOSITION MATERIALS:

Table 3.61 and figure 3.86 give the results of the dilatometric investigation of RW14 glass which had been annealed at about 650°C. The glass transition temperature (see section 1.6.1.) is found to be around 450°C and the dilatometric softening temperature 720°C.

The theoretical expansion coefficient, below Tg, was calculated (see section 3.4.2.) as $9.6 \times 10^{-6} K^{-1}$ which is in agreement with the range of values found experimentally for expansion below Tg. The expansion coefficients found for RW14 glass are generally higher than the coefficients of RW9 composition due to the presence of sodium oxide in RW14 composition (see table 2.2), a component of large atomic volume known to increase the thermal expansion of silicate glasses greatly (138).

The results obtained for RW14/2T tile material transverse specimens show the effect of a glass matrix (this material does not appear from X-ray analysis to give any crystalline secondary phase), see table 3.62 and figure 3.87. The thermal expansion behaviour shows a glass transition temperature at 465°C and the material just starts to soften at 650°C. The probable composition of the residual glass was calculated knowing the starting composition of RW14 glass, the composition of calcium metasilicate and assuming that all the calcium oxide in RW14 was incorporated into the crystallized fibres after devitrification, i.e. 35 wt % in RW14 is equivalent to

47 wt % in the calcium metasilicate fibres.

RW14 composition:		Average wollastonite mineral:
5.0	Na_2O wt %	0.05
35.0	CaO wt %	47.0
5.0	Al_2O_3 wt %	0.8
55.0	SiO_2 wt %	52.15

See table 2.2. Reference (85).

If all CaO in fibres:

$$35:47 \equiv x:52.15 \equiv y:0.05 \equiv z:0.8$$

$$x = 38.8, \quad y = 0.04, \quad z = 0.6$$

From 100 parts of original RW14 only 16.2 parts SiO_2, 5.0 parts Na_2O and 4.4 parts Al_2O_3 remain. Therefore RW14 residual glass is 64 wt % SiO_2, 19 wt % Na_2O and 17 wt % Al_2O_3 (see table 2.2), and there should be 26 wt % glass to 74 wt % fibres in the devitrified material. Taking the density of β-$CaSiO_3$ as 3Mg m^{-3} (135) and an average value of 2.5 Mg m^{-3} for a soda-aluminosilicate glass (138) as the density of RW14 residual then the devitrified material should be about 30 vol % glass matrix and 70 vol % fibres. This is in quite good agreement with the modal analyses of these materials, see table 3.54.

A glass of RW14 residual composition was made up, annealed at 650°C and specimens tested in the dilatometer. The thermal expansion results are given in table 3.63 and figure 3.88, the glass transition temperature being found at 425°C and the dilatometric softening temperature at 610°C. These values are somewhat lower than Tg and Ts found for RW14/2T transverse specimens but the presence

of the reinforcing fibres may stiffen the tile material so these effects are not appreciable until the actual temperature has been exceeded. The calculated expansion coefficient for RW14 residual glass below Tg (see section 3.4.1.) is 10.1 x 10^{-6} K^{-1}, which compares well with the experimentally determined coefficient measured from 20 to 400°C as 10.2 x 10^{-6} K^{-1}.

For RW14/2T transverse specimens the expansion coefficient up to Tg (400°C) calculated using the additive relationship (see section 3.4.1.) and the volume percentages found from modal analysis (see table 3.54) is 7.5 x 10^{-6} K^{-1} which is higher than the measured coefficient of 6.4 x 10^{-6} K^{-1}. However, since in this case the thermal expansion of the matrix is greater than that of the fibres, and at high temperatures the matrix could flow and eliminate the stress generated at the fibre/matrix interfaces, this is unlikely to be due to open cracks at the interfaces.

Specimens of RW14/5T tile material were also tested perpendicular to the fibre axis. The results for these RW14/5T transverse specimens are given in table 3.64 and figure 3.89 and from these it is found that the glass transition temperature for this material is 475°C. The general form of the thermal behaviour is the same as for the RW14/2T transverse specimens but the expansion coefficients are slightly higher for the RW14/5T material. The calculated expansion coefficient up to Tg (using the modal analysis given in table 3.54 and the thermal data for the fibres and matrix for 20 to 400°C) for RW14/5T

transverse is 7.2 x 10^{-6} K^{-1} and the experimental value for 20 to 400°C is 6.6 x 10^{-6} K^{-1}, which again is lower but the calculated value is within the 95% confidence estimated error for this experimental value.

The RW14/5T tile material was also used to produce longitudinal (parallel to fibre axis) specimens. The thermal expansion characteristics of these specimens are shown in table 3.65 (fig. 3.90) from which it is found that this material behaves almost identically to the longitudinal wollastonite specimens. This indicates that the fibres in the RW14/5T material are in parallel alignment and are continuous along the length of the dilatometry specimens so that the measured thermal expansion is due solely to the fibres. Therefore the characteristic linear percentage expansion versus temperature graph (constant expansion coefficient) was obtained. The glass matrix has a much higher expansion coefficient than that of the fibres parallel to their axis and therefore there may be cracks in the matrix perpendicular to the fibre axis, produced on cooling this material from the fabrication temperature (see section 1.7.2.). This would mean that the matrix expansion parallel to the fibre axis would be taken up in closing these cracks and therefore the externally measured matrix coefficient would be less than the true value. This may be the explanation why the high expansion matrix does not dominate the expansion along the fibre axis.

The RW14/5T longitudinal specimens started to soften at about 550°C but did not completely comply to the

pressure from the thrust rod, i.e. the transducer output only decreased gradually with temperature. This may be due to the residual glass starting to flow under the stress generated by differential thermal expansion at the fibre/matrix interfaces.

3.4.4. RW14F INTERNALLY NUCLEATED MATERIAL:

Table 3.66 and figure 3.91 show the experimentally determined expansion characteristics of the internally nucleated form of the RW14 composition material (see section 3.1.7.). The results for these specimens are similar to those found for the RW14 transverse specimens (see section 3.4.3.) except that in this case the expansion coefficients at each temperature are nearly 20% lower than the corresponding transverse specimen coefficients. This could be due to the "random" orientation of the fibres in this material which would result in the overall expansion coefficient of the fibres being intermediate between the values transverse to and along wollastonite fibres (see section 3.4.1.), i.e. the fibre expansion coefficient will be lower than that in RW14 transverse specimens.

The glass transition temperature observed for RW14F material is 450°C which is in good agreement with the RW14 tile materials (see section 3.4.3.) and demonstrates the substantial influence the residual glass phase has on the thermal properties of these materials. RW14F and RW14 have the same Si:Ca ratio (see section 3.1.7.) and therefore a similar silica network structure within the glass. This explains the apparently negligible effect on Tg in RW14F

due to the fluoride ions, the presence of which lowers the viscosity and Tg compared to a glass of the same composition except for the absence of CaF (i.e. higher Si:Ca ratio).

3.4.5. RW17 COMPOSITION MATERIALS:

The thermal expansion results found for RW17 glass, see table 3.67 and figure 3.92, show the expansion coefficient for this glass is similar to that of RW9 glass since neither of these glasses contain large atomic volume oxides. The Tg of RW17 glass is about 410°C and the dilatometric softening temperature 705°C. The experimentally determined coefficient, 20 to 300°C, is 7.4 x $10^{-6}K^{-1}$ which is lower than the calculated value below Tg which is 8.5 x $10^{-6}K^{-1}$ (138).

All the crystalline RW17 specimens were machined from rods produced by the pulling technique (see section 3.1.8.).

Three types of transverse specimens were prepared, RW17/50β (β-$CaSiO_3$ spherulitic fibres in a matrix of glass with a small proportion of $Ca_2ZnSi_2O_7$, pulled at 50 microns per second), RW17/30β (β-$CaSiO_3$ spherulitic fibres in a glass with a larger proportion of $Ca_2ZnSi_2O_7$, pulled at 30 microns per second) and RW17/30α (α-$CaSiO_3$ dendrites in a matrix of glass and $Ca_2ZnSi_2O_7$). The thermal expansion behaviour of RW17/50β transverse specimens is shown in table 3.68 and figure 3.93, from which it is found that the expansion coefficient decreases to a minimum around 525°C and then starts to increase at higher temperatures. The values of the coefficient are lower

than those for RW17 glass or for transverse wollastonite fibres (see section 3.4.1.). There is no evidence of a glass transition temperature on the percentage expansion versus temperature graph.

RW17/30β transverse specimen dilatometry results are given in table 3.69 and figure 3.94. These show a hysteresis loop, i.e. the cooling curves are different from the heating curve but when the same specimen is reheated its expansion follows the original heating curve. The average expansion coefficient is nearly constant at only about $3.9 \times 10^{-6} K^{-1}$ i.e. only about half the value for transverse wollastonite. A glass transition region can be identified on the heating curve of the percentage expansion versus temperature diagram at around 310°C.

Table 3.70 and figure 3.95 give the thermal expansion results for the RW17/30α transverse specimens. These again show a hysteresis loop and the expansion coefficients also decrease with temperature in a similar manner to those for the RW17/50β transverse specimens. The values of the expansion coefficient are very low compared with the reported coefficient for α-$CaSiO_3$ which is $11.8 \times 10^{-6} K^{-1}$ between 25 and 800°C (85).

The explanation of these anomolous RW17 transverse specimen results was found when the thermal expansion characteristics of a specimen of $Ca_2ZnSi_2O_7$ which was produced from RW17 glass by rod-pulling at only 10 microns per second were investigated; this material is described in section 3.1.8. Table 3.71 and figure 3.96 give the

thermal expansion results for this RW17/10 rod material measured both parallel to and perpendicular to the growth (pulling) axis. The transverse specimens showed a small percentage expansion during heating but on cooling a rapid contraction produced a hysteresis loop and resulted in negative expansion, i.e. an overall contraction. The longitudinal specimens show a very small contraction on heating and again on cooling rapid additional contraction produced a hysteresis loop.

A negative expansion coefficient can be produced in open, network type of silicate structures (see section 1.6.2. and reference 95). However this would not explain the hysteresis effect, which is similar to the expansion characteristics of zirconia-yttria solid solutions (142, 143). The hysteresis in this system is due to the tetragonal to monoclinic polymorphic change in the zirconia structure which occurs during heating and involves a large volume change. Since the solid-solution is not completely homogeneous and the amount of yttria present controls the temperature of the transformation therefore the transformation is spread over a range of temperatures. The volume change in this system, up to 4 mol % yttria, is sufficiently great to give an overall negative expansion coefficient. Hardystonite, the mineral analogue of $Ca_2ZnSi_2O_7$, has the melilite structure (see section 1.5.2.) which is known to be capable of accommodating a complete range of solid solution (92). The melilites have no known polymorphs (144), but there is some evidence of a volume change

resulting from a polymorphic inversion (the "peg structure" found in some melilite minerals). Attempts to resolve the "new" phase using an electron microprobe technique have been unsuccessful due to the very small size of the transformed regions (144). This phenomenon has probably not been investigated in hardystonite, which is a rare and not an economically important mineral. Therefore the large hysteresis and negative expansion found for the $Ca_2ZnSi_2O_7$ material could be due to a reversible polymorphic inversion distributed over a range of temperatures due to the solid solution of excess calcium ions in this structure, as was found from the powder X-ray analysis, see figure 3.62, table 3.39 and section 3.1.8. The anisotropy of the thermal expansion of RW17/10 is a result of the directional crystallization in the rods, see figure 3.63, but the lath type crystals were too short and tended to crumble as a rod was crushed so a pinhole transmission X-ray technique could not be used to find the crystallographic orientation of the growth axis. It was attempted to use differential thermal analysis to identify the transformation temperature of the polymorphic inversion (i.e. an endothermic or exothermic peak which would confirm the occurrence of the inversion) but the transformation did not show as a sharp peak probably due to being spread over a temperature range by solid-solution.

The RW17 α and β rods transverse thermal behaviour can be related to the amount of $Ca_2ZnSi_2O_7$ present in each material. The RW17/50β rod has only a small amount of

this secondary crystalline phase in the matrix and therefore although the overall expansion coefficient is reduced by the presence of $Ca_2ZnSi_2O_7$ there is no hysteresis evident in this material. The RW17/30α and β rods contain larger amounts of $Ca_2ZnSi_2O_7$ and therefore display hysteresis effects in their thermal expansion behaviour in addition to reduced expansion coefficients.

Longitudinal type dilatometry specimens were also prepared from the RW17 rod materials. The results for RW17/50β longitudinal specimens, table 3.72 and figure 3.97, and RW17/30β longitudinal specimens, table 3.73 and figure 3.98, are very similar. Both show the constant expansion coefficient characteristic of wollastonite parallel to the fibre axis. Both coefficients are somewhat lower than that found for longitudinal wollastonite, which may be due to the low expansion $Ca_2ZnSi_2O_7$ phase in the matrix inhibiting the expansion of the fibres, particularly as this second phase probably nucleates at the fibre/matrix interfaces. However the β-$CaSiO_3$ fibres in these rod specimens must be well aligned and continuous in order to dominate the expansion behaviour in this way.

The RW17/30α longitudinal specimens also do not show any evidence of significant hysteresis, see table 3.74 and figure 3.99. There must be a relatively large amount of residual glass left between the dendritic arms in this material as a glass transition temperature of 350°C was found from the percentage expansion versus temperature plot, but there is no evidence of softening up to 650°C.

The expansion coefficients are again lower than the reported value (85) for α-$CaSiO_3$ but increase gradually with temperature, unlike those for the transverse specimens which decrease with temperature (see figure 3.95).

3.5. RESULTS OF MECHANICAL TESTS:

3.5.1. MODULI OF RUPTURE:

The moduli of rupture were found for specimens machined from the selected materials, see section 2.8. The anisotropic fibrous materials were sectioned so as to give three types of specimen, i.e. transverse, perpendicular and longitudinal (see figure 2.10). The three-point test apparatus was calibrated using specimens prepared from "Purox" recrystallized alumina (Morganite Refractories Ltd.) which has a known modulus of rupture of 160.7 MN m^{-2} (16.40 x 10^6 Kg m^{-2}). Two spans were used to test the materials (since the rod materials were not available in sufficient quantities to produce the large size specimens) but both tests had a span to depth ratio of 8:1. The specifications for these tests are given in appendix II. The bend tests were carried out as described in section 2.9. and the moduli of rupture calculated as shown in appendix III.

Table 3.75 shows the results obtained from the 20mm span three-point bend tests and table 3.76 those from the 7mm span tests. Only those specimens which gave a load versus deflection curve showing a Hook's law region (a straight line region) are included as the other specimens

failed at very low loads because they were precracked beams (cracked during machining) which fractured by crack extension at very low applied stresses. Table 3.77 gives the mean values of the moduli of rupture (R) for each type of specimen, and from this it can be seen that the mean R for 20mm span alumina specimens is lower and has a higher coefficient of variance than that for the 7mm span alumina specimens. From the size effect (see section 1.7.3.) this would be expected since a larger volume of material is below the top roller in the 20mm span tests than below the top knife-edge in the 7mm span tests. However both results are close to the reported value for the alumina material, i.e. within the corresponding deviation of the reported value. (The standard deviations in table 3.77 were calculated using the NPL code of practice (145), see appendix III.)

From table 3.77 the effect of fibre orientation on the bend strength of each type of fibrously crystallized material can be seen. The RW9 material may be regarded as a unidirectional fibre reinforced composite (see section 1.1.1.), β-$CaSiO_3$ fibres in a matrix mainly consisting of $CaAl_2Si_2O_8$ (see section 3.1.5.). This gives very similar moduli of rupture when tested in either the transverse or perpendicular orientation and these two types of specimens also give similar large coefficients of variance. In these orientations the tensile stress of the bottom surface of the test beams acts across the fibre/matrix interfaces, and although in RW9 material the

secondary, matrix, crystalline phase is nucleated on the fibre surfaces, these interfaces are likely to be cracked, and therefore weak, due to differential thermal expansion during cooling from the fabrication temperature (see sections 1.7.2. and 3.4.2.). Figure 3.100 is an SEM micrograph of the fracture surface of the RW9/6T.8 transverse type beam in which it can be seen that fracture has occured interfibrillarly. The fracture resulting from bending of these beams is tensile since the neutral axis (the axis across the beam below which stresses are tensile and above which they are compressive when a bending moment is applied to the beam (109)) moves upwards through the beam ahead of the growing crack, and these fibrous materials do not fail in the catastrophic manner typical of brittle materials (99), see section 3.5.3. Therefore in the RW9/6T.8 specimen the tensile stresses have fractured the weak interface leaving the fibres intact, as can be seen in the micrograph. There also appears to be some orientation of the fibres normal to the fibre axis since the fibres all seem to have an approximately square cross-section (see appendix V). Some areas of matrix can be seen.

The modulus of rupture of the longitudinal type RW9 specimens is about three times that for the transverse or perpendicular, see table 3.77. In this orientation failure occurs by a combination of interfibrillar (interface) separation and fracture across fibre bundles, see figure 3.101, a SEM micrograph of the fracture face of RW9/7C.1.

The fracture steps across the fibres again reveal the approximately square section of these β-$CaSiO_3$ fibres. The crystal structures of β-$CaSiO_3$ are either triclinic, wollastonite, or monoclinic, parawollastonite, (see section 1.5.1.), both of which give an approximately square (010) plane in the lattice and since each spherulitic fibre is a single crystal (see section 1.4.2.) this explains the fibre cross-section.

The modulus of rupture of longitudinal specimens is strongly dependent on the exact angle between the fibre axis and the direction of maximum stress, see section 1.7.2., and the 10 degree misorientation inherent in the RW9/7C material reduces the value of R to approximately 40% of the maximum value, see figure 1.10.

The coefficient of variance is much lower for the longitudinal specimens than for the other RW9 specimens. This probably is due to the relative ease of machining these specimens compared to the transverse or perpendicular specimens which tended to break up whilst being ground and in which therefore large flaws or cracks could develop. The longitudinal specimens, however, could be ground along the fibre axis and this, together with the higher strength of these beams, means that less were damaged during manufacture.

The SEM investigations of the fracture surfaces of all types of RW9 specimens did not reveal any features by which a single flaw which initiated fracture could be identified. This was due to the standard abrasion treatment given to the tensile face of the beams so that an

array of flaws approximately 30 microns deep covered this surface and to the weak fibre/matrix interfaces which may have contained cracks sufficiently long to initiate fracture in the interior of the beam, i.e. in the region just above the lower surface where the tensile stresses are relatively large (see section 1.7.1. and 1.7.3.).

The values found for the mean moduli of rupture for the three types of RW9 specimen are all relatively low for glass-ceramic materials, typical bend strength about 150 MN m^{-2}, and are also lower than the bend strength of glass, about 100 MN m^{-2} (102). This is probably due to the extremely weak interfaces present in the RW9 material, but may also be a result of the effects of the points of load application which have been found to reduce the apparent tensile modulus measured by flexure of beams in three-point bending when highly anisotropic materials are tested (115), see section 1.7.3.

The RW14 material could only be tested as transverse or perpendicular specimens as it was impossible to grow fibres sufficiently long without distortion to be able to cut longitudinal specimens (see sections 2.5. and 3.1.8.). This material may be regarded as a composite of unidirectional, continuous β-$CaSiO_3$ fibres in a matrix of RW14 residual glass, the fibre volume fraction being about 0.6 (see table 3.54). The results for these specimens are given in table 3.75 and the mean values of R in table 3.77. The specimens were cut from the same tile but it is seen that the mean modulus of rupture of the perpendicular beams

is greater than that for the transverse beams and the coefficient of variance is lower for the perpendicular specimens. However both the R values are much lower than the modulus of rupture of glass, but are in good agreement with the mean strengths found from testing carbon fibre reinforced glass composites in three-point bending with both transverse and perpendicular type of fibre orientation (13). The higher and more consistant value of R for the perpendicular specimens must be due to this type of specimen being more resistant to severe damage during machining since both types of specimen came from adjacent sections of the same tile.

Figure 3.102 is a SEM micrograph of RW14/2T.6, i.e. the strongest perpendicular specimen, which shows that failure occured by interfibrillar fracture together with some shearing of the fibre layers. Although in RW14 material the differential thermal expansion is not such that cracks are formed at the fibre/matrix interface during cooling after fabrication (see section 3.4.3.) there may be stress-raisers such as crystal facets and imperfections present at the interface which could give a loss of crystal/glass coherence at low applied tensile stresses (possibly during fabrication of bend test specimens). If the interfacial tensile strength is zero (i.e. no coherence between the matrix and fibres) the transverse (or perpendicular) tensile strength of the material will then be that of the equivalent volume of glass containing cylindrical voids (13). A typical strength of glass is 100 MN m^{-2},

and therefore using the law of mixtures (see section 1.7.2.) and allowing for 0.6 volume fraction of fibres the composite strength is reduced to 40 MN m^{-2}. The stress concentrating effect of a circular cross-section cylinder is a factor of 3 (13), and this again reduces the theoretical transverse composite strength to 13 MN m^{-2} which is in good agreement with both the transverse and perpendicular results for the RW14/2T material.

In figure 3.102 the "square" cross-section of the fibres can again be seen and the orientated packing of the fibres normal to the fibre axis is also clearly shown.

The RW14F internally nucleated, i.e. random fibre orientation material, gave the moduli of rupture shown in table 3.75. The mean value of R, table 3.77, is somewhat lower than those for the transverse or perpendicular RW14 specimens but the coefficient of variance is much lower (only about 1.5 times that for the 20mm span alumina specimens). Figure 3.103, which shows the centre of large spherulite in which the sheaf-like structure can be seen (see section 1.4.2.), is an SEM micrograph of the fracture surface of RW14F.1. From this it is evident that the fracture path passes through the spherulite centres, which can be seen standing proud on the fracture surface, and not along the boundaries between the spherulites. Figure 3.104 shows a close-up view of a boundary between two spherulites and from this it can be seen that there is no cracking where the crystal growth fronts impinge. Therefore, it would seem that fracture again occurs at the fibre/glass interface

inside the spherulites. The relatively low variability of the RW14F moduli may be a reflection of the random fibre orientation, i.e. the crack or flaw length introduced during machining this material is limited as the inter-fibrillar cracks are deflected by fibres in other orientations whereas in a unidirectionally crystallized material there are crack paths which theoretically could extend right across one dimension of a specimen.

Only longitudinal type bend test specimens, 7mm span, could be fabricated from the RW17/30 rod materials, and the results for the RW17/30α and RW17/30β materials (see section 3.1.8.) are given in table 3.76, the mean values being given in table 3.77. The moduli for the α-$CaSiO_3$ dendritic material and for the β-$CaSiO_3$ spherulitic fibrous material are similar and are about 3 times that found for the RW9 longitudinal specimens. This has two explanations; the fibre orientation in the rod material only varies by about 5 degrees which means that the measured modulus was at least 70% of the maximum, and the shorter span, 7mm, bend tests give higher moduli than the 20mm span tests (see results for the alumina specimens). The coefficient of variance for both materials is high, that for the spherulitic being the higher, and this may be due to only a few specimens being cut from each rod (a maximum of four) and therefore there could be some variability between the specimens, since the exact pulling rates and cooling rates of the rods could vary. (The cooling rate depends on the melt temperature and the rod diameter, see section 3.1.8.)

Figure 3.105 is a SEM micrograph of the strongest RW17/30β specimen in which the fracture face can be seen to consist of large fracture steps, failure being primarily trans-fibrillar. However deflected cracks can be seen running between the "cones" of fibres (i.e. the fibres which have nucleated from the same site and which have related (010) plane orientations, see section 3.1.5.) and the fracture steps are produced when a trans-fibrillar crack is deflected by one of these intercone cracks. The matrix thermal expansion is less than that of the β-$CaSiO_3$ fibres (see section 3.4.5.) and therefore this material is likely to have weak fibre/matrix interfaces, although since there is a large proportion of glass in the matrix (capable of relieving stresses at temperatures above Tg) and the fibres are relatively fine (less than 15 microns, see table 3.51) there may not be open cracks at these interfaces, i.e. the tensile stress across the interface may not exceed the fracture stress. This conclusion results from the comparison of the fracture surfaces of the RW9 longitudinal and RW17 longitudinal specimens, see figures 3.101 and 3.105.

The fracture surface of a typical RW17/30α specimen is shown in figure 3.106. This is a close-up of the uniform surface which does not show any fracture steps as were found for the RW17/30β material. In figure 3.106 it would appear that trans-dendrite failure has occured with no "fibre-pullout" (see section 1.7.2.) which implies that there are strong dendrite/matrix interfaces in this material. These strong interfaces may be due to the secondary

dendrite arms which "key" the dendrite into the matrix in a manner similar to the mechanical bond produced by growing whiskers on the surface of carbon fibres prior to their incorporation into a resin matrix (107).

3.5.2. INTERLAMINAR SHEAR STRENGTHS:

The interlaminar shear strengths (B) of the unidirectionally crystallized materials were found using short beam three-point bend tests (section 2.9.3. and appendix IV) on longitudinal type specimens. The test specifications (appendix II) were based on the work of Phillips et al on carbon fibre reinforced glass (13). Only results which corresponded to fracture surfaces showing some oblique character were used to calculate B values, i.e. fracture had occurred at least partially by shear along planes parallel to the neutral axis of the beam. Table 3.78 gives the B values for the tile crystallized materials, and table 3.79 the results for the materials produced by the rod-pulling technique. The mean values of B are given in table 3.77.

Figure 3.107 is an SEM micrograph of the fracture surface of a typical RW9/3T specimen. Fracture steps can be seen showing that fracture occurred partially by failure of the fibre/crystalline matrix interfaces (along the direction of the maximum shear stress) and also by trans-fibrillar fracture (in direction of tensile stress), probably at weak regions in the fibres. Since the fracture path takes the weakest route through the material, therefore the crack travels along the weak interface (see discussion in

previous section) until it reaches a weak part of a fibre (due to a crack or other imperfection) when it is deflected through this fibre and continues along the next interface.

The fracture surface of a typical RW14/4T specimen is shown in figure 3.108. RW14 material contains much finer fibres than RW9 (5 microns as compared to 60 microns diameter in RW9) and in the case of RW14 the matrix is glass whereas for RW9 the matrix is predominantly crystalline. In figure 3.108 the shear, interface fracture can be seen to extend in a plane across a group of fibres with related (010) orientations (as in figure 3.102) and the tensile, intra-fibrillar fracture also occurs through the whole of the fibre group. The fracture step does not have a straight edge which suggests that the intra-fibrillar fracture only occurs when the shear failure path intersects a crack running along a jagged, deflected, path through the fibre bundle. This is in contrast to the RW9 material in which the fracture steps are associated with individual fibres, see figure 3.107.

Despite these differences between the RW9 and RW14 materials the mean values of B found for them are similar, although the extremely large scatter of the results makes it difficult to draw any very exact conclusions. (Even for RW9/3T for which 45 results were found the coefficient of variance is 28%.) This scatter is due to the specimens fracturing with differing amounts of shear type and tensile type behaviour. Theoretically in shear tests shear failure occurs if the maximum shear stress exceeds the

shear strength before the maximum tensile stress exceeds the tensile strength, and therefore in specimens containing imperfect fibres the measured values of B may be regarded as the lower limit of the shear strength. However it has been found for carbon fibre reinforced glass that the accuracy of short beam tests improves at high fibre volume fractions (13), and both RW9/3T and RW14 materials contain more than 60 volume percent of β-$CaSiO_3$ fibres (see table 3.54).

RW17/30β specimens failed with very oblique fractures ("green-stick" type of fracture), i.e. almost totally in shear. This is reflected in the higher B values found for these specimens. Figure 3.109 shows a typical fracture surface and from this it can be seen that fracture is primarily along the fibre/matrix interface. The trans-fibrillar fracture gives irregular non-planar fracture steps, so some cracks propagate through fibre bundles and others only through a single fibre. This behaviour is intermediate between the RW9 and RW14 materials, which is in agreement with the RW17/30β microstructure which is also intermediate between these materials, i.e. fibre diameter about 15 microns and the matrix a mixture of glass and crystals.

The fracture surfaces for the RW17/30α specimens are not so oblique and do not show the same amount of interface fracture when observed in the scanning electron microscope. Figure 3.110 is an SEM micrograph of a typical specimen, showing that the fracture seems to be mainly through the

matrix, only a few dendritic arms penetrating the surface. This is a consequence of the relatively strong dendrite/matrix interface in this material (see previous section). It is therefore rather surprising that the interlaminar shear strength found for RW17/30◊ is similar to that for the weak interface RW9 material, although the very large scatter associated with these results makes it possible that in fact the correct mean B value for the dendritic material is higher than that found due to results from pre-cracked specimens which failed in tension being included in the calculated mean, see section 1.7.2.

3.5.3. WORK OF FRACTURE:

The work of fracture of the bend test specimens was found using the method of Tattersall and Tappin (106), i.e. the area under controlled fracture load versus deflection curves (Instron output) was found. The areas were found by approximating triangles.

A schematic load-deflection curve is shown in figure 3.111. Tattersall and Tappin found that negligible energy loss occurs during the catastrophic crack growth and therefore the area under the curve represents all the work done in the growth of the fracture crack and unavoidable damage directly related with the crack-growth. The total work is divided by the area of the two fracture faces to give the value for the work of fracture.

For the determinations of the work of fracture of the RW9, RW14 and RW17 materials the pre-cracked specimens, rejected for strength measurements, were used.

The failure loads attained with these specimens are so small that if they were not pre-cracked no permanent damage would have been produced in the material, and therefore no damage should occur in the beam remote from the region of maximum stress. Figure 3.112 shows the types of load versus deflection curves obtained from transverse (or random) fibrous specimens, from longitudinal fibrous specimens and from dendritic specimens. The area of the fracture faces was taken as twice the cross-sectional area of the beams, an approximation, particularly in the case of the longitudinal fibrous specimens in which the jagged fracture surfaces produced actually had a somewhat larger surface area.

The results obtained are given in table 3.77. Those for the transverse, perpendicular or random fibrous specimens are an order of magnitude lower than those for the longitudinal fibrous specimens. This is a result of crack deflection due to the weak interfaces in these materials. When a crack is propagating under stress in addition to the stress concentration tending to open the crack further in its own plane there are also subsidiary stresses which tend to open cracks on planes normal to the plane of the crack. Therefore if there are planes of weakness parallel to the tensile stress axis (as in longitudinal specimens), then cracks propagating normal to this stress could be deflected along these weak paths (146). In this way energy is expended in creating new surfaces and in increasing the length of the fracture path and thus the work of

fracture is increased.

The RW17/30d dendritic material does not contain these weak interfaces (see section 3.5.1.) and therefore the work of fracture is not increased in these longitudinal specimens.

The work of fracture for the longitudinal β-$CaSiO_3$ fibre specimens, with either a crystalline or glass matrix is an order of magnitude less than that for deal wood (106) or carbon fibre reinforced glass, a fibre reinforced ceramic for which it has been proved that the work of fracture values agree well with toughness values derived from linear elastic fracture mechanics (147). The work of fracture for the transverse (or perpendicular) or random fibrous, or longitudinal dendritic materials is the same order of magnitude to that found for commercial aluminas (106). (The work of fracture could not be calculated for the alumina specimens used to calibrate the bend test apparatus as none failed by controlled crack growth, i.e. they were not pre-cracked and therefore suffered catastrophic failure.)

3.5.4. YOUNG'S MODULI:

The Young's modulus (E) could be calculated from the results of the 20mm span three-point bend tests as described in appendix III. The mean values of E, listed in table 3.77, are all rather low, compared with modulus of soda-glass, 60 GN m^{-2}. This may be another example of the effect of the points of load application on a highly anisotropic material (see section 1.7.3. (115)).

The Young's moduli vary for the different materials tested in the same way as the moduli of rupture. Therefore for the RW9 materials the value of E for longitudinal specimens is about three times that for the transverse or perpendicular specimens. The E result for RW14 transverse is lower (although within the standard deviation) than that for the perpendicular specimens cut from the same tile. The value of the modulus of RW14F random fibre material is only about half that for RW14 transverse but has a lower coefficient of variance.

d Å	I/I_o
7.3	12
3.92	30
3.55	76
3.38	11
3.35	88
3.28	4
3.23	11
3.22	3
3.13	5
3.03	12
3.00	100
2.850	12
2.750	9
2.620	7
2.575	11
2.500	50
2.375	4
2.360	15
2.320	43
2.200	38
2.230	8
2.155	47
2.040	6
2.000	9
1.950	9
1.935	3
1.920	4
1.800	60
1.600	12

Table 3.1 : Experimentally determined X-ray diffraction intensities of wollastonite.

d Å	I/I_o
5.80	8
3.52	27
3.30	100
2.900	10
2.825	80
2.675	4
2.500	25
2.260	5
2.150	5
2.010	44
2.000	75
1.860	12

Table 3.2 : Experimentally determined X-ray diffraction intensities of pseudo-wollastonite.

d Å	I/I_o
6.75	41
4.80	16
4.15	59
4.00	8
3.87	34
3.83	27
3.70	36
3.50	19
3.45	32
3.32	48
3.25	82
3.24	100
3.23	84
3.18	37
3.10	19
3.00	28
2.980	25
2.950	14
2.870	23
2.850	11
2.720	22
2.600	10
2.575	19
2.530	25
2.475	6
2.340	10
2.300	8
2.200	23
2.120	18
2.020	22
1.960	24
1.900	8
1.860	57
1.840	17
1.810	11

Table 3.3 : Experimentally determined X-ray diffraction intensities of anorthite.

d Å	I/I_o
9.20	40
7.55	60
5.39	40
5.25	20
4.92	50
4.41	80
3.98	50
3.75	80
3.44	60
3.38	80
3.33	80
3.15	40
3.09	40
3.04	40
2.950	20
2.700	40
2.670	100
2.620	90
2.570	40
2.530	50
2.480	50
2.380	40
2.350	50
2.280	40
2.240	50
2.200	50
2.190	50
2.150	50
2.090	40
2.080	20
2.055	40
2.020	40
1.990	40
1.980	10
1.957	40
1.899	20
1.867	80
1.840	60
1.819	10
1.801	50

Table 3.4 : X-ray diffraction intensities of $Na_2Ca_2Si_3O_9$, from reference (121).

d Å	I/I_o
9.90	30
4.76	35
4.17	40
3.84	20
3.31	80
3.25	70
3.09	10
2.990	100
2.934	6
2.778	14
2.561	35
2.504	12
2.477	30
2.315	25
2.163	18
2.062	10
2.036	6
2.031	10
2.009	16
1.982	4
1.957	10
1.885	12
1.841	40
1.808	25
1.675	10
1.651	8
1.587	20
1.494	20
1.480	20
1.425	6
1.416	18
1.387	20

Table 3.5 : X-ray diffraction intensities of devitrite, from reference (121).

d Å	I/I_o
5.018	35
4.220	10
3.711	50
3.493	6
3.085	60
2.951	6
2.868	100
2.779	12
2.506	16
2.473	30
2.420	12
2.384	14
2.314	8
2.283	10
2.219	6
2.037	18
1.991	2
1.949	2
1.896	6
1.856	12
1.761	35
1.730	8
1.640	4
1.600	8
1.537	8
1.508	10
1.468	6
1.431	8
1.407	4
1.395	6
1.385	6
1.330	4

Table 3.6 : X-ray diffraction intensities of hardystonite, from reference (121).

d Å	I/I_o
5.2	3
5.1	14
3.90	8
3.80	2
3.55	17
3.35	24
3.20	49
3.10	19
3.00	100
2.820	42
2.750	25
2.580	3
2.500	19
2.360	12
2.330	10
2.240	7
2.200	19
2.040	3
2.000	42
1.940	2
1.902	3
1.855	30
1.790	2
1.780	5
1.740	8
1.620	14
1.490	12
1.470	3
1.440	2
1.375	8
1.280	2
1.220	2
1.195	2

Table 3.7 : X-ray diffraction intensities of RW1 after 18 hours at 1080°C.

d Å	I/I_o
7.7	4
5.2	24
5.1	46
3.90	3
3.82	26
3.70	13
3.55	15
3.50	4
3.40	48
3.25	100
3.15	17
3.10	15
3.05	7
3.00	83
2.975	20
2.850	9
2.825	9
2.700	4
2.550	22
2.500	15
2.375	7
2.325	9
2.200	11
2.150	4
2.000	7
1.940	7
1.900	7
1.850	39
1.810	4
1.792	17
1.725	11
1.620	9
1.610	9
1.550	4
1.365	7
1.275	4
1.190	4

Table 3.8 : X-ray diffraction intensities of RW2 after 56 hours at 1075°C.

d Å	I/I_o
6.6	9
4.1	33
3.90	11
3.80	9
3.65	10
3.55	29
3.45	8
3.35	9
3.30	34
3.25	46
3.20	100
3.15	14
3.10	36
3.00	94
2.840	38
2.600	9
2.500	33
2.475	16
2.375	16
2.325	18
2.200	31
2.150	8
2.025	9
2.000	22
1.980	22
1.940	7
1.900	9
1.840	48
1.810	12
1.770	19
1.730	20
1.630	7
1.610	21
1.540	7
1.490	20
1.370	14
1.275	8

Table 3.9 : X-ray diffraction intensities of RW3 after 72 hours at 1075°C.

d Å	I/I_o
7.8	14
7.3	6
4.2	10
4.1	40
3.90	20
3.55	33
3.40	11
3.35	40
3.20	66
3.13	26
3.00	100
2.850	10
2.750	6
2.600	10
2.500	33
2.375	19
2.350	14
2.325	19
2.250	11
2.200	40
2.050	18
1.995	15
1.940	13
1.910	9
1.860	58
1.780	14
1.740	29
1.620	19

Table 3.10 : X-ray diffraction intensities of RW6 tile after 66 hours at 1025°C.

d Å	I/I_o
5.8	12
4.5	21
4.1	26
3.75	11
3.45	37
3.28	98
3.20	7
3.00	13
2.840	100
2.480	45
2.020	75
2.000	76
1.845	28
1.695	14
1.630	16
1.482	38

Table 3.11 : X-ray diffraction intensities of RW7 crystallization from a roughened surface, after 22 hours at 1020°C.

d Å	I/I_o
5.8	9
4.5	17
4.1	47
3.75	16
3.55	9
3.45	30
3.40	13
3.35	13
3.30	92
3.28	100
3.15	9
3.03	86
2.860	75
2.550	16
2.520	13
2.500	43
2.390	8
2.320	7
2.200	8
2.020	86
2.000	59
1.860	43
1.780	13
1.730	11
1.700	8
1.630	11
1.550	9
1.495	34
1.440	12

Table 3.12 : X-ray diffraction intensities of RW7 crystallization from a smooth surface, after 22 hours at 1020°C.

d Å	I/I_o
4.5	9
4.1	16
3.80	9
3.55	18
3.35	35
3.30	44
3.25	100
3.14	22
3.02	78
2.850	31
2.510	29
2.480	11
2.380	11
2.320	13
2.200	16
2.020	15
2.000	16
1.850	56
1.785	16
1.735	16
1.620	18
1.490	16

Table 3.13 : X-ray diffraction intensities of RW7 tile after 54 hours at 1020°C.

d Å	I/I_o
7.7	5
4.1	21
3.85	9
3.70	19
3.50	15
3.45	5
3.35	6
3.30	17
3.20	84
3.10	14
3.00	100
2.950	5
2.670	5
2.570	6
2.500	15
2.360	7
2.350	7
2.310	8
2.200	14
1.845	22
1.770	5
1.740	6
1.615	8

Table 3.14 : X-ray diffraction intensities of RW8 after 20 hours at 950°C.

d Å	I/I_o
7.8	4
6.5	5
4.4	4
4.1	32
3.85	5
3.70	23
3.55	11
3.45	6
3.35	13
3.20	100
3.10	7
3.00	65
2.950	8
2.850	24
2.680	6
2.560	4
2.500	11
2.480	15
2.370	5
2.320	6
2.210	8
2.160	4
2.020	17
2.000	14
1.930	5
1.850	32
1.790	6
1.740	7
1.615	5
1.490	10

Table 3.15 : X-ray diffraction intensities of RW8 after 20 hours at 975°C.

d Å	I/I_o
5.8	8
4.5	7
4.1	35
3.75	16
3.45	13
3.35	13
3.25	73
3.20	100
3.00	29
2.950	5
2.850	55
2.700	7
2.550	5
2.500	24
2.020	38
1.850	22
1.700	5
1.490	14

Table 3.16 : X-ray diffraction intensities of RW8 after 20 hours at 1025°C.

d Å	I/I_o
6.0	20
4.5	25
4.1	15
3.85	15
3.50	40
3.40	40
3.30	100
3.05	90
2.870	60
2.580	15
2.500	25
2.030	30
2.010	60
1.860	30
1.820	20
1.630	15
1.490	20
1.430	15
1.405	20

Table 3.17 : X-ray diffraction intensities of RW9 after 10 minutes at 1160°C.

d Å	I/I_o
11.4	11
11.0	25
4.1	18
3.90	11
3.55	25
3.27	29
3.22	36
3.12	11
3.00	100
2.830	18
2.750	29
2.500	18
2.380	11
2.320	11
2.250	11
2.200	14
2.000	21
1.850	14
1.730	11
1.640	14
1.610	14
1.490	18

Table 3.18 : X-ray diffraction intensities of RW9 after 20 minutes at 1160°C.

d Å	I/I_o
6.8	12
5.2	12
4.1	28
3.80	12
3.56	16
3.50	28
3.40	12
3.35	12
3.29	100
3.21	76
3.13	12
3.00	68
2.860	68
2.700	12
2.550	8
2.500	28
2.340	12
2.220	20
2.020	32
2.000	52
1.860	32
1.610	12
1.490	12

Table 3.19 : X-ray diffraction intensities of RW9 after 30 minutes at 1160°C.

d Å	I/I_o
7.5	3
6.4	5
4.05	27
3.84	6
3.70	10
3.55	10
3.50	11
3.40	7
3.35	7
3.22	100
3.10	8
3.00	49
2.950	6
2.825	11
2.660	7
2.560	8
2.540	5
2.500	10
2.470	6
2.360	5
2.310	4
2.220	3
2.200	7
2.110	8
2.020	6
1.980	14
1.840	19
1.780	7
1.770	3
1.750	4
1.730	3
1.700	3
1.620	12
1.488	6
1.420	4

Table 3.20 : X-ray diffraction intensities of RW9/3T tile after 1 hour at 1180°C.

d Å	I/I_o
8.5	4
7.8	6
4.1	10
3.75	6
3.55	14
3.35	14
3.22	50
3.10	20
3.00	100
2.820	6
2.550	4
2.500	14
2.370	14
2.320	8
2.200	8
2.100	8
2.030	6
1.840	54
1.730	12
1.725	10
1.610	8
1.580	6
1.490	28
1.440	8
1.405	4
1.380	4

Table 3.21 : X-ray diffraction intensities of RW9/4T after 1 hour at 1180°C.

d Å	I/I_o
7.7	6
5.2	6
4.1	36
3.85	14
3.80	12
3.65	8
3.55	20
3.30	26
3.25	28
3.23	84
3.20	70
3.10	12
3.00	100
2.860	8
2.820	8
2.660	6
2.540	12
2.480	14
2.350	10
2.320	10
2.200	14
2.030	4
1.980	8
1.930	6
1.895	6
1.845	42
1.840	16
1.780	8
1.765	10
1.760	4
1.730	10
1.610	8
1.485	16

Table 3.22 : X-ray diffraction intensities of RW9/6T after 1 hour at 1180°C.

d Å	I/I_o
5.1	17
4.1	21
3.90	21
3.80	42
3.58	21
3.40	12
3.35	12
3.24	100
3.10	54
3.00	96
2.900	83
2.840	8
2.660	8
2.490	42
2.430	17
2.330	8
2.300	21
2.220	8
2.200	12
2.050	12
1.900	12
1.830	38
1.785	21
1.775	42
1.730	8
1.610	12
1.545	17
1.450	8
1.392	17

Table 3.23 : X-ray diffraction intensities of RW9/7C material after 9 hours at 1180°C.

d Å	I/I_o
7.7	14
4.5	10
4.1	14
3.85	37
3.45	55
3.30	3
3.10	6
2.875	2
2.800	14
2.700	100
2.600	2
2.550	5
2.400	5
2.300	2
2.210	6
2.050	2
1.910	43
1.840	12
1.790	2
1.660	9
1.550	20
1.400	5

Table 3.25 : X-ray diffraction intensities of RW10 after 30 minutes at 906°C.

Maximum Absolute Error		Weighed-out Compositions				Analysed Compositions							
		RW9	RW14	RW14 Residual	RW17	RW9 Glass	RW9 Crystal-lized Tile	RW14 Glass	RW14 Residual Glass	RW14 Crystal-lized Tile	RW14 Crystal-lized Rods	RW17 Glass	RW17 Crystal-lized Rods
0.25	SiO_2 wt %	50.9	55.0	64.0	50.0	51.70	52.93	54.71	64.15	53.85	53.92	49.51	51.71
0.15	CaO wt %	29.6	35.0	--	30.0	30.01	28.17	35.01	--	34.88	34.94	30.24	29.47
0.10	Al_2O_3 wt %	12.0	5.0	17.0	--	11.04	12.11	5.61	18.01	7.46	8.97	--	--
0.15	ZnO wt %	7.4	--	--	20.0	7.25	6.79	--	--	--	--	20.25	18.82
0.15	Na_2O wt %	--	5.0	19.0	--	--	--	4.67	17.84	3.81	2.37	--	--

Table 3.24 : Results of wet chemical analyses of selected compositions before and after heat-treatments.

d Å	I/I$_o$
7.6	13
5.7	13
4.9	3
4.5	15
3.77	29
3.43	37
3.40	21
3.35	29
3.28	100
3.08	4
2.850	98
2.700	40
2.660	69
2.600	4
2.490	22
2.380	4
2.250	4
2.025	66
2.000	79
1.880	31
1.850	18
1.730	9
1.700	9
1.630	15
1.555	3
1.535	4
1.495	26
1.415	6

Table 3.26 : X-ray diffraction intensities of RW10 after 30 minutes at 1059°C.

d Å	I/I$_o$
7.7	16
6.1	7
4.4	8
4.05	34
3.75	32
3.40	75
3.02	12
2.700	100
2.550	5
2.410	8
2.300	4
2.240	5
2.200	6
2.040	5
1.920	6
1.880	43
1.710	5
1.645	11
1.635	4
1.545	17
1.450	4
1.402	4

Table 3.27 : X-ray diffraction intensities of RW13 after 30 minutes at 990°C.

d Å	I/I_o
7.8	11
4.4	6
4.2	8
4.05	25
3.90	11
3.80	26
3.55	18
3.45	9
3.40	38
3.35	37
3.25	38
3.14	12
3.00	100
2.850	28
2.775	8
2.690	74
2.650	11
2.620	8
2.560	6
2.520	11
2.490	11
2.380	9
2.330	9
2.220	14
2.030	14
2.000	18
1.880	26
1.850	34
1.780	8
1.740	8
1.650	8
1.620	8
1.540	9
1.495	6

Table 3.28 : X-ray diffraction intensities of RW13 after 30 minutes at 1030°C.

d Å	I/I_o
7.8	11
7.7	10
4.5	10
4.15	21
3.95	18
3.75	25
3.50	36
3.40	44
3.38	49
3.15	27
3.00	100
2.800	6
2.750	10
2.650	68
2.550	6
2.490	26
2.350	17
2.310	19
2.190	24
2.030	6
2.000	6
1.880	28
1.840	50
1.770	12
1.740	17
1.640	6
1.605	12
1.530	12
1.490	6
1.465	8
1.400	8

Table 3.29 : X-ray diffraction intensities of RW14 after 30 minutes at 950°C.

d Å	I/I_o
8.2	10
7.7	9
4.6	14
4.4	14
4.2	16
3.90	25
3.75	15
3.55	38
3.45	25
3.40	47
3.14	34
3.01	100
2.850	10
2.770	9
2.700	41
2.600	5
2.570	6
2.520	36
2.375	22
2.325	20
2.220	35
2.100	6
2.020	7
1.900	28
1.850	65
1.770	13
1.735	19
1.640	9
1.620	20
1.595	5
1.545	11
1.490	11
1.475	9

Table 3.30 : X-ray diffraction intensities of RW14 after 30 minutes at 1000°C.

d Å	I/I_o
7.8	11
3.90	25
3.60	46
3.40	53
3.15	35
3.00	100
2.800	9
2.570	8
2.500	32
2.360	20
2.340	20
2.200	34
2.050	10
1.860	81
1.780	15
1.740	23
1.620	21
1.500	10

Table 3.31 : X-ray diffraction intensities of RW14 after 30 minutes at 1045°C.

d Å	I/I_o
7.8	8
7.0	4
4.4	7
3.90	23
3.60	27
3.40	27
3.15	24
3.05	100
2.850	8
2.620	6
2.590	6
2.525	23
2.400	14
2.360	13
2.220	26
2.060	8
1.915	6
1.860	97
1.820	4
1.755	14
1.745	15
1.650	6
1.540	4
1.500	6
1.480	7
1.450	6

Table 3.32 : X-ray diffraction intensities of RW14/2T tile after 30 minutes at 1104°C.

d Å	I/I_o
7.8	10
3.90	17
3.55	26
3.45	10
3.32	39
3.28	21
3.12	28
3.02	100
2.850	26
2.750	7
2.700	7
2.500	29
2.460	9
2.370	14
2.320	19
2.200	30
2.040	7
2.020	9
2.000	18
1.840	95
1.770	12
1.730	17
1.640	7
1.550	20
1.490	14
1.430	8
1.395	27

Table 3.33 : X-ray diffraction intensities of RW14/4T tile after 45 minutes at 1098°C.

d Å	I/I_o
7.8	9
3.85	22
3.55	25
3.33	36
3.10	28
3.00	100
2.830	7
2.750	5
2.580	8
2.550	4
2.500	26
2.370	14
2.330	14
2.240	5
2.200	24
2.040	8
2.000	5
1.900	88
1.860	8
1.840	68
1.800	6
1.770	9
1.735	17
1.725	16
1.630	6
1.620	16
1.585	3
1.560	3
1.550	3
1.525	4
1.495	12
1.485	6
1.465	8
1.440	4

Table 3.34 : X-ray diffraction intensities of RW14/5T tile after 45 minutes at 1091°C.

d Å	I/I_o
7.1	6
4.4	8
4.2	14
3.85	8
3.65	19
3.62	8
3.53	11
3.32	12
3.22	32
3.02	100
2.860	42
2.730	26
2.520	18
2.370	7
2.340	8
2.200	9
2.030	25
1.960	32
1.850	46
1.845	43
1.770	8
1.730	7
1.710	12
1.635	7
1.610	8
1.530	14
1.530	14

Table 3.35 : X-ray diffraction intensities of RW14F tile after 1 hour at 900°C.

d Å	I/I_o
5.7	6
5.4	15
3.40	27
3.18	100
2.770	95
2.670	6
2.430	19
1.995	48
1.825	15
1.670	15
1.605	13
1.470	31
1.400	16

Table 3.36 : X-ray diffraction intensities of RW14 rod pulled from 1470°C at 52 microns per second.

d Å	I/I_o
3.80	28
3.42	100
2.975	21
2.820	76
2.460	24
2.000	41
1.980	83
1.840	14
1.835	21
1.825	14
1.620	7
1.475	10
1.405	10
1.390	24
1.380	17

Table 3.37 : X-ray diffraction intensities of RW15 rod pulled from 1450°C at 280 microns per second.

d Å	I/I_o
6.0	14
5.7	14
4.25	10
3.80	8
3.47	47
3.40	10
3.37	12
3.30	100
3.28	90
3.20	12
2.870	90
2.850	47
2.700	27
2.660	27
2.500	76
2.020	41
2.000	82
1.890	14
1.855	16
1.845	10
1.840	4
1.705	10
1.635	6
1.620	4
1.560	6
1.495	8
1.480	6
1.450	4
1.410	4
1.405	4
1.385	14

Table 3.38 : X-ray diffraction intensities of RW16 rod pulled from 1450°C at 114 microns per second.

d Å	I/I_o
5.9	22
5.5	17
4.6	6
4.2	16
3.45	35
3.25	94
3.22	75
3.15	10
2.870	100
2.820	63
2.660	6
2.450	38
2.430	6
2.420	6
2.020	35
2.000	52
1.840	14
1.830	14
1.800	5
1.760	5
1.690	6
1.620	10
1.610	8
1.530	6
1.525	8
1.520	8
1.480	17
1.475	30
1.470	11
1.435	5
1.400	10
1.385	8

Table 3.40 : X-ray diffraction intensities of RW17/a rod, see table 3.39.

RW17 Rod Specimen	Pulling Rate Micron per Second	Air Blast cc per Minute	Initial Cooling Rate °C per Second	Steady Cooling Rate °C per Second	Crystal-lization Temperature °C	Major Phase/s Present	Nucleating Agent
a	19	--	2.0	1.5	1210	α-$CaSiO_3$	Pt/Pt 13% Rh
b	21	1000	2.5	1.5	1220	"	Thermocouple
c	21	2000	4.7	1.5	1110	"	"
d	32	--	3.7	2.5	1180	"	"
e	30	1000	5.5	2.5	1085	"	"
f	29	2000	5.8	2.5	1075	"	"
g	41	--	3.9	2.8	1175	"	"
h	42	1000	6.6	2.8	1055	β-$CaSiO_3$ α-$CaSiO_3$	"
i	40	2000	7.5	2.8	1025	"	"
j	49	--	6.7	2.9	1050	"	"
k	50	1000	8.1	2.9	1000	"	"
l	49	2000	10.0	2.9	--	Glass	"
m	10	--	1.0	1.0	1270	$Ca_2ZnSi_2O_7$	β-$CaSiO_3$
n	15	--	1.7	1.1	1220	α-$CaSiO_3$	(RW14)
o	20	2000	2.5	1.4	1210	"	Seed Plus
p	25	--	2.9	1.5	1125	β-$CaSiO_3$ α-$CaSiO_3$	Pt/Pt 13% Rh
q	25	2000	5.7	2.0	1100	β-$CaSiO_3$	Thermocouple
r	40	2000	7.2	2.5	1025	"	"
s	50	--	4.2	2.2	1060	"	"
t	50	2000	9.2	2.7	1000	"	"
u	80	--	13.0	2.5	--	Glass	"

Table 3.39 : Results of investigation into the effects of pulling rate, nucleating agent and temperature gradient on the crystallization of RW17 rods.

d Å	I/I$_o$
5.6	7
4.4	5
4.2	5
3.88	7
3.55	11
3.45	18
3.35	14
3.25	45
3.10	11
3.00	100
2.860	48
2.820	25
2.480	11
2.460	11
2.370	5
2.350	7
2.320	7
2.225	5
2.200	14
2.020	23
2.000	39
1.840	82
1.795	39
1.720	5
1.625	16
1.610	9
1.580	7
1.560	7
1.540	5
1.530	5
1.480	11

Table 3.41 : X-ray diffraction intensities of RW17/i rod, see table 3.39.

d Å	I/I$_o$
7.6	4
6.7	3
6.2	2
4.9	2
4.5	3
3.90	10
3.75	3
3.70	3
3.65	4
3.55	11
3.45	2
3.22	5
3.14	12
3.00	100
2.870	13
2.750	5
2.600	2
2.525	12
2.390	8
2.350	7
2.320	4
2.300	2
2.250	6
2.240	5
2.200	15
2.050	4
1.910	2
1.840	45
1.800	12
1.770	2
1.730	6
1.640	4
1.610	8
1.490	5

Table 3.42 : X-ray diffraction intensities of RW17/s rod, see table 3.39.

d Å	I/I$_o$
6.0	24
5.6	21
4.2	29
3.55	34
3.30	76
3.20	13
2.870	100
2.850	63
2.730	11
2.500	53
2.350	11
2.030	45
2.005	71
1.870	11
1.700	13
1.665	11
1.540	13
1.530	11
1.497	32
1.490	24
1.480	39
1.425	13

Table 3.43a : X-ray diffraction intensities of RW17/n, see table 3.39.

d Å	I/I$_o$
5.1	13
4.2	4
3.75	31
3.56	6
3.14	47
3.05	8
3.00	100
2.820	14
2.570	6
2.520	49
2.460	15
2.360	10
2.325	9
2.250	9
2.070	9
2.020	4
1.930	8
1.880	10
1.860	8
1.850	10
1.795	12
1.780	36
1.765	22
1.740	6
1.670	9
1.610	8
1.550	8
1.520	4
1.485	10
1.440	8
1.405	12

Table 3.43b : X-ray diffraction intensities of RW17/m, see table 3.39.

Natural Wollastonite			RW17/30 β			RW17/50 β			Pseudomono-clinic Index
Mean Radius	Θ	d Å	Mean Radius	Θ	d Å	Mean Radius	Θ	d Å	
33.5	17.46	2.98	33.5	17.46	2.98	33.75	17.56	2.97	310
24.25	13.40	3.86	24.5	13.52	3.83	24.5	13.52	3.83	400
27.25	14.80	3.50	27.0	14.68	3.53	27.25	14.80	3.50	002
27.75	15.02	3.45	28.25	15.24	3.41	28.75	15.46	3.36	$20\bar{2}$
32.0	16.84	3.09	32.25	16.95	3.07	32.25	16.95	3.07	202
38.0	19.18	2.72	37.75	19.09	2.74	39.0	19.55	2.68	$40\bar{2}$
41.5	20.42	2.57	42.0	20.59	2.55	41.75	20.51	2.55	600
43.75	21.17	2.48	44.0	21.26	2.47	44.0	21.26	2.47	402

Table 3.44 : Indexed pinhole transmission X-ray diffraction patterns.

Crystallization Temperature		Primary β-$CaSiO_3$ Crystal Growth Rate. U microns per second	Primary α-$CaSiO_3$ Crystal Growth Rate. U microns per second	log U_β	log U_α	$\frac{1}{T} \times 10^3$ K^{-1}
T °C	T K					
1180	1453	1.167	1.500	-5.933	-5.824	0.688
1160	1433	0.967	1.417	-6.015	-5.849	0.698
1130	1403	0.800	0.875	-6.097	-6.058	0.713
1100	1373	0.472	--	-6.326	--	0.728
1050	1323	0.208	0.483	-6.682	-6.316	0.756
1025	1298	0.122	0.392	-6.914	-6.407	0.770
1015	1288	0.087	--	-7.060	--	0.776
1000	1273	0.055	0.267	-7.260	-6.573	0.785
960	1233	0.095	--	-7.022	--	0.811
940	1213	0.090	--	-7.046	--	0.824
920	1193	0.047	--	-7.328	--	0.838

Table 3.45 : Crystal growth rate data for RW9 composition, see figure 3.22.

Crystallization Temperature		β-$CaSiO_3$ Crystal Growth Rate. U Microns per second	log U	$\frac{1}{T} \times 10^3$ K^{-1}
T °C	T K			
1099	1372	5.000	-5.301	0.729
1090	1363	4.000	-5.398	0.734
1050	1323	3.416	-5.466	0.756
1030	1303	0.980	-6.009	0.767
1000	1273	0.812	-6.090	0.786
954	1227	0.116	-6.936	0.815
901	1174	0.038	-7.420	0.852
860	1133	0.004	-8.398	0.883

Table 3.46 : Crystal growth rate data for RW14 composition, see figure 3.47.

Crystallization Temperature		β-$CaSiO_3$ Crystal Growth Rate. U Microns per second	log U	$\frac{1}{T} \times 10^3$ K^{-1}
T °C	T K			
1125	1398	26	-4.585	0.715
1100	1373	34	-4.468	0.728
1080	1353	39	-4.409	0.739
1060	1333	50	-4.301	0.750

Table 3.47 : Crystal growth rate data for RW17 composition, see figure 3.67.

Composition and Crystallizing Phase	Slope of log U versus $1/T \times 10^4$	Calculated "Activation" Energy E_a kJ mol^{-1}	Slope of log D versus $1/T \times 10^4$	Calculated "Diffusion" Energy E_DkJ mol^{-1}
RW9 β-$CaSiO_3$	-1.665	319	-1.921	368
RW9 α-$CaSiO_3$	-0.835	160	--	--
RW14 β-$CaSiO_3$	-2.000	383	-2.381	456
RW17 β-$CaSiO_3$	0.767	-147 Thermodynamic Free Energy Term (see text)	-1.665	319

Table 3.48 : "Activation" and "diffusion" energies for crystal growth from RW9, RW14 and RW17 compositions.

Crystallization Temperature T K	Spherulitic β-$CaSiO_3$ Crystal Growth Rate U microns per second	Spherulitic Fibre Diameter δ microns	Diffusion Coefficient $D = \delta U$ $m^2\ s^{-1}$	log D	$\frac{1}{T} \times 10^3$ K^{-1}
1453	1.167	60	1×10^{-10}	-10.07	0.688
1433	0.967	50	5×10^{-11}	-10.30	0.698
1403	0.800	30	2.5×10^{-11}	-10.60	0.713
1373	0.472	25	1×10^{-11}	-11.00	0.728
1323	0.208	20	4×10^{-12}	-11.39	0.756
1298	0.122	15	2×10^{-12}	-11.70	0.770
1288	0.087	10	9×10^{-12}	-12.05	0.776
1273	0.055	8	4×10^{-13}	-12.39	0.786
1213	0.090	2 to 3	2×10^{-13}	-12.70	0.824
1193	0.047	1 to 2	1×10^{-13}	-13.00	0.838

Table 3.49 : Spherulitic crystallization data for RW9 composition.

1372	5.000	5	2.5×10^{-11}	-10.60	0.729
1363	4.000	4	1.6×10^{-11}	-10.80	0.734
1323	3.416	2	7.0×10^{-12}	-11.15	0.756
1303	0.980	1 to 2	1.5×10^{-12}	-11.82	0.767

Table 3.50 : Spherulitic crystallization data for RW14 composition.

1398	26	20	5×10^{-10}	-9.30	0.715
1373	34	10	3×10^{-10}	-9.52	0.728
1353	39	5	2×10^{-10}	-9.70	0.739
1333	50	2 to 3	1×10^{-10}	-10.00	0.750

Table 3.51 : Spherulitic crystallization data for RW17 composition.

Composition (see table 2.2)	Material	Mean Density Mg m^{-3}
RW9	Glass	2.85
	Crystalline Tile	2.78
	Crystalline Intracrucible	2.75
RW14	Glass	2.75
	Crystalline Tile	2.60
RW14F	Glass	2.75
	Crystalline Tile	2.61
RW17	Glass	2.97
	RW17/30β Rod	2.85
	RW17/30α Rod	2.93

Table 3.52 : Densities of RW9, RW14 and RW17 compositions glasses and devitrified materials.

	RW9 Glass Calculated	RW9 Crystalline Tile		RW9 Crystalline Intracrucible		Wollastonite Calculated	Anorthite Calculated
		Fibres	Interfibre	Fibre	Interfibre		
CaO wt %	29.6	49.0	22.0	48.9	23.0	48.2	20.1
ZnO wt %	7.4	0.6	7.5	0.7	6.0	--	--
Al_2O_3 wt %	12.0	0.0	11.0	0.0	17.0	--	36.6
SiO_2 wt %	50.9	50.4	59.5	50.4	54.0	51.8	43.3
		EPMA Analysis				Reference 127	

Table 3.53 : EPMA analyses of RW9 crystallized materials

Specimen	Phases (C=CaO, A=Al_2O_3, S=SiO_2, Z=ZnO)	Volume Percentage of Phase vol. %	Ref. 125		Ref. 124
			2σ Value %	Relative 2σ Value rel. %	Angle of Fibres to Transverse
RW9/3T Tile	β-CS fibres	62	± 3	5	40°
	CAS_2 + α-CS	26	± 3	10	
	Cracks + glass	12	± 2	16	
RW9/4T Tile	β-CS fibres	59	± 3	5	35°
	CAS_2 + α-CS	33	± 2.5	8	
	Cracks + glass	8	± 1.5	16	
RW9/6T Tile	β-CS fibres	52	± 2.5	5	40°
	CAS_2 + α-CS	36	± 2.5	7	
	Cracks + glass	12	± 2	16	
RW9/7C Intra-crucible	β-CS fibres	46	± 2	5	45°
	CAS_2 + α-CS	42	± 2	6	
	Cracks + glass	12	± 1.5	12	
RW14/2T Tile	β-CS fibres	62	± 3	4	45°
	Glass	35	± 2.5	8	
	Cracks	3	± 1	24	
RW14/4T Tile	β-CS fibres	64	± 3	5	40°
	Glass	24	± 3	12	
	Cracks	8	± 2	24	
RW14/5T Tile	β-CS fibres	66	± 3.5	5	45°
	Glass	29	± 3.5	12	
	Cracks	5	± 1.5	32	
RW17/30β Rod	β-CS fibres	74	± 2.5	3	45°
	C_2ZS_2 + glass	23	± 2.5	10	
	Cracks	3	± 1	24	
RW17/30α Rod	α-CS dendrites	67	± 3.5	6	40°
	C_2ZS_2 + glass	31.5	± 3.5	12	
	Cracks	1.5	± 1	40	

Table 3.54 : Modal analyses results for RW9, RW14 and RW17 materials

Table 3.55 : Thermal expansion characteristics of "spec-pure" silver.

Room temperature = 20°C. dT = 20°C. dl = 2.0 x 10^{-6} m.

Temp. T °C	(T-20) K	Mean %Expn. Up	Mean %Expn. Down	Mean Expn. Coeff. Up α x $10^6 K^{-1}$ $_{20\to T}$	Mean Expn. Coeff. Down α x $10^6 K^{-1}$ $_{T\to 20}$	$d\alpha$ Up x $10^6 K^{-1}$	$d\alpha$ Down x $10^6 K^{-1}$
650	630	1.275	1.275	20.35	20.35	1.0	1.0
600	580	1.142	1.112	19.70	19.18	1.0	1.0
500	480	0.937	0.887	19.01	17.97	1.1	1.1
400	380	0.751	0.711	19.26	18.06	1.5	1.4
300	280	0.506	0.496	18.06	17.70	2.0	1.9
200	180	0.340	0.340	18.89	18.89	3.2	3.2
100	80	0.134	0.174	16.81	21.81	6.7	8.0

Table 3.56 : Thermal expansion characteristics of wollastonite - transverse.

Room temperature = 20°C. dT = 20°C. dl = 2.4 x 10^{-6} m.

Temp. T °C	(T-20) K	Mean %Expn.	Mean Expn. Coeff. α x $10^6 K^{-1}$	$d\alpha$ x $10^6 K^{-1}$
650	630	0.490	7.78	0.6
550	530	0.381	7.19	0.7
450	430	0.296	6.88	0.9
350	330	0.215	6.52	1.1
250	230	0.139	6.04	1.6
150	130	0.066	5.08	2.6

Table 3.57 : Thermal expansion characteristics of wollastonite - longitudinal.

Room temperature = 20°C. dT = 20°C. dl = 1.8 x 10^{-6} m.

Temp. T °C	(T-20) K	Mean %Expn.	Mean Expn. Coeff. α x $10^6 K^{-1}$	$d\alpha$ x $10^6 K^{-1}$
650	630	0.392	6.23	0.5
550	530	0.329	6.21	0.6
450	430	0.263	6.12	0.7
350	330	0.198	6.00	0.9
250	230	0.136	5.91	1.3
150	130	0.069	5.31	2.2

Table 3.58 : Thermal expansion characteristics of RW9 glass.

Room temperature = 20°C. dT = 20°C. dl = 1.6 x 10^{-6} m.

Temp. T °C	(T-20) K	Mean %Exp. Up	Mean Expn. Coeff.Up $\alpha_{20\to T}$ x $10^{6}K^{-1}$	dα Up x $10^{6}K^{-1}$
755	735	0.540	7.34	0.4
700	680	0.499	7.34	0.4
600	580	0.418	7.21	0.5
500	480	0.343	7.15	0.6
400	380	0.261	6.87	0.8
300	280	0.184	6.57	1.0
200	180	0.114	6.33	1.6
100	80	0.047	5.86	2.7

Table 3.59 : Thermal expansion characteristics of RW9/3T - transverse.

Room temperature = 20°C. dT = 20°C. dl = 1.8 x 10^{-6} m.

Temp. T °C	(T-20) K	Mean %Expn. Up	Mean %Expn. Down	Mean Expn. Coeff.Up $\alpha_{20\to T}$ x $10^{6}K^{-1}$	Mean Expn. Coeff.Down $\alpha_{T\to 20}$ x $10^{6}K^{-1}$	dα Up x $10^{6}K^{-1}$	dα Down x $10^{6}K^{-1}$
650	630	0.393	0.393	6.23	6.23	0.5	0.5
600	580	0.345	0.344	5.96	5.94	0.5	0.5
500	480	0.271	0.267	5.64	5.56	0.6	0.6
400	380	0.206	0.198	5.43	5.22	0.8	0.7
300	280	0.142	0.139	5.06	4.99	1.0	1.0
200	180	0.090	0.086	5.00	4.78	1.5	1.5
100	80	0.037	0.037	4.68	4.68	3.5	3.5

Table 3.60 : Thermal expansion characteristics of RW9/7C - longitudinal.

Room temperature = 20°C. dT = 20°C. dl = 2.0 x 10^{-6} m.

Temp. T °C	(T-20) K	Mean %Expn. Up	Mean %Expn. Down	Mean Expn. Coeff.Up $\alpha_{20\to T}$ x $10^{6}K^{-1}$	Mean Expn. Coeff.Down $\alpha_{T\to 20}$ x $10^{6}K^{-1}$	dα Up x $10^{6}K^{-1}$	dα Down x $10^{6}K^{-1}$
650	630	0.383	0.383	6.08	6.08	0.5	0.5
600	580	0.336	0.334	5.80	5.77	0.5	0.5
500	480	0.264	0.261	5.50	5.44	0.6	0.6
400	380	0.204	0.198	5.38	5.22	0.8	0.8
300	280	0.141	0.137	5.03	4.92	1.0	1.1
200	180	0.084	0.087	4.67	4.84	1.6	1.6
100	80	0.039	0.032	4.94	4.06	3.8	3.5

Table 3.61 : Thermal expansion characteristics of RW14 glass.

Room temperature = 20°C. dT = 20°C. dl = 2.0 x 10^{-6} m.

Temp. T °C	(T-20) K	Mean %Expn. Up	Mean Expn. Coeff.Up $\alpha_{20\rightarrow T}$ x $10^{6}K^{-1}$	$d\alpha$ Up x $10^{6}K^{-1}$
700	680	0.724	10.65	0.5
600	580	0.610	10.52	0.6
500	480	0.492	10.25	0.8
400	380	0.383	10.08	1.0
300	280	0.275	9.82	1.3
200	180	0.168	9.33	2.0
100	80	0.067	8.38	3.8

Table 3.62 : Thermal expansion characteristics of RW14/2T - transverse.

Room temperature = 20°C. dT = 20°C. dl = 1.6 x 10^{-6} m.

Temp. T °C	(T-20) K	Mean %Expn. Up	Mean %Expn. Down	Mean Expn. Coeff.Up $\alpha_{20\rightarrow T}$ x $10^{6}K^{-1}$	Mean Expn. Coeff.Down $\alpha_{T\rightarrow 20}$ x $10^{6}K^{-1}$	$d\alpha$ Up x $10^{6}K^{-1}$	$d\alpha$ Down x $10^{6}K^{-1}$
650	630	0.457	0.457	7.26	7.26	0.5	0.5
600	580	0.420	0.390	7.24	6.72	0.5	0.5
500	480	0.313	0.291	6.52	6.06	0.6	0.6
400	380	0.241	0.217	6.34	5.71	0.8	0.7
300	280	0.169	0.156	6.04	5.57	1.0	0.9
200	180	0.104	0.095	5.78	5.28	1.6	1.5
100	80	0.042	0.040	5.25	5.00	3.3	3.2

Table 3.63 : Thermal expansion characteristics of RW14 residual glass.

Room temperature = 20°C. dT = 20°C. dl = 1.2 x 10^{-6} m.

Temp. T °C	(T-20) K	Mean %Expn. Up	Mean Expn. Coeff.Up $\alpha_{80\rightarrow T}$ x $10^{6}K^{-1}$	$d\alpha$ Up x $10^{6}K^{-1}$
600	580	0.609	10.50	0.5
500	480	0.497	10.35	0.6
400	380	0.386	10.16	0.8
300	280	0.272	9.71	1.1
200	180	0.178	9.89	1.8
100	80	0.068	8.50	3.6

Table 3.64 : Thermal expansion characteristics of RW14/5T - transverse.

Room temperature = 20°C. dT = 20°C. dl = 1.5 x 10^{-6} m.

Temp. T °C	(T-20) K	Mean %Expn. Up	Mean %Expn. Down	Mean Expn. Coeff.Up $\alpha_{20\to T}$ x $10^6 K^{-1}$	Mean Expn. Coeff.Down $\alpha_{T\to 20}$ x $10^6 K^{-1}$	$d\alpha$ Up x $10^6 K^{-1}$	$d\alpha$ Down x $10^6 K^{-1}$
650	680	0.464	0.464	7.36	7.36	0.4	0.4
600	580	0.411	0.414	7.09	7.14	0.5	0.5
500	480	0.336	0.316	7.00	6.58	0.6	0.6
400	380	0.269	0.235	7.08	6.18	0.8	0.7
300	280	0.186	0.164	6.64	5.86	1.0	0.9
200	180	0.114	0.103	6.33	5.72	1.6	1.5
100	80	0.044	0.040	5.50	5.00	3.2	3.2

Table 3.65 : Thermal expansion characteristics of RW14/5T - longitudinal.

Room temperature = 20°C. dT = 20°C. dl = 3.0 x 10^{-6} m.

Temp. T °C	(T-20) K	Mean %Expn. Up	Mean %Expn. Down	Mean Expn. Coeff.Up $\alpha_{20\to T}$ x $10^6 K^{-1}$	Mean Expn. Coeff.Down $\alpha_{T\to 20}$ x $10^6 K^{-1}$	$d\alpha$ Up x $10^6 K^{-1}$	$d\alpha$ Down x $10^6 K^{-1}$
520	500	0.305	0.301	6.10	6.02	0.5	0.5
500	480	0.287	0.281	5.98	5.83	0.5	0.5
400	380	0.239	0.241	6.29	6.34	0.7	0.7
300	280	0.167	0.183	5.96	6.54	0.9	0.8
200	180	0.096	0.101	5.33	5.61	1.4	1.5
100	80	0.028	0.050	3.5	6.25	2.8	3.4

Table 3.66 : Thermal expansion characteristics of RW14F crystallized material.

Room temperature = 20°C. dT = 20°C. dl = 1.6 x 10^{-6} m.

Temp. T °C	(T-20) K	Mean %Expn. Up	Mean %Expn. Down	Mean Expn. Coeff.Up $\alpha_{20\to T}$ x $10^6 K^{-1}$	Mean Expn. Coeff.Down $\alpha_{T\to 20}$ x $10^6 K^{-1}$	$d\alpha$ Up x $10^6 K^{-1}$	$d\alpha$ Down x $10^6 K^{-1}$
650	630	0.405	0.405	6.43	6.43	0.4	0.4
600	580	0.364	0.340	6.28	6.00	0.4	0.5
500	480	0.293	0.267	6.10	5.56	0.6	0.6
400	380	0.227	0.202	5.97	5.32	0.7	0.7
300	280	0.160	0.144	5.71	5.14	1.0	0.9
200	180	0.094	0.088	5.22	4.89	1.5	1.4
100	80	0.034	0.032	4.25	4.00	3.1	3.0

Table 3.67 : Thermal expansion characteristics of RW17 glass.

Room temperature = 20°C. dT = 20°C. dl = 3.0 x 10^{-6} m.

Temp. T °C	(T-20) K	Mean %Expn. Up	Mean %Expn. Down	Mean Expn. Coeff.Up α x $10^6 K^{-1}$ $_{20\to T}$	Mean Expn. Coeff.Down α x $10^6 K^{-1}$ $_{T\to 20}$	$d\alpha$ Up x $10^6 K^{-1}$	$d\alpha$ Down x $10^6 K^{-1}$
700	680	0.480	—	7.064	—	0.6	—
600	580	0.449	—	7.733	—	0.8	—
500	480	0.364	—	7.583	—	0.9	—
400	380	0.286	—	7.526	—	1.2	—
300	280	0.202	—	7.214	—	1.6	—
200	180	0.136	—	7.556	—	2.5	—
100	80	0.056	—	7.000	—	5.7	—

Table 3.68 : Thermal expansion characteristics of RW17/50β - transverse.

Room temperature = 20°C. dT = 20°C. dl = 2.4 x 10^{-6} m.

Temp. T °C	(T-20) K	Mean %Expn. Up	Mean %Expn. Down	Mean Expn. Coeff.Up α x $10^6 K^{-1}$ $_{20\to T}$	Mean Expn. Coeff.Down α x $10^6 K^{-1}$ $_{T\to 20}$	$d\alpha$ Up x $10^6 K^{-1}$	$d\alpha$ Down x $10^6 K^{-1}$
650	630	0.292	0.288	4.63	4.57	0.5	0.5
600	580	0.260	0.260	4.48	4.48	0.5	0.5
500	480	0.226	0.206	4.71	4.29	0.7	0.7
400	380	0.188	0.174	4.95	4.58	0.9	0.9
300	280	0.152	0.144	5.43	5.14	1.2	1.2
200	180	0.098	0.090	5.44	5.00	1.9	1.9
100	80	0.048	0.044	6.00	5.50	4.5	4.3

Table 3.69 : Thermal expansion characteristics of RW17/30B - transverse.

Room temperature = 20°C. dT = 20°C. dl = 2.9 x 10^{-6} m.

Temp. T °C	(T-20) K	Mean %Expn. Up	Mean %Expn. Down	Mean Expn. Coeff.Up α x $10^6 K^{-1}$ $_{20\to T}$	Mean Expn. Coeff.Down α x $10^6 K^{-1}$ $_{T\to 20}$	$d\alpha$ Up x $10^6 K^{-1}$	$d\alpha$ Down x $10^6 K^{-1}$
650	630	0.262	0.251	4.16	3.98	0.4	0.4
600	580	0.248	0.216	4.28	3.72	0.4	0.4
500	480	0.204	0.169	4.25	3.52	0.6	0.5
400	380	0.158	0.138	4.16	3.63	0.7	0.7
300	280	0.114	0.106	4.07	3.79	0.9	0.9
200	180	0.070	0.066	3.89	3.67	1.4	1.4
100	80	0.036	0.033	4.50	4.12	3.4	3.2

Table 3.70 : Thermal expansion characteristics of RW17/30α - transverse.

Room temperature = 20°C. dT = 20°C. dl = 2.2 x 10^{-6} m.

Temp. T °C	(T-20) K	Mean %Expn. Up	Mean %Expn. Down	Mean Expn. Coeff.Up $\alpha_{20\to T}$ x $10^6 K^{-1}$	Mean Expn. Coeff.Down $\alpha_{T\to 20}$ x $10^6 K^{-1}$	dα Up x $10^6 K^{-1}$	dα Down x $10^6 K^{-1}$
650	630	0.315	0.333	5.00	5.28	0.5	0.5
600	580	0.313	0.287	5.40	4.95	0.5	0.5
500	480	0.275	0.242	5.73	5.04	0.7	0.7
400	380	0.217	0.205	5.71	5.39	0.9	0.9
300	280	0.168	0.169	6.00	6.04	1.2	1.2
200	180	0.116	0.116	6.44	6.44	1.9	1.9
100	80	0.057	0.051	7.12	6.38	4.6	4.3

Table 3.71 : Thermal expansion characteristics of RW17/10 - transverse and longitudinal.

Room temperature = 20°C. dT = 20°C. dl = 1.2 x 10^{-6} m.

Temp. T °C	(T-20) K	Mean %Expn. Up	Mean %Expn. Down	Mean %Expn. Up	Mean %Expn. Down
650	630	0.125	0.080	-0.038	-0.058
600	580	0.137	0.035	-0.017	-0.077
500	480	0.132	0.010	-0.007	-0.085
400	380	0.108	0.020	-0.001	-0.083
300	280	0.075	-0.003	-0.003	-0.047
200	180	0.050	-0.030	-0.006	-0.047
100	80	0.040	0.000	-0.011	-0.019
		Transverse		Longitudinal	

Table 3.72 : Thermal expansion characteristics of RW17/50β - longitudinal.

Room temperature = 20°C. dT = 20°C. dl = 1.6 x 10^{-6} m.

Temp. T °C	(T-20) K	Mean %Expn. Up	Mean %Expn. Down	Mean Expn. Coeff.Up $\alpha_{20\to T}$ x $10^6 K^{-1}$	Mean Expn. Coeff.Down $\alpha_{T\to 20}$ x $10^6 K^{-1}$	dα Up x $10^6 K^{-1}$	dα Down x $10^6 K^{-1}$
650	630	0.335	0.335	5.317	5.317	0.4	0.4
600	580	0.319	0.316	5.500	5.448	0.4	0.4
500	480	0.278	0.262	5.792	5.458	0.6	0.5
400	380	0.211	0.186	5.553	4.895	0.7	0.7
300	280	0.153	0.136	5.464	4.857	0.9	0.9
200	180	0.085	0.086	4.722	4.778	1.4	1.4
100	80	0.040	0.038	5.000	4.750	3.2	3.2

Table 3.73 : Thermal expansion characteristics of RW17/30β - longitudinal.

Room temperature = 20°C. dT = 20°C. dl = 1.2 x 10^{-6} m.

Temp. T °C	(T-20) K	Mean %Expn. Up	Mean %Expn. Down	Mean Expn. Coeff.Up $\alpha_{20\to T}$ x $10^{6}K^{-1}$	Mean Expn. Coeff.Down $\alpha_{T\to 20}$ x $10^{6}K^{-1}$	dα Up x $10^{6}K^{-1}$	dα Down x $10^{6}K^{-1}$
650	630	0.365	0.365	5.794	5.794	0.3	0.3
600	580	0.346	0.327	5.966	5.638	0.3	0.3
500	480	0.287	0.255	5.979	5.312	0.4	0.4
400	380	0.222	0.199	5.842	5.237	0.5	0.5
300	280	0.164	0.144	5.714	5.143	0.7	0.6
200	180	0.092	0.081	5.111	4.500	0.9	0.9
100	80	0.047	0.037	5.875	4.568	2.2	2.2

Table 3.74 : Thermal expansion characteristics of RW17/30α - longitudinal.

Room temperature = 20°C. dT = 20°C. dl = 1.0 x 10^{-6} m.

Temp. T °C	(T-20) K	Mean %Expn. Up	Mean %Expn. Down	Mean Expn. Coeff.Up $\alpha_{20\to T}$ x $10^{6}K^{-1}$	Mean Expn. Coeff.Down $\alpha_{T\to 20}$ x $10^{6}K^{-1}$	dα Up x $10^{6}K^{-1}$	dα Down x $10^{6}K^{-1}$
650	630	0.545	0.545	8.651	8.651	0.6	0.6
600	580	0.482	0.494	8.310	8.517	0.6	0.6
500	480	0.408	0.396	8.500	8.250	0.8	0.7
400	380	0.320	0.306	8.421	8.053	0.9	1.0
300	280	0.229	0.222	8.179	7.929	1.3	1.3
200	180	0.140	0.138	7.778	7.667	1.9	1.9
100	80	0.065	0.055	8.125	6.875	4.5	4.5

Table 3.75 : Results of 20mm span three-point bend tests.

Specimen		R MN m^{-2}
Purox alumina	A1	203.78
	A2	198.55
	A3	171.54
	A4	200.24
	A5	210.17
	A7	131.39
	A8	163.32
	A9	165.58
	A10	175.26
	A11	143.18
	A13	188.86
RW9 Perpendicular	4T1	9.61
	4T2	10.21
	4T3	10.41
	4T5	19.26
	4T7	8.32
	4T8	10.49
	4T9	9.65
RW9 Transverse	6T1	12.89
	6T2	6.77
	6T3	5.70
	6T4	12.20
	6T7	14.34
	6T8	18.01
RW9 Longitudinal	7C1	35.37
	7C2	28.68
	7C3	25.27
	7C4	40.29
	7C5	38.49
	7C6	33.03
RW14 Perpendicular	2T1	11.67
	2T5	13.23
	2T6	22.74
	2T7	18.22
	2T8	14.21
RW14 Transverse	2T9	16.34
	2T10	19.65
	2T11	9.63
	2T12	8.71
	2T13	7.49
	2T14	10.22
	2T16	10.48
RW14F Random	F1	11.89
	F2	8.86
	F3	8.47
	F4	8.63
	F5	7.01
	F7	10.43
	F8	6.41
	F9	8.74
	F10	9.88

Table 3.76 : Results of 7mm span three-point bend tests.

Specimen		R MN m^{-2}
Purox alumina	a1	206.3
	a2	196.3
	a3	192.4
	a4	213.2
	a5	205.5
	a6	166.9
	a7	219.0
	a8	212.1
	a9	190.2
	a10	189.6
	a11	185.5
	a12	178.9
	a13	198.1
	a14	212.2
	a15	177.6
	a16	192.9
	a17	198.4
	a18	183.4
	a19	153.6
	a20	171.5
RW17/30β β-$CaSiO_3$ Longitudinal	12	111.4
	14	145.1
	16	57.1
	41	72.1
	45	93.3
	47	106.0
	52	101.1
	53	82.4
	54	187.8
	59	84.3
	60	132.1
	63	134.2
RW17/30α α-$CaSiO_3$ Longitudinal	1	45.3
	2	78.5
	3	62.9
	6	71.0
	7	75.2
	8	89.9
	9	100.8
	10	80.9
	11	79.5
	19	113.4
	20	87.8
	21	87.2
	22	84.1
	25	79.9
	27	102.9
	28	88.9
	29	116.0
	30	122.5
	31	118.4
	32	102.8
	33	103.7
	34	123.2
	35	95.2
	36	106.5
	37	107.5
	40	71.4
	42	79.2

Table 3.77 : Results of all mechanical tests.

Material	Fibre Orientation	Test Span x 10^3m	Number of Results n	Mean Modulus of Rupture $\bar{R}$ MN m^{-2}	Mean Interlaminar Shear Strength $\bar{B}$ MN m^{-2}	Standard Deviation S	Coefficient of Variance $\frac{S}{\bar{x}_{mean}}$ x 100%	Mean Corrected Young's Modulus $\bar{E}$ GN m^{-2}	Standard Deviation S	Coefficient of Variance $\frac{S}{\bar{x}_{mean}}$ x 100%	Work of Fracture kJ m^{-2}
Purox Alumina	--	20	11	177.4	--	23.5	13	--	--	--	--
Purox Alumina	--	7	20	192.2	--	17.0	9	--	--	--	--
RW9/4T	Perpendicular	20	7	11.1	--	3.7	33	6.6	3.0	47	0.01
RW9/6T	Transverse	20	6	11.1	--	4.7	40	5.7	2.4	42	0.01
RW9/7C	Longitudinal	20	6	33.5	--	5.8	17	22.5	7.6	34	0.16
RW9/3T	Longitudinal	4	45	--	6.4	1.8	28	--	--	--	--
RW14/2T	Perpendicular	20	6	16.0	--	4.5	28	11.7	3.7	31	0.02
RW14/2T	Transverse	20	7	11.8	--	4.5	38	8.9	3.7	42	0.02
RW14/4T	Longitudinal	4	22	--	5.8	2.7	47	--	--	--	0.13
RW14/5T	Longitudinal	4	18	--	5.8	2.9	49	--	--	--	0.13
RW14F	Random	20	9	8.9	--	1.7	19	6.0	1.3	22	0.02
RW17/30β	Longitudinal	7	12	108.9	--	36.1	33	--	--	--	0.17
RW17/30β	Longitudinal	4	15	--	10.6	5.5	52	--	--	--	--
RW17/30α	Longitudinal	7	26	91.8	--	19.6	21	--	--	--	0.02
RW17/30α	Longitudinal	4	6	--	6.6	3.1	47	--	--	--	--

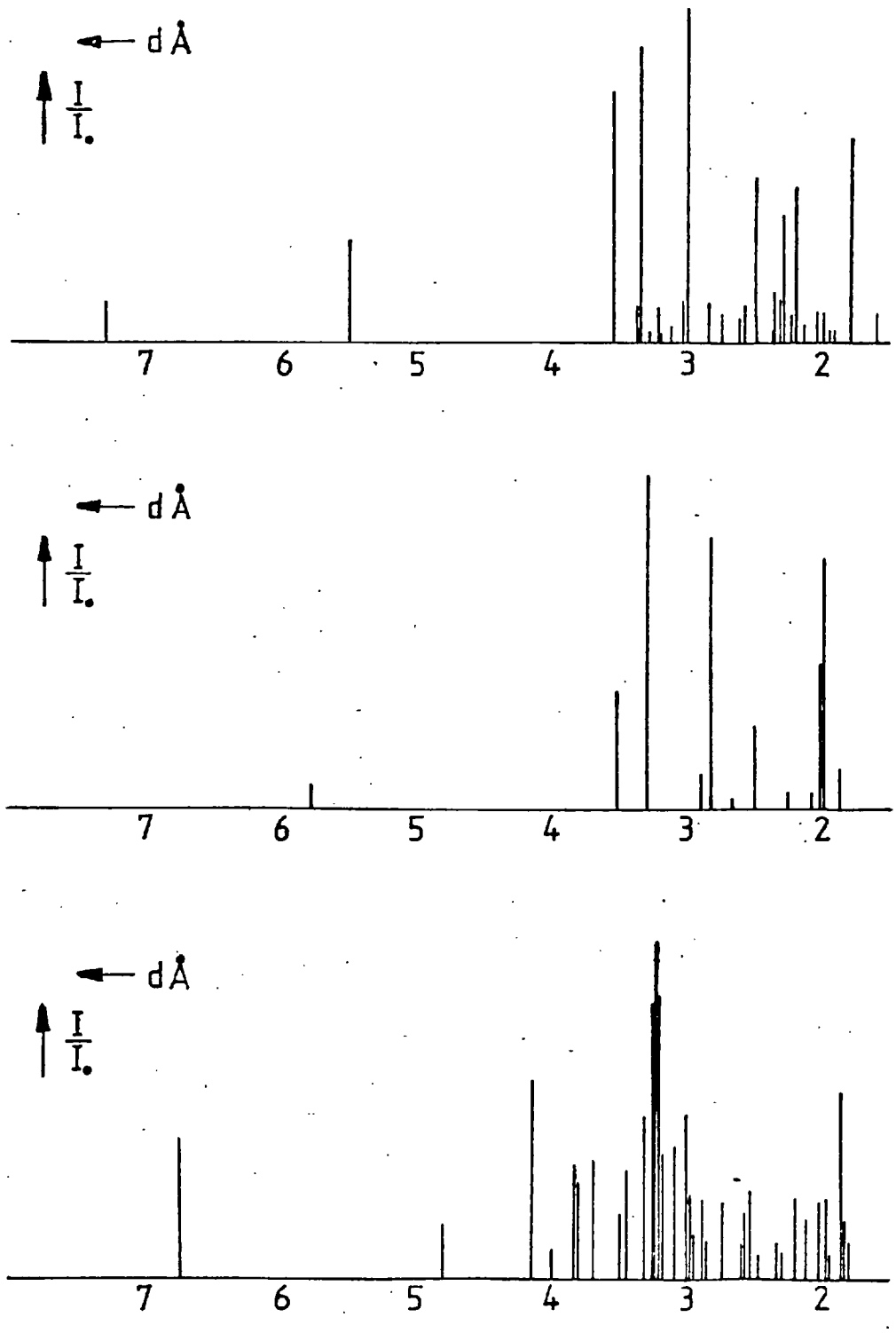
Table 3.78 : Results of short beam tests - tile materials.

Specimen		B MN m^{-2}
RW9/3T	1	6.68
	2	9.11
	3	8.05
	4	7.02
	5	6.76
	6	6.55
	7	4.42
	8	6.28
	9	4.04
	10	9.03
	11	5.71
	12	4.34
	13	7.88
	14	6.12
	15	7.35
	16	4.25
	17	6.68
	18	8.90
	20	12.17
	21	6.02
	22	5.54
	23	3.16
	24	5.25
	25	5.52
	26	6.89
	27	6.21
	28	7.34
	29	6.66
	30	6.42
	31	4.03
	32	4.22
	33	5.77
	34	5.75
	35	4.78
	36	2.91
	37	5.35
	38	8.34
	40	8.40
	41	5.56
	43	7.74
	44	6.98
	46	8.60
	47	4.49
	48	6.74
	50	5.56

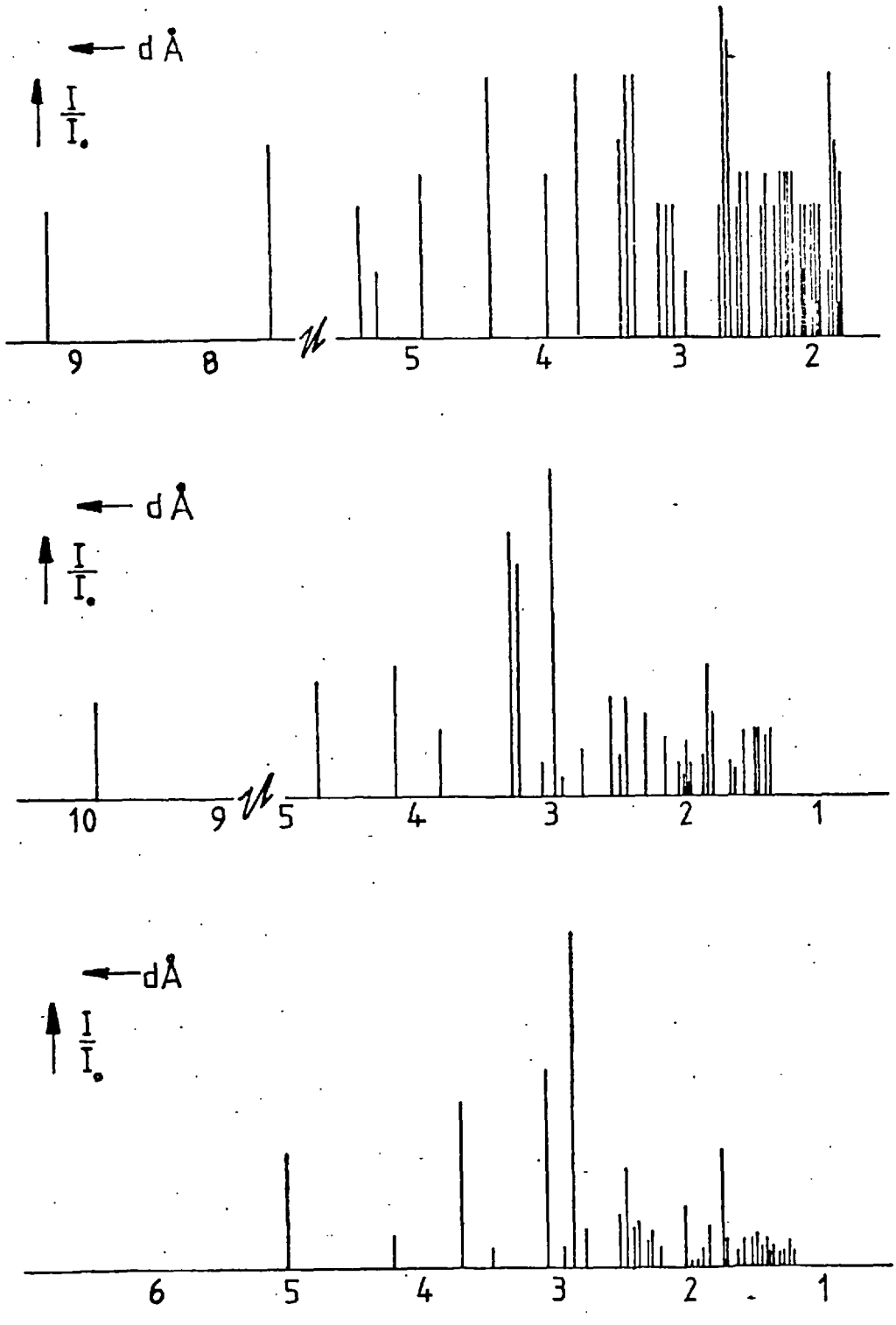
Specimen		B MN m^{-2}
RW14/4T	1	3.29
	2	4.84
	3	11.60
	4	4.25
	5	3.10
	6	2.65
	7	10.23
	8	3.55
	10	4.35
	11	6.79
	12	8.29
	13	6.40
	14	4.51
	15	11.60
	16	3.40
	17	8.30
	18	7.82
	19	4.91
	20	4.33
	21	5.43
	22	4.64
	23	3.12
RW14/5T	1	5.08
	3	14.66
	4	5.11
	5	10.02
	6	3.75
	8	3.08
	9	3.39
	10	5.07
	11	2.98
	12	4.45
	14	8.54
	15	6.01
	16	4.02
	17	5.05
	18	5.55
	19	5.73
	20	4.68
	21	7.27

Table 3.79 : Results of short beam tests - rod materials.

Specimen		B MN.m^{-2}
RW17/30β	11	16.76
	17	4.15
	18	5.80
	22	4.20
	23	6.91
	24	5.69
	25	12.77
	26	7.70
	27	21.70
	28	8.42
	29	16.82
	30	13.68
	31	10.43
	32	16.90
	33	6.32
RW17/30α	1	4.51
	2	8.88
	3	10.12
	4	8.99
	10	2.94
	21	4.02



Experimentally determined X-ray diffraction intensities.
Fig. 3.1 Wollastonite.
Fig. 3.2 Pseudowollastonite.
Fig. 3.3 Anorthite.



X-ray diffraction intensities found from ref. 121.

Fig. 3.4 $Na_2Ca_2Si_3O_9$.

Fig. 3.5 Devitrite.

Fig. 3.6 Hardysonite.

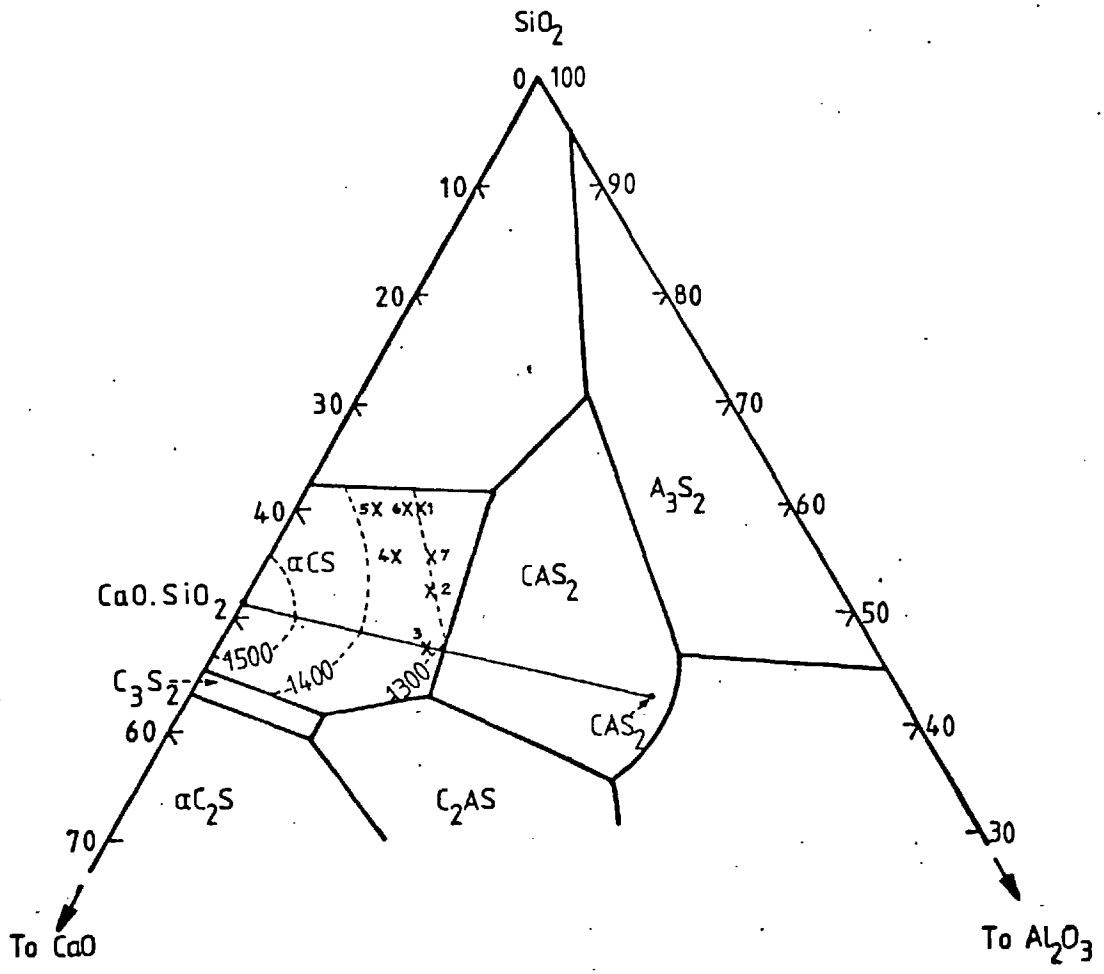
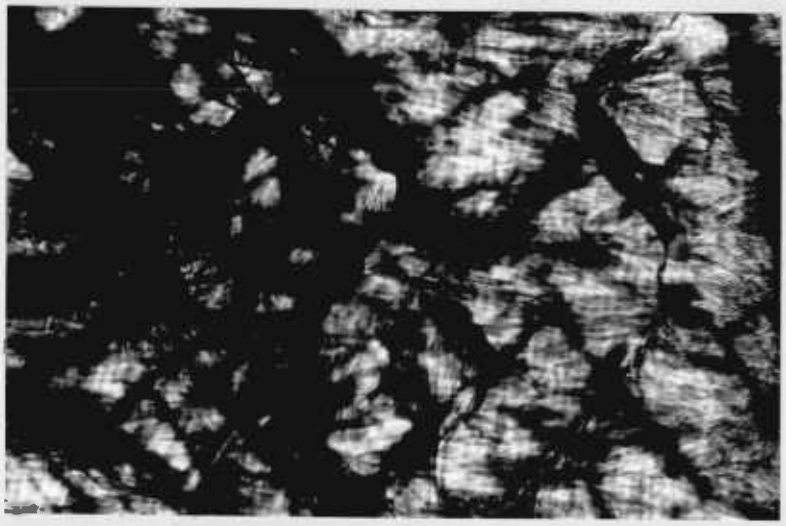


Fig. 3.7 $CaO-Al_2O_3-SiO_2$ phase diagram (ref. 127).



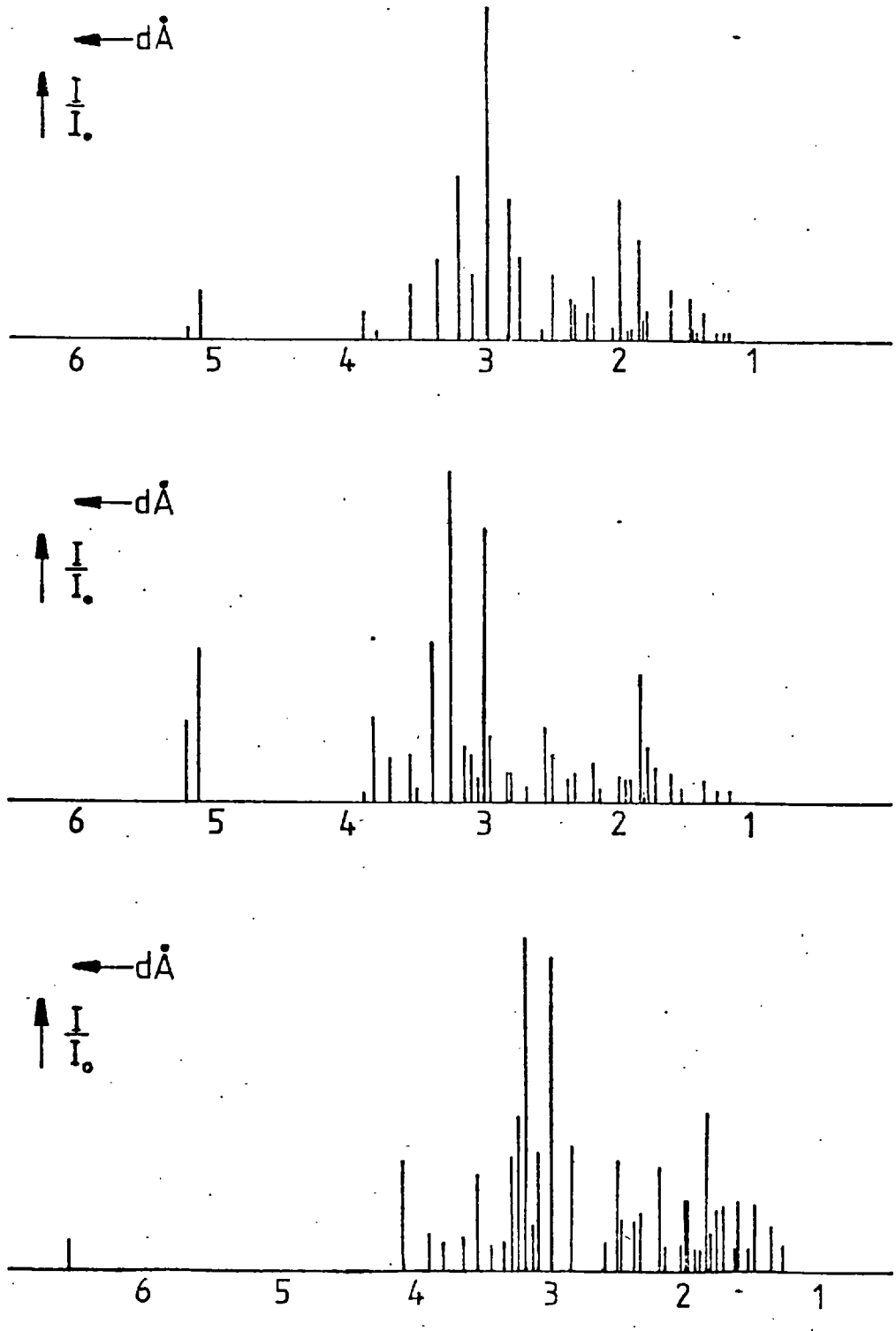
42 μm

Fig. 3.8 RW1 after 18 hours at 1080°C, X-polars .



42 μm

Fig. 3.12 RW3 after 18 hours at 1040°C, X-polars .



X-ray diffraction intensities .

Fig. 3.9 RW1 after 18 hours at 1080°C .

Fig. 3.10 RW2 after 56 hours at 1075°C .

Fig. 3.11 RW3 after 72 hours at 1075°C .

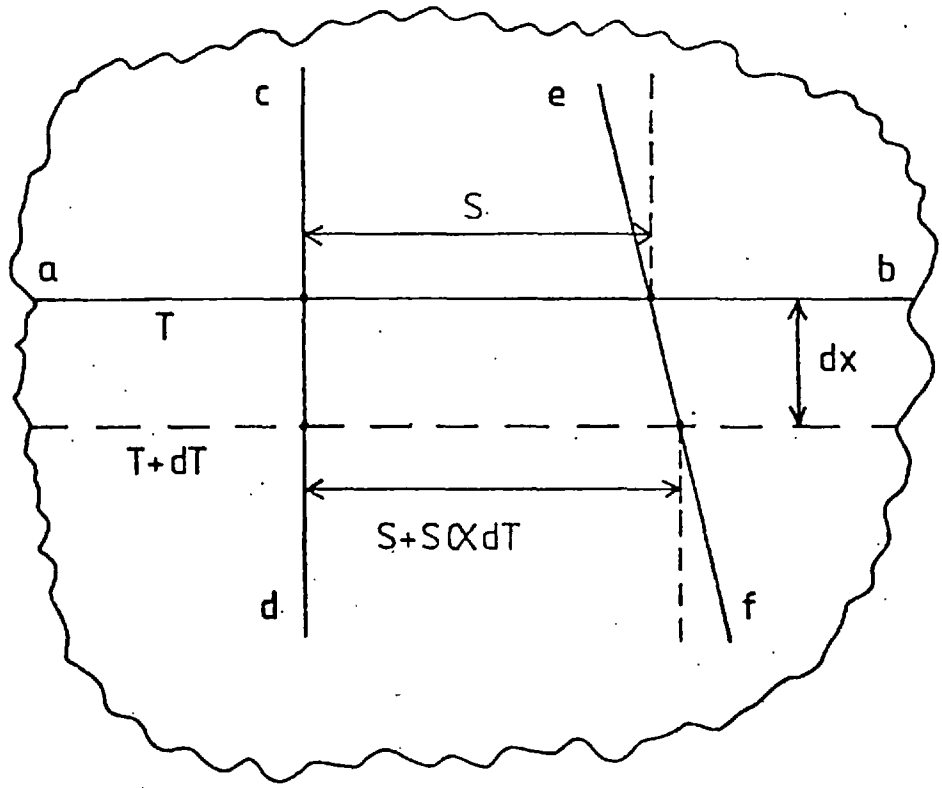
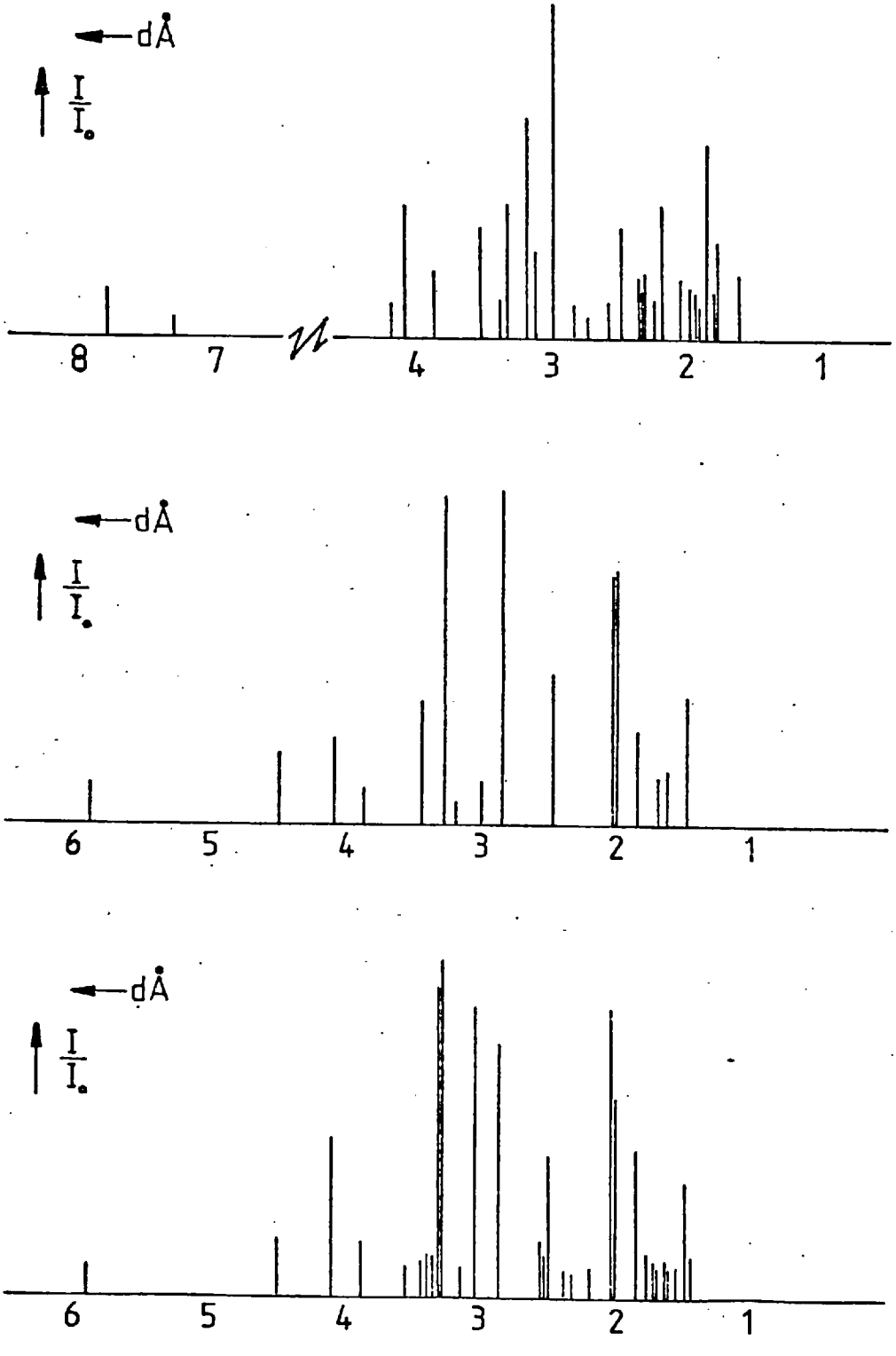


Fig. 3.13 A portion of a heating or cooling tile (ref. 130).

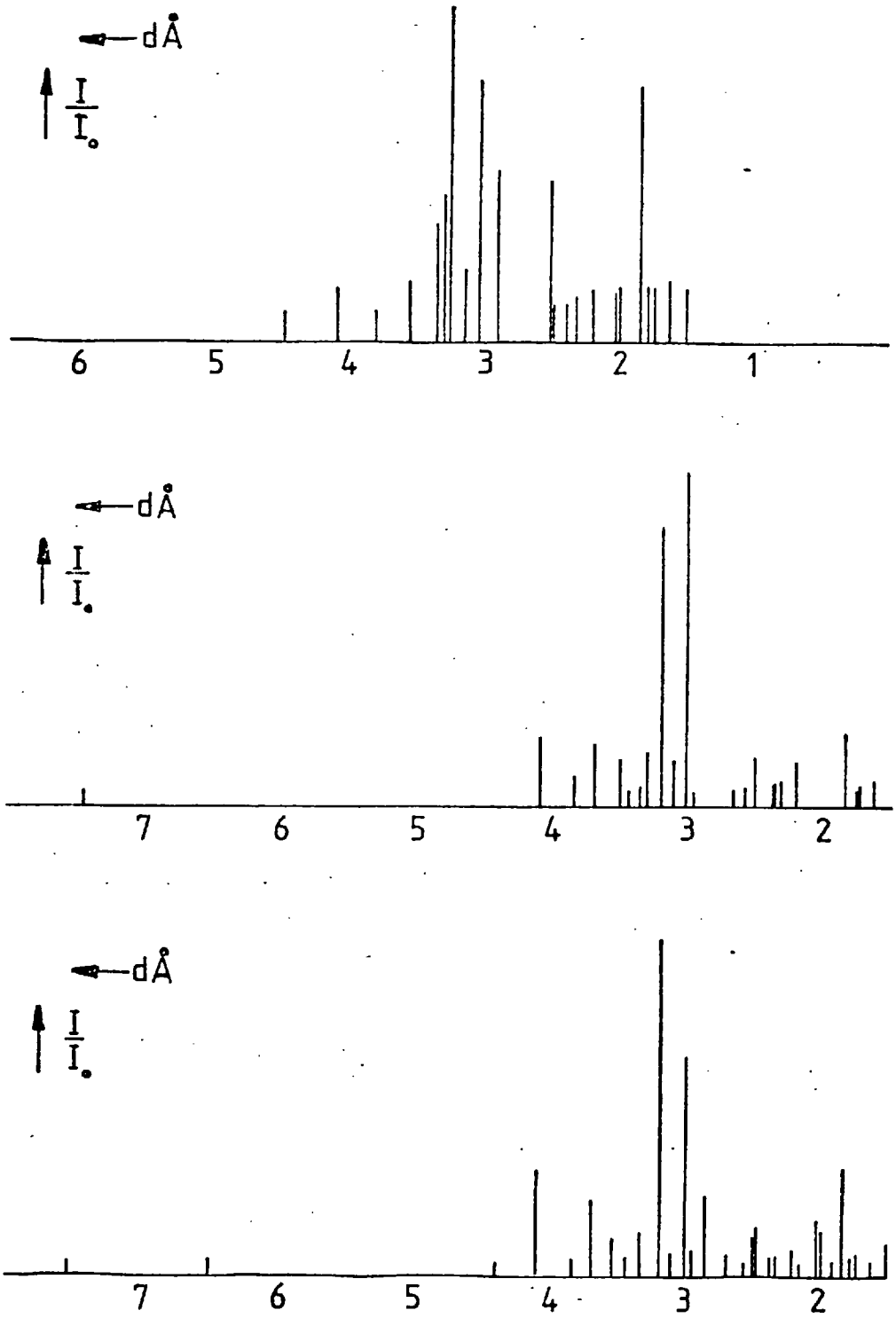


X-ray diffraction intensities.

Fig. 3.14 RW6 tile after 66 hours at 1025 °C.

Fig. 3.15 RW7, roughened surface, after 22 hours at 1020 °C.

Fig. 3.16 RW7, smooth surface, after 22 hours at 1020 °C.

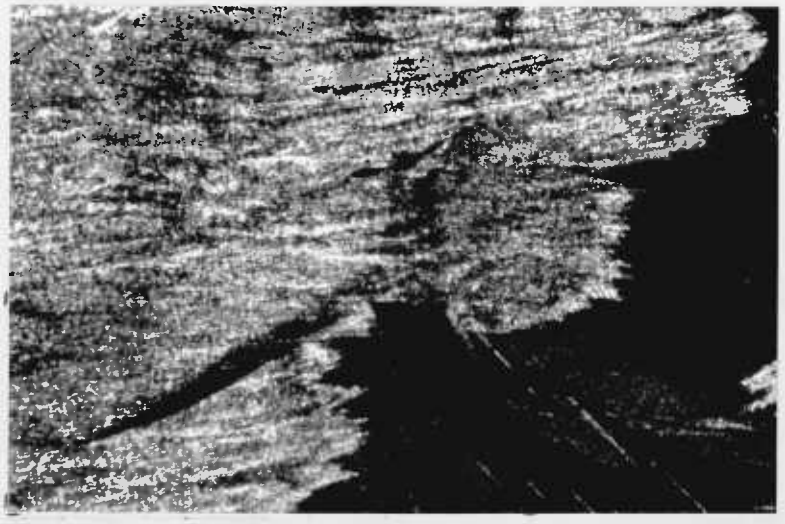


X-ray diffraction intensities.

Fig. 3.17 RW7 tile after 54 hours at 1020 °C.

Fig. 3.19 RW8 after 20 hours at 950 °C.

Fig. 3.20 RW8 after 20 hours at 975 °C.



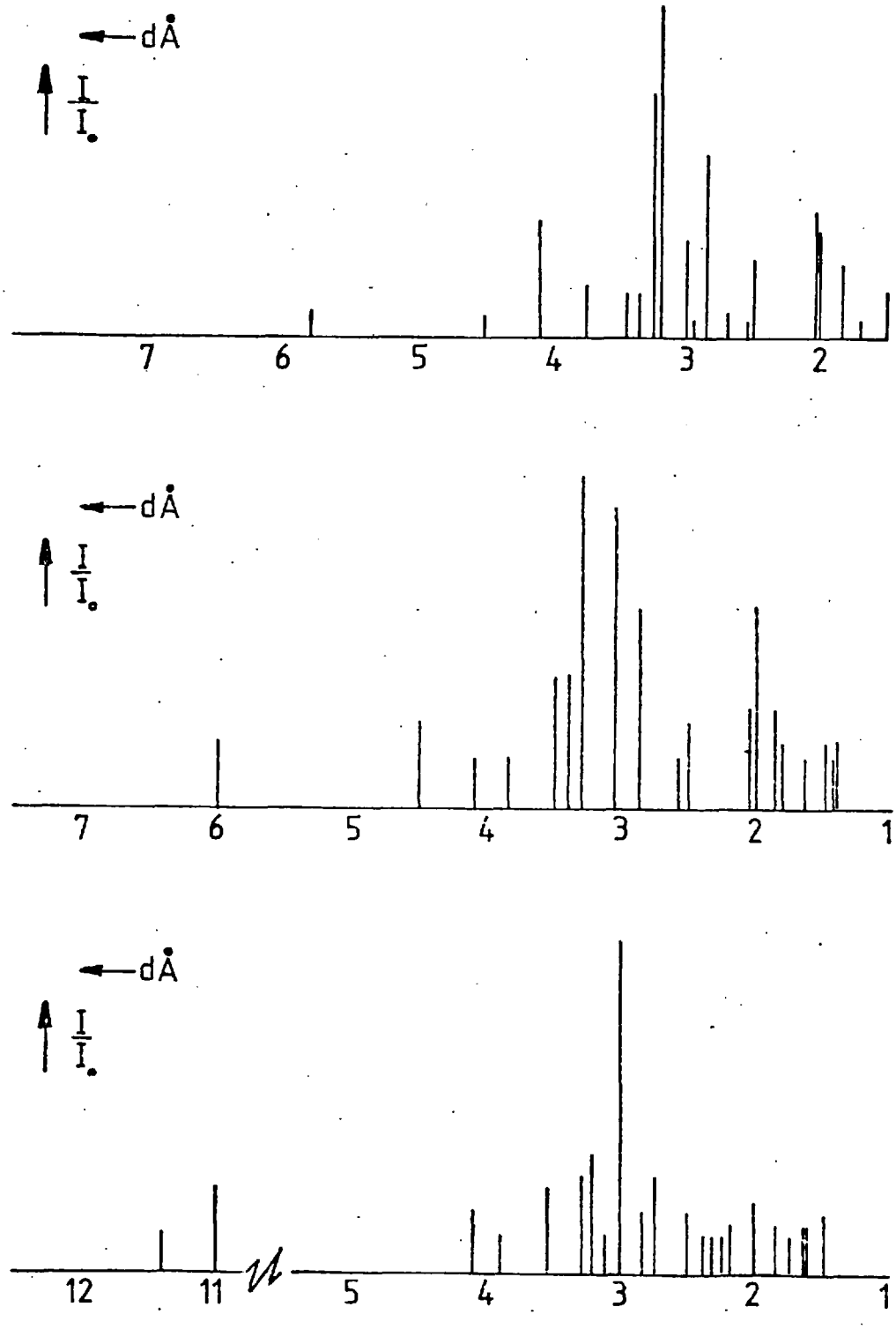
42 µm

Fig. 3.18 RW7 after 54 hours at 1020 °C, X-polars.



42 µm

Fig. 3.26 α-$CaSiO_3$ dendrites grown at 1160 °C in RW9, X-polars.



X-ray diffraction intensities.

Fig. 3.21 RW8 after 20 hours at 1025 °C.

Fig. 3.23 RW9 after 10 minutes at 1160 °C.

Fig. 3.24 RW9 after 20 minutes at 1160 °C.

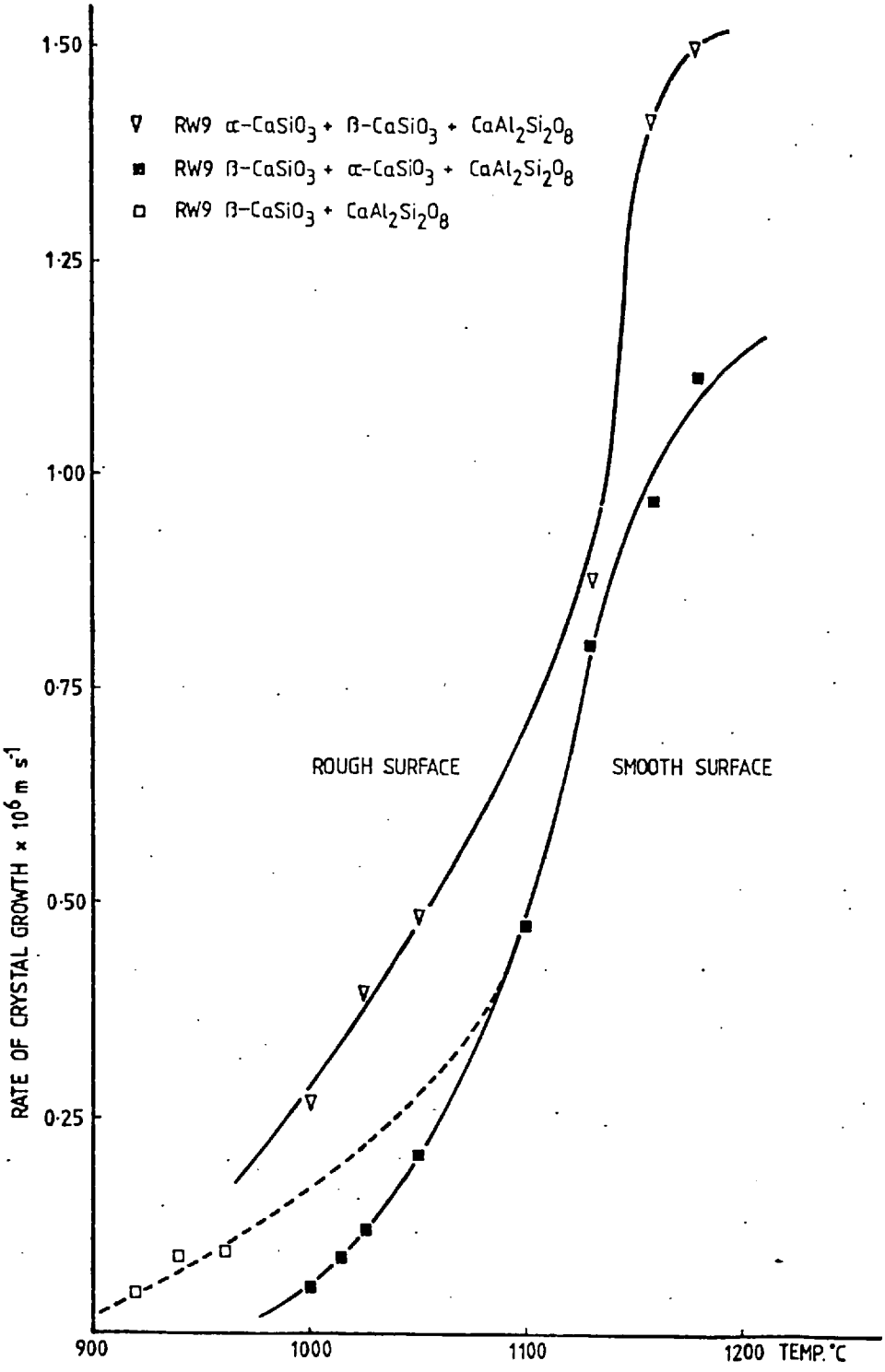
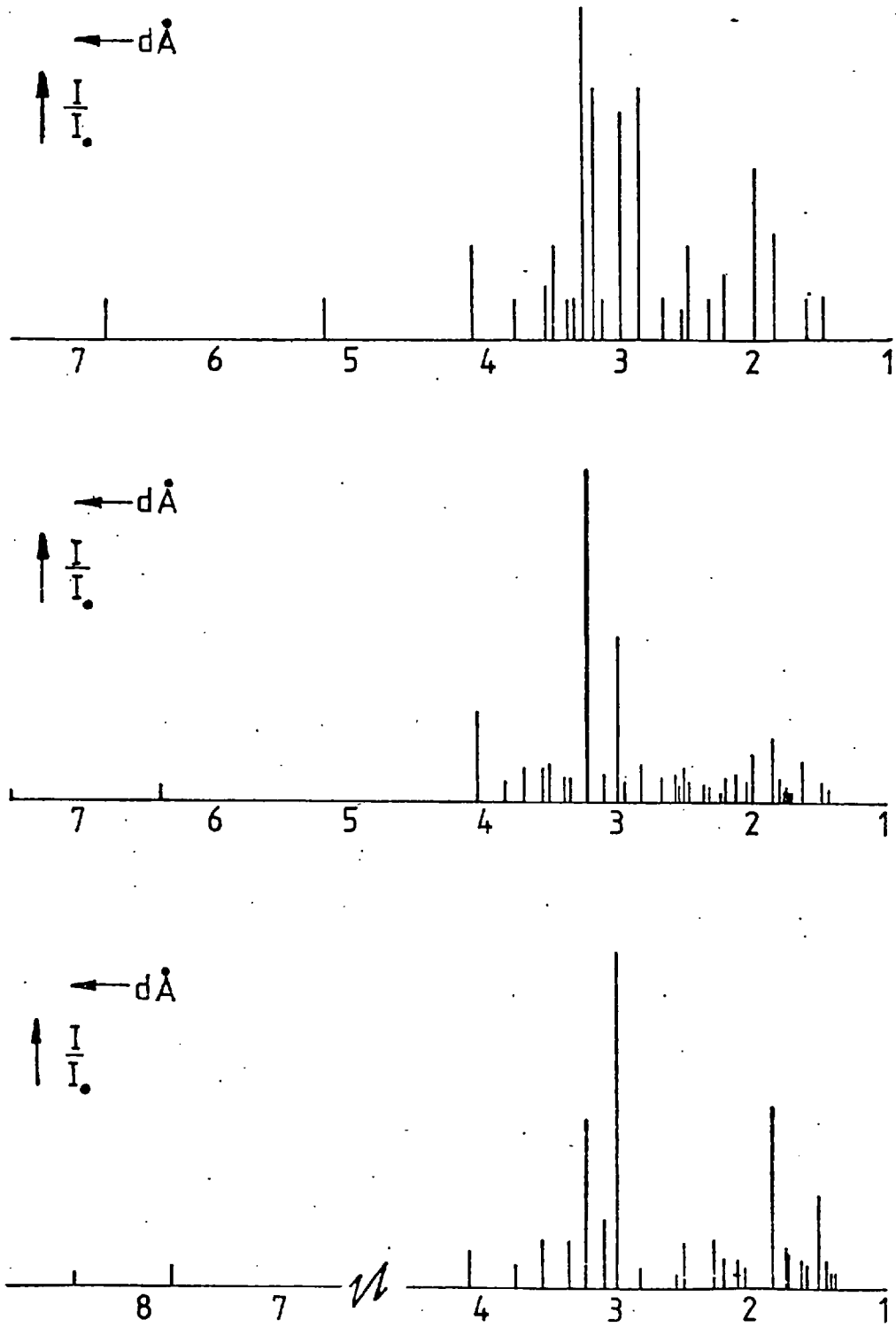


Fig. 3.22 Crystal growth rate versus temperature, RW9 composition.



X-ray diffraction intensities .

Fig. 3.25 RW9 after 30 minutes at 1160 °C

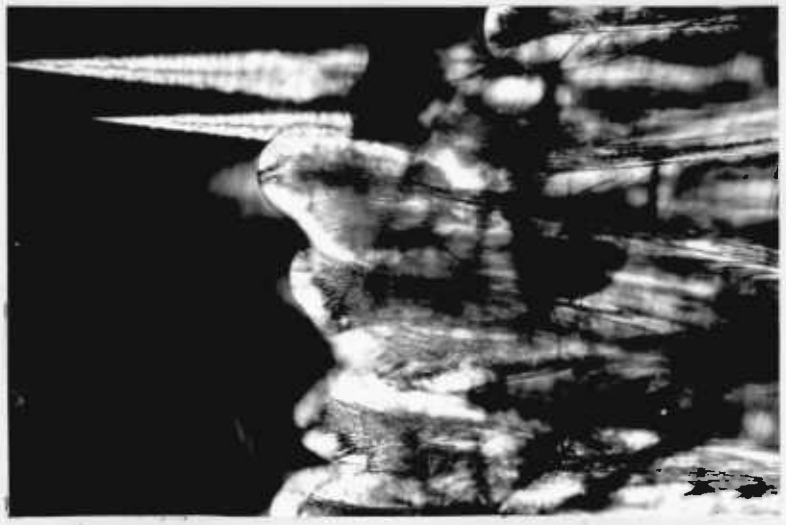
Fig. 3.28 RW9/3T tile after 1 hours at 1180 °C .

Fig. 3.30 RW9/4T tile after 1 hours at 1180 °C .



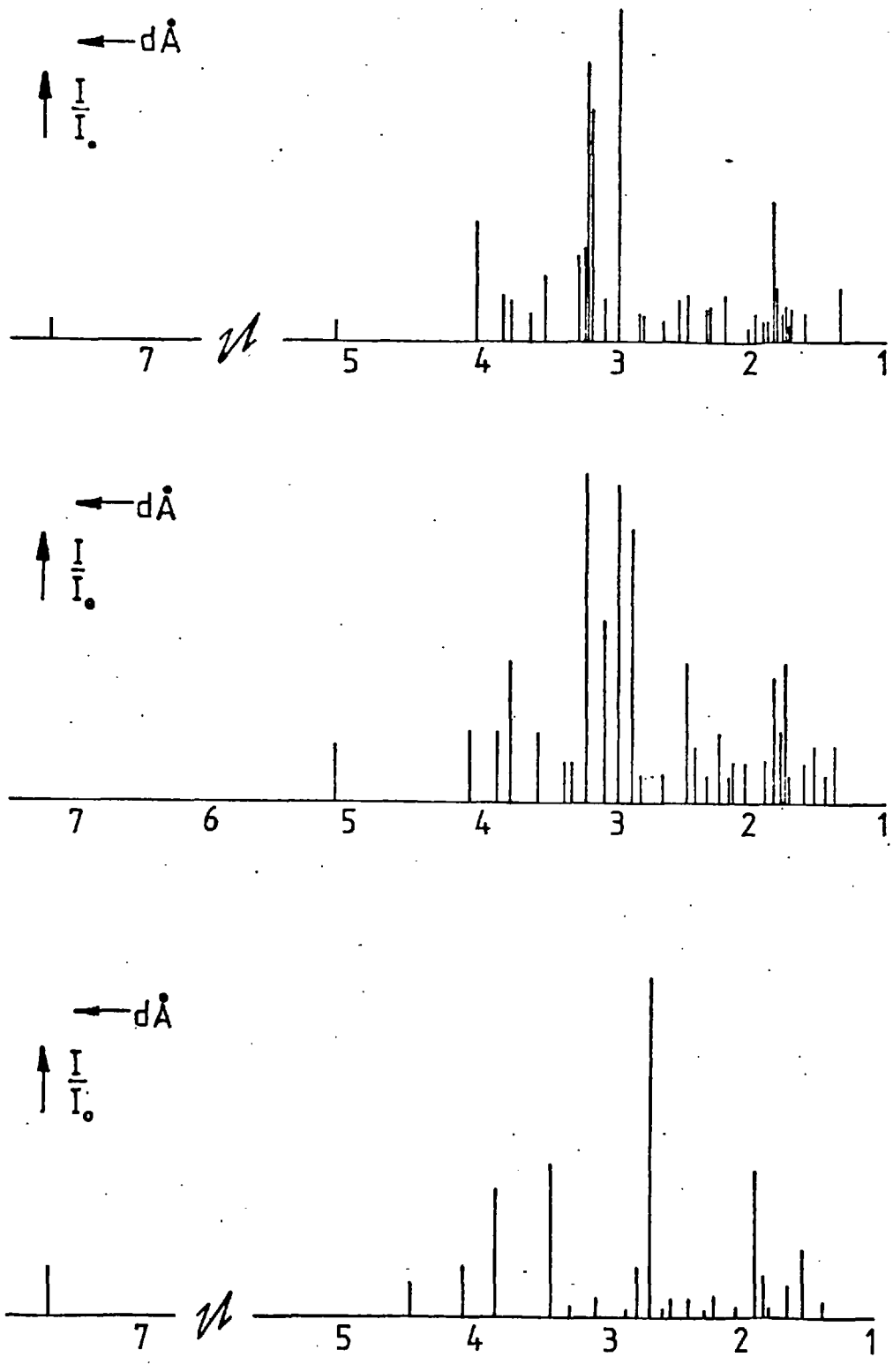
42 µm

Fig. 3.27 Surface nucleation in RW9 at 980°C, X-polars.



42 µm

Fig. 3.29 β-$CaSiO_3$ spherulitic fibres and α-$CaSiO_3$ dendrites coexisting in RW9/3T tile, X-polars.

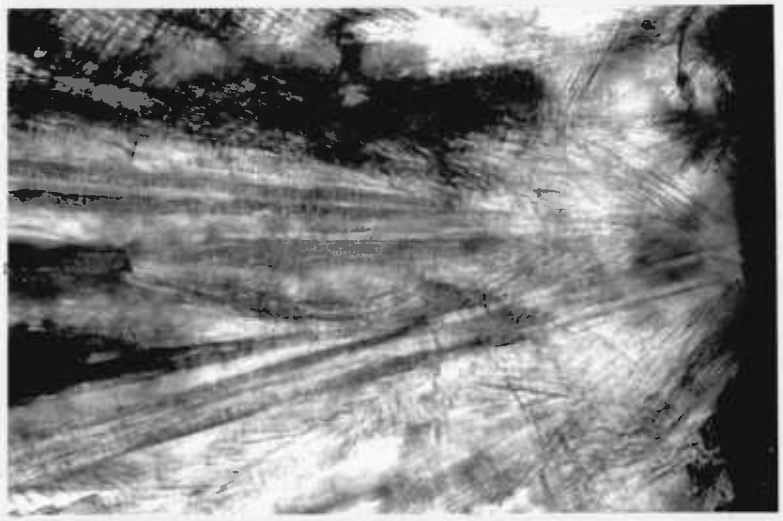


X-ray diffraction intensities.

Fig. 3.31 RW9/6T tile after 1 hour at 1180 °C.

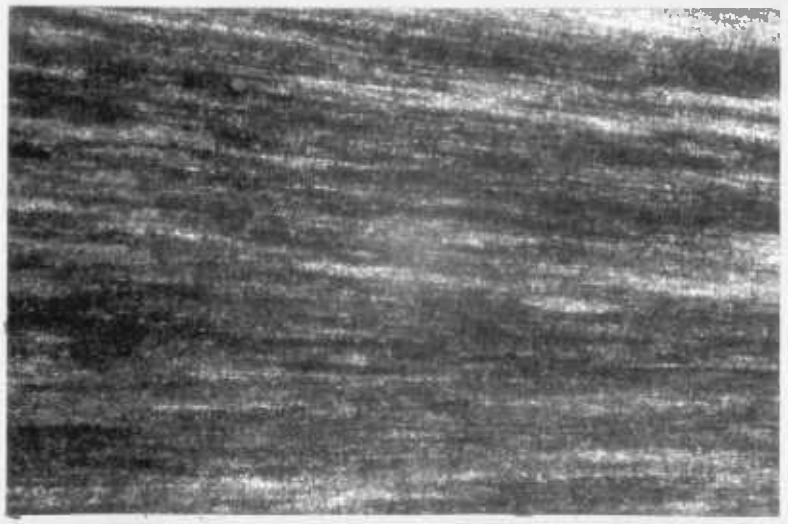
Fig. 3.33 RW9/7C intracrucible material after 9 hours at 1180 °C.

Fig. 3.36 RW10 after 30 minutes at 906 °C.



10 µm

Fig. 3.32 Surface nucleation of β-$CaSiO_3$ and $CaAl_2Si_2O_8$ secondary crystallization in RW9/4T tile, X-polars .



42 µm

Fig. 3.43 RW14 after 30 minutes at 1104 °C, X-polars .

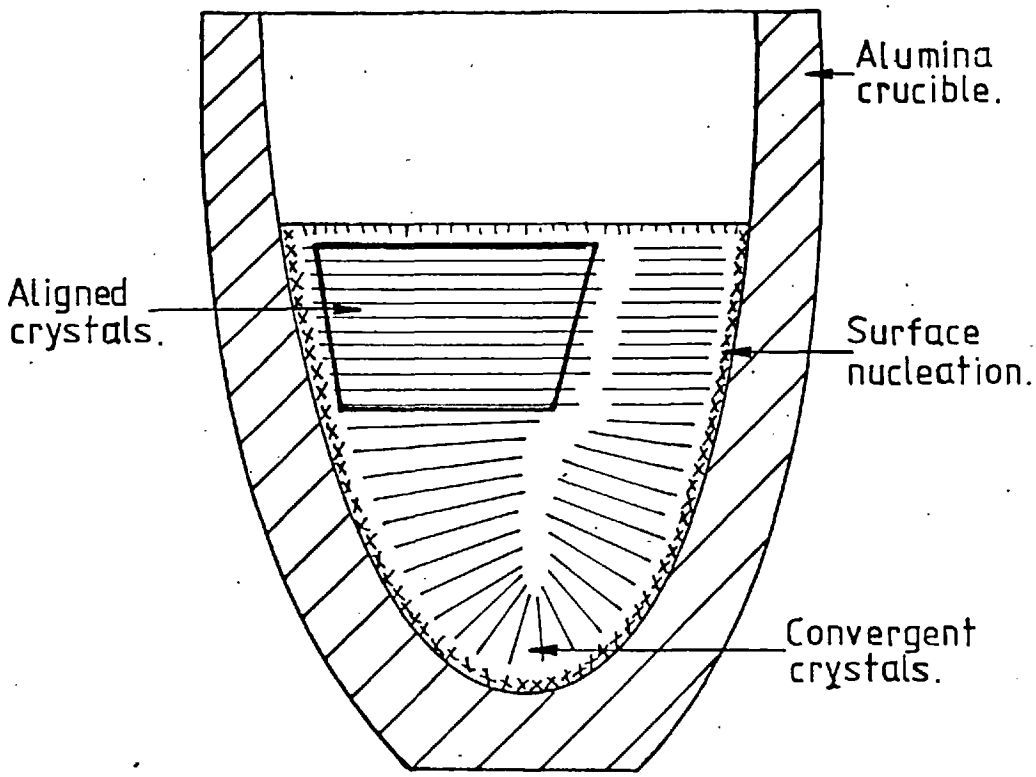


Fig. 3.34 Diagramatic section through crucible containing RW9/7C after 9 hours at 1180 °C .

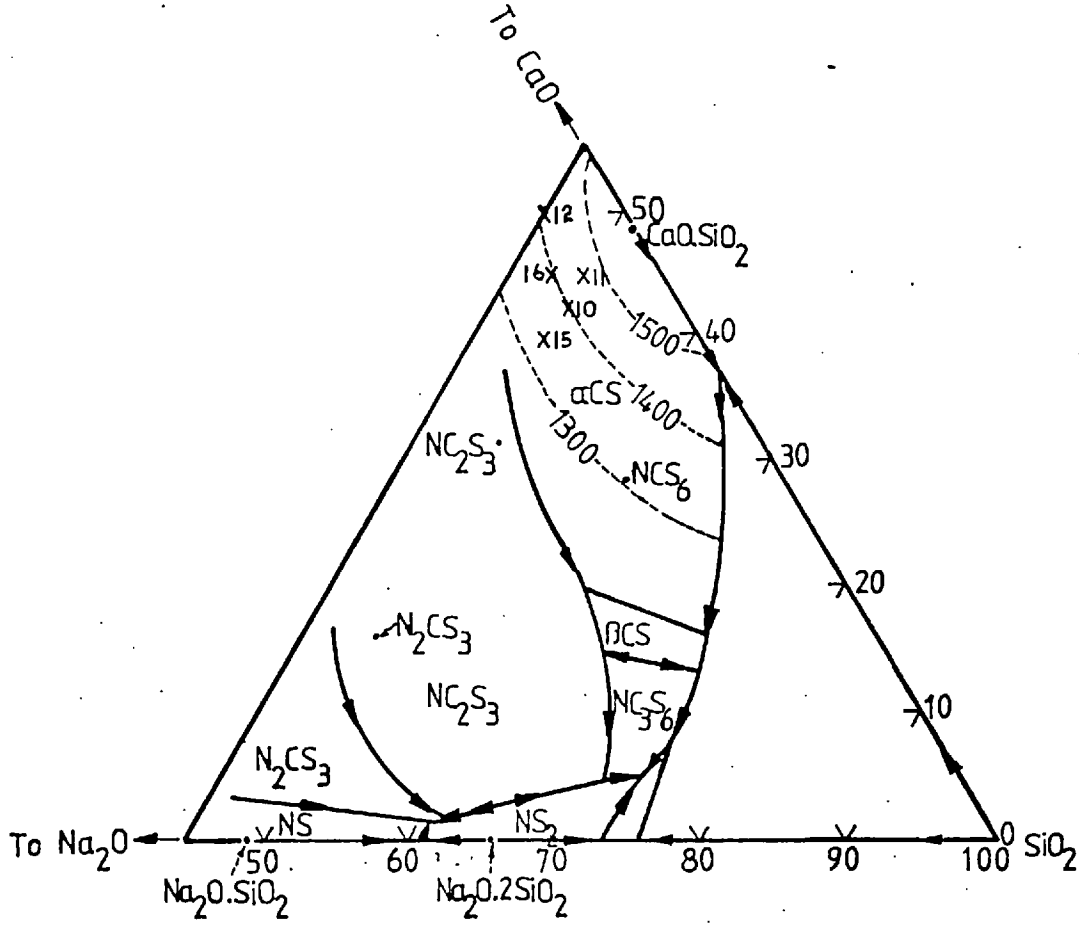
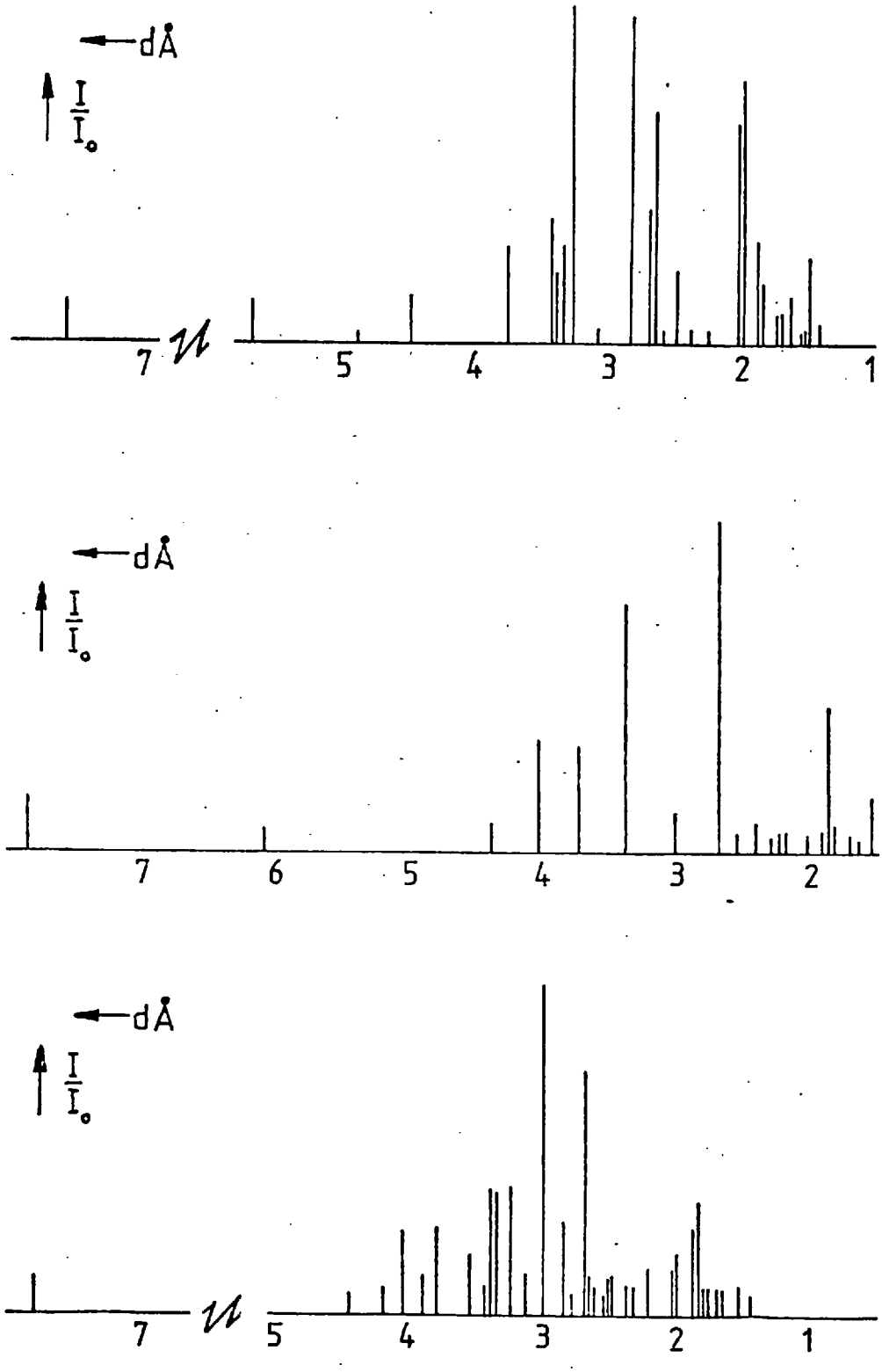
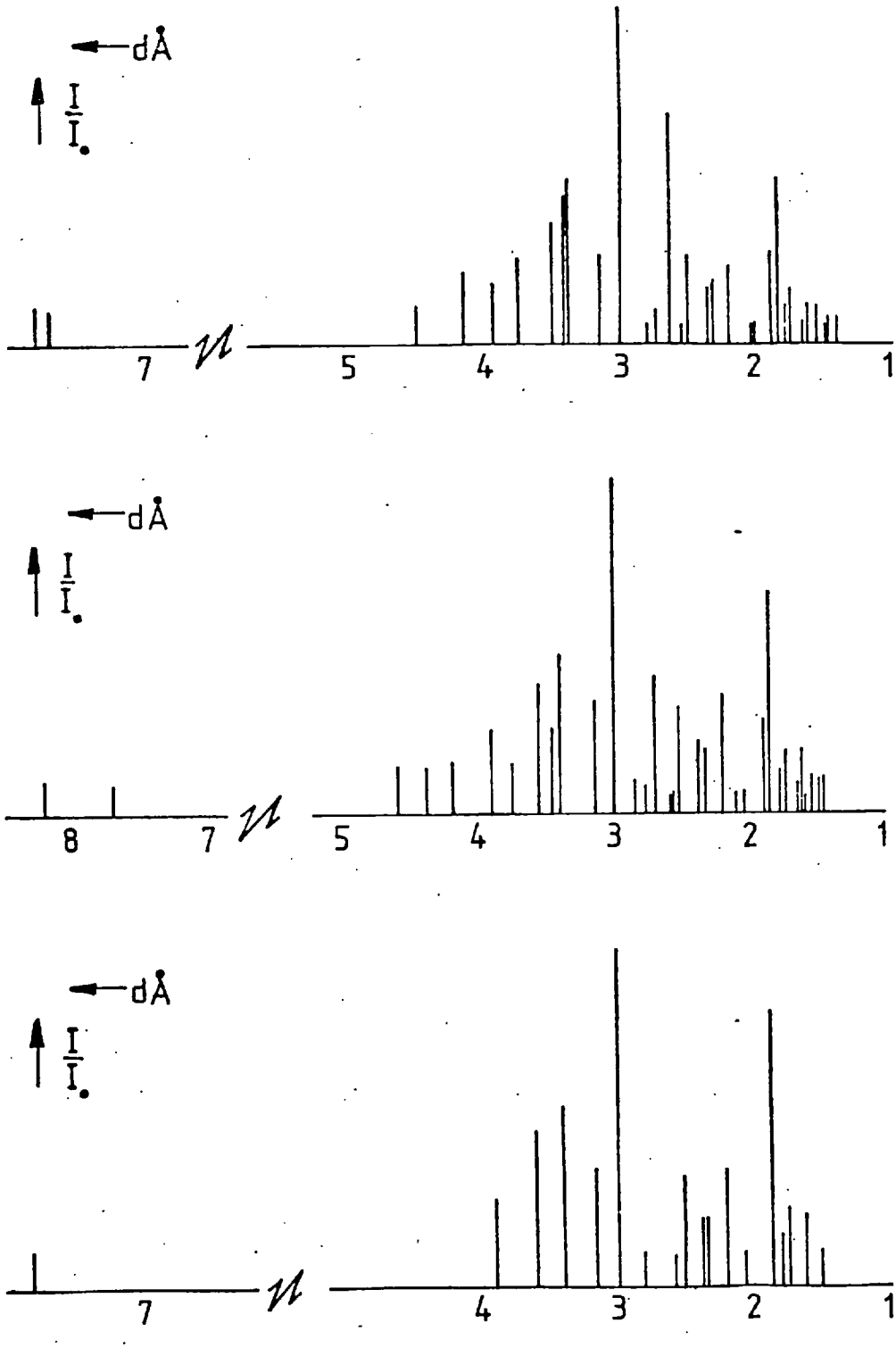


Fig. 3.35 $Na_2O-CaO-SiO_2$ phase diagram (ref. 127).



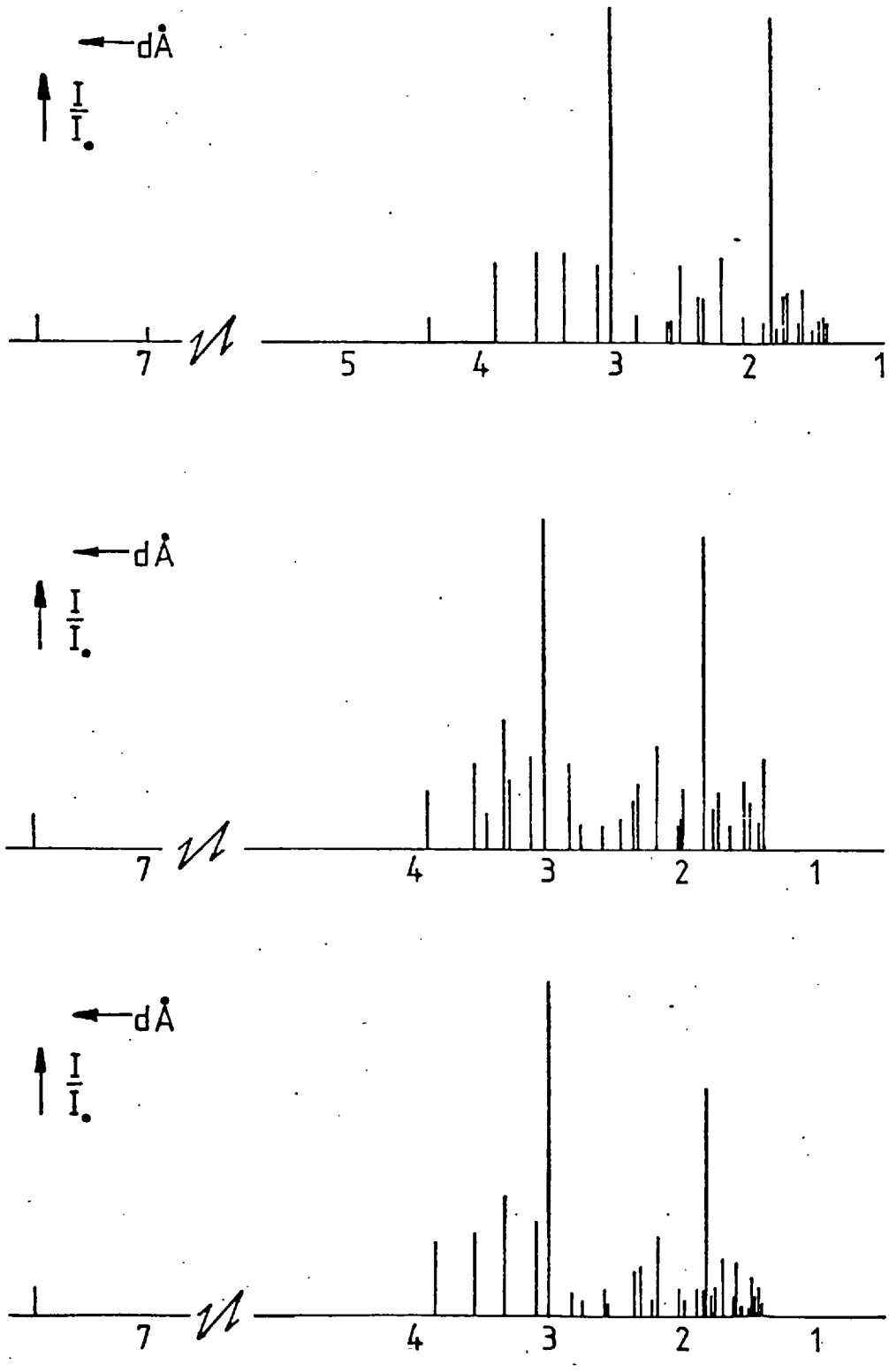
X-ray diffraction intensities .

Fig. 3.37 RW10 after 30 minutes at 1059 °C .
Fig. 3.38 RW13 after 30 minutes at 990 °C .
Fig. 3.39 RW13 after 30 minutes at 1030 °C .



X-ray diffraction intensites.

Fig. 3.40 RW14 after 30 minutes at 950 °C.
Fig. 3.41 RW14 after 30 minutes at 1000 °C.
Fig. 3.42 RW14 after 30 minutes at 1045 °C.



X-ray diffraction intensities.

Fig. 3.44 RW14/2T tile after 30 minutes at 1104 °C.
Fig. 3.45 RW14/4T tile after 30 minutes at 1098 °C.
Fig. 3.46 RW14/5T tile after 30 minutes at 1091 °C.

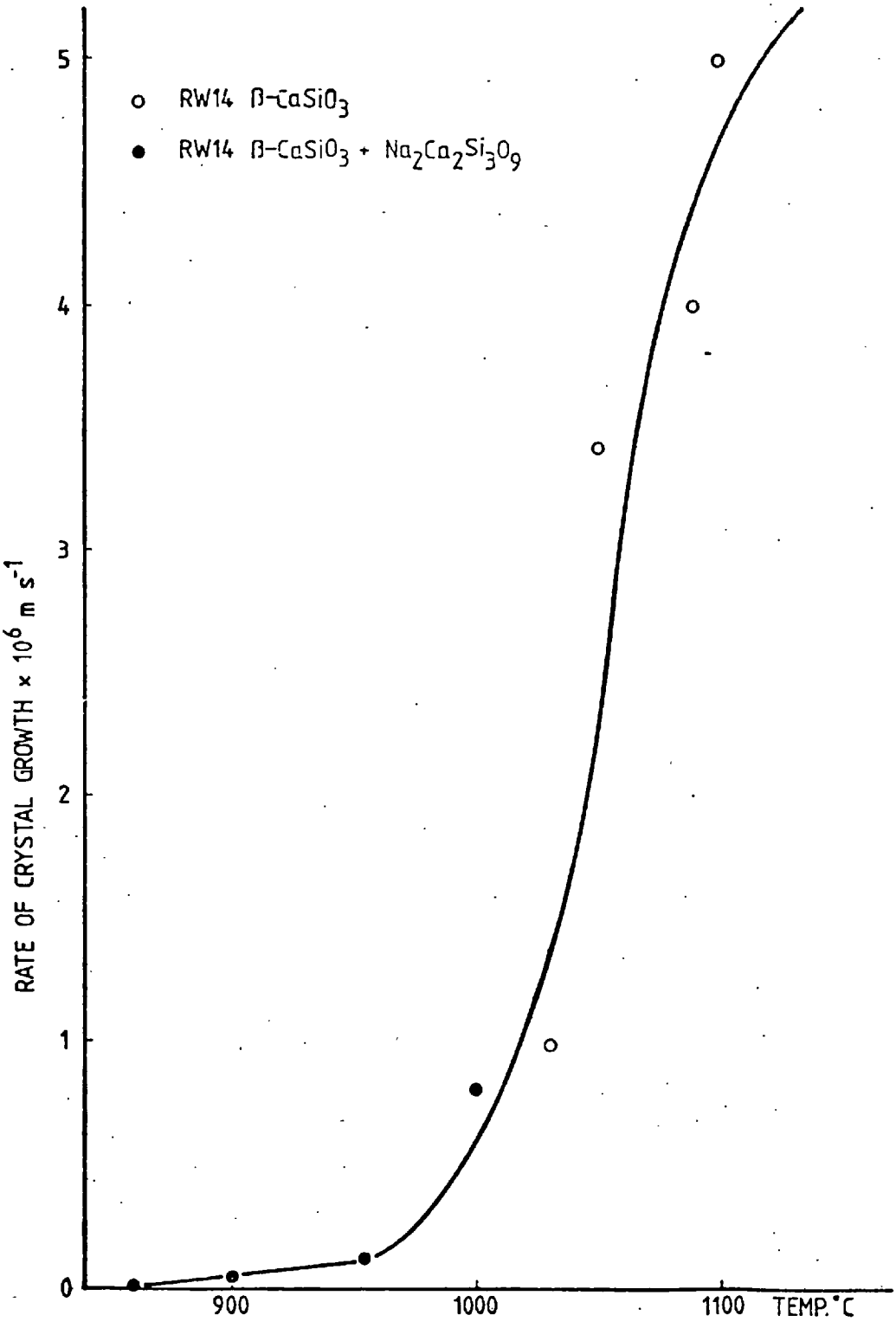
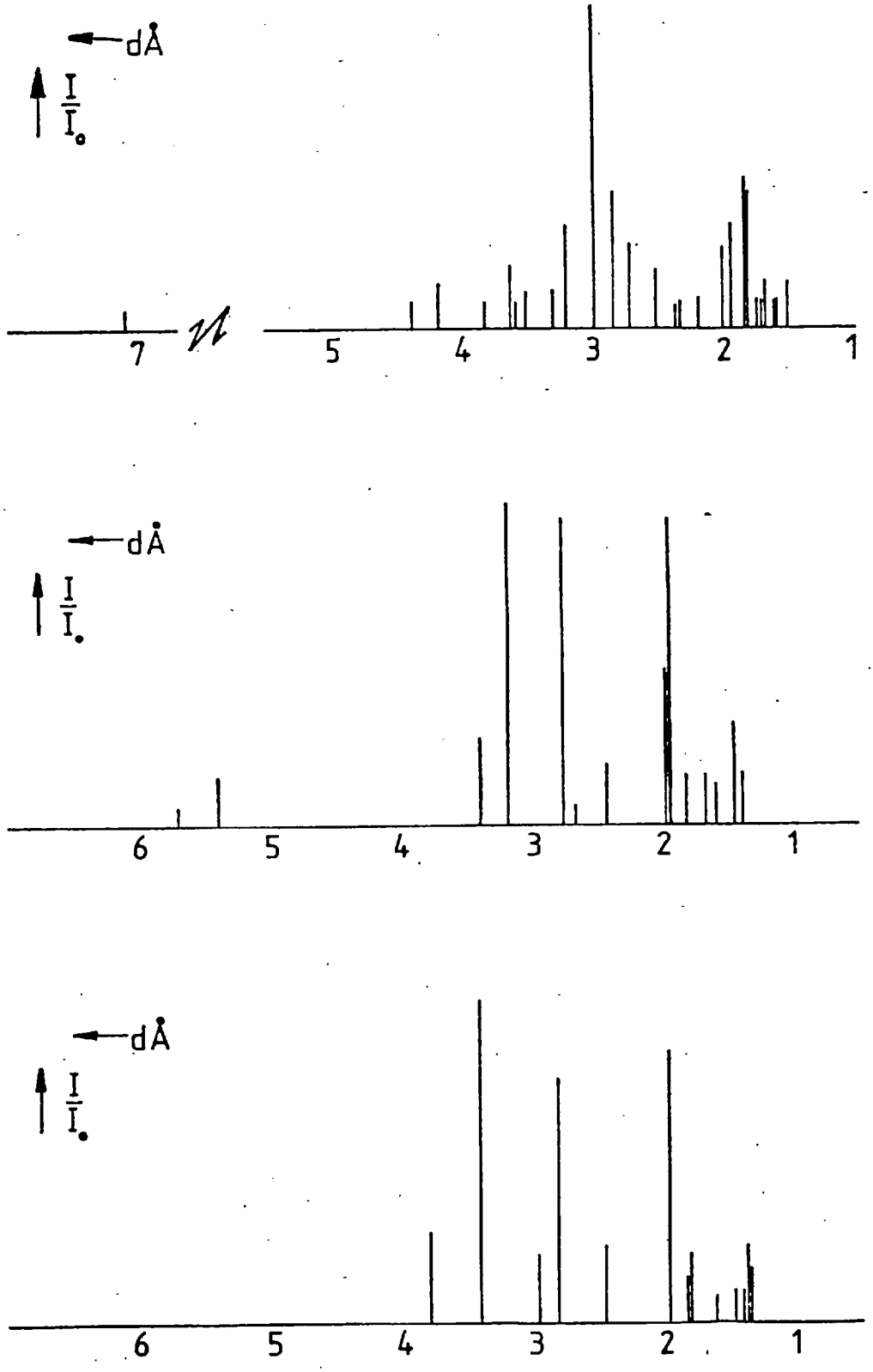


Fig. 3.47 Crystal growth rate versus temperature, RW14 composition.

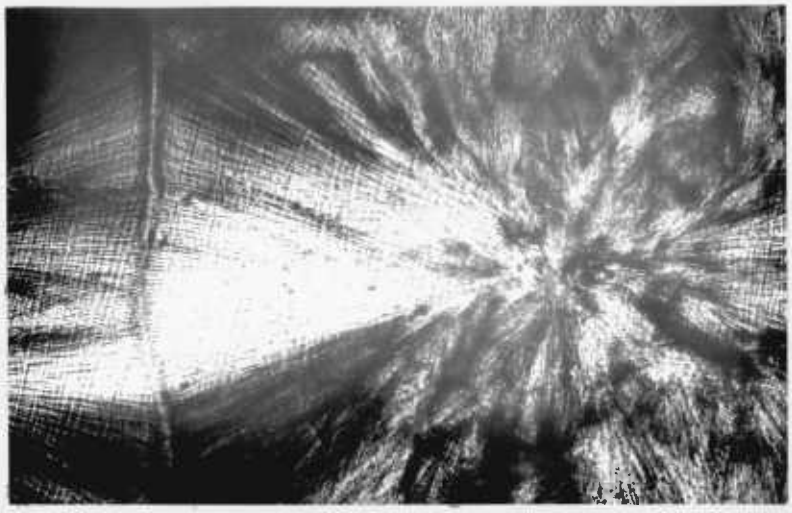


X-ray diffraction intensities.

Fig. 3.48 RW14F tile after 1 hour at 900 °C.

Fig. 3.50 RW14 rod, pulled from 1470 °C at 52 μm s^{-1}.

Fig. 3.52 RW15 rod, pulled from 1450 °C at 280 μm s^{-1}.



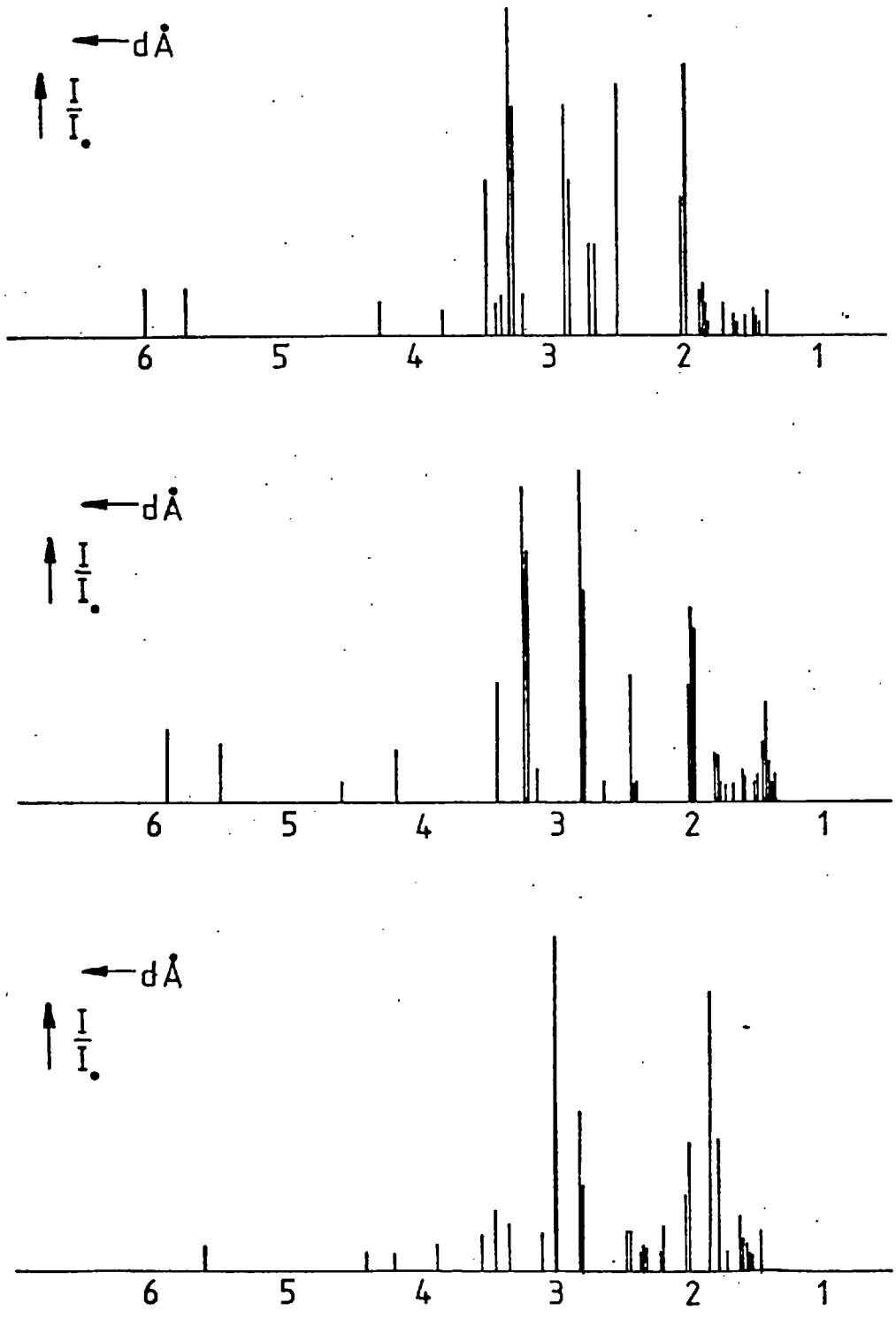
42 μm

Fig. 3.49 RW14F after 1 hour at 900 °C, X-polars .



42 μm

Fig. 3.51 RW14 rod, pulled from 1470 °C at 20 μm s^{-1}, quenched growth front, X-polars .



X-ray diffraction intensities.

Fig. 3.53 RW16 rod, pulled from 1450 °C at 114 μm s^{-1}.

Fig. 3.57 RW17/a rod, see table 3.39.

Fig. 3.58 RW17/i rod, see table 3.39.

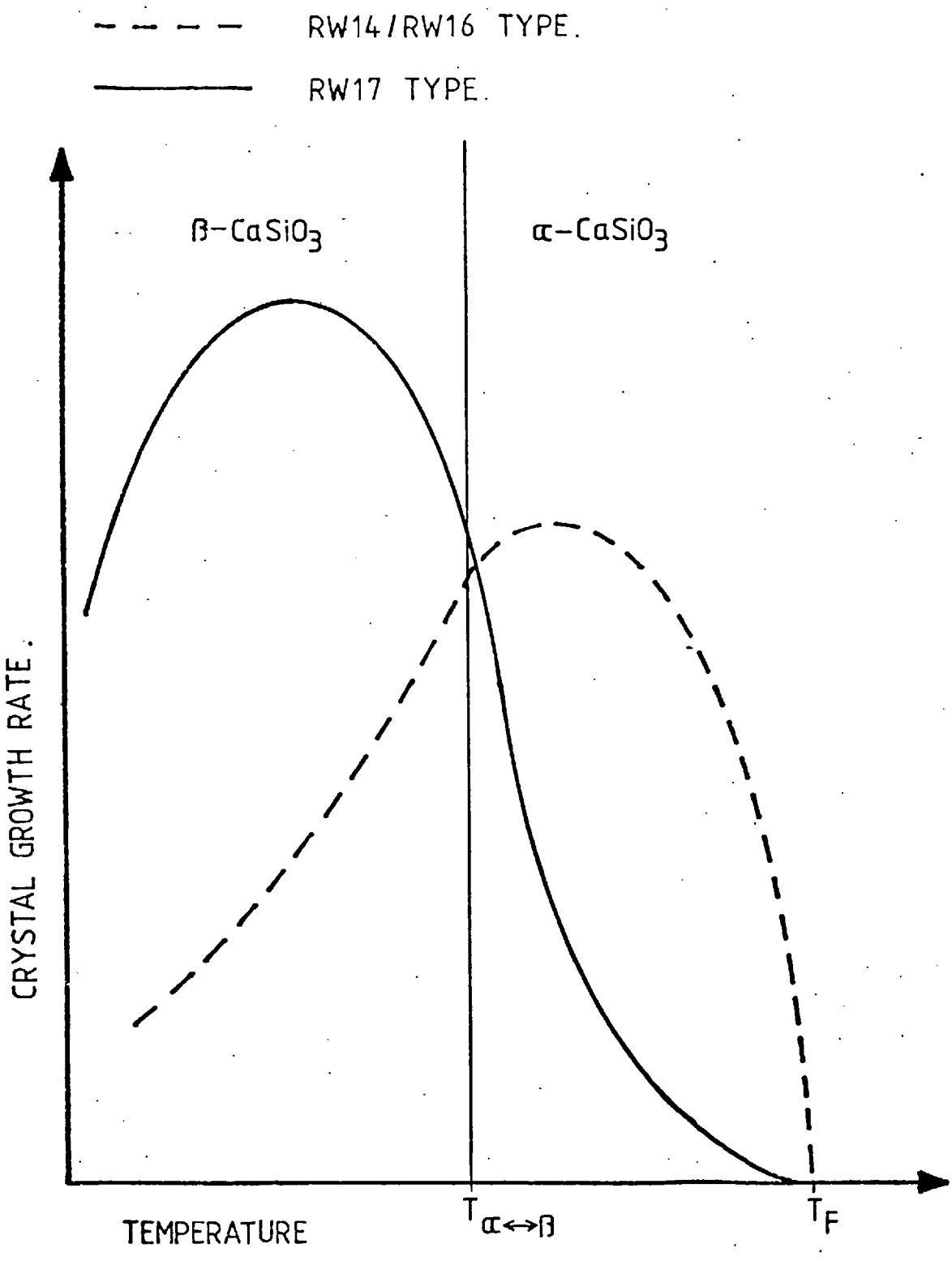


Fig. 3.54 Hypothetical U versus T curves.

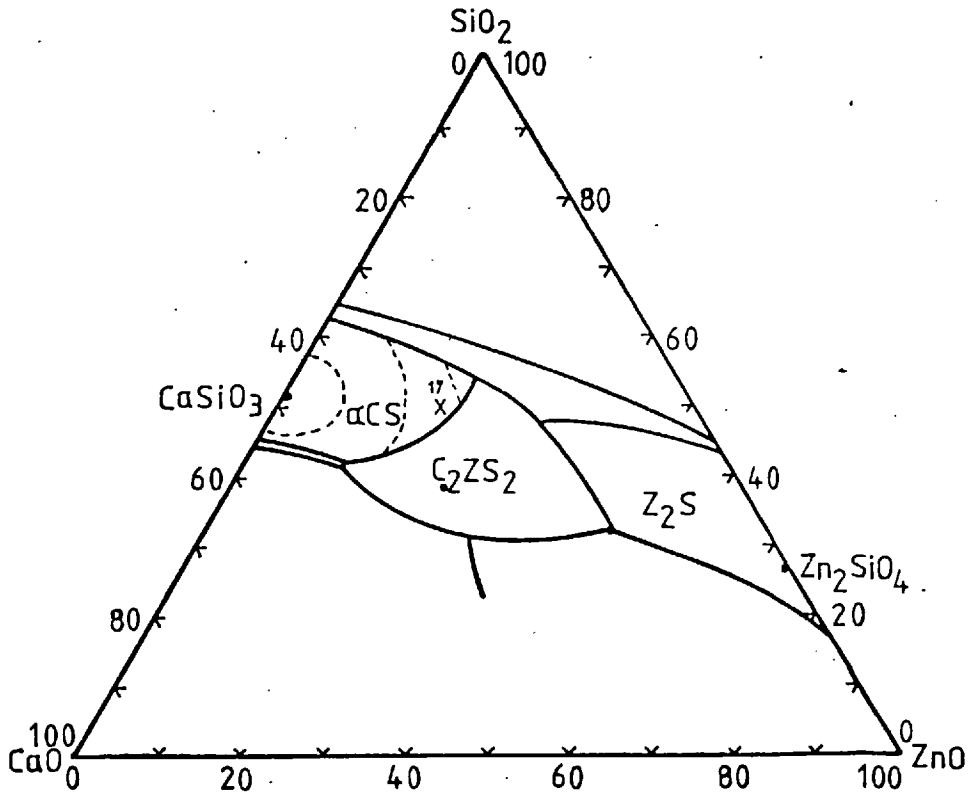


Fig. 3.55 · CaO-ZnO-SiO_2 phase diagram (ref. 127) .

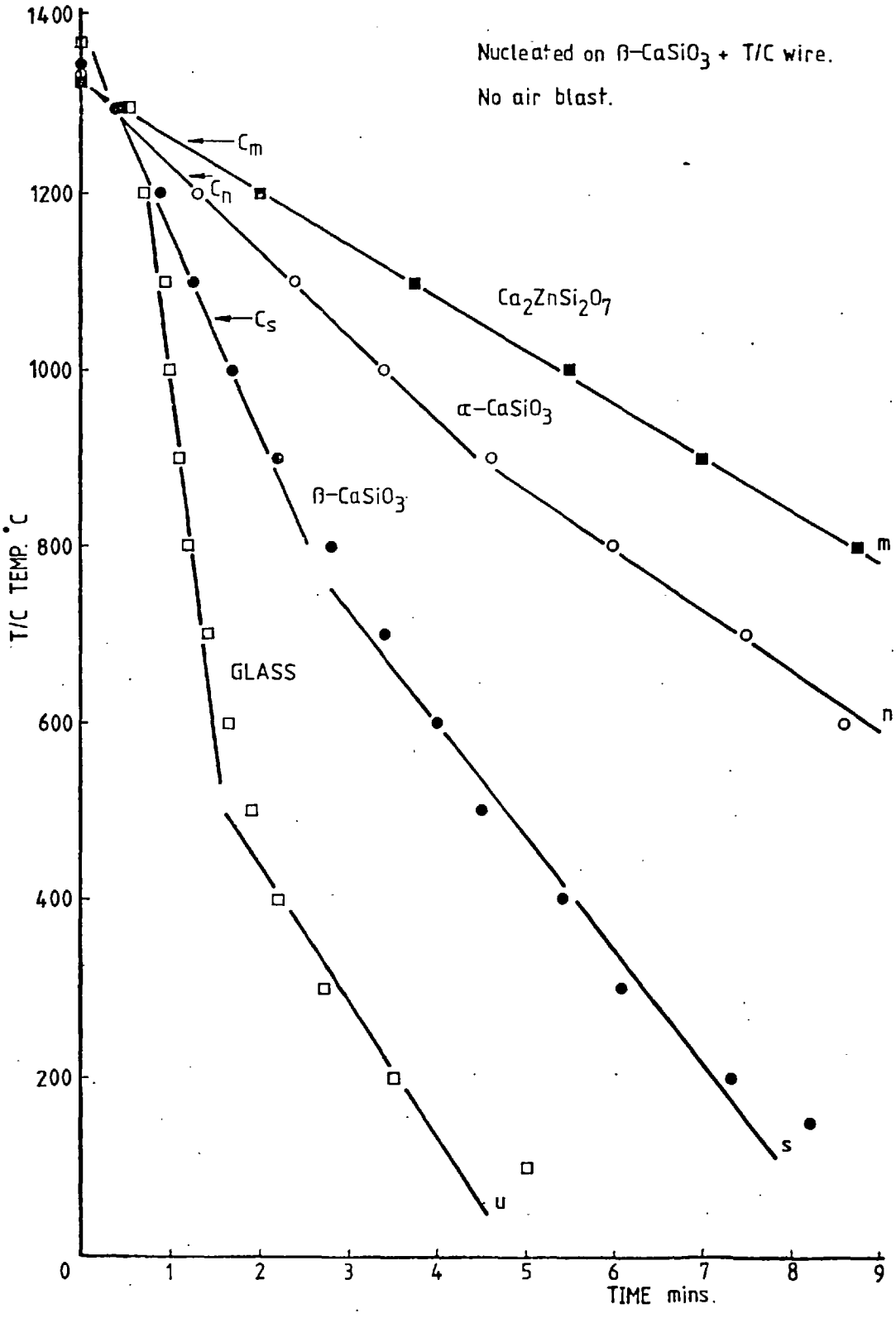


Fig. 3.56 Cooling rate of RW17 rods nucleated on β-$CaSiO_3$ + Pt/Pt-13%Rh T/C, no air blast.

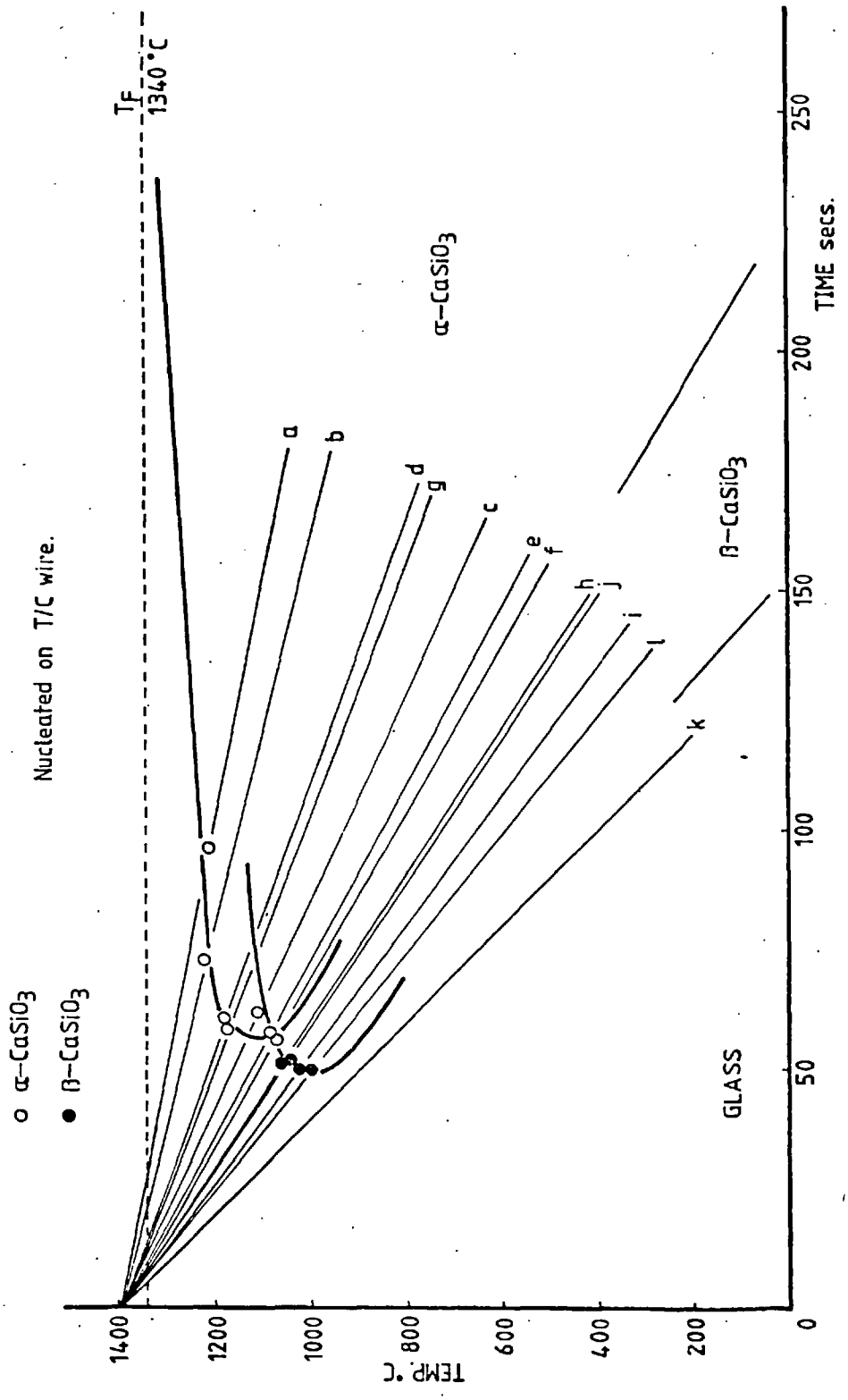
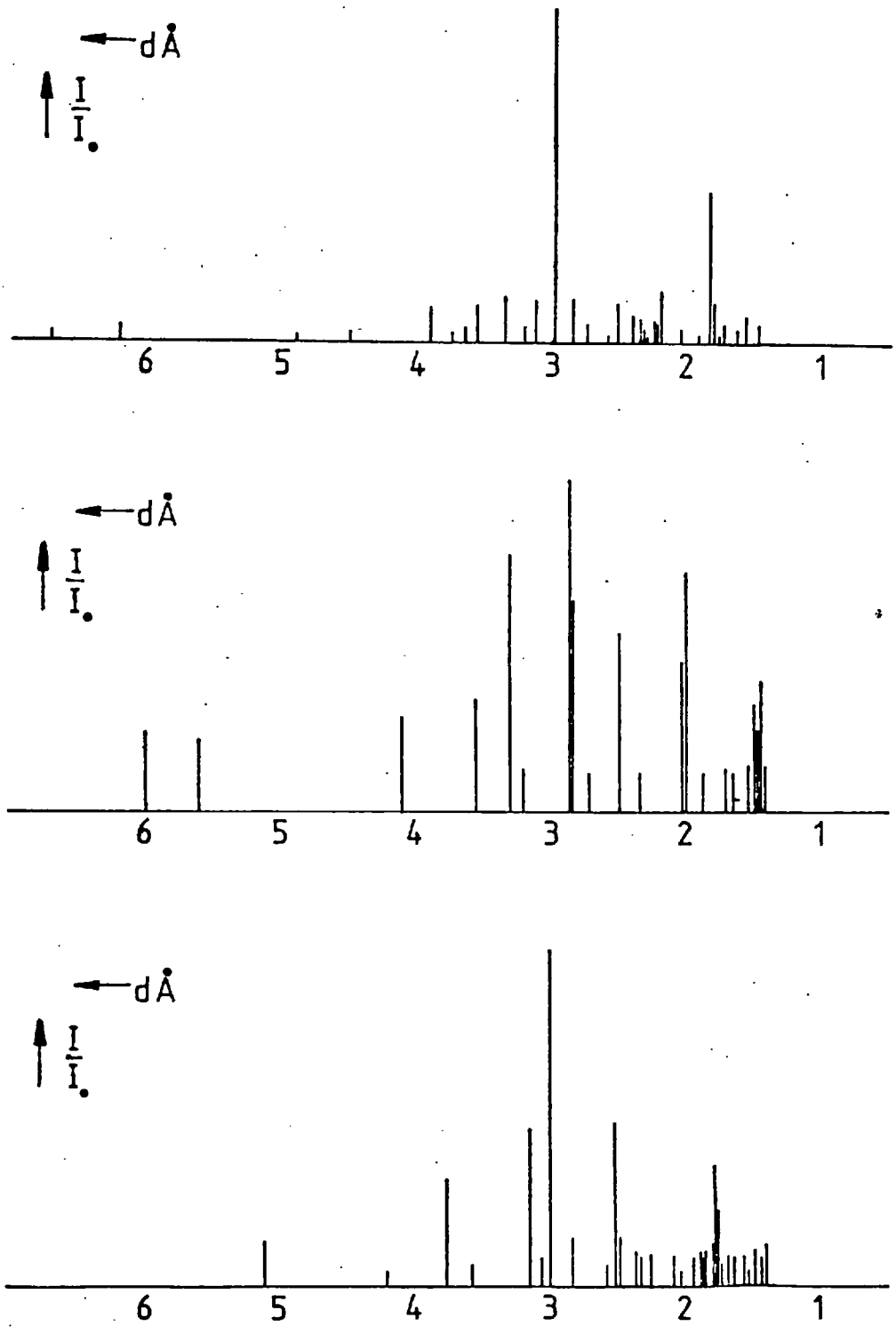


Fig. 3.59 T–T–T diagram for RW17 rods nucleated on Pt/Pt-13Rh T/C wire .

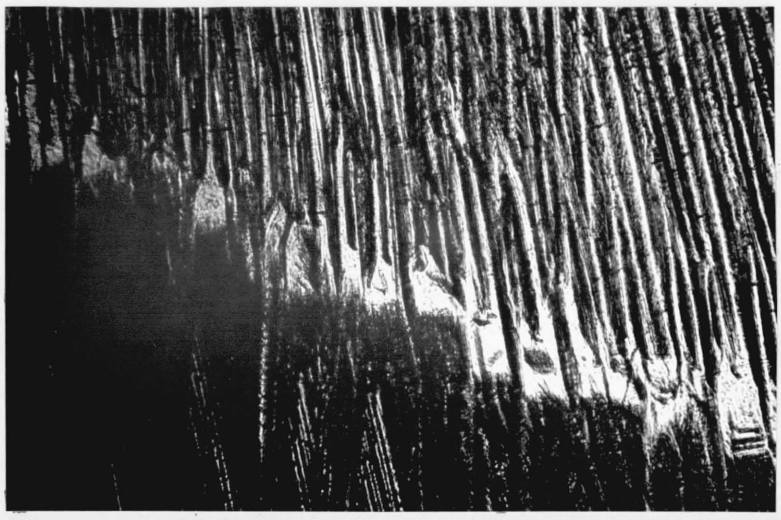


X-ray diffraction intensities .

Fig. 3.60 RW17/s rod, see table 3.39 .

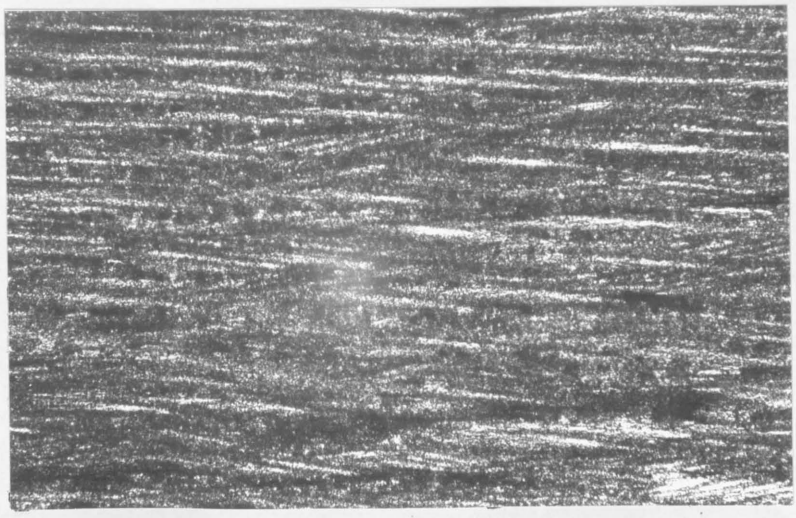
Fig. 3.61 RW17/n rod, see table 3.39 .

Fig. 3.62 RW17/m rod, see table 3.39 .



42 µm

Fig. 3.63 RW17/m rod (see table 3.39), tabular directional crystallization of $Ca_2ZnSi_2O_7$, X-polars.



42 µm

Fig. 3.65 RW17/30B rod, pulled from 1410 °C at 30 µm s^{-1}, X-polars.

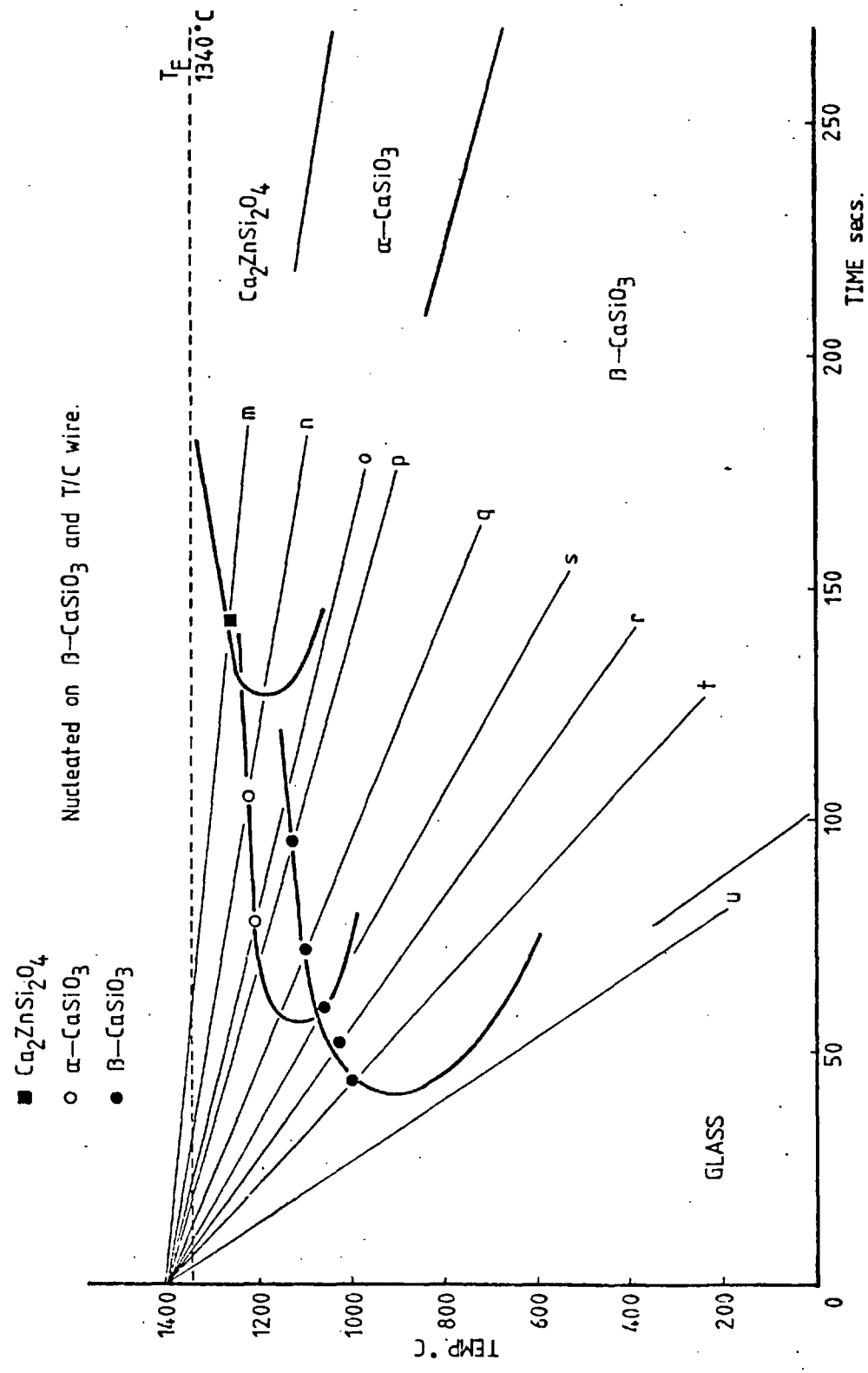
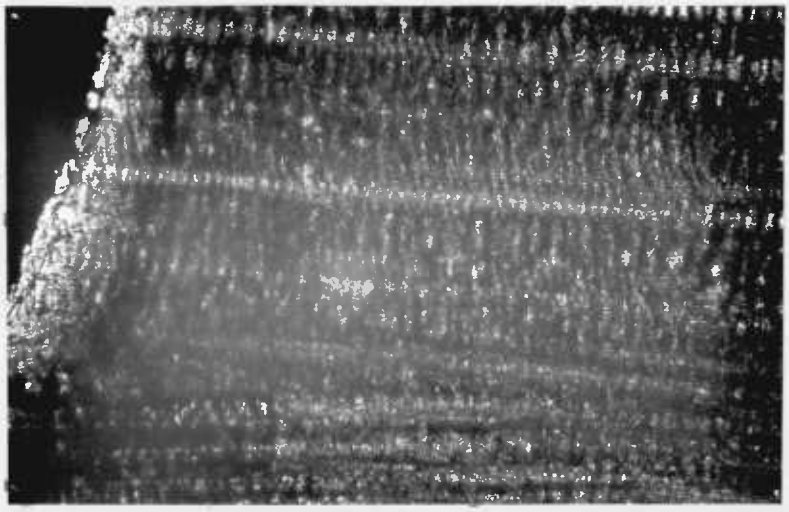


Fig. 3.64 T–T–T diagram for RW17 rods nucleated on β-$CaSiO_3$ seed crystal.



42 μm

Fig. 3.66 RW17/30α rod, pulled from 1410 °C at 30 μm s^{-1}, X-polars.



38 μm

Fig. 3.73 Reflected light photomicrograph of RW9/7C EPMA specimen.

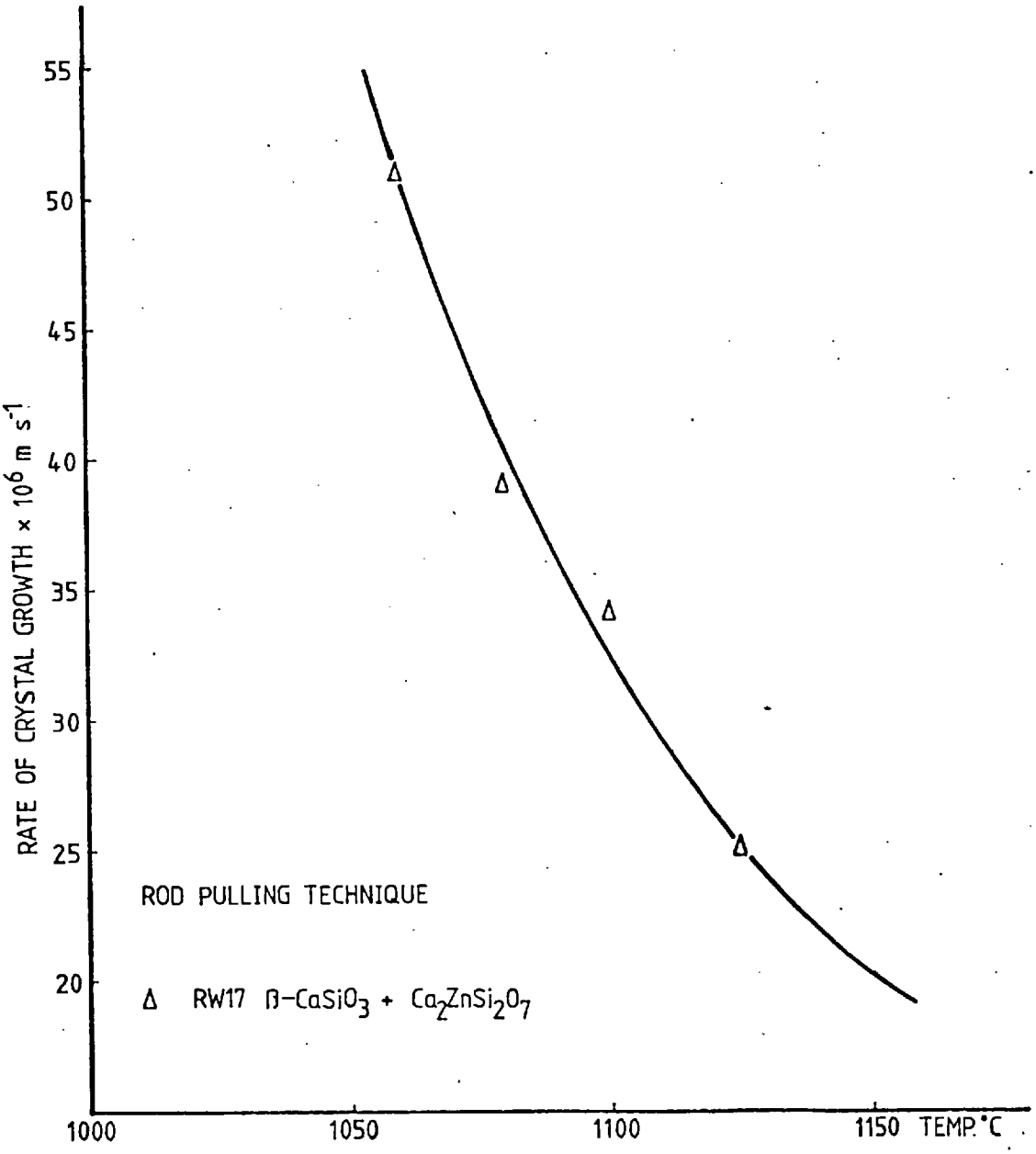
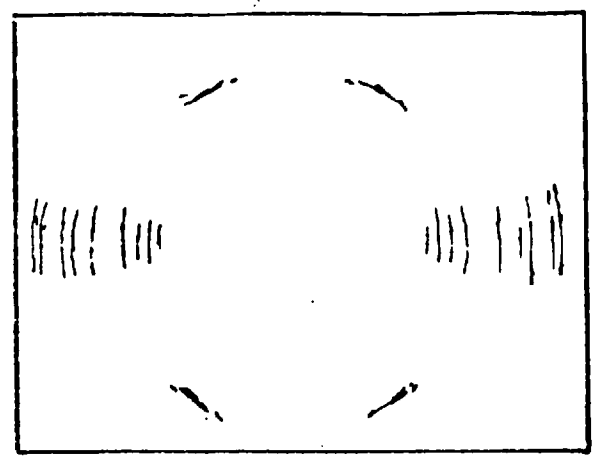
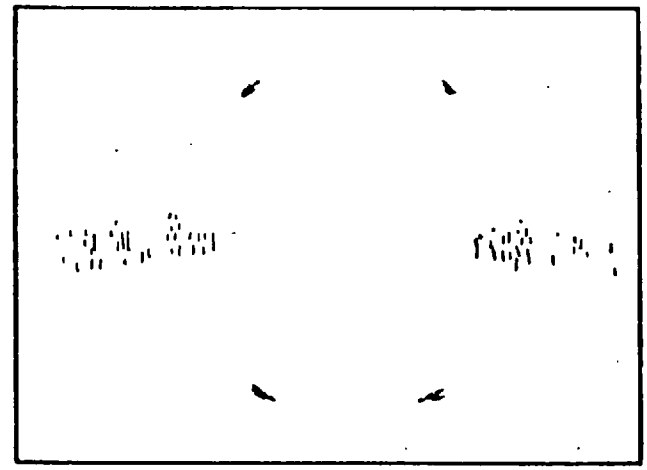
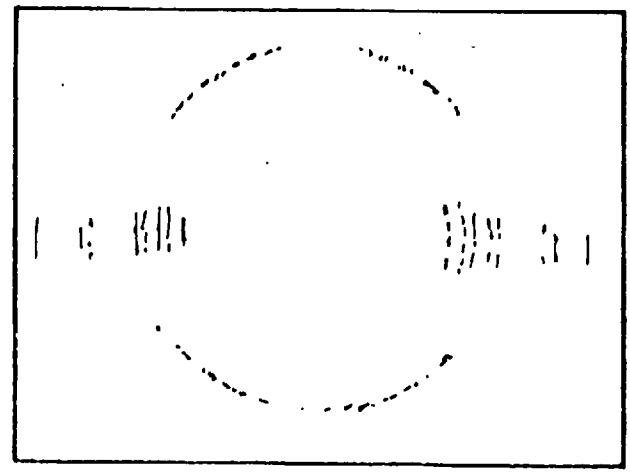


Fig. 3.67 Crystal growth rate versus temperature for β-$CaSiO_3$ rods pulled from RW17 melts.







Pinhole transmission X-ray diffraction patterns, fibre axes vertical.

Fig. 3.68 Wollastonite.

Fig. 3.69 RW17/30B rod, pulled at 30 $\mu m\ s^{-1}$.

Fig. 3.70 RW17/50B rod, pulled at 50 $\mu m\ s^{-1}$.

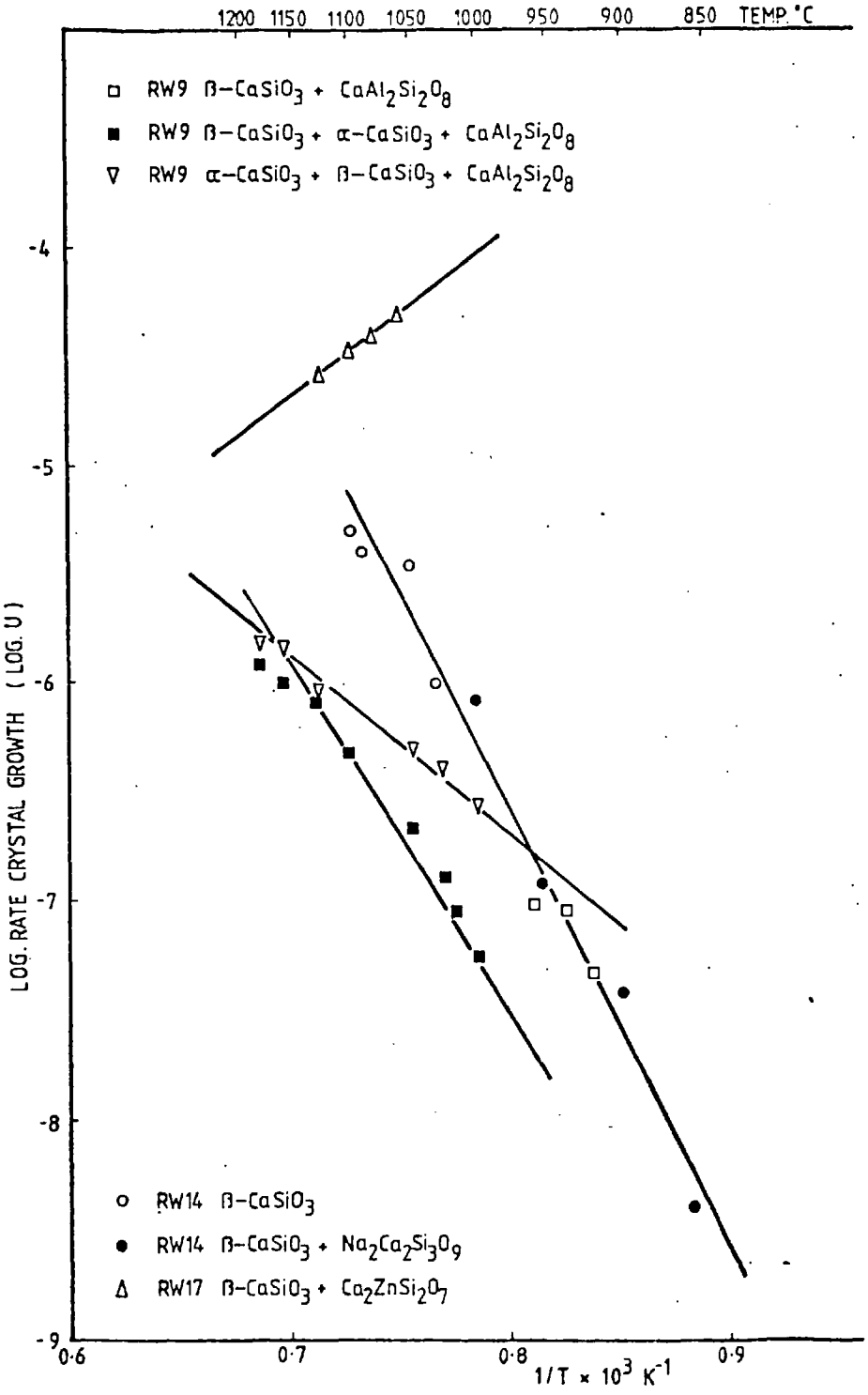


Fig. 3.71 Log U versus 1/T plots for crystal growth in RW 9, RW14 and RW17 glasses .

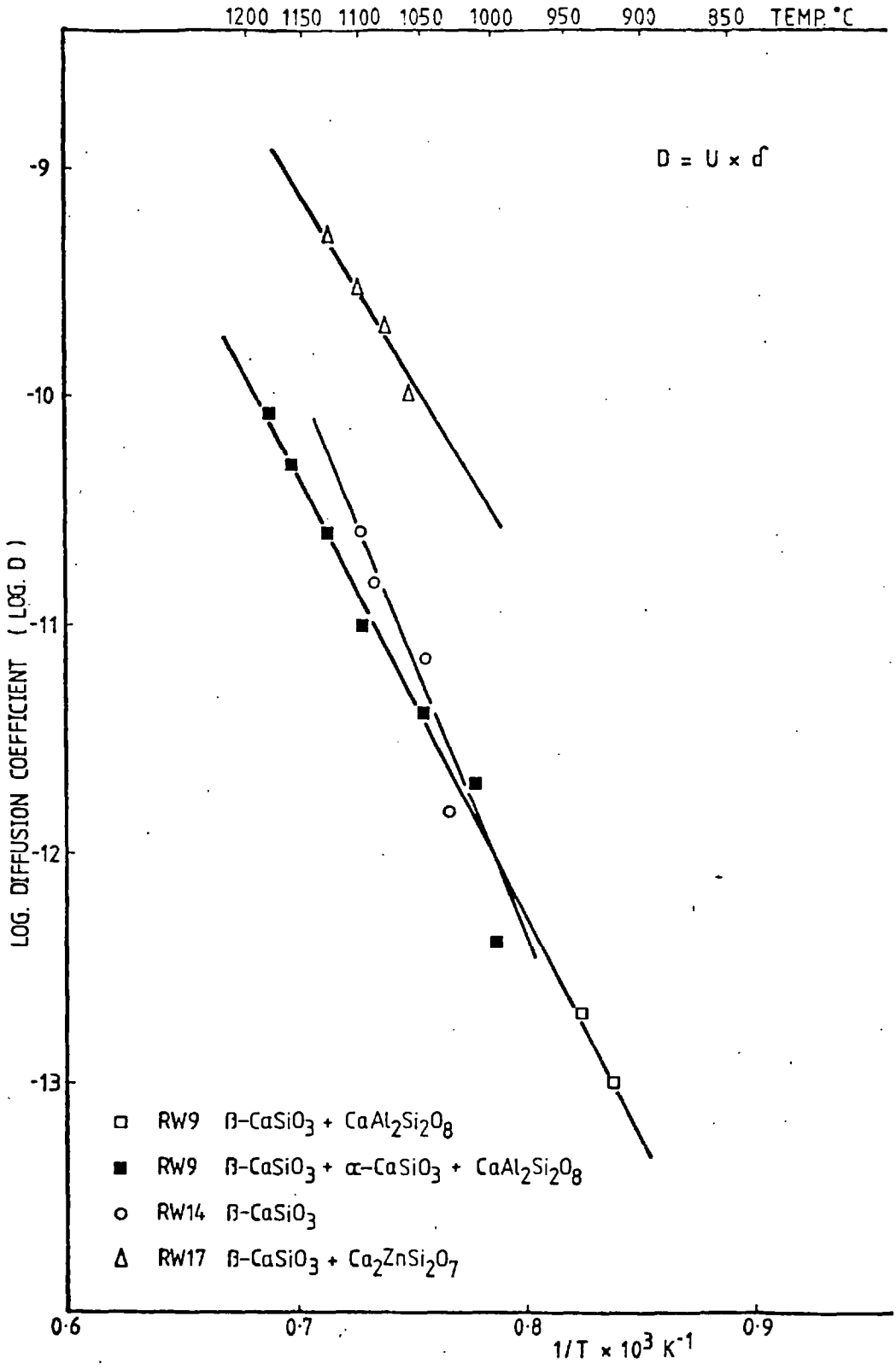
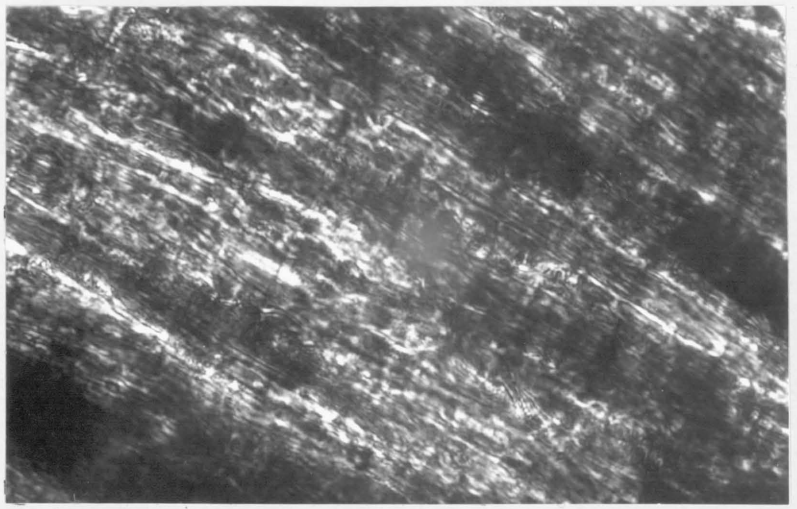
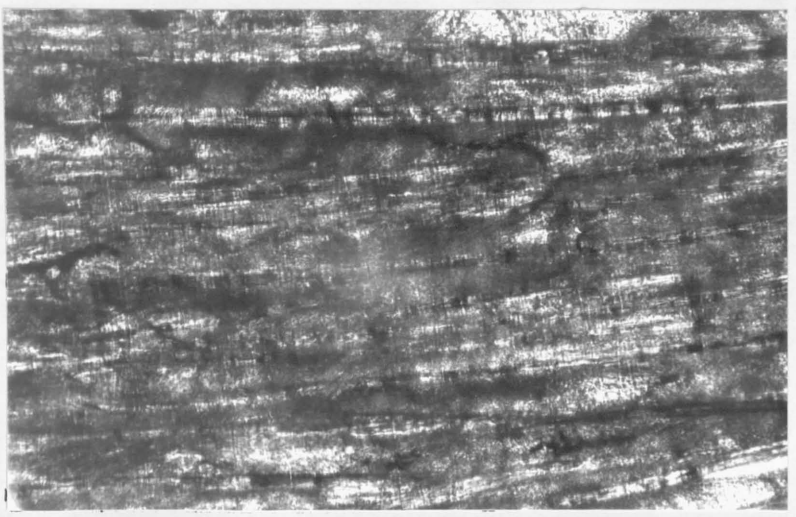


Fig. 3.72 Log D versus 1/T plots for spherulitic crystal growth in RW.9, RW14 and RW17 glasses .



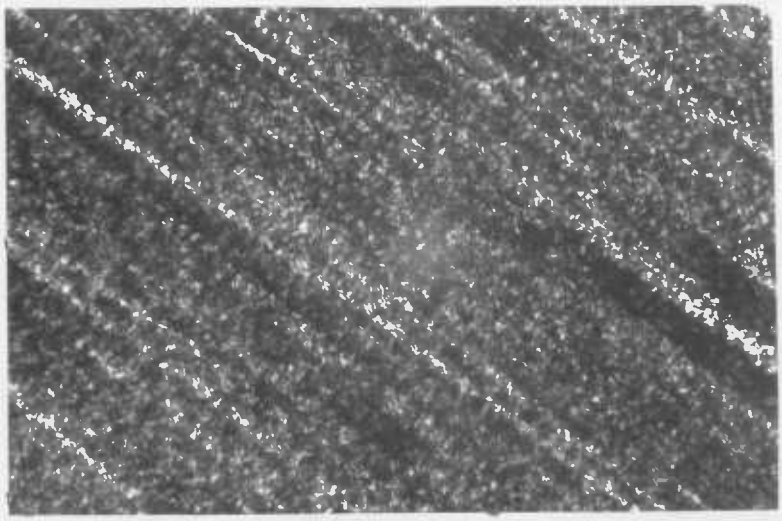
10 µm

Fig. 3.74 RW9 tile material, X-polars.



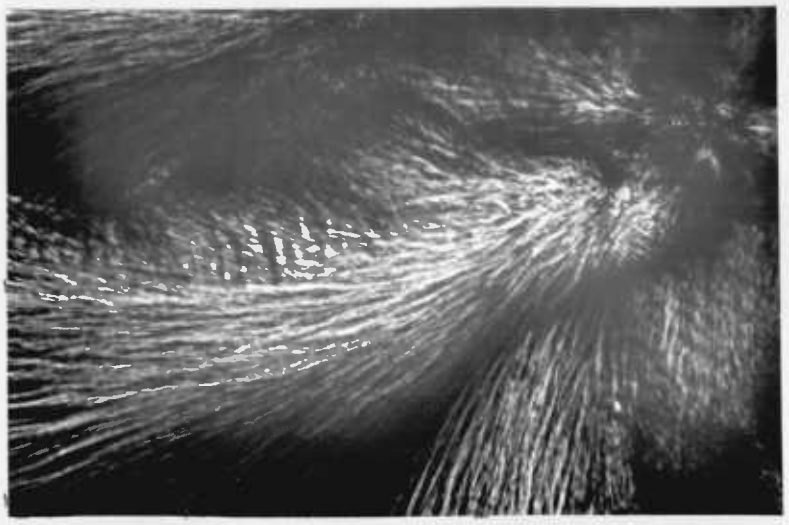
10 µm

Fig. 3.75 RW9 intracrucible material, X-polars.



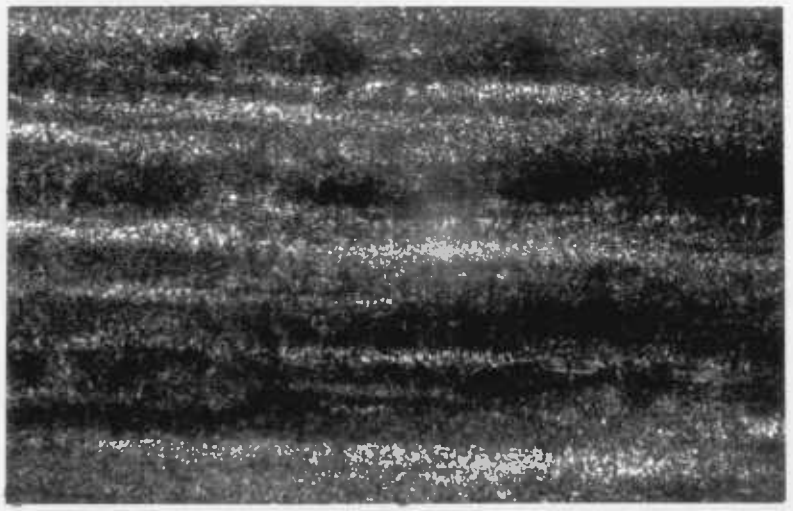
10 µm

Fig. 3.76 RW14 tile material, X-polars .



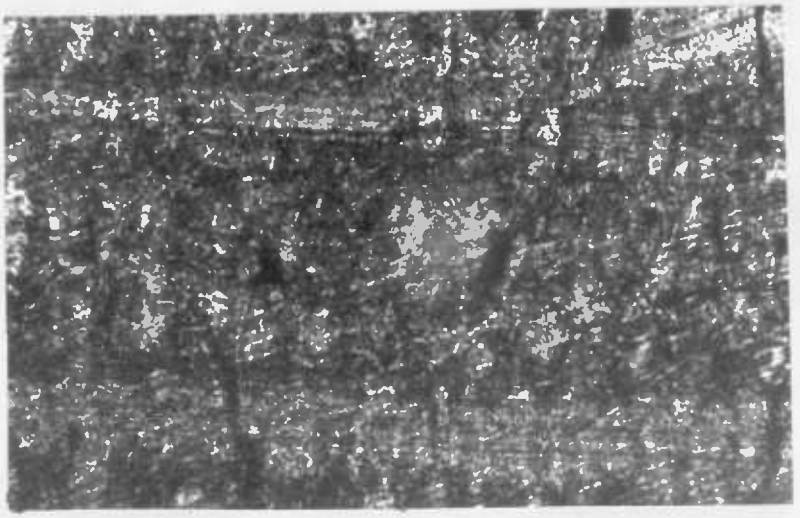
10 µm

Fig. 3.77 RW14F internally nucleated tile material, X-polars .



10 µm

Fig. 3.78 RW17/30β rod material, X-polars .



10 µm

Fig. 3.79 RW17/30α rod material, X-polars .

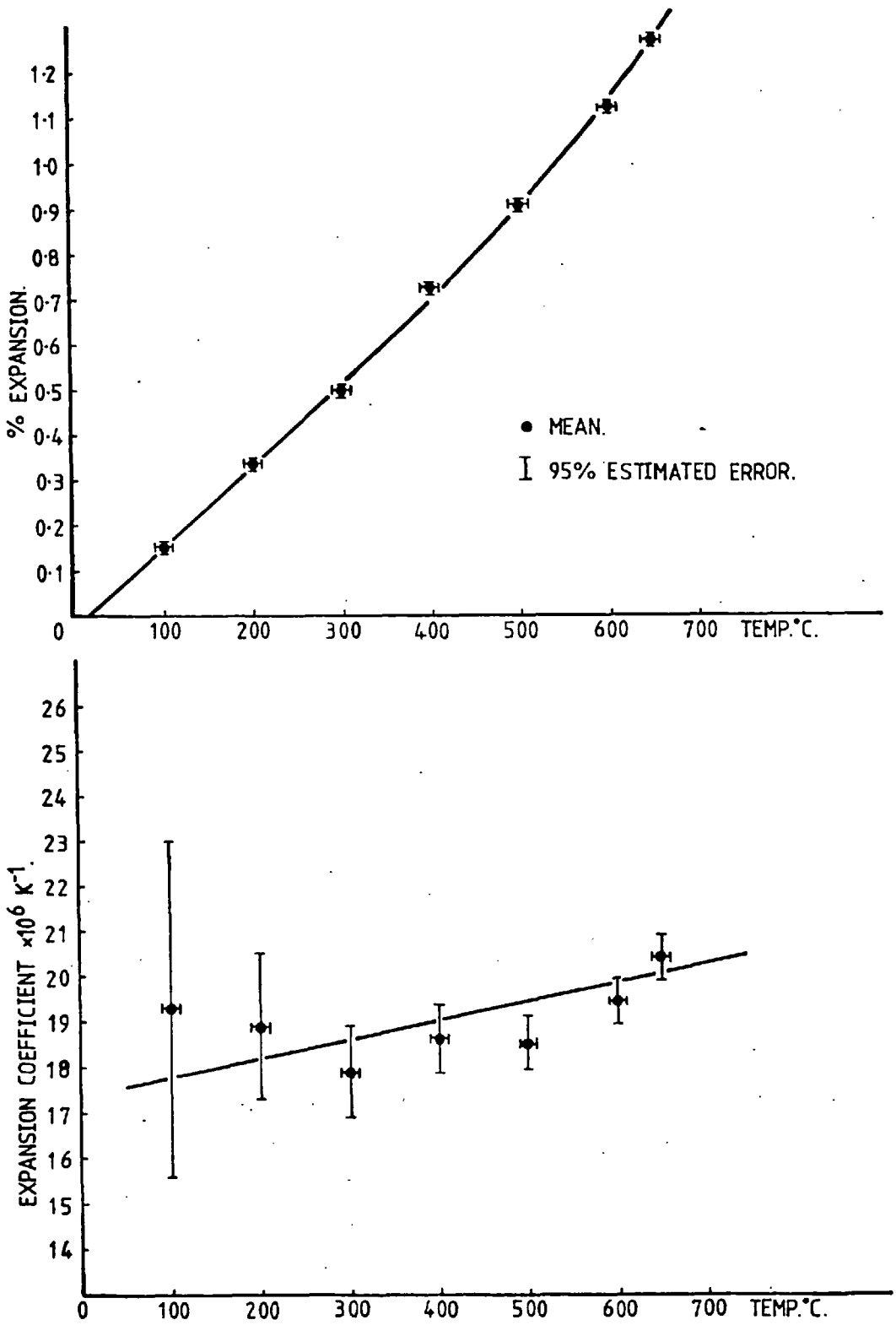


Fig. 3.80 Thermal expansion characteristics of "spec-pure" silver .

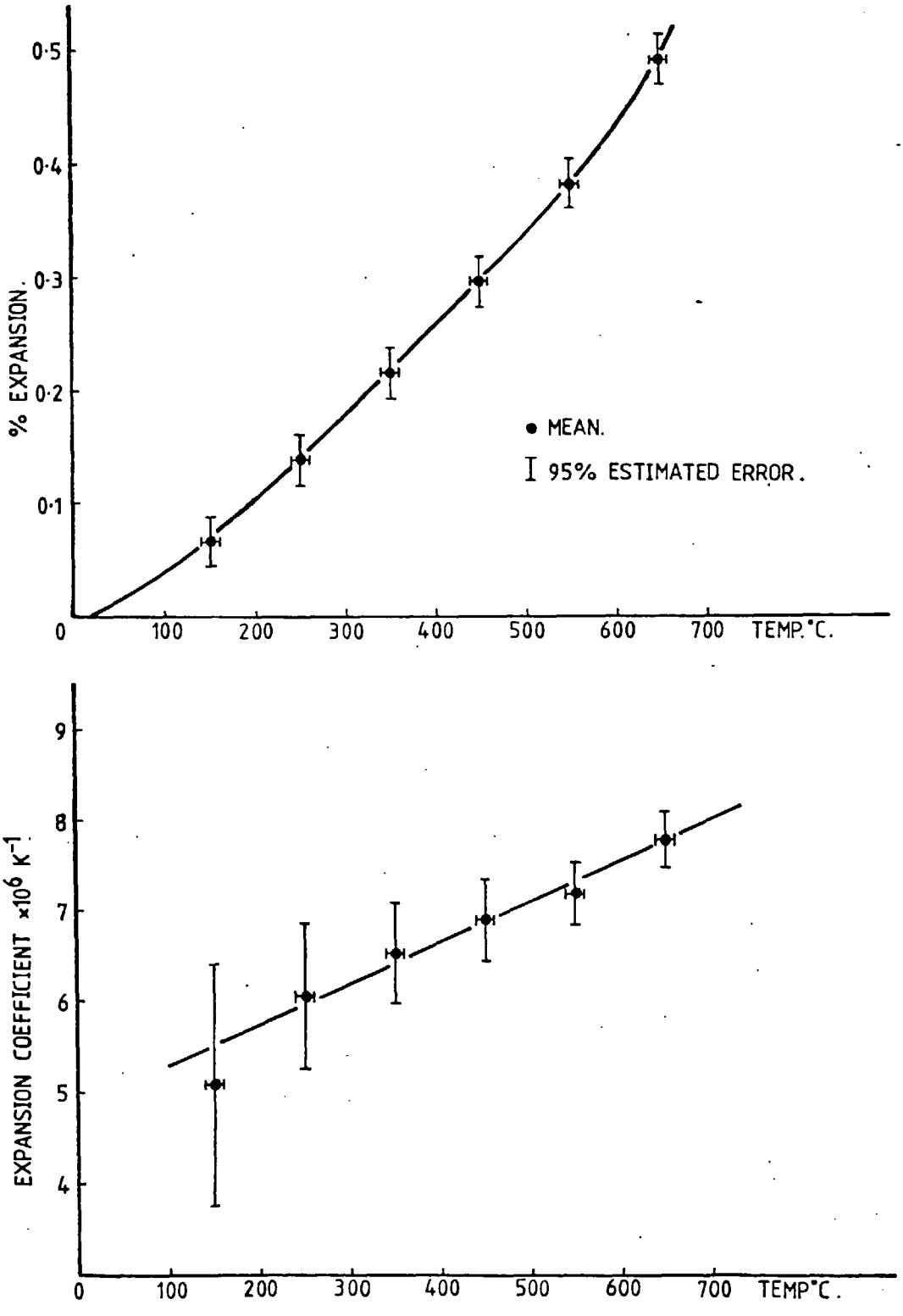


Fig. 3.81 · Thermal expansion characteristics of wollastonite, transverse .

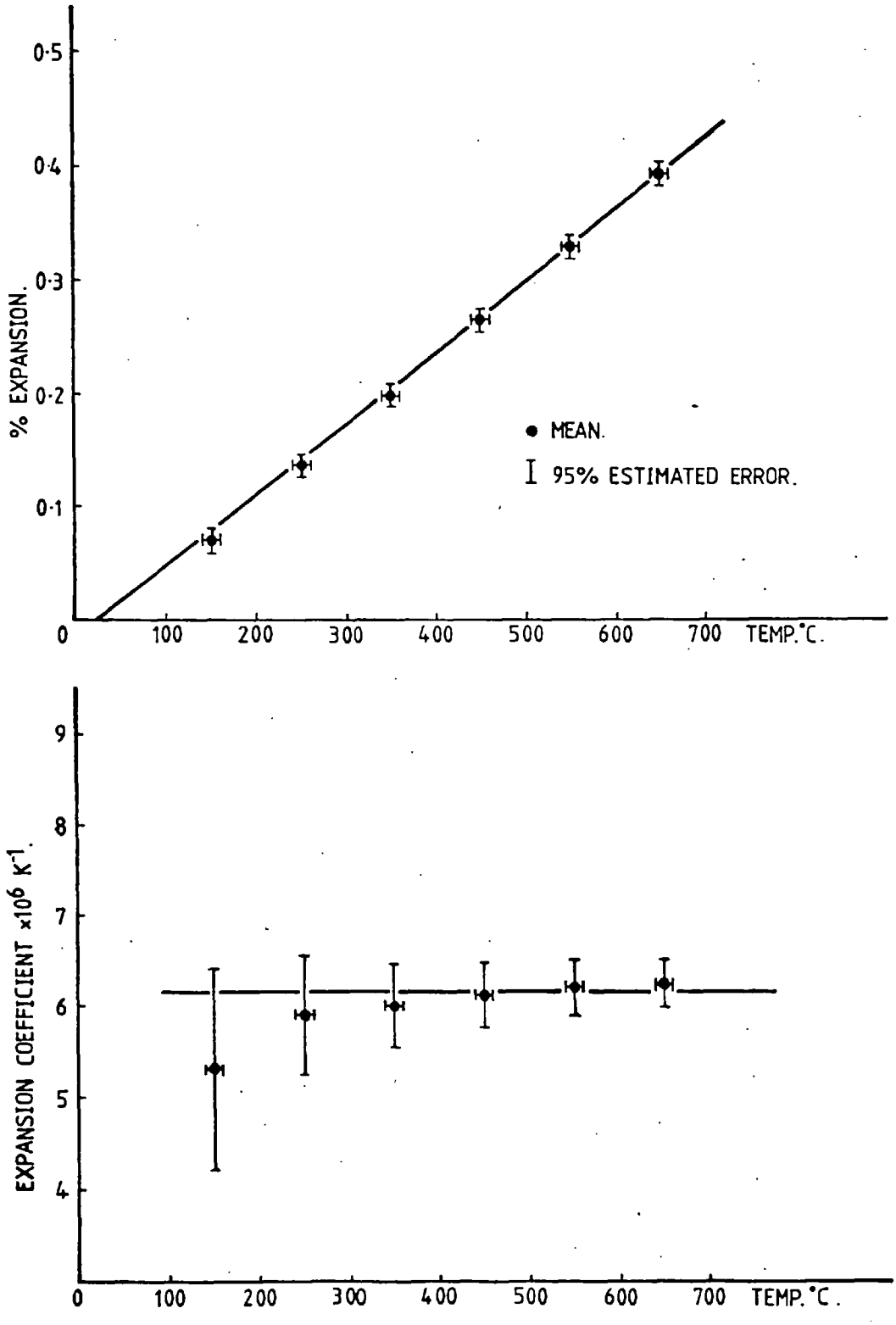


Fig. 3.82 Thermal expansion characteristics of wollastonite, longitudinal .

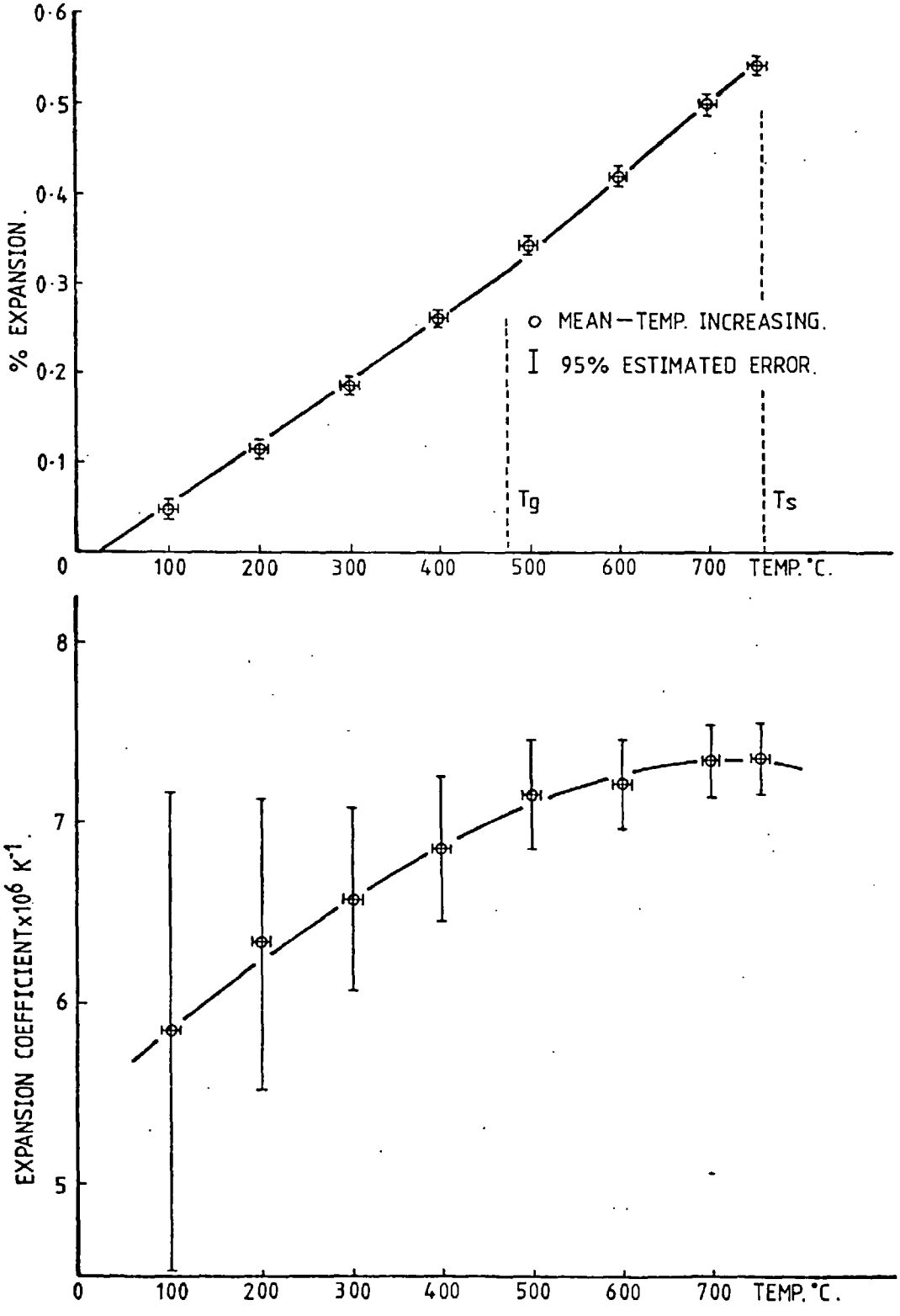


Fig. 3.83 Thermal expansion characteristics of RW9 glass.

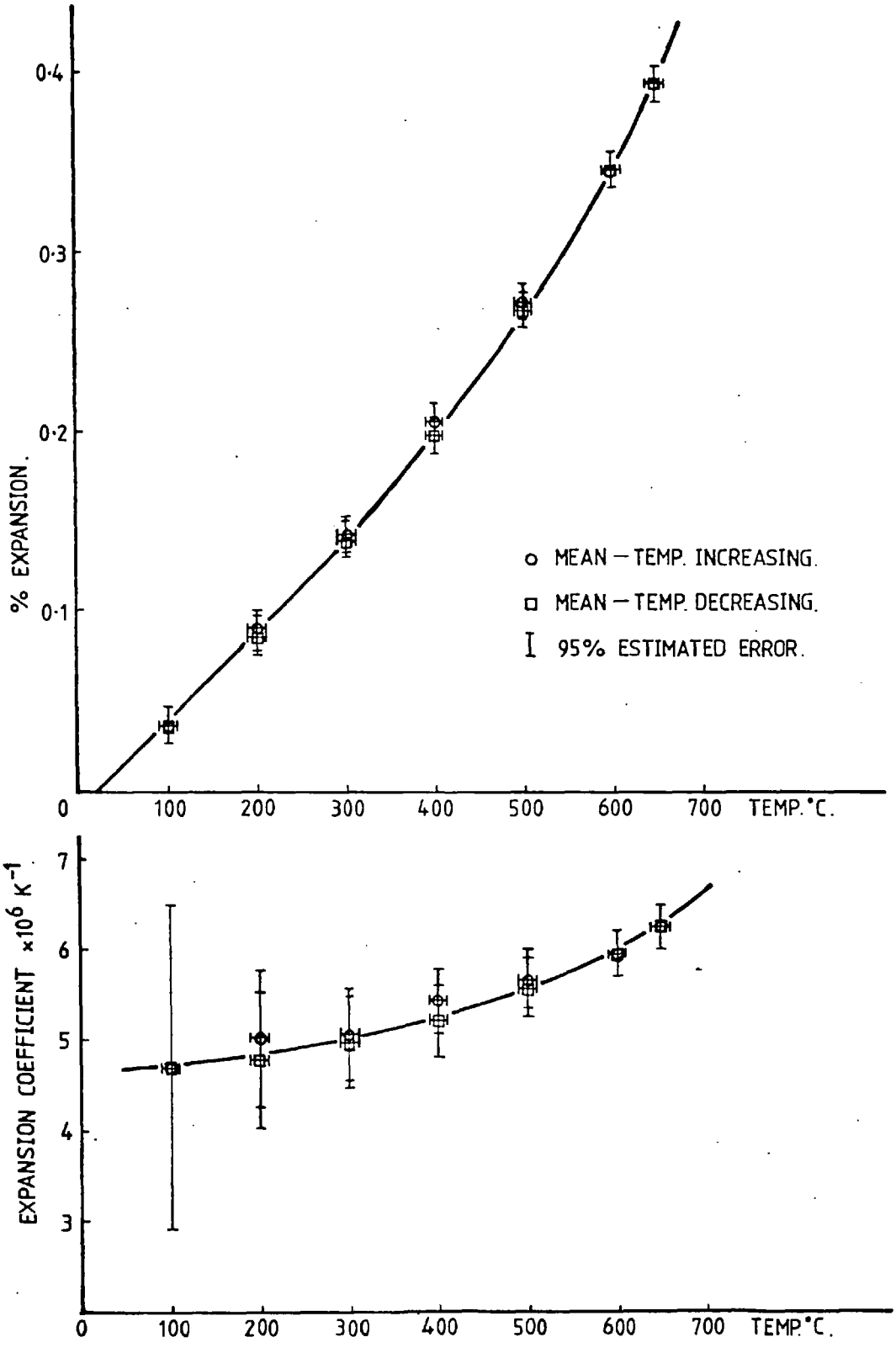


Fig. 3.84 Thermal expansion characteristics of RW9/3T, transverse.

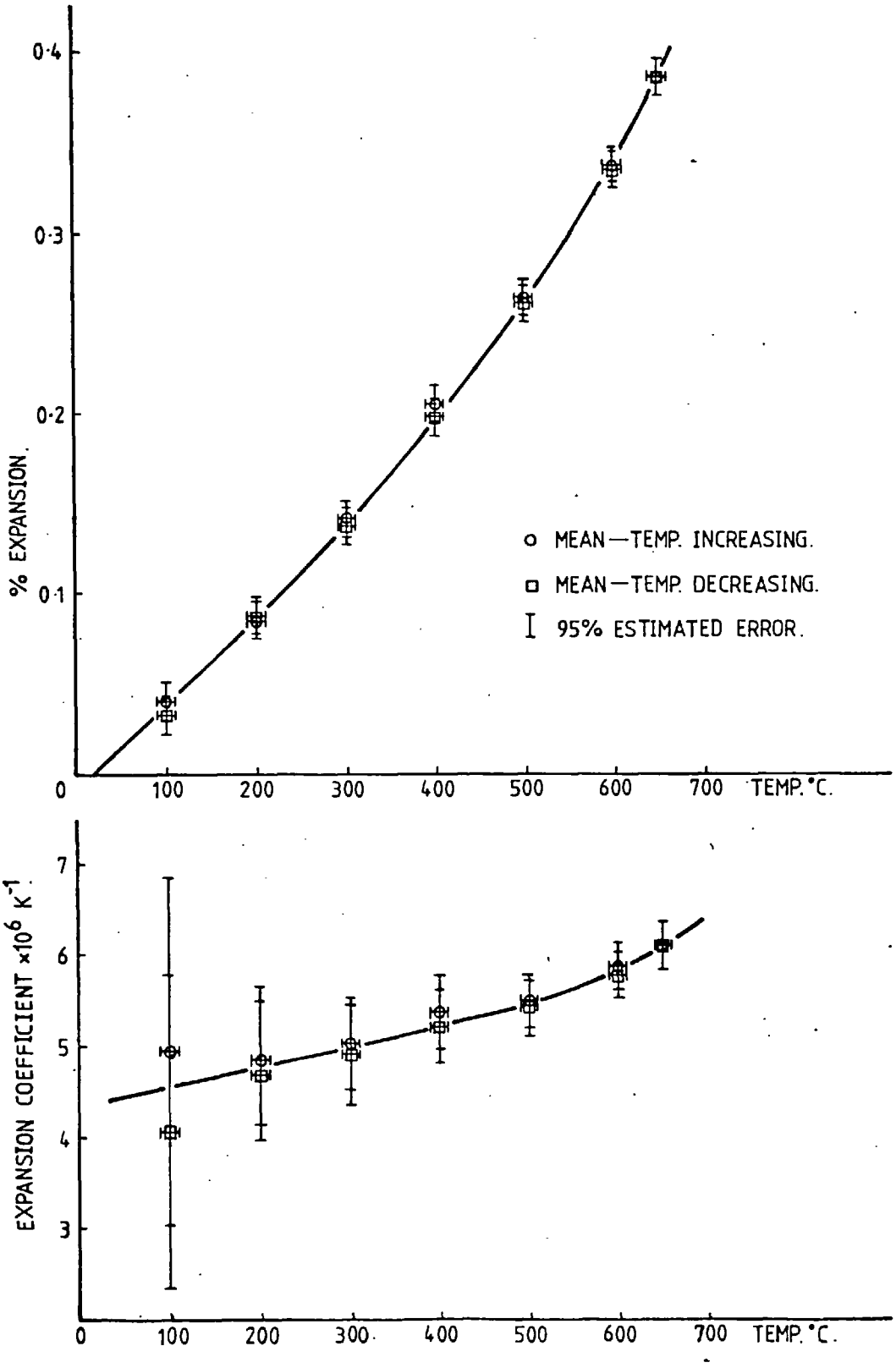


Fig. 3.85 Thermal expansion characteristics of RW9/7C, longitudinal.

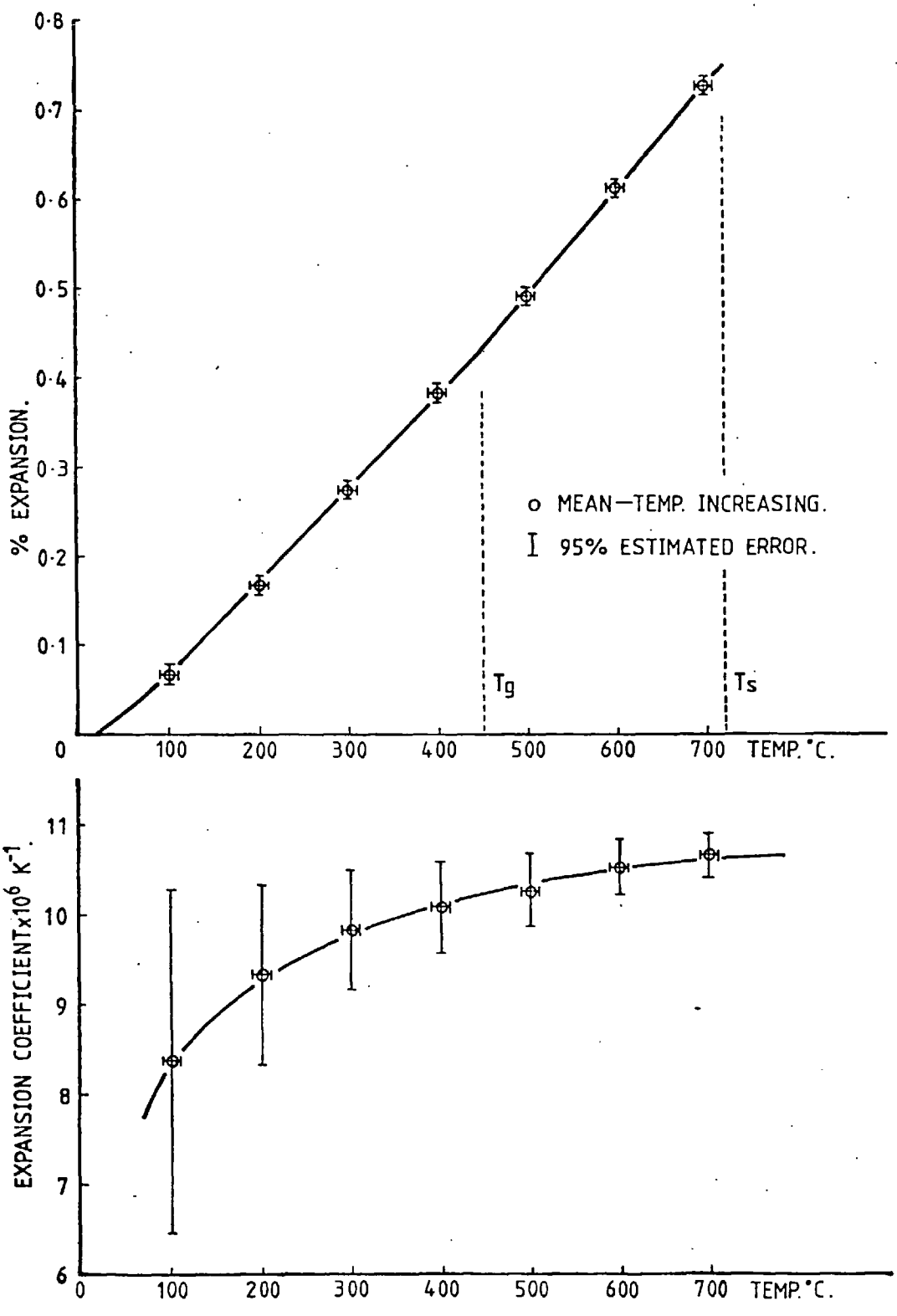


Fig. 3.86 Thermal expansion characteristics of RW14 glass .

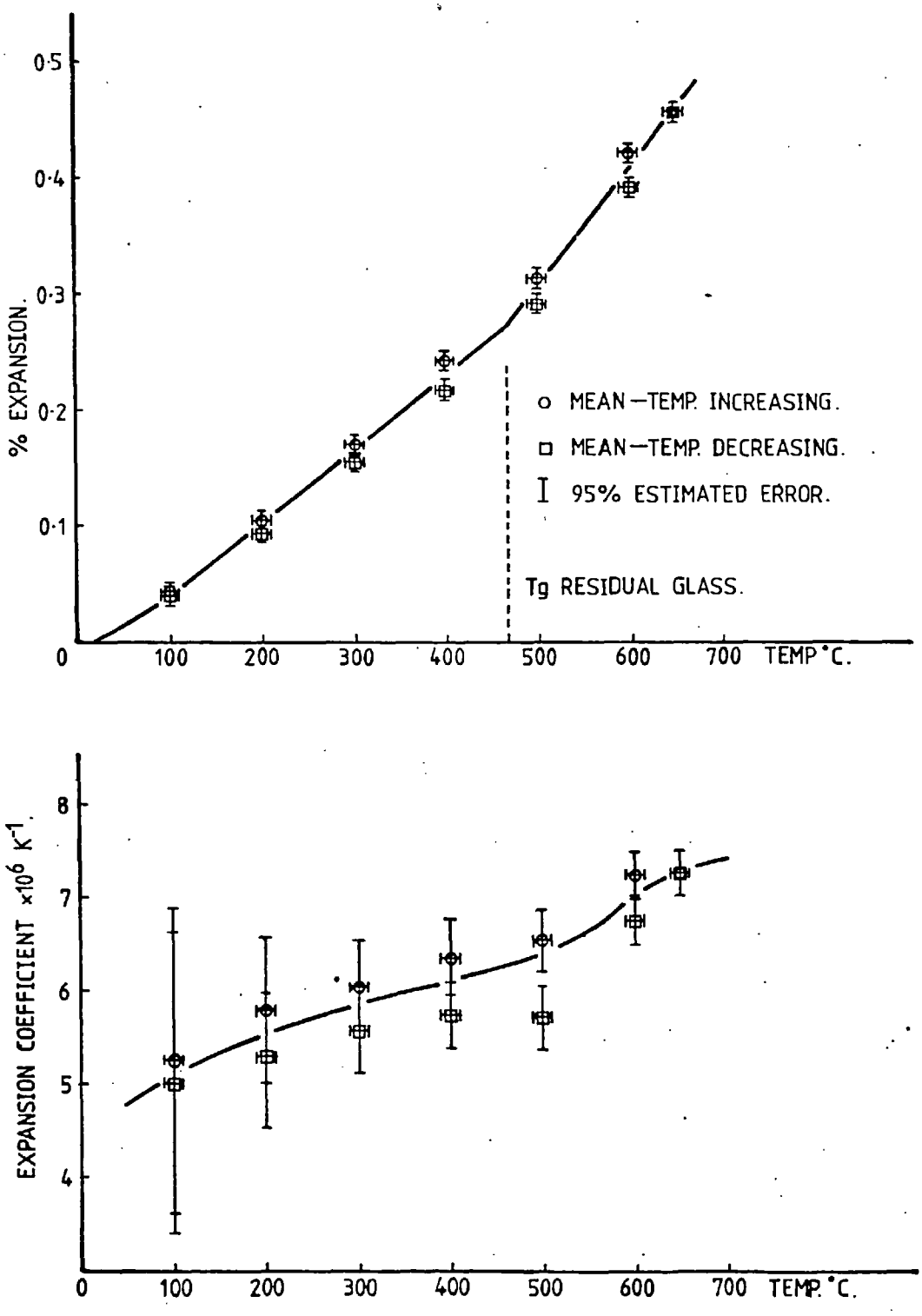


Fig. 3.87 Thermal expansion characteristics of RW14/2T, transverse

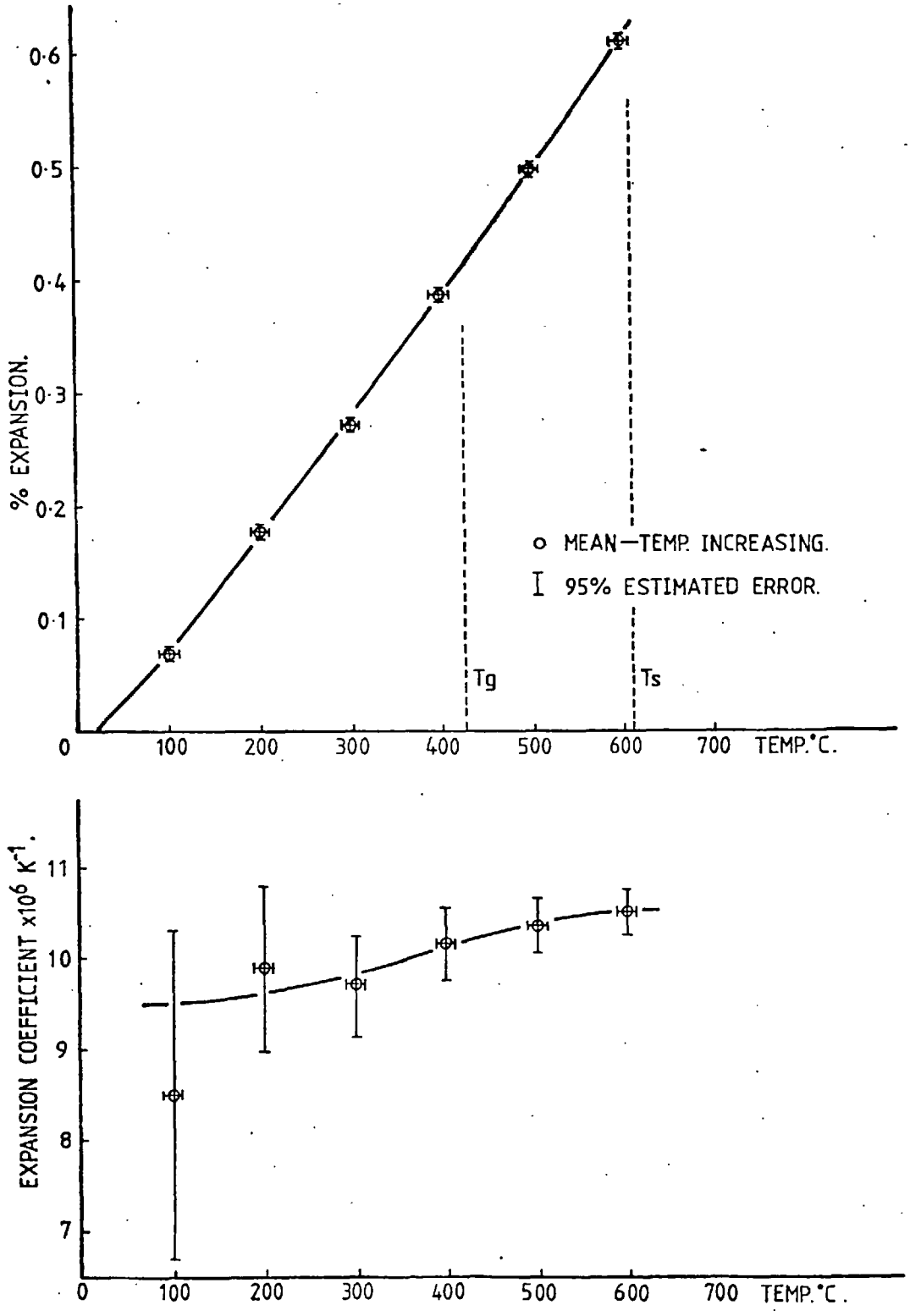


Fig. 3.88 Thermal expansion characteristics of RW14 residual glass.

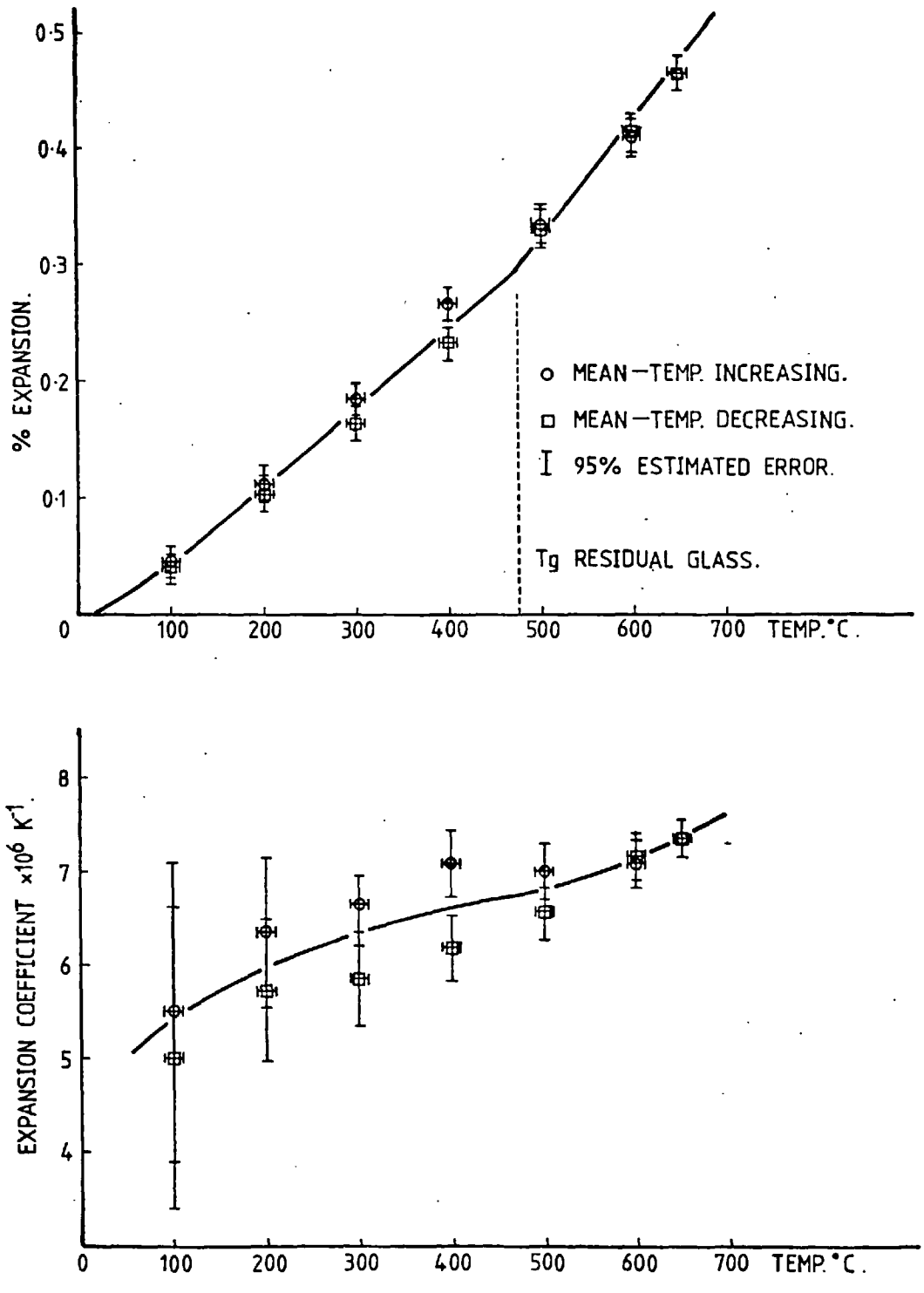


Fig. 3.89 Thermal expansion characteristics of RW14/5T, transverse.

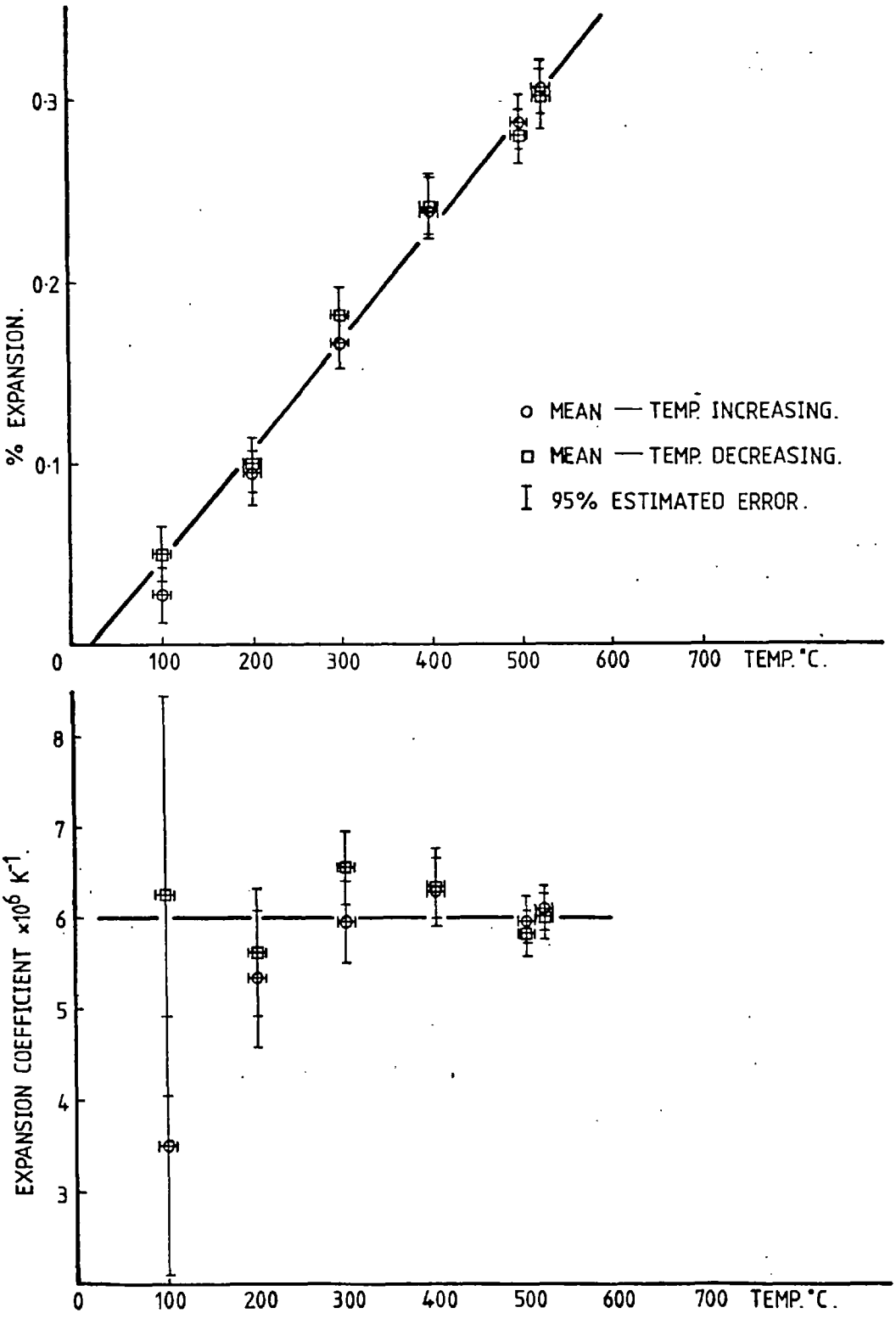


Fig. 3.90 Thermal expansion characteristics of RW14/5T, longitudinal .

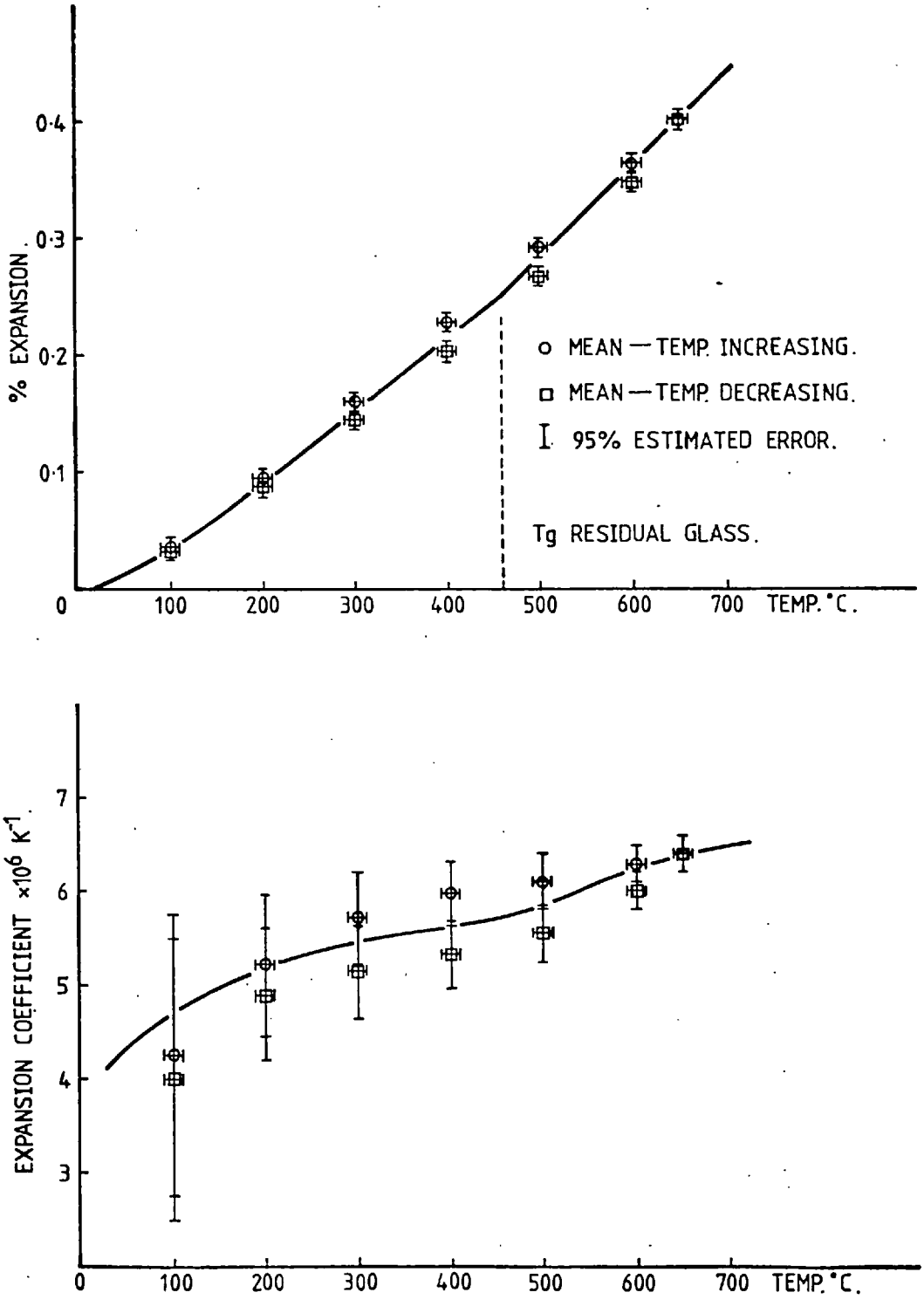


Fig. 3.91 Thermal expansion characteristics of RW14F, internally nucleated.

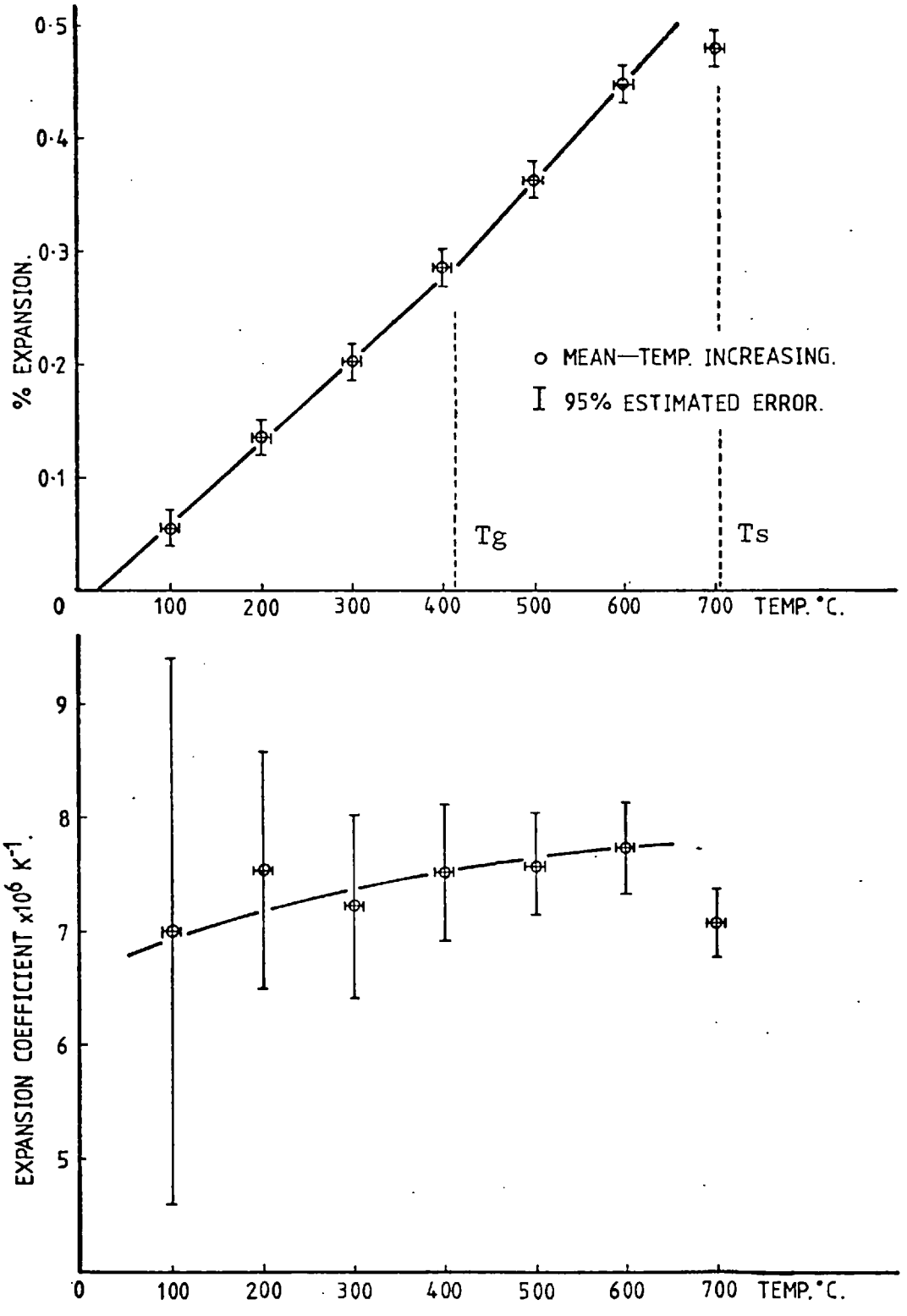


Fig. 3.92 Thermal expansion characteristics of RW17 glass .

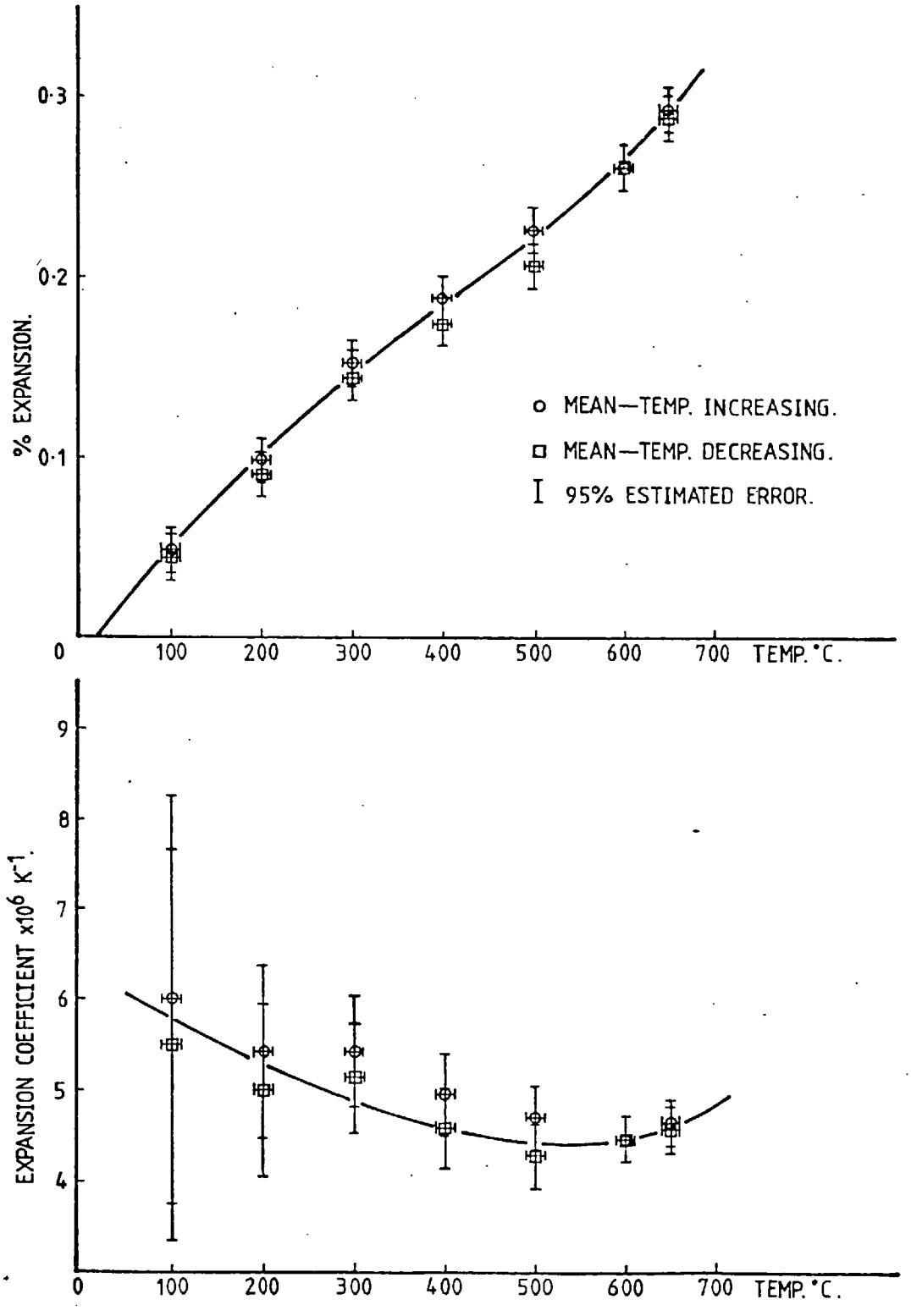


Fig. 3.93 Thermal expansion characteristics of RW17/50B, transverse

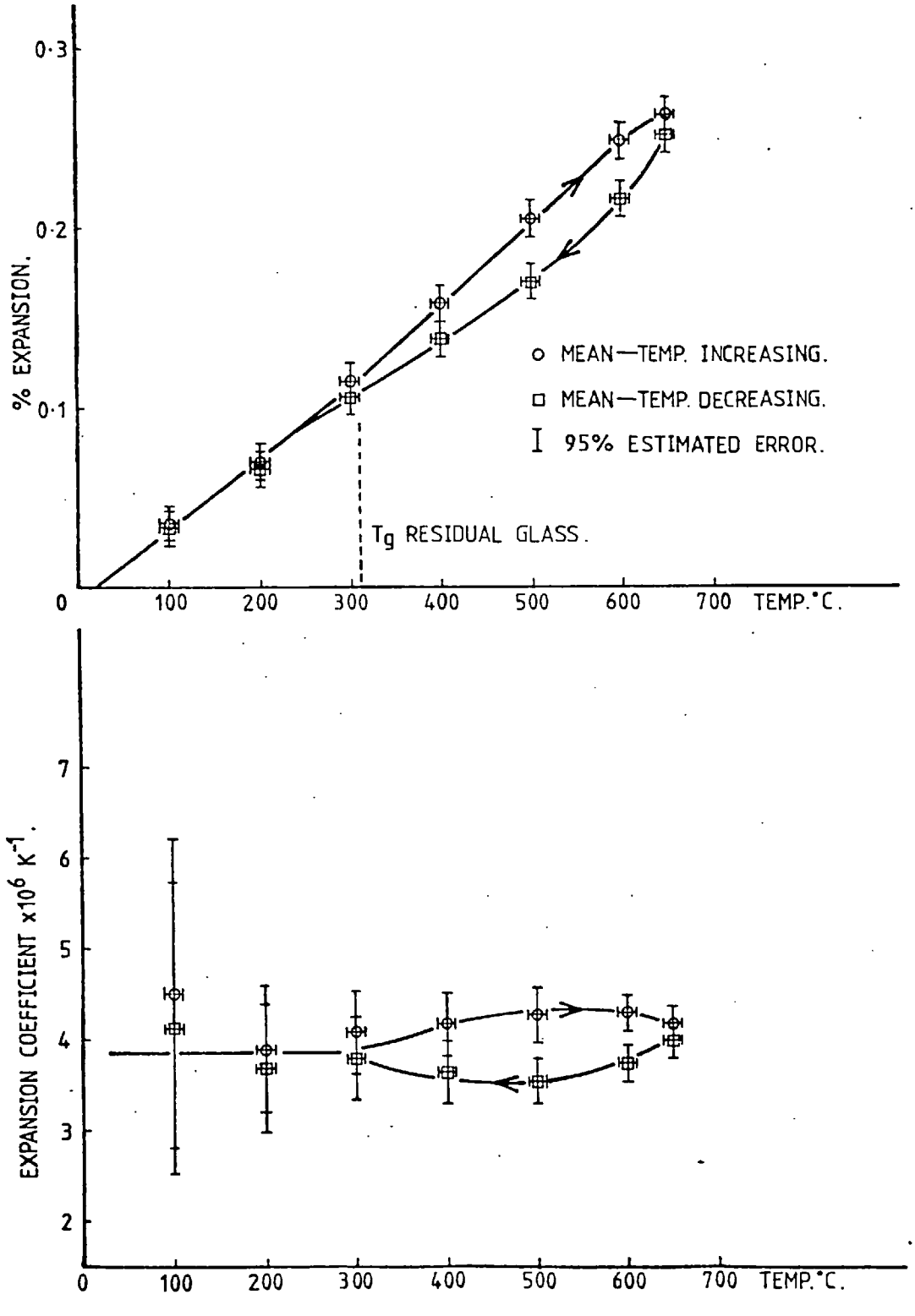


Fig. 3.94 Thermal expansion characteristics of RW17/30B, transverse.

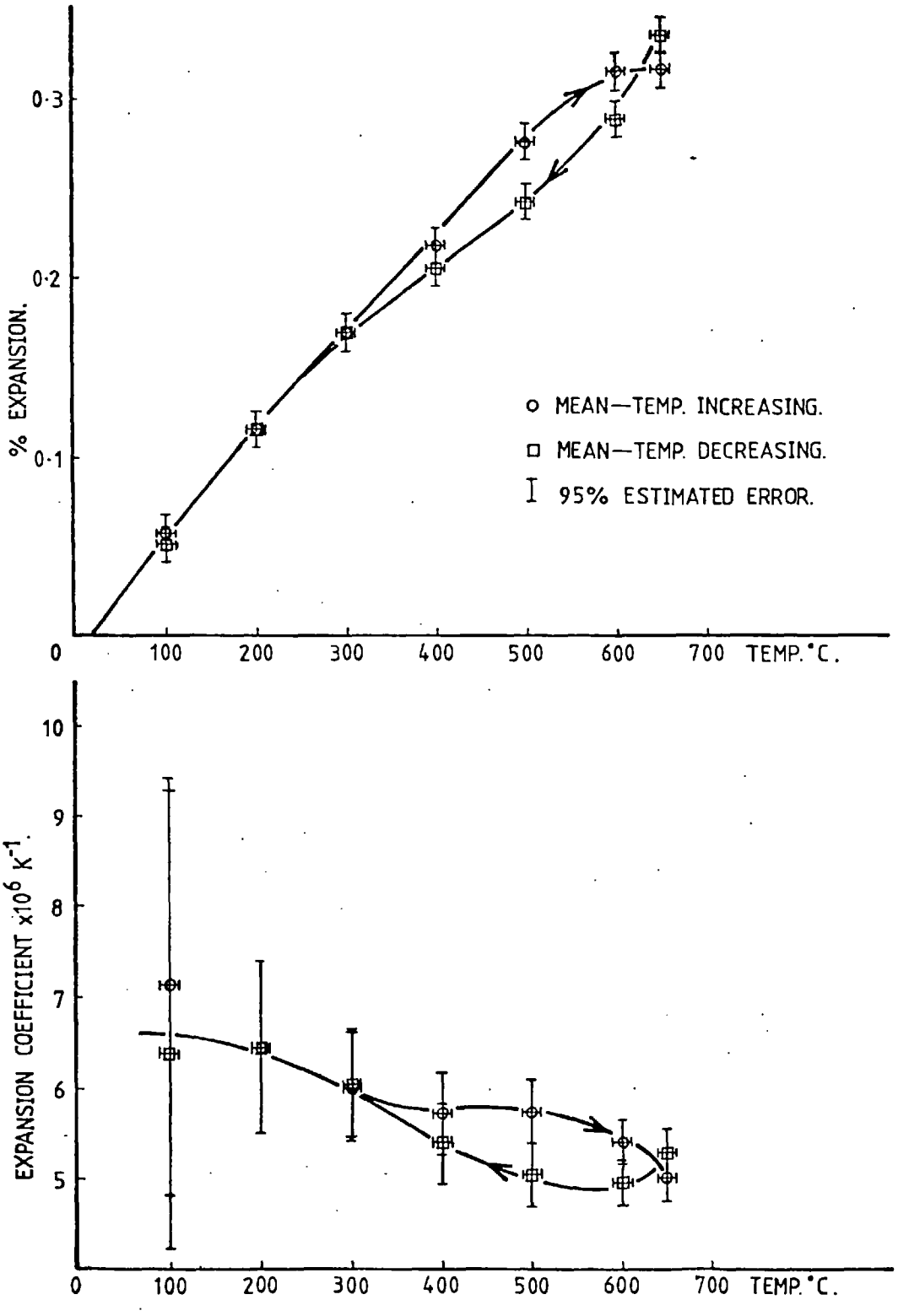


Fig. 3.95 Thermal expansion characteristics of RW17/30α, transverse.

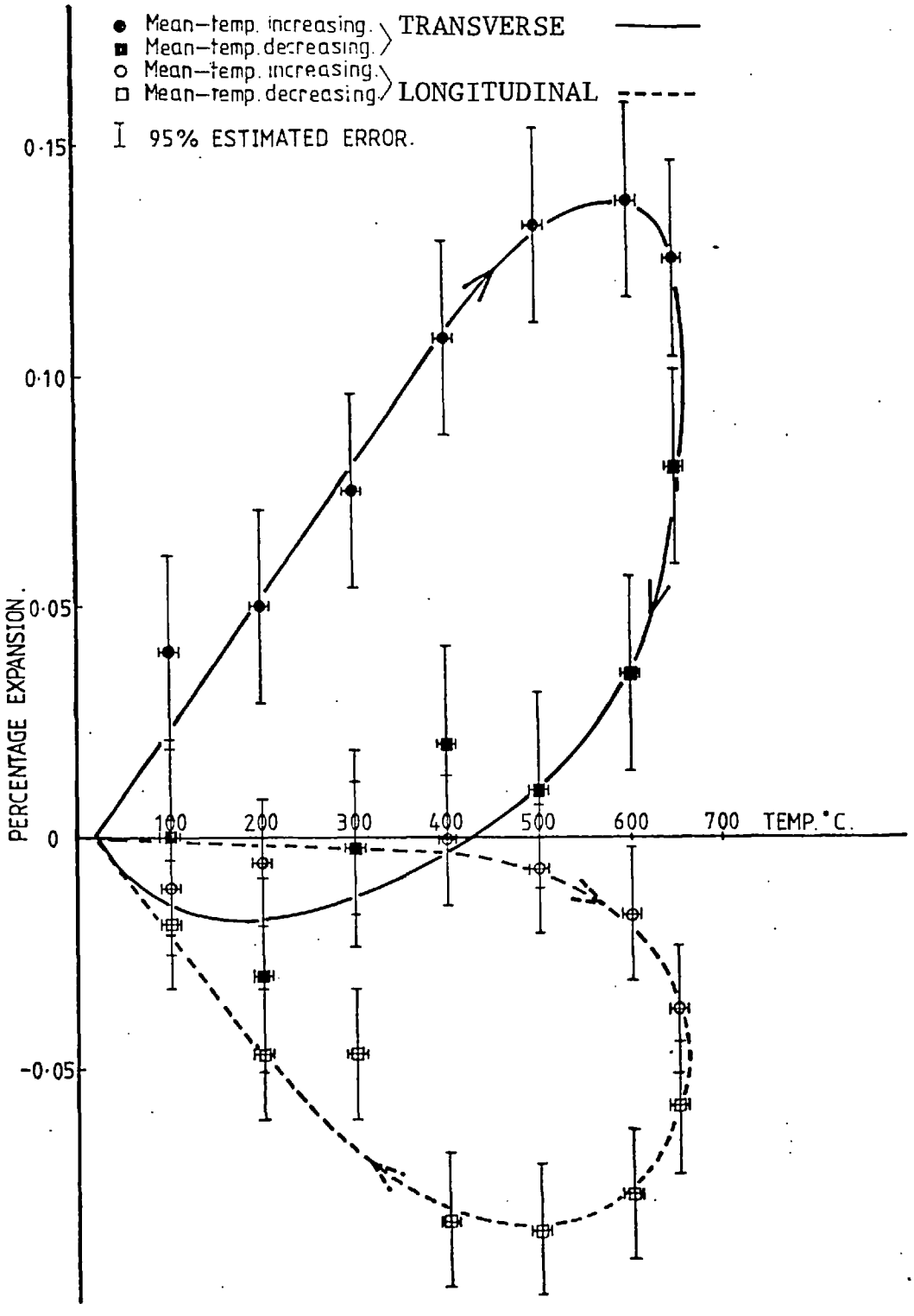


Fig. 3.96 Thermal expansion characteristics of RW17/10, $Ca_2ZnSi_2O_7$, transverse and longitudinal .

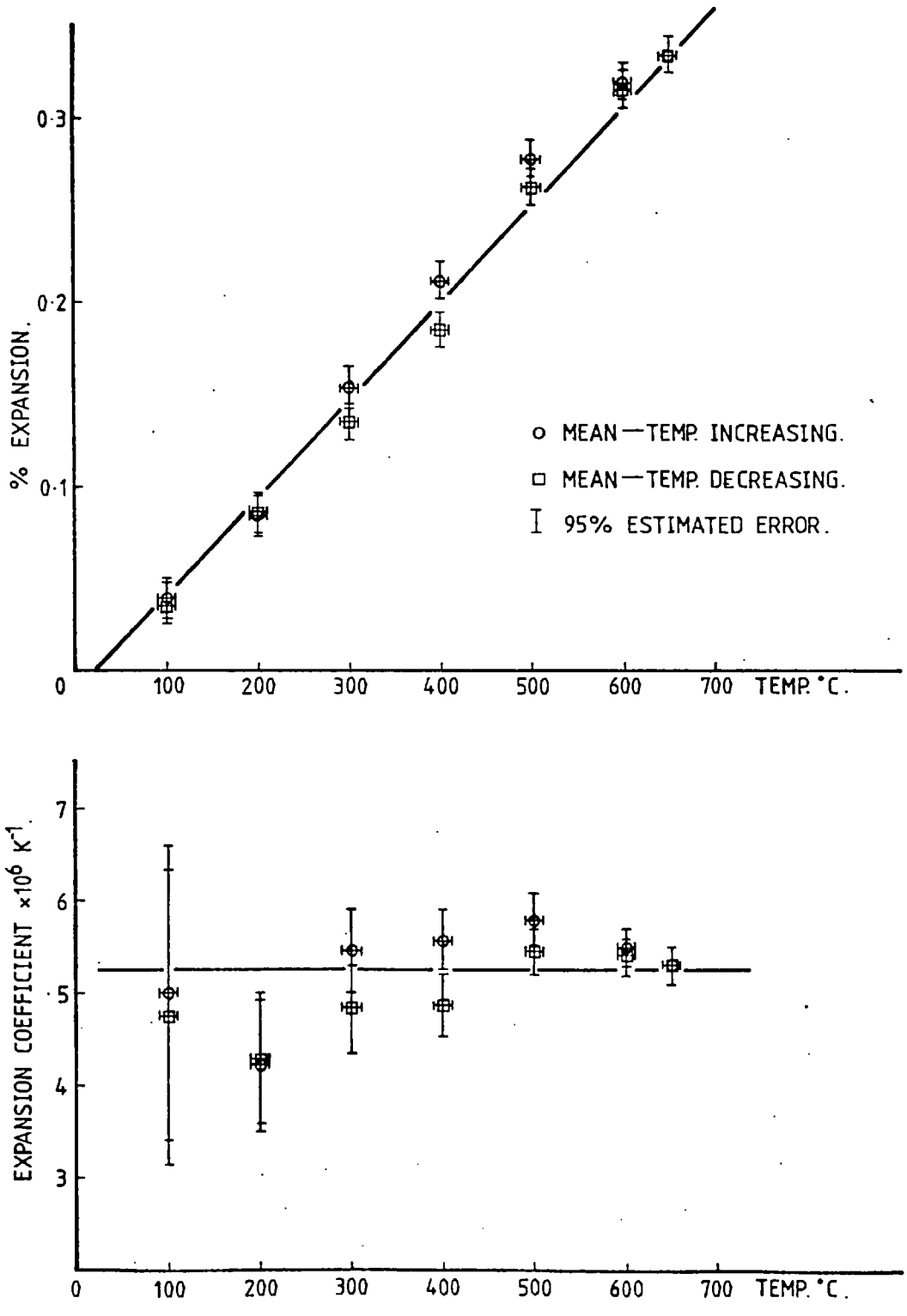


Fig. 3.97 Thermal expansion characteristics of RW17/50B, longitudinal .

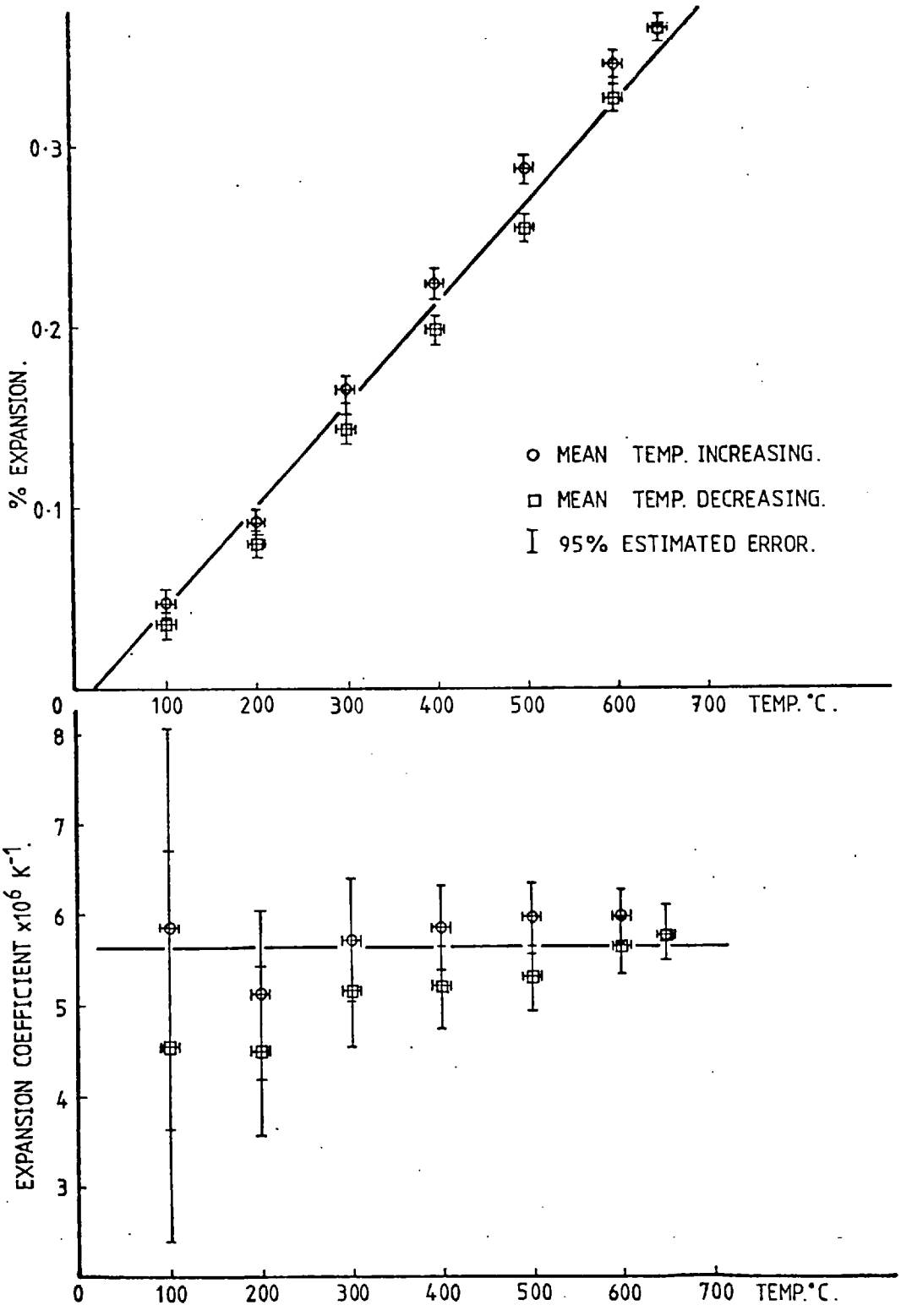


Fig. 3.98 Thermal expansion characteristics of RW17/30 B , longitudinal

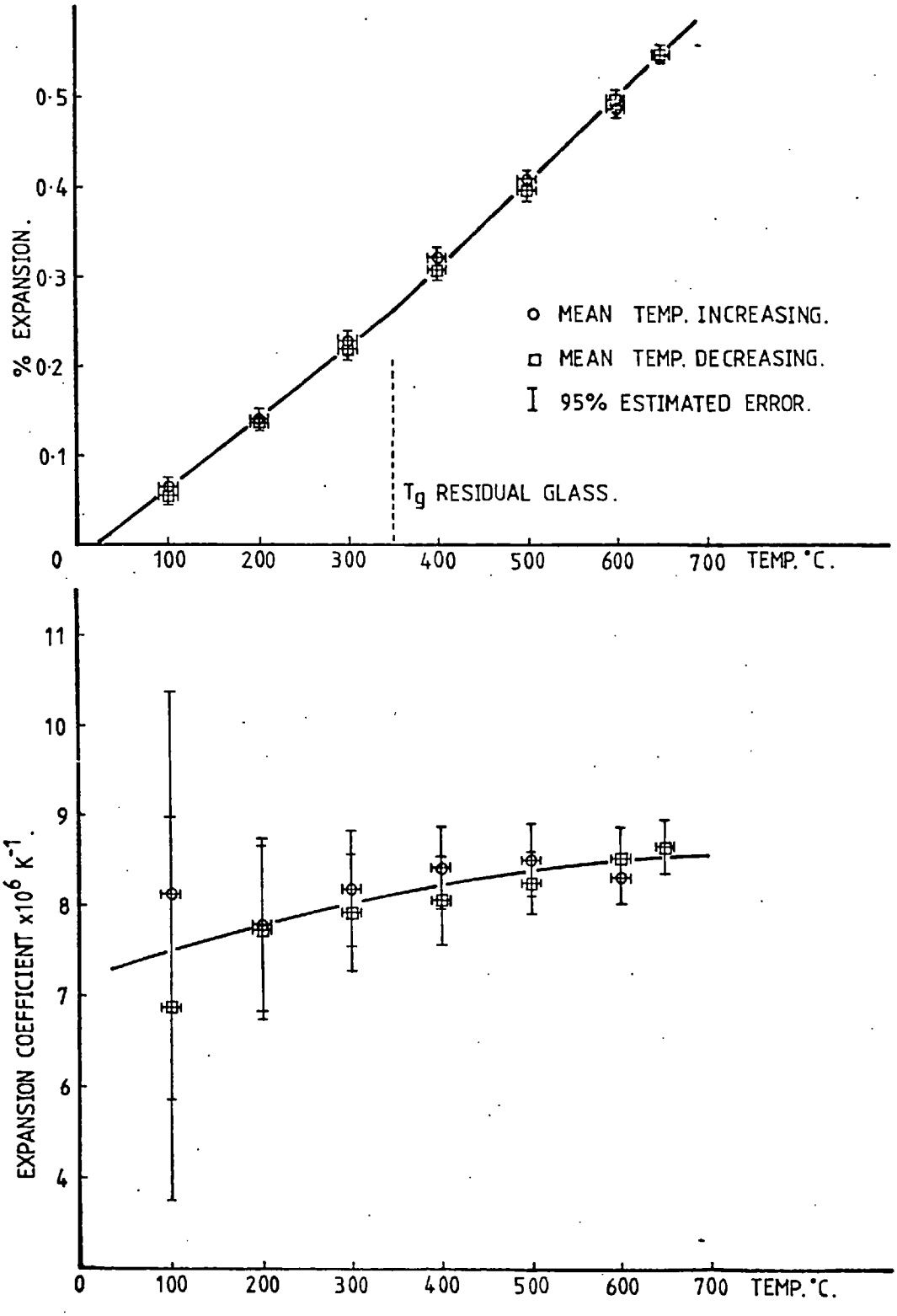
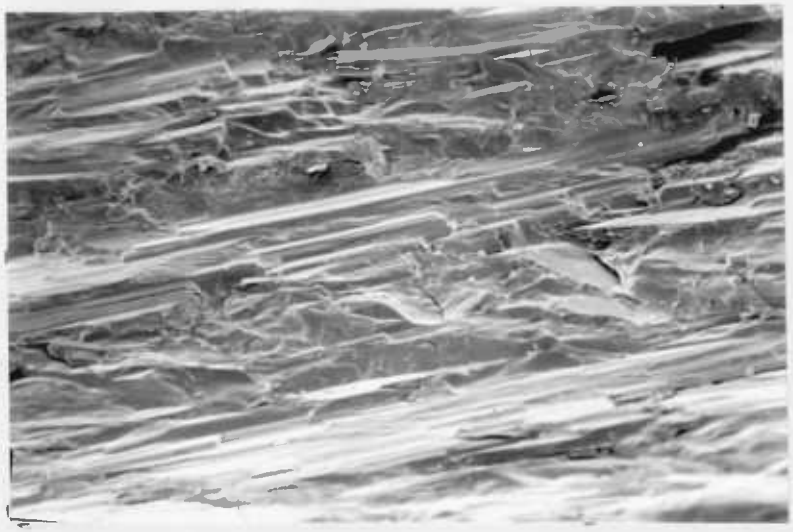
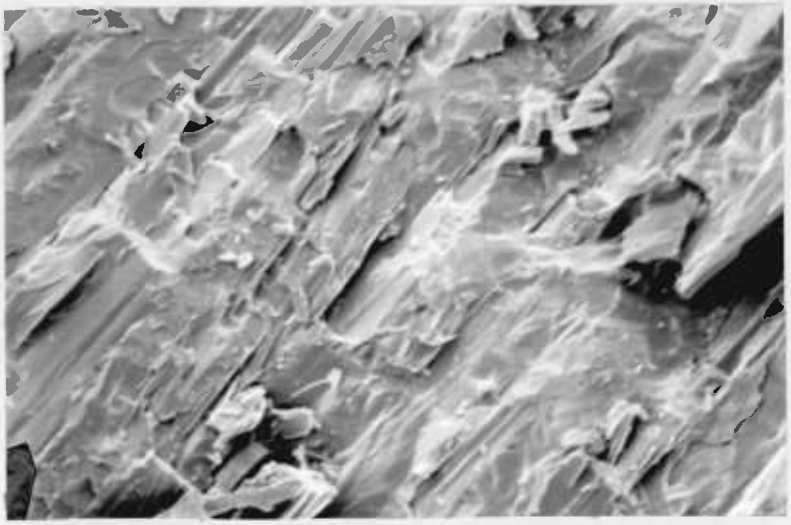


Fig. 3.99 Thermal expansion characteristics of RW17/30α, longitudinal.



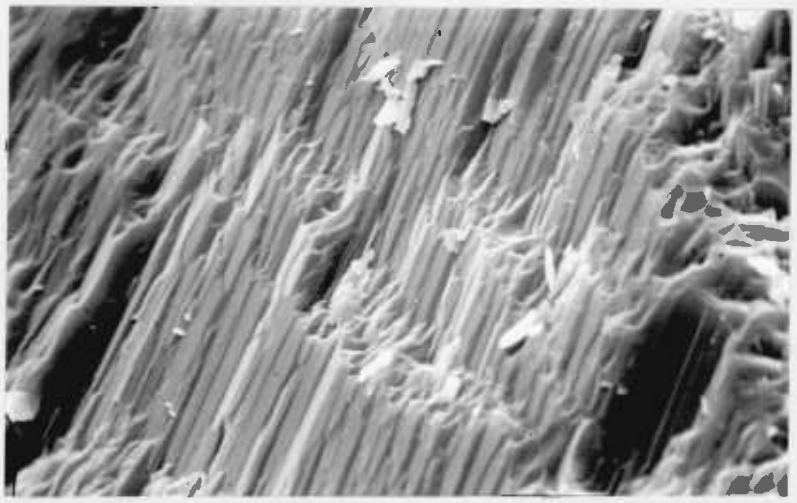
40 µm

Fig. 3.100 Fracture face of RW9/6T.8 transverse beam, 20 mm span, (SEM).



20 µm

Fig. 3.101 Fracture face of RW9/7C.1 longitudinal beam, 20 mm span, (SEM).



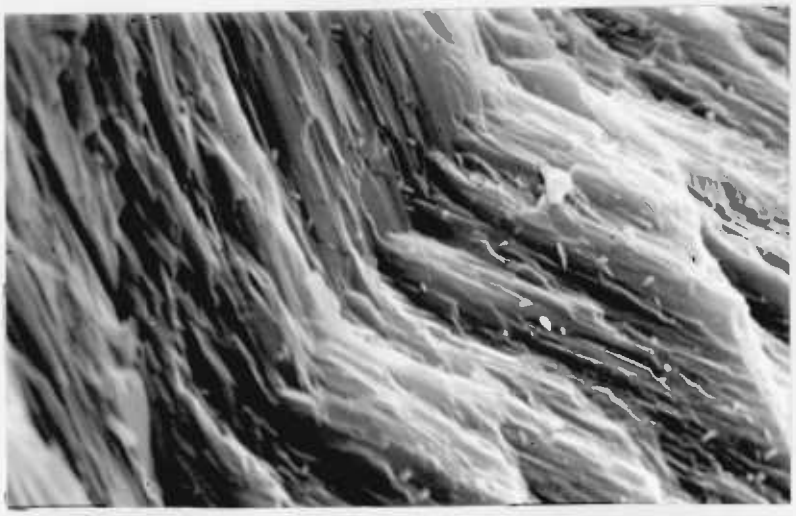
10 µm

Fig. 3.102 Fracture face of RW14/2T.6 perpendicular beam, 20 mm span, (SEM).



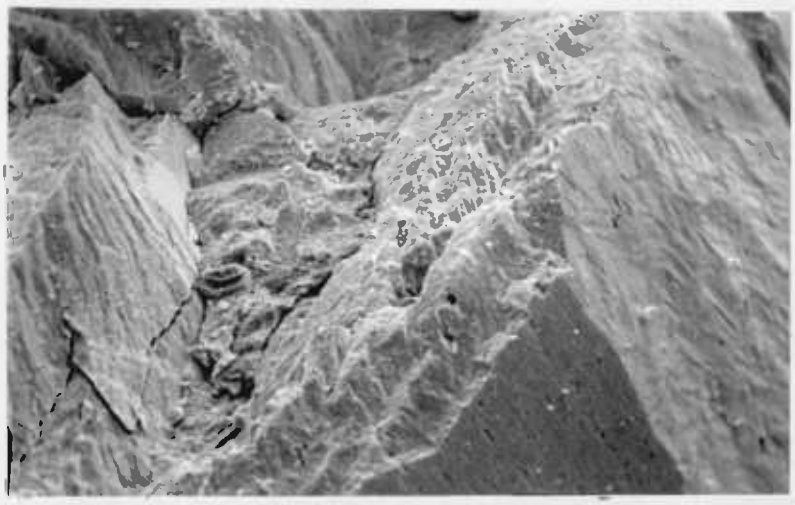
200 µm

Fig. 3.103 Fracture face of RW14F.1 random beam, 20 mm span, (SEM).



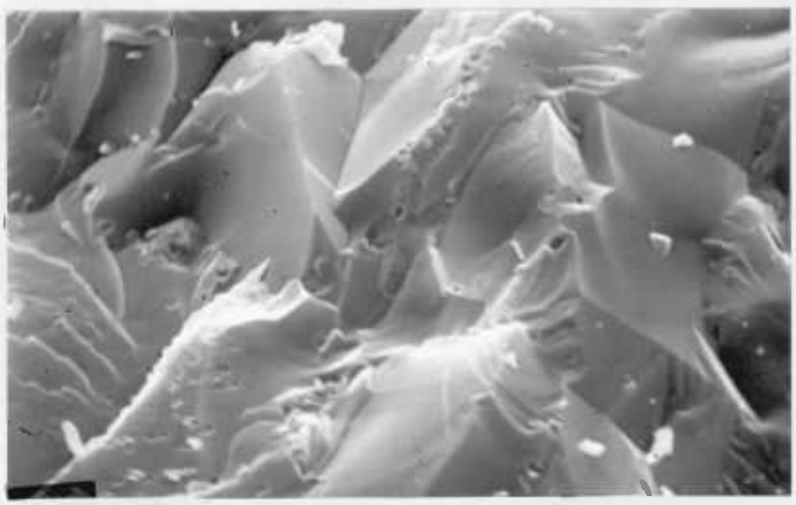
4 µm

Fig. 3.104 As fig. 3.103, close-up of interspherulite boundary, (SEM).



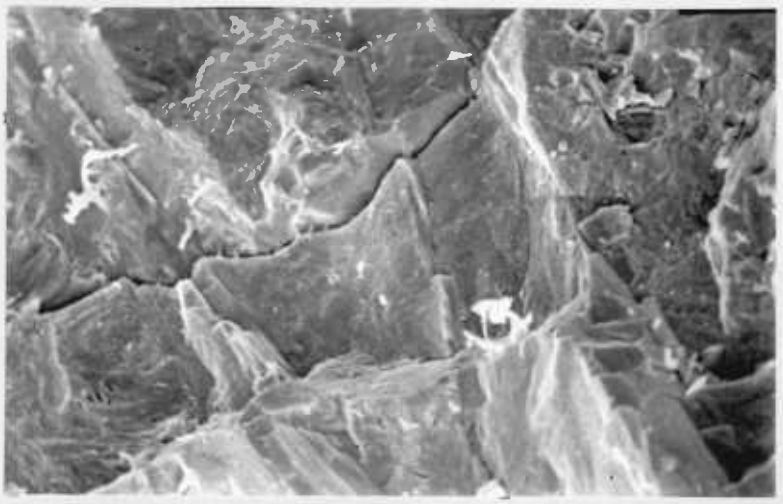
100 µm

Fig. 3.105 Fracture face of RW17/30 ß strongest specimen, 7 mm span, (SEM)



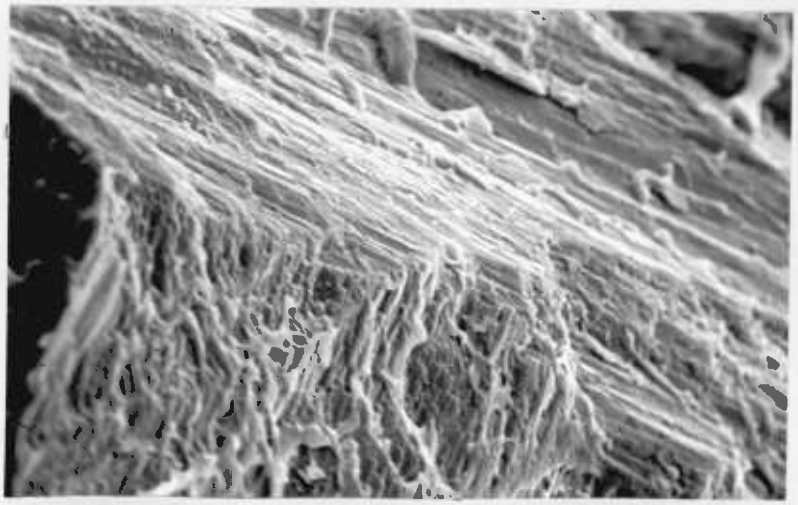
4 µm

Fig. 3.106 Fracture face of RW17/30 α typical specimen, 7 mm span, (SEM)



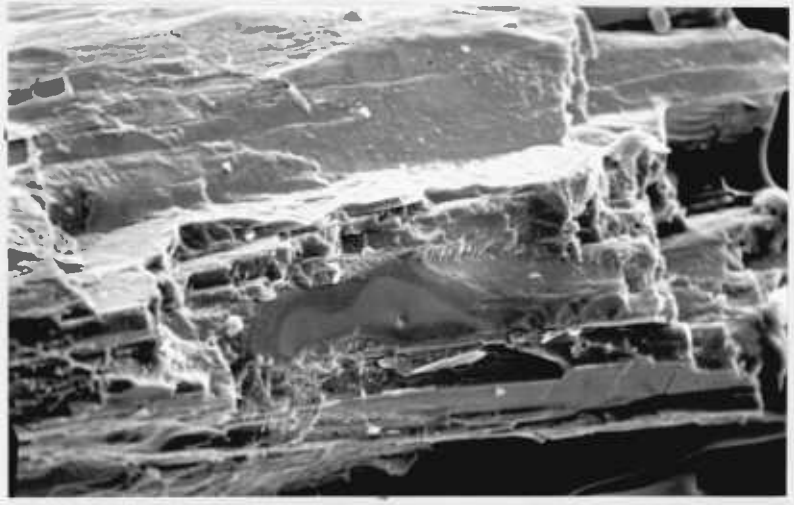
40 µm

Fig. 3.107 Fracture face of RW9/3T typical short beam test specimen, (SEM)



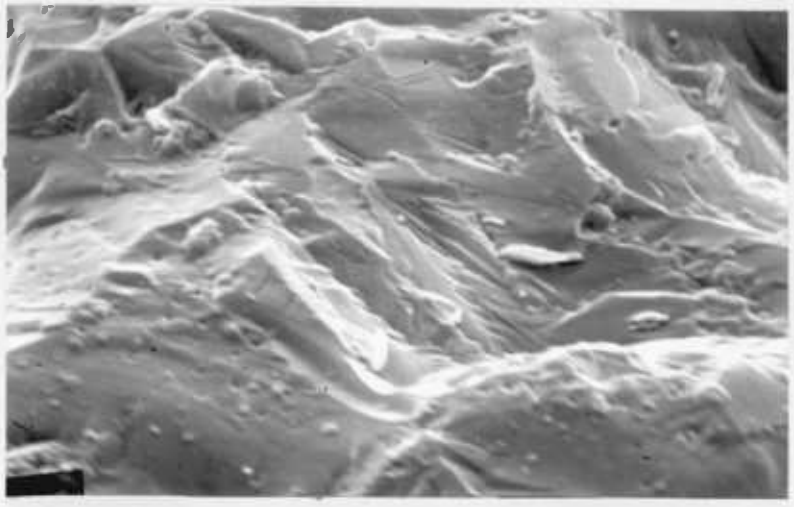
20 µm

Fig. 3.108 Fracture face of RW14/4T typical short beam test specimen, (SEM)



40 µm

Fig. 3.109 Fracture face of RW17/30 β typical short beam test specimen, (SEM)



4 µm

Fig. 3.110 Fracture face of RW17/30 α typical short beam test specimen, (SEM)

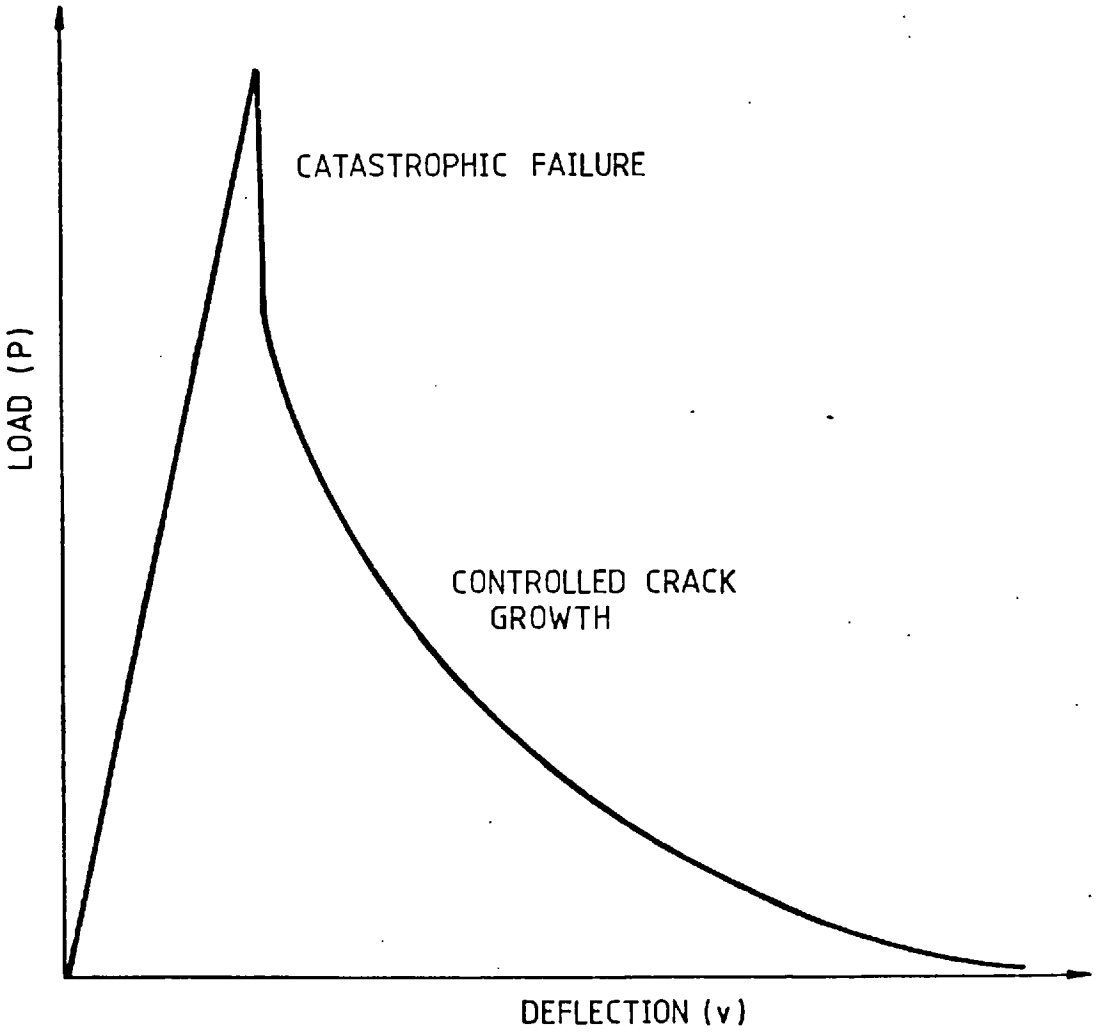


Fig. 3.111 Schematic load versus deflection curve for controlled crack growth .

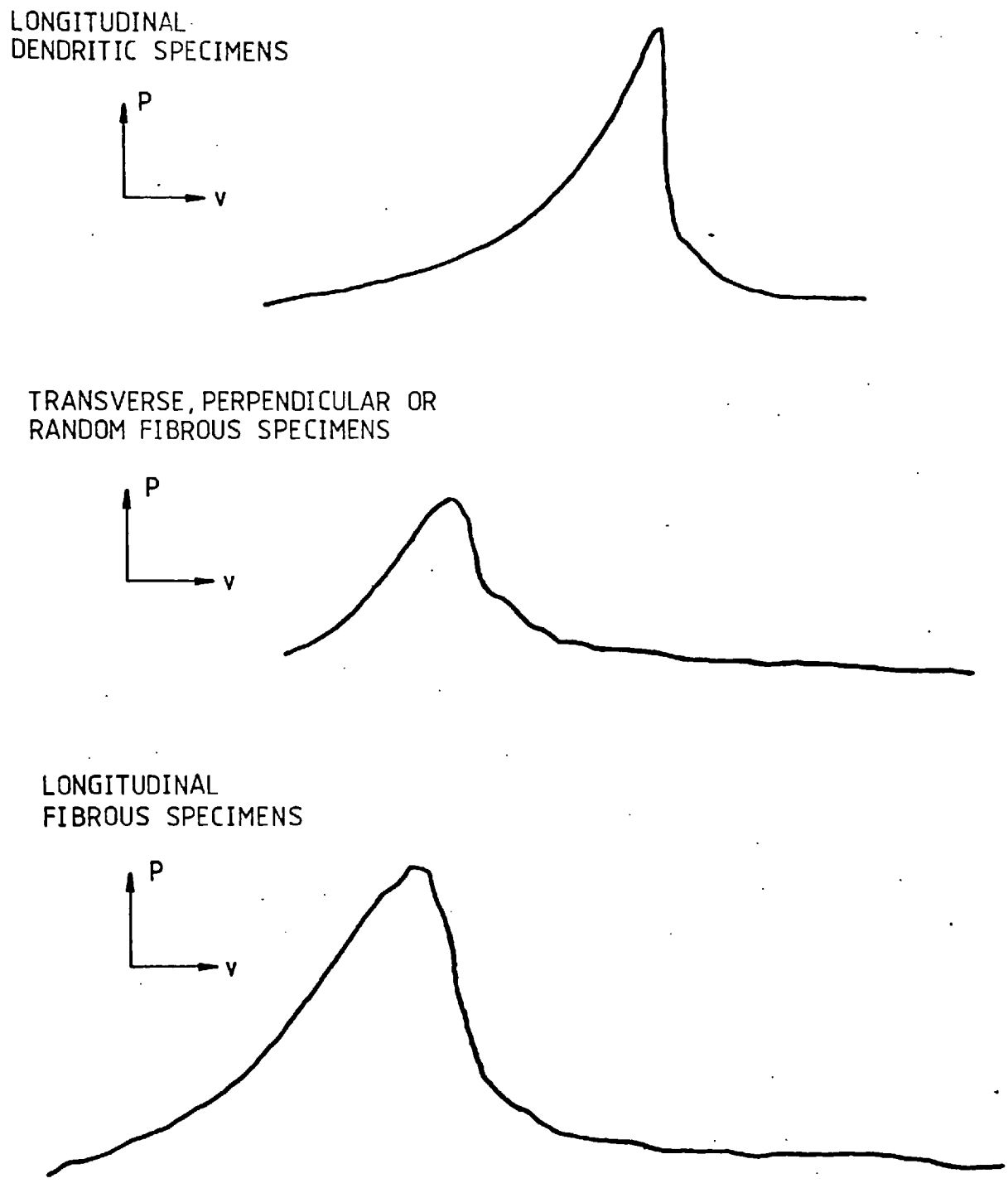


Fig. 3.112. Typical load versus deflection curves for the different types of bend test specimens.

CHAPTER 4

CONCLUSIONS

4.1. GLASS COMPOSITIONS:

From the systematic investigation of the unidirectional crystallization of calcium metasilicate in both the $CaO-ZnO-Al_2O_3-SiO_2$ and $Na_2O-CaO-Al_2O_3-SiO_2$ systems it was found that the compositions containing between 53 and 56 mol % silica gave the most accurately aligned and undistorted fibrous materials. Too high a silica content resulted in materials containing broad, divergent fibres. However it was found to be necessary to have a sufficiently high silica content to give at least a small proportion of residual glass after heat treatment, in order to avoid thermal shock damage to the material on cooling from the fabrication temperature.

4.2. CRYSTAL GROWTH:

A static, isothermal heat treatment was found to be suitable for the production of relatively large amounts of unidirectionally crystallized calcium metasilicate from glasses in which the maximum rate of crystal growth at the appropriate temperatures was 5 microns per second. It was found to be unnecessary to use any special surface treatment to obtain sufficient surface nucleation sites.

For those systems which crystallize at 5 microns per

second or greater at the desired heat treatment temperature it was necessary to use a dynamic, temperature gradient technique in order to grow undistorted fibres of any substantial length. For this a novel modification had to be made to a relatively new technique in which glass rods pulled from a melt crystallize in the temperature gradient below the melt. This resulted in 10mm diameter rods, over 10mm long, containing fibres aligned parallel to the rod (pulling) axis.

4.3. FIBRE MORPHOLOGY:

Spherulitic type fibres gave the most accurately aligned materials, since these fibres do not have any secondary arms and only branch at very small angles (non-crystallographic branching). This crystal morphology was generally only found in association with the low-temperature polymorph of calcium metasilicate, since spherulitic growth is given at high undercoolings, i.e. from glasses and melts of high viscosity. Fibres between 5 and 50 microns in diameter were found to give the most perfect microstructures. Fibres that were too wide tended to be divergent, since this morphology was associated with somewhat sparse surface nucleation, and also tended to have relatively low aspect ratios. Conversely very fine fibres gave a structure consisting of an array of slightly divergent cones (segments of spherulites) and tended to recrystallize into lath shaped crystals if the heat treatment was too prolonged, due to the extremely large surface area to volume ratio of narrow

fibres. The crystallographic fibre orientation was found using long fibres produced by the rod-pulling technique and pinhole transmission X-ray analysis. The fibre axis was confirmed as corresponding to the [010] axis of the β-$CaSiO_3$ structure (the Dreirketten silica tetrahedra chain axis).

Dendritic type fibres only produced exact alignment in materials manufactured by the rod-pulling technique, when the development of secondary arms was somewhat inhibited and the primary dendrite spines could not coarsen as the rods were pulled down and cooled out of the crystal growth temperature region before this could occur. This crystal morphology was only found in association with the high-temperature polymorph of calcium metasilicate, since dendritic crystallization is given at intermediate under-coolings.

The fibre volume fractions were found, by a point counting technique, for the materials selected for testing. The fibre volume fractions were in all cases high, between 0.5 and 0.7, i.e. between 50 and 70 vol %.

4.4. CRYSTAL GROWTH KINETICS:

The activation energy for spherulitic, β-$CaSiO_3$, growth was found to be equivalent to the activation energy for viscous flow (energy required to break Si-O bonds) in the corresponding glass or melt. For dendritic, α-$CaSiO_3$, growth the activation energy was found to be equivalent to the activation energy for the diffusion of calcium ions through the corresponding glass. From this it was inferred

that for the growth of α-$CaSiO_3$ only the rearrangement of structures already existing in the metasilicate glass was necessary, whereas for the growth of the β-$CaSiO_3$ chain silicate these pre-existing silica tetrahedra structures had to be broken up prior to incorporation into the crystal lattice.

The kinetics of spherulitic crystallization were also calculated from the fibre width versus temperature characteristics, and these results agreed with the activation energy results, thereby verifying the Keith and Padden theory of spherulitic crystallization for calcium metasilicate crystallization from approximately metasilicate composition glasses.

4.5. THERMAL EXPANSION:

The thermal expansion characteristics parallel and perpendicular to the fibre axis were determined for natural wollastonite (calcium metasilicate) mineral. The longitudinal and transverse expansions were also found for several selected examples of the synthetic materials, from which it was generally seen that the expansion characteristics parallel to the fibre axis were dominated by the expansion of the fibres whereas perpendicular to the fibres the interfibre materials dominated the measured expansions. Materials containing about 30% residual glass showed a glass transition temperature transverse to the fibre axis, and rod-pulled materials containing $Ca_2ZnSi_2O_7$ as a secondary crystalline phase gave a hysteresis loop in the transverse thermal expansion versus temperature plots,

possibly due to a previously unreported, reversible phase change in this interfibre (secondary) crystallization phase.

4.6. MECHANICAL PROPERTIES:

The mechanical properties of the selected materials, reviewed in table 3.77, show that these unidirectionally crystallized specimens can be treated as unidirectional fibre reinforced, ceramic matrix composites. It was found that the strengths of the materials were generally low, due to the damaging thermal shock effect of the difference in expansion between the fibres and matrix. However the strengths parallel to the fibre axis were far greater than those perpendicular to the fibres, agreeing with the theories for composite materials. The strength results were similar for materials with a glass or crystalline interfibre matrix, and SEM micrographs revealed that in both cases the fracture paths were along the fibre/matrix interfaces. Comparing the transverse strength of a glass matrix material (RW14) to the calculated transverse strength of a glass matrix composite indicated that the fibre/matrix interfaces had zero tensile strength.

The dendritic material tested behaved more like a homogeneous brittle solid since it contained strong dendrite/matrix interfaces due to the keying effect of the secondary dendrite arms.

The work of fracture results also showed that these materials have similar properties to ceramic matrix composites since it was found that when spherulitic fibre specimens were fractured parallel to the fibre axis a

relatively large work of fracture value was obtained. This increased toughness was a result of the fracture cracks being deflected down the weak fibre/matrix interfaces and to fibre pull-out, as evidenced by the jagged "fibrous" type of fracture surfaces. In contrast the longitudinal dendritic material gave a small work of fracture since in this case there were no weak interfaces to deflect the cracks and there was no pull-out, giving a smooth, "brittle-fracture" type of fracture surface.

The Young's moduli found followed the same general trends as the strength results, and were again very low.

The mechanical properties confirm the opinion that these unidirectionally crystallized materials are very weak as macroscopic specimens. However the fine, crystalline fibres they contain should be individually very strong and stiff, since even the short length, distorted mineral wollastonite fibres, used to reinforce green ceramic ware bodies and Portland cement (85), are known to increase significantly the strengths of these substances. The finer the fibres the less are needed to give the same increase in strength, since it is thought that the essential factor is the chemical reactivity of the fibre (to form strong fibre/cement bonds) and this increases with the surface to volume ratio of the fibre (85). The increasing aspect ratio of the fibres may also increase their efficiency as reinforcing elements (see section 1.7.2.).

Maries tested approximately 1mm diameter RW17 composition crystalline rods, produced by the thin

rod-pulling technique, and found these to be somewhat stronger than glass rods of the same diameter (78) (although, since these glass rods were not flame polished, etched, or otherwise treated to eliminate surface flaws, they would not have been particularly strong (118)). This shows that the strength of the unidirectionally crystallized materials parallel to the fibre axis increases as the cross-sectional area of the specimen decreases.

To obtain 1 to 10 micron diameter spherulitic fibres, i.e. of similar diameter to the commonly used E-glass reinforcement fibres, it will be necessary to crush large cross-section rod-pulled specimens, when the individual fibres can be easily separated without damage due to the fracture occurring along the very weak fibre/matrix interfaces. It will not be possible to pull such narrow diameter fibres directly from the melt and crystallize them down the temperature gradient using a modified rod-pulling technique because as the rod diameter decreases the rod cooling rate increases and therefore the rods must be pulled more slowly to keep the glass in the critical crystal growth temperature range for a sufficiently long time for the desired devitrification to occur. For very fine rods this rate would be impractically slow.

4.7. SUGGESTIONS FOR FUTURE WORK:

In order to find out more about the kinetics of spherulitic and dendritic growth from melts over a wide range of undercoolings, including the conditions controlling the change over from the spherulitic to dendritic mechanisms,

it would be necessary to use glass systems which are known to give fibrous crystals under suitable circumstances and which do not give a crystalline phase transformation in the critical temperature range for crystallization. This would enable a much wider temperature range to be studied than was possible with calcium metasilicate. The rod-pulling technique would provide an elegant experimental tool for this investigation since the crystal growth rate, and hence undercooling, is easily controllable and using a seed nucleus metastable phases can be crystallized. The cooling rate, and temperature of onset of crystallization, can be found by incorporating a thermocouple junction into the nucleation point and this enables a T-T-T diagram to be constructed very quickly and simply, as was shown in section 3.1.8.

β-$CaSiO_3$ is known to be crystallographically similar to one of the polymorphs of sodium metaphosphate (135), i.e. the fibrous crystalline material known as Kurrol's salt ($NaPO_3$ - IV) (150), and therefore this may be a suitable phase to use for the study of the kinetics and morphology of crystallization from sodium metaphosphate glass, Graham's salt. The use of a phosphate glass system would have two main advantages; one that the glass would melt at a relatively low temperature (627°C for $NaPO_3$ glass (150)) thus simplifying the experimental techniques required, and the other that phosphate glasses are water soluble and can therefore be analysed by chromatography to determine the degree of polymerization of the anionic groups making

up the glass structure (22). Unfortunately a disadvantage of this system may be that the fibrous crystalline $NaPO_3$ - IV is reported as only being obtained by seeding a metaphosphate melt at between 550 and 600°C (150). However, since it was found that a metastable phase could be produced when a seed crystal is used with the rod pulling technique then it may prove to be possible to grow Kurrol's salt over a wider temperature range using this dynamic crystal growth technique.

The suitability of the synthetic fibrous calcium metasilicate materials for incorporation into a metallic matrix could be investigated using sectioned, polished surfaces of blocks cut from unidirectionally crystallized tiles as substrates for sessile drops of the metal or alloy under consideration. The wetting properties of the molten metal on the fibrous material could be found by analysing the shape of the drops.

Individual fibres of fibrous calcium metasilicate could be made any desired length and the required diameter by crushing rods produced by the rod-pulling technique, the pulling rate controlling the crystallization temperature and therefore the diameter of the individual spherulitic fibres produced. These fibres could be used to reinforce metallic matrices, possibly in association with fibre coatings designed to aid the metal wetting the fibres and to help alleviate the fibre/matrix thermal expansion mismatch. They could also be used to reinforce cement or plaster, since natural wollastonite fibres have already

been found to strengthen Portland cement and these fibres may be more resistant to alkaline environments than the glass fibres used at present.

APPENDIX I

CALCULATION OF DILATOMETER RESULTS

For this example calculation the results obtained from the RW14/5T tile material tested perpendicular to the β-$CaSiO_3$ fibre axis, i.e. RW14/5T transverse sample, are used.

Room temperature = 20°C.

Specimen length = 1.60cm.

Transducer input = 10mV.

Transducer output (coefficient) = 21.66mV per thou.in., i.e. for an output of x mV $\Delta\ell$, the equivalent change in length, is

$$\Delta\ell = \frac{x}{21.66} \times \frac{2.54}{1000} \text{ cm}$$

The temperatures from 100°C to the maximum were marked on the chart at the positions found from the thermocouple output trace and the millivolt output found at each temperature both for the increasing temperature (Up) and decreasing temperature (Down) ranges of the complete heating/cooling cycle. The appropriate "blank-run" correction for each particular temperature was added to the measured output at that temperature to allow for the imperfectly matched expansion of the dilatometer thrust rod and specimen holder, see section 2.11. The mean value of the mV output for each temperature was then found from all the results obtained for that type of sample, i.e. mean Up mV and mean Down mV in table I.1.

From the mV outputs the actual expansions were calculated, knowing the transducer coefficient (q.v.). However, an addition to these expansions had to be made to compensate for the expansion of the excess length of silica glass tube which supports the specimen over its length, i.e. expansion coefficient of pure silica glass is $0.56 \times 10^{-6} K^{-1}$ (146) and therefore at temperature T°C the correction added to the expansion for RW14/5T transverse specimens was,

$$\text{silica corr.} = 0.56 \times 10^{-6} \times 1.60 \times 10^{-2} \times (T - 20) \text{ m}$$

The true percentage expansion for each temperature, both Up and Down, could now be found,

$$\% \text{ Expn.} = \frac{\text{Expn. + Silica corr.}}{1.60 \times 10^{-2}} \times 100$$

This enabled a graph of percentage expansion versus temperature to be drawn, see figure 3.89.

The coefficients of expansion (α) corresponding to each percentage expansion were calculated by dividing the true expansion by the appropriate temperature interval multiplied by the original length of the specimen,

i.e. $$\alpha = \frac{\text{Expn. + Silica corr.}}{(1.60 \times 10^{-2}) \times (T - 20)} K^{-1}$$

See table I.1. This allowed an expansion coefficient versus temperature graph to be drawn, see figure 3.89.

95% probability errors were estimated at ± 10°C on the temperature scale, i.e. dT = 20°C, and ± 1mV on the expansion scale normalised for the varying specimen lengths, i.e. for RW14/5T transverse specimen

$$d\ell = \frac{1 \times 2.54 \times 10^{-2}}{21.66 \times 1000} \Big/ 1.6 \times 10^{-2}$$

$$d\ell = 1.5 \times 10^{-6}\ \text{m}$$

Therefore for the expansion coefficient,

since $$\alpha = \frac{\text{Expn.}\,\%}{(T - 20)}\ K^{-1}$$

then $$\frac{d\alpha}{\alpha} = \frac{(dT.\Delta\ell)/\Delta T^2}{\Delta\ell/\Delta T} + \frac{d\ell/\Delta T}{\Delta\ell/\Delta T}$$

i.e. $$\frac{d\alpha}{\alpha} = \frac{dT}{\Delta T} + \frac{d\ell}{\Delta\ell}$$

Table I.2 gives the calculated values of the above quantities and the resulting error in the expansion coefficient for each temperature range for RW14/5T transverse.

Temp. T°C	(T-20) K	Mean Up mV	Mean Down mV	Silica Corr. $x10^{5}$ m	True Expn. Up $x10^{5}$ m	True Expn. Down $x10^{5}$ m	%Expn. Up	%Expn. Down	Expn. Coeff. $x10^{6}K^{-1}$	Expn. Coeff. $x10^{6}K^{-1}$
650	630	58.5	58.5	0.56	7.42	7.42	0.464	0.464	7.36	7.36
600	580	51.7	52.2	0.52	6.58	6.64	0.411	0.414	7.09	7.14
500	480	42.1	39.4	0.43	5.37	5.05	0.336	0.316	7.00	6.58
400	380	33.8	29.2	0.34	4.30	3.76	0.269	0.235	7.08	6.18
300	280	23.2	20.1	0.25	2.97	2.61	0.186	0.164	6.64	5.86
200	180	14.25	12.75	0.16	1.83	1.66	0.114	0.103	6.33	5.72
100	80	5.25	4.75	0.07	0.62	0.56	0.044	0.040	5.50	5.00

Table I.1 :' Dilatometry data for RW14/5T - transverse.

$\frac{\Delta T}{K}$	$\frac{dT}{\Delta T}$ %	$\frac{d\ell}{\Delta\ell}$ % Up	$\frac{d\ell}{\Delta\ell}$ % Down	$\frac{d\alpha}{\Delta\alpha}$ % Up	$\frac{d\alpha}{\Delta\alpha}$ % Down	$d\alpha$ Up $\times 10^{6} K^{-1}$	$d\alpha$ Down $\times 10^{6} K^{-1}$
630	3.2	3	3	6	6	0.4	0.4
580	3.4	4	4	7	7	0.5	0.5
480	4.2	5	5	9	9	0.6	0.6
380	5.3	6	7	11	12	0.8	0.7
280	7.1	8	9	15	16	1.0	0.9
180	11.1	14	15	25	26	1.6	1.5
80	25.0	34	38	59	63	3.2	3.2

Table I.2 : 95% estimated errors for RW14/5T - transverse.

APPENDIX II

THREE-POINT BEND TEST SPECIFICATIONS

20mm Span (L) (73):

Specimen length = greater than 30 x 10^{-3}m.

Specimen breadth (b) = 5 x 10^{-3}m $\pm$ 0.25 x 10^{-3}m.

Specimen depth (d) = 2.5 x 10^{-3}m $\pm$ 0.25 x 10^{-3}m.

Cross-head speed ($\dot{y}$) = 0.1 x 10^{-3}m min^{-1}.

Strain rate = $6\dot{y}d/L^2$ min^{-1} (114)

= 3.75 x 10^{-3} min^{-1}.

Tungsten carbide rollers, 5 x 10^{-3}m diameter.

Span to depth ratio = 8 : 1.

7mm Span (see section 2.8.3.):

Specimen length = greater than 10 x 10^{-3}m.

Specimen breadth = 1.7 x 10^{-3}m $\pm$ 0.2 x 10^{-3}m.

Specimen depth = 0.9 x 10^{-3}m $\pm$ 0.2 x 10^{-3}m.

Cross-head speed = 0.1 x 10^{-3}m min^{-1}.

Strain rate = 11.0 x 10^{-3} min^{-1}.

Steel knife-edges, covered with PTFE tape.

Span to depth ratio = 8 : 1.

4mm Span (13):

Specimen length = greater than 5 x 10^{-3}m.

Specimen breadth = 2.5 x 10^{-3}m $\pm$ 0.2 x 10^{-3}m.

Specimen depth = 1.0 x 10^{-3}m $\pm$ 0.2 x 10^{-3}m.

Cross-head speed = 0.1 x 10^{-3} m min^{-1}.

Strain rate = 37.5 x 10^{-3} min^{-1}.

Steel knife-edges, covered with PTFE tape.

Span to depth ratio = 4 : 1.

APPENDIX III

CALCULATION OF MODULUS OF RUPTURE AND YOUNG'S MODULUS FROM LONG BEAM TEST RESULTS

The modulus of rupture (R) can be calculated from the load at fracture (P) found using a three-point bend test by using the formula

$$R = \frac{3PL}{2bd^2} \times g \text{ N m}^{-2}$$

(see section 1.7.3.), where

L = span of lower rollers.

b = specimen breadth.

d = specimen depth.

g = acceleration due to gravity.

For these example calculations the dimensions and experimental results for two of the recrystallized alumina "standards" will be used, one for the 20mm span three-point bend apparatus and the other the 7mm span three-point bend apparatus (see section 2.9.1. and 2.9.2. respectively).

	Specimen Al	Specimen al
L m	2×10^{-2}	7×10^{-2}
P g	22.0×10^{3}	3.71×10^{3}
b m	4.71×10^{-3}	1.68×10^{-3}
d m	2.62×10^{-3}	1.05×10^{-3}
g m s^{-2}	9.81	9.81
R N m^{-2}	2.038×10^{8}	2.063×10^{8}

Using the above calculation the values of R for a

complete set of specimens were found and from these the mean modulus of rupture ($\bar{R}$) calculated for that type of specimen.

The standard deviation for the set of results was calculated using the formula (148)

$$S(R) = \sqrt{\frac{1}{n-1} \sum_{i=1}^{n} (R - \bar{R})^2}$$

In order to compare the scatters of results for different sets of specimens the coefficient of variance was found, i.e.

$$\frac{S(R)}{\bar{R}} \times 100\ \%$$

For example, using the results from the RW14F internally nucleated material specimens,

	R MN.m	Mean $\bar{R}$ MN m^{-2}	S (R)	S (R) / $\bar{R}$ x 100%
F1	11.89			
F2	8.86			
F3	8.47			
F4	8.62			
F5	7.01	8.9	1.7	19%
F7	10.43			
F8	6.41			
F9	8.74			
F10	9.88			

The Young's modulus (E) may be found from three-point bend test results using the formula

$$E = \frac{PL^3}{4vbd^3} \times g\ N\ m^{-2}$$

(see section 1.7.3.), where

v = deflection at bottom of beam.

The deflections were measured from the load versus deflection output of the Instron testing machine by extrapolating the straight line regions of these curves back to the base line and measuring the distance from this intersection to the perpendicular from the point of fracture to the base line. This gives the distance travelled by the cross-head but eliminates the extra deflection introduced by the rollers settling into their grooves. Knowing the cross-head and chart speeds the deflection of the beam can be found, e.g. for alumina specimen Al (q.v.) the deflection, v, was found to be 5×10^{-5} m and therefore

$$E = 100.73 \text{ GN m}^{-2}$$

The mean of all the E results for the large alumina "standards" is 101.25 GN m^{-2}, less than half the manufacturer's (Morganite Refractories Ltd.) value for this "Purox" alumina which is 240.3 GN m^{-2} (245×10^{8} Kg m^{-2}). This is due to the testing apparatus not being perfectly hard. Substituting the higher (true) value for E into the formula for each specimen the corresponding "true" deflections can be found, i.e. for Al, using $E = 240.3 \times 10^{9}$ N m^{-2},

$$\text{"true" } v = 2.10 \times 10^{-5} \text{m}$$

The "true" deflection of each alumina specimen was calculated and the average found, then the difference between the average "measured" deflection and this average "true" deflection gave a value for the mean "machine" deflection

(the extra deflection due to the "softness" of the testing apparatus) of 2.57×10^{-5} m. From this a result for the "machine" Young's modulus was found using the average fracture load of the alumina specimens (19.35kg).

$$\text{"machine" } E = \frac{19.35 \times 10^{3}}{2.57 \times 10^{-5}} = 0.75 \times 10^{9} \text{ kg m}^{-2}$$

Therefore for the 20mm span bend tests on devitrified materials the "measured" deflection was found from the load versus deflection charts as described above and the "machine" deflection for that sample was calculated knowing the load at fracture (P kg)

$$\text{"machine" } v = \frac{P}{\text{"machine" } E} \text{ m}$$

Taking this "machine" v from the "measured" v leaves the "true" v for that particular specimen from which the corresponding value of E can be found using the formula given above, e.g. specimen RW9/4T1

P = 1.27 kg

b = 4.90×10^{-3} m

d = 2.82×10^{-3} m

"measured" v = 2.5×10^{-5} m

$$\text{"machine" } v = \frac{1.27 \times 10^{3}}{0.75 \times 10^{9}} = 0.17 \times 10^{-5} \text{ m}$$

$$\text{"true" } v = (2.5 - 0.17) \times 10^{-5} = 2.33 \times 10^{-5} \text{ m}$$

$$E = 9.76 \text{ GN m}^{-2}$$

It was found to be impossible to find the Young's modulus from the 7mm span test results as the test apparatus was far too soft, i.e. "machine" v was much greater than "true" v.

APPENDIX IV

CALCULATION OF INTERLAMINAR SHEAR STRENGTH FROM SHORT BEAM TEST RESULTS

The interlaminar shear strength (B) can be calculated from the load at fracture (P) found from a short span three-point bend test, in which the specimen failed in the shear mode, by using the formula

$$B = \frac{3P}{4bd} \times g \text{ N m}^{-2}$$

(see section 1.7.3.), where

b = specimen breadth

d = specimen depth

g = acceleration due to gravity.

For example, using the results obtained from RW14/5T1 specimen, i.e.

P = 1.82 kg

b = 2.40×10^{-3} m

d = 1.10×10^{-3} m

$$B = 5.08 \text{ MN m}^{-2}$$

APPENDIX V

During the preparation of this thesis Lewis and Smith published a paper (149) on spherulitic growth and recrystallization in barium silicate glasses, studied by optical and electron microscopy and electron diffraction. Spherulites grown at 700°C were found to consist of monoclinic fibres approximately 10nm wide. An electron microscope image of a diametrical section of a typical spherulite (figure 2a in the paper) does not reveal a sheaf-type structure at the centre, which in my opinion is probably a reflection of this very fine stable width causing prolific small angle branching at an early stage of growth and therefore establishing spherical symmetry within a very small distance of the nucleus. Selected area diffraction patterns were found from the fibres both parallel to and transverse to the fibre axis. From these Lewis and Smith found that there is a preferred growth axis along the fibre axis and also that neighbouring fibres are not randomly orientated with respect to rotation about the preferred growth axis. They concluded that this is due to a large group of neighbouring fibres evolving by a branching process from a common origin in order to maintain uniformity of interfibre spacing during radial growth.

This result is in agreement with the observed microstructure of the directionally crystallized, spherulitic type calcium metasilicate materials described in this thesis. The scanning electron micrographs of fracture

surfaces revealed evidence of related fibre orientation perpendicular to the growth axis (e.g. see figure 3.102), and in the optical micrographs of fine fibre transcrystallized materials the common birefringence of all the fibres constituting a cone (segment of spherulite) also indicates that these are in closely matched orientations transverse to the fibre axis.

REFERENCES

1. Livingston, J.D., Mater. Sci. Eng., 7, 1971, p. 61.
2. Davies, G.J., "Directionally-Grown Metallic Composites", Practical Metallic Composites, Inst. Metallurgists Spring Meeting 1973, Series 3, No. 1.
3. Kennard, F.L., Bradt, R.C. and Stubican, V.S., J. Amer. Ceram. Soc., 57, 1974, p. 428.
4. Stendera, J.W. and Benzel, J.F., J. Amer. Ceram. Soc., 58, 1975, p. 116.
5. Carpay, F.M.A. and Cense, W.A., Nature (Physical Science), 241, 1973, p. 19.
6. Carpay, F.M.A. and Cense, W.A., J. Cryst. Growth, 24/25, 1974, p. 551.
7. Carpay, F.M.A. and Cense, W.A., Scripta Metallurgica, 8, 1974, p. 11.
8. Reed-Hill, R.E., "Physical Metallurgy Principles", 1964, pub. by D. van Nostrand Co. Inc., New York.
9. Davies, G.J., Margaronis, I. and Broom, N.D., "Production of Composites by Dendritic Growth from the Melt", Practical Metallic Composites, Inst. Metallurgists Spring Meeting 1973, Series 3, No. 1.
10. McMillan, P.W., "Glass Ceramics", 1964, pub. by Academic Press, London.
11. Kelly, A., "Strong Solids", 1966, Clarendon Press, Oxford.
12. Veale, C., N.P.L. Report, 1965.
13. Phillips, D.C., Sambell, R.A.J. and Bowen, D.H., J. Mater. Sci., 7, 1972, p. 1454.
14. Ashbee, K.H.G., Nature, 252, 1974, p. 469.

15. Atkinson, D.I. and McMillan, P.W., J. Mater. Sci., 10, 1975, p. 2012.

16. Williamson, J., Tipple, A.J. and Rogers, P.S., J. Mater. Sci., 4, 1969, p. 1069.

17. Rogers, P.S. and Williamson, J., Verres Réfract, 26, 1972, p. 53.

18. Réamur, Memoires de l'Academie Royale, 1739, p. 370.

19. Jones, G.O., "Glass", 1971, pub. by Chapman and Hall Ltd. Science Paperbacks.

20. Doremus, R.H., "Glass Science", 1973, pub. by Wiley-Interscience, New York and London.

21. Eiss, R., "Chemical Bonding in Non-Crystalline Solids", in (118).

22. Rawson, H., "Inorganic Glass-Forming Systems", 1967, pub. by Academic Press Inc., New York.

23. Sun, K.H., Glass Ind., 27, 1946, p. 552, 580 and 581.

24. Stanworth, J.E., J. Amer. Ceram. Soc., 54, 1971, p. 61.

25. Zachariasen, W.H., J. Amer. Chem. Soc., 54, 1932, p. 3841.

26. Warren, B.E., "X-Ray Diffraction", 1969, pub. by Addison-Wesley Publishing Co., Massachusetts.

27. Urnes, S., "Modern Aspects of the Vitreous State", 1, 1960, ed. by Mackenzie, J.D., pub. by Butterworths, London.

28. Hägg, G., J. Chem. Phys., 3, 1935, p. 42.

28a Goodman, C.H.L., Nature, 257, 1975, p. 370.

29. Mackenzie, J.D., "Modern Aspects of the Vitreous State", 1, 1960, ed. by Mackenzie, J.D., pub. by Butterworths, London.

30. Huggins, M.L., Sun, K.H. and Silverman, M.S., J. Amer. Ceram. Soc., 26, 1943, p. 393.

30a. Hess, P.C., Geochimica et Cosomchimica Acta, 35, 1971, p. 289.

31. Tammann, G., "The States of Aggregation", 1925, pub. by D. van Nostrand and Co., New York.

32. Turnbull, D.J., J. Appl. Phys., 20, 1949, p. 817.

33. Turnbull, D.J. and Fisher, J.C., J. Chem. Phys., 17, 1949, p. 71.

34. Ainslie, N.G., Morelock, C.R. and Turnbull, D.J., Symposium on Nucleation and Crystallization in Glasses and Melts, Amer. Ceram. Soc., 1962, p. 97.

35. Turnbull, D.J. and Vonnegut, B., Industr. Engng. Chem., 44, 1952, p. 1292.

36. Stookey, S.D., Glastech, Ber. V International Glass Congress, 32K, Heft V.

37. Brockbank, C.J., Trans. Amer. Ceram. Soc., 15, 1913, p. 600.

38. Swift, H.R., J. Amer. Ceram. Soc., 30, 1947, p. 165.

39. Klause, K., Keram. Z., 8, 1956, p. 455; Interceram., No. 5, 1956, p. 14.

40. Leko, V.K. and Komarova, L.A., Inorg. Maters., 10, 1975, p. 1605.

41. Petticrew, R.W., U.S. Patent 3,754,881; 1973.

42. Burnett, D.G. and Douglas, R.W., Phys. Chem. Glasses, 12, 1971, p. 117.

43. Banerjee, B.K., J. Amer. Ceram. Soc., 36, 1953, p. 294.

44. Mukherjee, S.P. and Rogers, P.S., Phys. Chem. Glasses, 8, 1967, p. 81.

45. Doremus, R.H., "Modern Aspects of the Vitreous State", 1, 1960, ed. by Mackenzie, J.D., pub. by Butterworths, London.

46. Roginskaya, Yu.E., et al, Inorg. Maters., 11, 1975, p. 115.

47. Tamman, G., Z. Phys. Chem., 25, 1899, p. 441.

48. Kirkpatrick, R.J., Amer. Min., 60, 1975, p. 798.

49. Turnbull, D.J. and Cohen, M.H., "Modern Aspects of the Vitreous State", 1, 1960, ed. by Mackenzie, J.D., pub. by Butterworths, London.

50. Jackson, K.A., Uhlmann, D.R. and Hunt, J.D., J. of Cryst. Growth, 1, 1967, p. 1.

51. Hillig, R.W. and Turnbull, D.J., J. Phys. Chem., 24, 1956, p. 914.

52. Calvert, P.D. and Uhlmann, D.R., J. Cryst. Growth, 12, 1972, p. 291.

53. Uhlmann, D.R., Advances in Nucleation and Crystallization in Glasses, Amer. Ceram. Soc., 1971, p. 91.

54. Jackson, K.A., "Liquid Metals and Solidification", ASM, 1958, Cleveland.

55. Jackson, K.A., in "Growth and Perfection in Crystals", ed. by Doremus, R.H., 1958, pub. by Wiley, New York.

56. Cahn, J.W., Hillig, W.B. and Sears, G.W., Acta. Met., 12, 1964, p. 1421.

57. Jackson, K.A., Progress in Solid State Chemistry, 4, 1969, pub. by Pergammon Press, Oxford.

58. Cooper, A.R., Advances in Nucleation and Crystallization in Glasses, Amer. Ceram. Soc., 1971, p. 123.

59. Kelly, K.K., Bulletin 584, U.S. Bureau of Mines, 1960.

60. Lisovskaya, G.P., et al, Inorg. Maters., 11, 1975, p. 436.

61. Lofgren, G., Amer. J. Sci., 273, 1974, p. 243.

62. Weinburg, F. and Chalmers, B., Canadian J. Phys., 29, 1951, p. 382; 30, 1952, p. 488.

63. Rutter, J.W. and Chalmers, B., Canadian J. Phys., 31, 1953, p. 15.

64. Taylor, H.E. and Hill, D.K., "The Identification of Stones in Glass by Physical Methods", 1952, pub. by Glass Delegacy, Sheffield.

65. Keith, H.D. and Padden, F.J., J. of App. Phys., 34, 1963, p. 2409.

66. Mandelkern, L., Chem. Rev., 56, 1956, p. 903.

67. Bernauer, F., Gedrillte Kristalle, 1929, Borntträger, Berlin.

68. Morse, H.W. and Donnay, J.D.H., Amer. Mineralogist, 21, 1936, p. 391.

69. Tarján, I. and Matrai, M., "Laboratory Manual on Crystal Growth", 1972, Akad Kiadó, Budapest.

70. Hatch, F.H., Wells, A.K. and Wells, M.K., "The Petrology of the Igneous Rocks", 1949, pub. by Thos. Murby and Co., London.

71. Lofgren, G., J. Geophysical Res., 76, 1971, p. 5635.

72. Degen, M.G. and Toropov, N.A., Izvest. Akad. Nauk SSSR, Neorg. Mater., 2, 1966, p. 1621.

73. Barry, T.I., et al, J. Mater. Sci., 4, 1969, p. 596.

74. Freiman, S.W. and Hench, L.L., J. Amer. Ceram. Soc., 52, 1969, p. 111.

75. Johnson, W.A. and Mehl, R.F., Trans. AIME, 135, 1939, p. 416.

76. Maries, A. and Rogers, P.S., Nature, 252, 1975, p. 401.

77. Maries, A., NRDC Final Report, 1976.

77a. Glicksman, L.R., Glass Tech., 9, 1968, p. 131.

78. Maries, A., Rogers, P.S. and Weston, R.M., "Microstructure of Ceramics", Abstracts of British Ceramic Society Convention, 1975.

79. Livingston, J.D., Scripta Met., 7, 1973, p. 361.

80. Prewitt, C.T. and Peacor, D.R., Amer. Mineralogist, 49, 1964, p. 1527.

81. Tolliday, J., Nature, 182, 1958, p. 1012.

82. Jeffery, J.W., Acta. Cryst., 6, 1953, p. 821.

83. Jeffery, J.W. and Heller, L., Acta. Cryst., 6, 1953, p. 807.

84. Jeffery, J.W., "The Crystal Structures of the Anhydrous Compounds", in The Chemistry of Cements, I, ed. by Taylor, H.F.W., 1964, pub. by Academic Press, London.

85. Andrews, R.W., "Wollastonite", Inst. of Geological Sciences, 1970, pub. by HMSO.

86. Rostoker, D., U.S. Patent 3,552,915; 1971.

87. Buckner, D. and Roy, R., Bull. Geol. Soc. Amer., 66, 1955, p. 1536.

88. Ohnemuller, W. and Solf, A., Brit. Patent 1,301,172; 1972.

89. Rheinische Kalksteinwerke G.m.b.H., Brit. Patent 1,296,409; 1972.

90. Welch, J.H., "Phase Equilibria and High Temperature Chemistry in the Lime-Alumina-Silica and Related Systems", in The Chemistry of Cements, I, ed. by Taylor, H.F.W., 1964, pub. by Academic Press, London.

91. Louisnathan, S.J., Z. Kristallographie, 30, 1969, p. 427.

92. Deer, W.A., Howie, R.A. and Zussmann, J., "An Introduction to the Rock Forming Minerals", 1969, pub. by Longmans, London.

93. Pye, L.D., "The Vitreous State", in (118).

94. Smyth, H.T., J. Amer. Ceram. Soc., 38, 1955, p. 140.

95. Megaw, H.D., Mater. Res. Bull., 6, 1971, p. 1007.

96. Bayer, G., Proc. Brit. Cer. Soc., 22, 1973, p. 39.

97. Kittel, C., "Introduction to Solid State Physics", 4th ed., 1971, Wiley, New York.

98. Pugh, S.F., Brit. J. App. Phys., 18, 1967, p. 129.

99. Davidge, R.W. and Evans, A.G., Mater. Sci. Eng., 6, 1970, p. 281.

100. Evans, A.G. and Tappin, G., Proc. Brit. Cer. Soc., 20, 1972, p. 275.

101. Davidge, R.W. and Tappin, G., Proc. Brit. Cer. Soc., 15, 1970, p. 47.

102. Donald, J.W. and McMillan, P.W., J. Mater. Sci., 11, 1976, p. 949.

103. Davidge, R.W., 3rd International Meeting on Modern Ceramic Technologies, Rimini, Italy, 1976.

104. Bowen, D.H., Fibre Sci. and Tech., 1, 1968, p. 85.

105. Morley, J.G., Chem. in Britain, 10, 1974, p. 478.

106. Tattersall, H.G. and Tappin, G., J. Mater. Sci., 1, 1966, p. 296.

107. Goan, J.C. and Prosen, S.P., "Interfacial Bonding in Graphite Fibre-Resin Composites", 1969, ASTM STP 452.

108. Marschall, C.W. and Rudnick, A., "Conventional Strength Testing of Ceramics", in Fracture Mechanics of Ceramics, ed. by Bradt, R.C., Hasselman, D.P.H. and Lange, F.F., pub. by Plenum Press, New York.

109. Benham, P.P., "Elementary Mechanics of Solids", 1965, pub. by Pergammon Press, Oxford.

110. ASTM Standard C-158-72, "Flexure Testing of Glass (Determination of Modulus of Rupture)".

111. Shull, H.E., Bull. Amer. Ceram. Soc., 55, 1976, p. 202.

112. Hoagland, R.G., Marschall, C.W. and Duckworth, W.H., J. Amer. Ceram. Soc., 59, 1976, p. 189.

113. Neil, N.H., Bortz, S.A. and Firestone, R.F., Mater. Sci. Res., I, ed. by Stadelmaler, H.H. and Austin, W.W., pub. by Plenum Press, New York.

114. Hasselman, D.P.H., Kenny, G.B. and McKinney, K.R., J. Amer. Ceram. Soc., 58, 1975.

115. Bansal, G.K., Duckworth, W. and Niesz, D.E., Bull. Amer. Ceram. Soc., 55, 1976, p. 289.

116. Williamson, J., Tipple, A.J. and Rogers, P.S., J. Iron and Steel Inst., 206, 1968, p. 898.

117. Swarts, E.L., "Melting of Glass", in (118).

118. Pye, L.D., Stevens, H.G. and La Course, W.C., eds. of "Introduction to Glass Science", 1972, pub. by Plenum Press, New York.

119. Kerr, P.F., "Optical Mineralogy", 1959, pub. by McGraw-Hill Book Co., London.

120. Azároff, L.V., "Elements of X-Ray Crystallography", 1968, pub. by McGraw-Hill Book Co., London.

120a. Kleber, W., "An Introduction to Crystallography", 1970, pub. by Veb Verlag Technik, Berlin.

121. Berry, L.G. (ed), "Powder Diffraction File", pub. by Joint Committee on Powder Diffraction Standards, Pennsylvania.

122. Rowland, E.O., Min. Mag., 30, 1953, p. 254.

123. Clark, D.E., Hench, L.L. and Acree, W.A., J. Amer. Ceram. Soc., 58, 1975, p. 531.

124. Chayes, F., "Petrographic Modal Analysis", 1956, pub. by Wiley and Sons, Inc., New York.

125. Van der Plas, L. and Tobi, A.C., Amer. J. Sci., 263, 1965, p. 87.

126. Kumm, V.K-A. and Scholze, H., Tonid.-Ztg., 93, 1969, p. 332.

127. Levin, E.M., McMurdie, H.F. and Hall, F.P., "Phase Diagrams for Ceramists", 1956, ed. and pub. by Amer. Ceram. Soc. Inc..

128. Berezhnoi, A.I., "Glass-Ceramics and Photo-Sitalls", 1970, pub. by Plenum Press, New York.

129. Segnit, E.R., J. Amer. Ceram. Soc., 37, 1954, p. 273.

130. Norton, F.H., "Refractories", 3rd ed., 1949, pub. by McGraw-Hill Book Co. Inc., New York.

131. Strand, Z. and Douglas, R.W., Phys. Chem. Glasses, 14, 1973, p. 33.

132. Swift, H.R., J. Amer. Ceram. Soc., 30, 1947, p. 170.

133. Gutzow, I. and Toschev, S., Advances in Nucleation and Crystallization in Glasses, Amer. Ceram. Soc., 1971, p. 10.

134. Eitel, W., "Silicate Science", 1, 1964, Academic Press Inc., New York.

135. Heller, L. and Taylor, H.F.W., "Crystallographic Data for the Calcium Silicates", 1956, pub. by H.M. Stationery Office.

136. Rogers, B.A., Schooner, I.C. and Jorden, L., "Silver: Its Properties and Industrial Uses", 1936, National Bureau of Standards Circular C412.

137. Weston, R.M. and Rogers, P.S., Min. Mag., 40, 1976, p. 649.

138. Morey, G.W., "The Properties of Glass", 2nd ed., 1954, pub. by Reinhold Pub. Comp., New York.

139. Hall, F.P., J. Amer. Ceram. Soc., 13, 1930, p. 182.

140. Silverman, W.B., J. Soc. Glass Technol., 24, 1940, p. 59.

141. Stutzman, R.H., Salvaggi, J.R. and Kirchner, H.P., "An Investigation of the Theoretical and Practical Aspects of the Thermal Expansion of Ceramic Materials", 1959, U.S. Dept. of Commerce, Office of Technical Services.

142. Duwez, P., Borwn, F.H., and Odell, F., J. Electrochem. Soc., 98, 1951, p. 356.

143. Ryshkewitch, E., "Oxide Ceramics, Physical Chemistry and Technology", 1960, pub. by Academic Press, New York and London.

144. Yoder, H.S., Fortshr. Miner., 50, 1973, p. 140.

145. Campion, P.J., Burns, J.E. and Williams, A., "A Code of Practice for the Detailed Statement of Accuracy", 1973, pub. by NPL, HMSO.

146. Kelly, A. and Cooper, G.A. "Role of Interface in the Fracture of Fibre-Composite Materials", 1969, ASTM STP 452.

147. Phillips, D.C., J. Mater. Sci., 9, 1974, p. 1847.

148. Weast, R.C. (ed.), "Handbook of Chemistry and Physics", 55th ed., 1974-1975, pub. by CRC Press Inc., Cleveland.

149. Lewis, M.H. and Smith, G., J. Mater. Sci., 11, 1976, p. 2015.

150. Moeller, T., "Inorganic Chemistry: An Advanced Textbook", 1963, pub. by J. Wiley Inc., New York.

MINERALOGICAL MAGAZINE, JUNE 1976, VOL. 40, PP. 649–51

Anisotropic thermal expansion characteristics of wollastonite

VALUES quoted in the literature for the linear thermal expansion coefficient of wollastonite ($CaSiO_3$) vary between $9{\cdot}4\times10^{-6}$ °C^{-1} (100 to 200 °C) Stutzman, Salvaggi, and Kirchner (1959), $6{\cdot}5\times10^{-6}$ °C^{-1} (25 to 800 °C) Whitmer (1969), and approximately 6×10^{-6} °C^{-1} (100 to 1000 °C) Rigby, Lovell, and Green (1945). These sources do not give the form of the temperature dependence of the expansion coefficient. Wollastonite has a triclinic crystal structure and forms orientated aggregates and therefore is likely to exhibit anisotropic thermal expansion (Bayer, 1973).

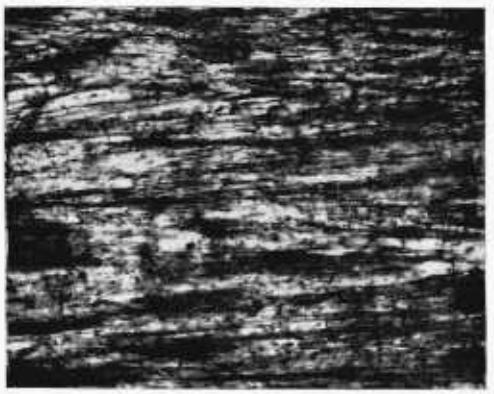


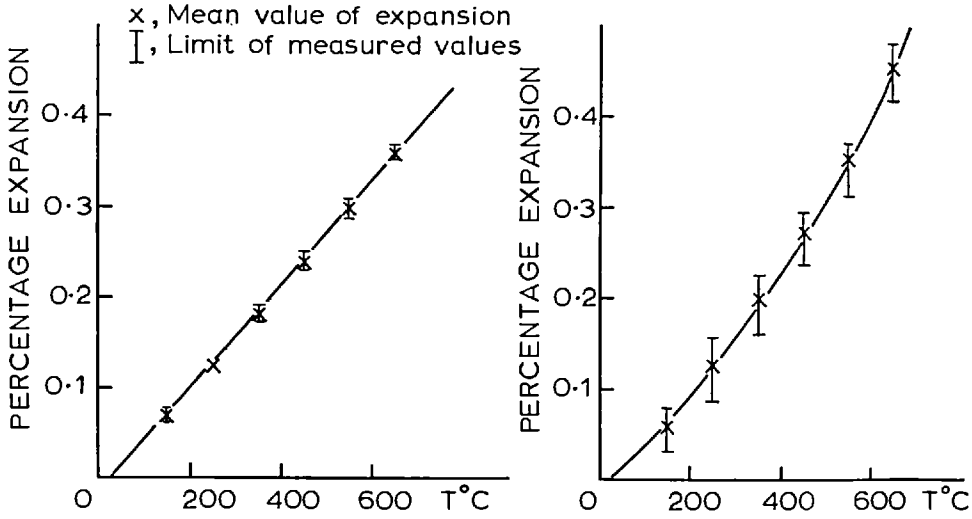
FIG. 1. Photomicrograph of the wollastonite sample showing the alignment and dimensions of the fibres. ×60.

In the crystal structure of wollastonite the silicon–oxygen tetrahedra form chains that run parallel to the crystallographic *b*-axis and have a repeat distance of three tetrahedra. The calcium ions are linked by irregular octahedral coordination to six of the oxygen ions in the chain tetrahedra. Parawollastonite, the other low-temperature polymorph, has a monoclinic structure closely related to the triclinic wollastonite structure by a simple packing disorder (Tolliday, 1958). Some wollastonite deposits have been shown to be composites of these two structures (Jeffery, 1953).

A sample of wollastonite from Meldon, Devon (BM 1913, 253) in the form of an aggregate of parallel fibres was obtained from the British Museum (Natural History). Fig. 1 is an optical micrograph of this sample in thin section showing the fibres to be mutually parallel, approximately 20 μm thick and apparently continuous. The *b*-axis runs along the length of the aligned fibres, with the *a* and *c*-axes randomly orientated in the plane perpendicular to this fibre direction. Two rectangular prism test specimens were cut from the sample, one approximately $5\times5\times13$ mm, having its long side parallel to [010], and the other approximately $5\times5\times10$ mm, having the long side in the (010) plane.

The thermal expansion of each specimen was measured using a dilatometer in which one end of a horizontal silica glass thrust-rod was connected to a linear variable

differential transformer whilst the other bore on to the square end of the specimen, the whole assembly being supported in a silica-glass tube. The dilatometer furnace was fitted with a temperature controller allowing the expansion to be measured over complete heating and cooling cycles between 25 and 650 °C at the linear rate of 2 °C per minute. Runs without a specimen enabled corrections to be applied for the dimensional changes of the silica-glass system with changing temperature, and the coefficient



FIGS. 2*a* and 2*b*. FIG. 2*a* (*left*). Expansion characteristics in the direction of the fibres, i.e. [010]. FIG. 2*b* (*right*). Expansion characteristics perpendicular to the fibre direction, i.e. (010).

of expansion of silica glass was added to the calculated coefficients to allow for the expansion of the outer tube. The coefficient of expansion of pure silver was measured in this manner and found to be $20{\cdot}1\times10^{-6}$ °C^{-1} (25 to 650 °C), which is within 2·5 % of the tabulated value of $20{\cdot}6\times10^{-6}$ °C^{-1} (0 to 500 °C), Rogers, Schooner, and Jordan (1936).

The percentage expansion over the temperature range 25 to 650 °C was calculated for each of the wollastonite specimens, using the data obtained from both the heating and cooling measurements, see fig. 2. The expansion along the fibre axis, i.e. [010], showed a linear increase in dimension with temperature, but perpendicular to the fibres, i.e. (010) the rate of expansion increased with increasing temperature. The expansion coefficients (25 to 650 °C) calculated for each orientation are:

[010] : $6{\cdot}23\times10^{-6}$ °C^{-1}, standard deviation = 0·108

(010) : $7{\cdot}77\times10^{-6}$ °C^{-1}, standard deviation = 0·361

The larger scatter given in the results for the (010) specimen was due to the shorter specimen length (governed by the dimensions of the sample of natural mineral), to the less rigid crystallographic orientation in this specimen, and to the effect of inter-fibre

grain boundaries. Since fig. 2*b* shows a non-linear relationship between expansion and temperature a series of coefficients for various temperature ranges were derived.

Expansion coefficient $\times 10^6$ °C^{-1} :	5·7	6·3	6·7	7·0	7·5
T °C (range 25 to T °C):	200	300	400	500	600

It can be seen that these rise from a value below the constant [010] coefficient at room temperature to one above it at 650 °C, the expansion anisotropy of wollastonite reversing at approximately 300 °C.

The reasons for the anisotropy must lie in the different forms of crystal structure and bonding predominating in each direction. In the [010] specimen the SiO_4 tetrahedra chain may control the rate of expansion, as in a network structure in which the coordination polyhedra are tilted with respect to each other the simple bond-length expansions are modified by the manner in which the angle of tilt changes with temperature (Megaw, 1971). In the (010) orientation the presence of the calcium ions between the SiO_4 tetrahedra may determine the magnitude of the thermal expansion and the amount of the expansion anisotropy (Bayer, 1973). However, any conclusions must be tentative as there is no generally applicable theory for the interpretation of the expansion coefficients of complex crystal structures (Austin, 1952).

Acknowledgements. We are grateful to the Department of Mineralogy, British Museum (N. H.) for the provision of samples and to the S.R.C. for financial support.

R. M. Weston
P. S. Rogers

Department of Metallurgy and Materials Science
Imperial College
London, SW7 2BP

REFERENCES

Austin (J. B.), 1952. *Journ. Amer. Ceram. Soc.* **35** [10], 243–53.
Bayer (G.), 1973. *Proc. Brit. Ceram. Soc.* **22**, 39–53.
Jeffery (J. W.), 1953. *Acta Cryst.* **6**, 821–5.
Megaw (H. D.), 1971. *Mater. Res. Bull.* **6**, 1007–18.
Rigby (G. R.), Lovell (G. H. B.), and Green (A. T.), 1945. *Trans. Brit. Ceram. Soc.* **44** [3], 37–52.
Rogers (B. A.), Schooner (I. C.), and Jordan (L.), 1936. *Silver: Its Properties and Industrial Uses*, National Bureau of Standards Circular C412.
Stutzman (R. H.), Salvaggi (J. R.), and Kirchner (H. P.), 1959. *An Investigation of the Theoretical and Practical Aspects of the Thermal Expansion of Ceramic Materials*, U.S. Department of Commerce, Office of Technical Services.
Tolliday (J.), 1958. *Nature*, **182**, 1012–13.
Whitmer (M. T.), 1969. *Industrial Minerals*, **19**, 16–20.

[*Manuscript received 4 October 1975*]

© Copyright the Mineralogical Society.